

Cationic Cellulose Nanocrystals for the Flocculation of Mature Fine Oil Sands Tailings

by

Salha Alharthi

A thesis

presented to the University of Waterloo

in fulfillment of the

thesis requirements for the degree of

Doctor of Philosophy

in

Chemical Engineering (Nanotechnology)

Waterloo, Ontario, Canada, 2021

© Salha Alharthi 2021

Examining committee membership

The following served on the Examining Committee for this thesis. The decision of the Examining Committee is by majority vote.

External Examiner	NAME: Hu Xiao Title: Professor
Supervisor	NAME: Michael K. C. Tam Title: Professor
Internal Member	NAME: Boxin Zhao Title: Professor
Internal Member	NAME: Ting Tsui Title: Professor
Internal-external Member	NAME: Jean Duhamel Title: Professor

Author's declaration

This thesis consists of material all of which I authored or co-authored: see Statement of Contributions included in the thesis. This is a true copy of the thesis, including any required final revisions, as accepted by my examiners.

I understand that my thesis may be made electronically available to the public.

Statement of Contributions

The work presented in this thesis is the result of work performed by the author and several scientific collaborators. Contributions from each researcher and the resulting publications are described here. The manuscripts for each part were written by me and edited by the supervisor Prof. Michael Tam.

The work in Chapter 4 has been accepted as: Salha Alharthi, Nathan Grishkewich, Dr. R. M. Berry and Prof. Michael Tam. (2020). Functional cellulose nanocrystals containing cationic and thermo-responsive polymer brushes. *Carbohydrate polymers*, 246, 116651. Salha performed all the experiments and wrote the manuscript. Nathan helped in revising the manuscript. Dr. Berry proofread the manuscript. Prof. K.C. Tam edited the manuscript. The work in Chapter 5 has been performed by Salha. Prof. K.C. Tam edited the manuscript. The work in Chapter 6 has been performed by Salha. Prof. K.C. Tam edited the manuscript. The work in Chapter 7 has been performed by Salha. Yingzhan Li helped in functionalization of CNC. Mohankandhasamy Ramasamy helped me in the conductometric titration settings. Prof. K.C. Tam edited the manuscript.

Abstract

As the volume of oil sands tailings continues to increase each year with a concurrent need for better flocculants to replace the inorganic electrolytes and synthetic polymers, natural polymers are being considered as good substitutes. Cellulose nanocrystals (CNCs) possess interesting properties such as high specific area, biodegradability, surface functionalization capabilities and their large scale availability. This thesis explores the development of CNC-based flocculants for bentonite clay removal.

Cationic and thermo-responsive CNC-based copolymers were prepared via the free radical polymerization technique. The thermo-responsive characterization of the CNC-g-poly(oligo(ethylene glycol) methyl ether methacrylate) (CNC-POEGMA) indicated that the LCST could be tuned by adjusting the poly(2-methacryloyloxyethyl) trimethyl ammonium chloride (PDMC) content. The cloud point measurements revealed that the LCST of CNC-POEGMA decreased in the presence of salt following a typical salting-out effect. Additionally, CNC-POEGMA-PDMC displayed two salt-responsiveness behaviors depending on the DMC content. CNC-POEGMA-PDMC with low DMC ratio displayed salting-in effect at low salt concentrations due to the extension of adsorbed PDMC caused by the screening of negative charges on CNCs by sodium cations. On the other hand, higher salt concentrations led to salting-out effect due to the strong ion-pair formation that removed the hydration shell around PDMC along with the polarization of water around POEGMA. The flocculation results of CNC-POEGMA-PDMC revealed that the thermo-responsive property could facilitate the formation of compact flocs at low dosage.

The use of CNC-PDMCs cationic copolymers synthesized via the Activators ReGenerated by Electron Transfer polymerization (ARGET-ATRP) as flocculants for bentonite removal was also investigated. CNC-PDMC with different chain length demonstrated pH and salt-responsiveness. The hydration and conformation of the CNC-PDMC were more sensitive in the presence of salt due to the higher hydrophobicity of the ion-pair formed between the chloride ions and the quaternary ammonium groups. The flocculation results indicated that CNC-PDMCs had better performance compared to inorganic electrolytes at low dosage. The flocculation performance of the CNC-PDMCs and inorganic electrolytes after 5 min settling followed the Hofmeister series, and the flocculation behavior after 24 h settling agreed with DLVO theory.

Three cationic-biopolymers were synthesized: CNC-g-PDMC, PDADMAC-coated-CNC and PDADMAC-coated-CNF. The CNC-g-PDMC prepared via the ARGET-ATRP possessed a branched-cationic structure while the other two polymers prepared via physical adsorption had a flat-cationic structure. The effect of cationic charge distribution of three cationic-biopolymer based flocculants on bentonite removal was evaluated. The flocculation results indicated that the cationic charge distribution affected the performance of the flocculants. The extended-cationic brushes of CNC-PDMC possessed better approachability toward bentonite particles compared to the coated-cationic layer of PDADMAC-CNC and PDADMAC-CNF. These findings are in agreement with the Singh's model on the dependence of flocculation efficiency on the conformation of the flocculants. The microscopic images showed that the flocs formed with CNC-PDMC were more compact compared to flocs formed with the PDADMAC-CNC and PDADMAC-CNF.

The effect of brush sequence, charge density and salt concentration on the thermo-responsive behavior of cationic and thermos-responsive CNC-based copolymers was studied. The LCST of CNC-PMEO₂MA was found to be 24.5 °C, and after grafting with two different ratios of PDMC

brushes on PMEO₂MA brushes, the LCST could be tuned by adjusting the PDMC content. The CNC-PMEO₂MA-PDMC with a relatively low PDMC content exhibited a broad phase transition and the LCST increased to 28.5 °C. However, the CNC-PMEO₂MA-PDMC with higher PDMC content, resulted in a sharp transition behavior similar to the CNC-PMEO₂MA and the LCST was 25 °C. The observed trend was due to steric hindrance of the polymer brushes. The higher the grafting density yielded brushes with lower hydration and the stronger hydrophobic interactions between the polymethacrylate backbone of the chains being densely grafted on the CNC substrate. For the copolymers with the opposite sequence, CNC-PDMC-PMEO₂MA, the LCST was very close to CNC-PMEO₂MA indicating that the presence of PDMC brushes on the inner layer had no effect on its thermo-responsive property. The addition of salt tuned the LCST of the CNC-PMEO₂MA leading to a typical salting-out effect as the chloride ions polarized the water molecules around the polar groups of PMEO₂MA. On the other hand, the CNC-PMEO₂MA-PDMC and CNC-PDMC-PMEO₂MA displayed similar salt-responsiveness behavior; displaying a salting-out effect at low salt concentrations and salting-in effect at high salt concentrations.

Acknowledgements

First of and foremost, I thank God for providing me this opportunity and granting me the strength and courage to complete this thesis.

This thesis appears in its current form due to the assistance of several people who contributed to the research, dissertation and study of this work. I am forever grateful to Professor Michael Tam for agreeing to be my thesis advisor. He has supported me throughout my thesis with his patience and expertise. He has gone beyond the call of a thesis advisor to assume the role of an academic father, making an effort to support me during difficult times when I needed to move to another country to study.

I am sincerely grateful to the committee members Prof. Hu Xiao, Prof. Boxin Zhao, Prof. Ting Tsui and Prof. Jean Duhamel for their insightful remarks and suggestions regarding my research and thesis.

I offer my sincerest gratitude to Professor Juewen Liu for allowing me to use his facilities. I would also like to thank Howard Siu as a laboratory instructor in the Chemistry department for his assistance to preform FTIR analysis. Special thanks also go to all the staff members of Department of Chemical Engineering especially Judy Caron who has helped me in several administrative aspects during my graduate studies at University of Waterloo.

I am also grateful to the scholarship provided by the Saudi Arabia government, Imam Abdulrahman Bin Faisal University (IAU), enabling me to pursue the doctoral study at the University of Waterloo. I also wish to thank the Saudi Arabian Cultural Bureau (SACB) for the support and constant encouragement and for funding the project.

I would also like to extend my deepest gratitude to all my kind lab-mates who were willing to help me whenever I needed their support.

Words fail to express my appreciation to my husband Mohammed who gave up his job to move with me to Canada. Without your support and encouragement, I could not have finished this work, and it was you who take care of our family, and may the God give you all the best in return.

To my lovely sons, Nasser, Mesfer, and Gaith, a big thank you for your great patience and understanding. I want to express my gratitude and deepest appreciation to my family especially my parents Mrs. Sabta, and Mr. Nasser who offered their unceasing encouragement, unconditional love, support and attention. My sisters and brothers, thank you so much for being supportive especially my sister Amal who has made countless sacrifices to help me get to this point.

Table of Contents

<i>Abstract</i>	<i>v</i>
<i>Acknowledgements</i>	<i>viii</i>
<i>List of Figures</i>	<i>xiii</i>
<i>List of Tables</i>	<i>xviii</i>
<i>List of Schemes</i>	<i>xix</i>
<i>List of Abbreviations</i>	<i>xx</i>
Chapter 1. Introduction	1
1.1 Statement of problem	1
1.2 Objectives and Scope of Research.....	2
1.3 Outline of the thesis	3
Chapter 2. Literature Review	4
2.1. Oil sands extraction processes.....	4
2.1.1. Clark hot water extraction process (CHWE).....	4
2.2.2 Steam assisted gravity drainage process (SAGD).....	5
2.2 Environmental issues posed by oil sands processing.....	6
2.2.1 Issues related to tailings management.....	6
2.2.2 Current industry practices for tailings treatment.....	7
2.3 Theory of coagulation and flocculation	9
2.3.1 Types of additives used	10
2.4 Mature fine tailings composition	13
2.5 Mature fine tailings stability	14
2.6 Suspensions and particle dynamics.....	16
2.7 Clays and their behavior in suspension	16
2.8 Colloid - electrolyte interactions	21
2.9 Colloid particles interactions	23
2.10 Colloid - Polymer Interactions.....	25
2.10.1 Effect of polymers on zeta potential	28
2.11 Cellulose.....	30
2.11.1 Cellulose nanocrystals.....	31
2.11.2 Modification of cellulose nanocrystals.....	32
2.12 Introduction to stimuli-responsive polymers.....	37
2.13. Thermo-responsive polymers.....	38
2.13.1. Thermodynamics of thermo-transitions	39
2.13.2. Phase transition behaviors.....	42
2.13.3. Types of phase separation behaviors	46
2.13.4. Factors affecting the LCST.....	48
2.13.5. Thermo-responsive cellulose nanocrystals-based copolymers.....	62
Chapter 3. Analytical Instruments	64

3.1. Fourier Transform Infrared Spectrometry	64
3.2. Dynamic Light Scattering (DLS)	67
3.2.1. Particle size	67
3.2.2. Particle charge	70
3.3. Transmission Electron Microscopy	74
3.4. Ultraviolet-Visible (UV-Vis) Spectroscopy	76
3.5. Conductometric titration	78
Chapter 4. Functional Cellulose Nanocrystals Containing Cationic and Thermo-Responsive Polymer Brushes for Bentonite Removal.....	81
4.1. Introduction.....	83
4.2. Experimental section.....	86
4.2.1. Materials	86
4.2.2. Preparation of CNC-g-POEGMA	87
4.2.3. Preparation of CNC-g-POEGMA-g-PDMC.....	87
4.2.4. Characterization	88
4.3. Results and Discussion	89
4.3.1. Preparation and characterization of the CNC-g- POEGMA-g-DMC.....	89
4.3.2. Thermo-responsive characteristics of the copolymers	96
4.3.3. The effect of DMC composition on the thermo-responsive properties of CNC-g-POEGMA-g-PDMC.....	101
4.3.4. The effect of salt on the thermo-responsive properties of CNC-g-POEGMA-g-PDMC.....	103
4.3.5. The effect of dosage on the turbidity removal efficiency.....	107
4.3.6. The effect of dosage on the zeta potential.....	109
4.3.7. Proposed mechanisms.....	111
4.4. Conclusions.....	113
Chapter 5. Flocculation of Bentonite by Cationic Cellulose Nanocrystals	116
5.1. Introduction.....	117
5.2. Experimental section.....	120
5.2.1. Materials	120
5.2.2. Synthesis of the brominated CNC macroinitiators (CNC-Br)	120
5.2.3. Synthesis of the CNC-PDMC.....	120
5.2.4. Characterization	121
5.2.5. Flocculating characteristics	122
5.3. Results and discussion.....	123
5.3.1. Preparation and characterization of CNC-PDMC.....	123
5.3.2. The effect of pH on the pH-responsiveness of CNC-PDMCs	127
5.3.3. The effect of salt on the stability of the CNC-PDMC	129
5.3.4. The effect of dosage on the flocculation of bentonite clay	132
5.3.5. The effect of dosage on the zeta potential.....	133
5.3.6. Proposed mechanisms.....	134
5.3.7. The effect of different electrolytes on the zeta potential of bentonite clays	136
5.3.8. The effect of different electrolytes on the turbidity removal efficiency	137
5.3.9. Proposed mechanism	138
5.3.10. Comparison between the flocculation behavior of CNC-PDMC and inorganic electrolytes.....	139
5.4. Conclusions.....	141

Chapter 6. Evaluation of Cationic Biopolymer-Based Flocculants on Bentonite Removal: Effect of Cationic Charge Distribution.....	142
6.1. Introduction.....	143
6.2. Experimental section.....	146
6.2.1. Materials	146
6.2.2. Preparation of the PDADMAC-coated CNCs (CNC-PDADMAC).....	146
6.2.3. Preparation of the PDADMAC-coated CNFs (CNF-PDADMAC)	146
6.2.4. Synthesis of the brominated CNC macroinitiators (CNC-Br)	147
6.2.5. Synthesis of the CNC-PDMC.....	147
6.2.6. Characterization	147
6.2.7. Flocculating characteristics	148
6.3. Results and discussion.....	149
6.3.1. Preparation and characterization of the CNC-PDMC, PDADMAC-CNC, and PDADMAC-CNF	149
6.3.2. The effect of dosage on the zeta potential	153
6.3.3. The effect of dosage on the turbidity removal efficiency.....	155
6.3.4. The effect of dosage on the floc size	156
6.3.5. Proposed mechanisms.....	159
6.4. Conclusions.....	160
Chapter 7. Effects of Chain Architecture and Grafting Composition on the Thermo-responsive behavior of Cationic and Thermo-responsive Copolymers	162
7.1. Introduction.....	163
7.2.1. Materials	165
7.2.2. Synthesis of CNC-macroinitiator (CNC-Br)	165
7.2.3. Synthesis of CNC-PMEO ₂ MA	165
7.2.4. Synthesis of CNC-PMEO ₂ MA-PDMC.....	166
7.2.5. Synthesis of CNC-PDMC.....	166
7.2.6. Synthesis of CNC-PDMC-PMEO ₂ MA.....	167
7.2.7. Characterization	167
7.3. Results and discussion.....	168
7.3.1. Structural analysis	168
7.3.2. Thermo-responsive characteristics of the copolymers	175
7.3.3. The effect of salt on the thermo-responsive properties of the copolymers grafted on CNCs.....	181
7.4. Conclusions.....	187
Chapter 8. Original Contributions and Recommendations for Future Studies.....	189
8.1. Original contributions to research.....	189
8.1.1. Functional Cellulose Nanocrystals Containing Cationic and Thermo-Responsive Polymer Brushes for Bentonite Removal.....	190
8.1.2. Flocculation of Bentonite by Cationic Cellulose Nanocrystals.....	191
8.1.3. Evaluation of Cationic Biopolymer-Based Flocculants on Bentonite Removal: Effect of Cationic Charge Distribution	191
8.1.4. Effects of Chain Architecture and Grafting Composition on the Thermo-responsive behavior of Cationic and Thermo-responsive Copolymers.....	192
8.2. Recommendations for future studies	192
References	194

List of Figures

Figure 2. 1. Schematic flowsheet of Clark Hot Water Extraction process (CHWE) for oil sands ⁴ .	5
Figure 2. 2. Schematic diagram of Steam Assisted Gravity Drainage (SAGD) process ⁵	6
Figure 2. 3. Schematic diagram of consolidated/composite tailings (CT) technology ¹ .	8
Figure 2. 4. Schematic diagram of charge neutralization mechanism using inorganic coagulants (a), electrostatic patch mechanism using cationic polyelectrolyte (b) and bridging mechanism using polymeric flocculants (c) ¹¹ .	10
Figure 2. 5. Classification of additives used for waste-water treatment.	12
Figure 2. 6. Composition of mature fine tailings compared to that of oil sands ²³ .	14
Figure 2. 7. A model for the interactions between bitumen, minerals, and non-bitumen combustibles (NBC) in tailings ²⁷ .	15
Figure 2. 8. The organic model for MFT stability and the role of bitumen ²⁸ .	16
Figure 2. 9. Three-dimensional structure of the clay minerals ³⁰ .	18
Figure 2. 10. Schematic view of clay platelets and their anisotropic charging behavior. The faces (basal planes) exhibit permanent negative charge, whereas edge faces show amphoteric, pH-dependent behavior similar to oxide minerals ³² .	19
Figure 2. 11. Bentonite in solution A) swelling, B) “house of card structure” at low pH (below 7) and C) platelets dispersion at pH above 7 ³³ .	20
Figure 2. 12. (a) Molecular structure of MMT containing exchangeable sodium ion (MMT-Na ⁺), (b) high aspect ratio clay platelet, and (c) schematic representation of side view between layers ³⁵ .	20
Figure 2. 13. Schematic illustration of the electrical double layer ⁴⁰ .	23
Figure 2. 14. Schematic of repulsive and attractive potential as a function of distance between particle surfaces ⁴² .	25
Figure 2. 15. Possible conformations of polymer chains at solid-liquid interfaces: (a) thin layers with a low adsorbed layer thickness; (b) coils and loops with a moderate adsorbed layer thickness; (c) Trains, loops, and tails with a high adsorbed layer thickness ⁴⁴ .	26
Figure 2. 16. (a) Adsorption of polymer and formation of loops available for binding. (b) Polymer bridging between particles (aggregation). (c) Re-stabilization of colloid particles (floc breakup) ¹⁰ .	28
Figure 2. 17. Diagram showing the series of events when an uncharged, flexible polymer adsorbs at a clay mineral surface from a dilute aqueous solution. (A) Polymer in solution adapting a random coil conformation; (B) on adsorption, the polymer chain uncoils and adopts a train-loop-tail conformation, displacing relatively ordered water molecules from the interface into the external (bulk) solution ⁴⁵ .	28
Figure 2. 18. The effect of adsorbed uncharged homopolymers on the structure of the electrical double layer at a negatively charged (clay mineral) surface ¹⁰ .	29
Figure 2. 19. Chemical structure of cellulose chains ⁴⁹ .	30
Figure 2. 20. (a) Structural hierarchy of the cellulose fiber components from the tree to the anhydroglucose, (b) preparation of nanocrystals by selective acid hydrolysis of the disorganized regions of cellulose microfibrils ⁵⁰ .	31
Figure 2. 21. Schematic representation of the isolation of CNC ⁵³ .	32
Figure 2. 22. Diverse surface modifications on cellulose nanocrystals, red arrows represent the substitution of surface hydroxyl groups with small molecules, blue arrows represent the surface	

modification based on the “graft onto” strategy, and yellow arrows represent the surface modification based on the “graft from” strategy ⁵²	35
Figure 2. 23. Grafting of polymer brushes on CNCs by (a) the “grafting-to” approach whereby pre-synthesized polymer with end-functionality “B” react with CNC surface “A” groups and (b) the “grafting-from” approach whereby polymers are grown from surface-immobilized initiators (I) by adding monomers to the growing polymer chain active site ⁶³	36
Figure 2. 24. Schematic diagram showing the common surface - OH substitution approaches classified as (A) sulfonation; (B) acetylation/esterification; (C) silylation; (D) TEMPO-oxidation; (E) cationization, and (F) carbamation. Note that the newly introduced functional groups are highlighted in red ⁶²	36
Figure 2. 25. Schematic illustration of stimuli for stimuli-responsive polymers ⁶⁷	37
Figure 2. 26. Schematic example of the different types of responses of “stimuli” polymer systems to environmental stimuli ⁷¹	38
Figure 2. 27. Phase diagram for polymer solution (A) lower critical solution temperature (LCST) behavior and (B) upper critical solution temperature behavior ⁷⁶	39
Figure 2. 28. Placement of solute molecules on a lattice. (Left) N ₂ small molecules. (Right) A polymer chain occupying N ₂ cells ⁷⁸	40
Figure 2. 29. Schematic illustration of the four thermodynamic stable states of (PNiPAAm) homopolymer, and the typical hydrodynamic radius distribution as a function of temperature for (PNiPAAm) (B) ⁸²	43
Figure 2. 30. Temperature dependence of the apparent hydrodynamic average diameter for poly(BPEM-graft-DMA-stat-BA molecular brush, 0.1 wt% and 1.0 wt% solutions concentrations ⁸³	44
Figure 2. 31. Concentration dependence of the conformational changes of amphiphilic block copolymer ⁸⁴	45
Figure 2. 32. Schematic illustration of two types of the micellar structure of a block copolymer containing PNiPAAm in aqueous dispersion ⁸¹	46
Figure 2. 33. Schematic illustration of three types of the thermo-responsive polymers in aqueous dispersion ⁸⁵	47
Figure 2. 34. Transmittance curve of a 0.2 mg/ml aqueous dispersion of P(S-b-NIPMA) ⁸⁶	48
Figure 2. 35. The effect of M _n on the LCST of narrow-disperse PNiPAAm samples ⁸⁸	49
Figure 2. 36. The effect of M _n on the LCST of PHEMA samples ⁸⁹	50
Figure 2. 37. Turbidimetry curves of (A) PNiPAAm blends and (B) POEGMA blends ⁹⁰	51
Figure 2. 38. The effect of cross-linking on the cloud point of PDMAEMA with different dimerization degrees of coumarin groups ⁹¹	52
Figure 2. 39. Schematic illustrations of transmittance curves of random thermo-responsive copolymers (dashed lines) compared to their parent homopolymers (solid lines): (A) a LCST-LCST random copolymer, (B) a LCST-UCST random copolymer. In (B) the red and blue colors represent the UCST and LCST blocks ⁸⁷	54
Figure 2. 40. Schematic illustration of the phase transitions of PnPA ₁₂₄ -b-PiPA ₈₀ -b-PEMA ₄₄ triblock copolymer at different temperatures in aqueous solution ¹⁰²	55
Figure 2. 41. Schematic illustrations of transmittance curves of a LCST-LCST block thermo-responsive copolymers (dashed lines) compared to their parent homopolymers (solid lines) ⁸⁷ ..	56
Figure 2. 42. Schematic illustration of the self-assembly structures of PnPA ₈₄ -b-PEMA ₄₂ with increasing temperature ¹⁰⁴	57

Figure 2. 43. Schematic illustrations of transmittance curves of a LCST-UCST block thermo-responsive copolymers (dashed lines) compared to their parent homopolymers (solid lines). The red and blue colors represent the UCST and LCST blocks ⁸⁷	58
Figure 2. 44. Schematic illustrations of self-assembly behavior of P(A-Pro-OMe)-b -P(A-Hyp-OH) diblock thermo-responsive copolymer. The blue line represents the poly(A-Hyp-OH) chains and the orange line represents poly(A-Pro-OMe) chains ¹⁰⁶	58
Figure 2. 45. Schematic illustrations of transmittance curves of a UCST-LCST block thermo-responsive copolymers (dashed lines) compared to their parent homopolymers (solid lines). The red and blue colors represent the UCST and LCST blocks ⁸⁷	59
Figure 2. 46. The effect of dispersion concentration on the cloud point of PmDEGMA ⁶⁹	60
Figure 2. 47. Schematic of relative intensity of interactions of ions with the surrounding water molecules ¹¹⁰	61
Figure 3. 1. Examples of the vibrational modes occur at characteristic frequencies that are detected using FTIR spectroscopy ¹²¹	65
Figure 3. 2. The optical layout of an FTIR spectrometer ¹²¹	66
Figure 3. 3. Schematic illustration of the typical intensity fluctuations ¹²²	68
Figure 3. 4. Schematic illustration of the typical intensity (A), number (B), and volume (C) distribution ¹²²	68
Figure 3. 5. The optical layout of the DLS instrument ¹²³	70
Figure 3. 6. Schematic illustration of the basic concept of zeta potential ¹²⁴	71
Figure 3. 7. Schematic showing the cell used for zeta potential measurement by Laser Doppler Velocimetry technique ¹²²	73
Figure 3. 8. General layout of a typical TEM ¹²⁵	75
Figure 3. 9. Basic structure of single (A) and double (B) beam spectrophotometers ¹²⁸	78
Figure 3. 10. The change in the conductance of a sample containing chloride ions during titration with added AgNO ₃ solution.	80
Figure 4. 1. FTIR analysis of pristine CNCs, CNC-g-POEGMA, and CNC-g-POEGMA-g-PDMS	92
Figure 4. 2. TEM images of CNC (A), CNC-g-POEGMA (B), and CNC-g-POEGMA-g-PDMS (C)	92
Figure 4. 3. Zeta potential of CNC-g-POEGMA, and CNC-g-POEGMA-g-PDMS	93
Figure 4. 4. TGA analysis of pristine CNCs, CNC-g-POEGMA, and CNC-g-POEGMA-g-PDMS (A) and the first derivative of thermogravimetric data (B) to assess the amount of (POEGMA) grafted from cellulose nanocrystals surface	94
Figure 4. 5 Conductometric titrations of CNC-g-POEGMA-g-PDMS at different ratios of DMS	95
Figure 4. 6. The cloud point (T_{cp}) values obtained from the transmittance–temperature ($Tr-T$) curve of CNC-g-POEGMA, and CNC-g-POEGMA-g-PDMS at high concentrations (A), (B) and at low concentrations (C), (D). Insets: the corresponding photographs of the copolymers at different temperatures	97
Figure 4. 7. Phase diagram of CNC-g-POEGMA (A) and CNC-g-POEGMA-g-PDMS (B) aqueous solutions using transmittance temperature ($Tr-T$) curve.	98
Figure 4. 8. The cloud point (T_{cp}) values obtained by the derivate of the $Tr-T$ curve of CNC-g-POEGMA, and CNC-g-POEGMA-g-PDMS at high concentrations (A),(B) and at low concentrations (C),(D)	98

Figure 4. 9. The phase diagram of CNC-g-POEGMA (A) and CNC-g-POEGMA-g-PDMC (B) aqueous solutions obtained by the derivate of the Tr–T curve.	99
Figure 4. 10. Temperature dependences of the apparent hydrodynamic radii of CNC-g-POEGMA, and CNC-g-POEGMA-g-PDMC (1:0.5) at high concentrations (A),(B) and at low concentrations (C),(D).	100
Figure 4. 11. Phase diagram of CNC-g-POEGMA (A) and CNC-g-POEGMA-PDMC (B) aqueous solutions using DLS.	101
Figure 4. 12. The cloud point (T_{cp}) values obtained by the transmittance–temperature (Tr–T) of CNC-g-POEGMA-g-PDMC (1:0.25) (A), CNC-g-POEGMA-g-PDMC (1:1.25) (B), and the corresponding phase diagram (C), (D) respectively.	102
Figure 4. 13. The cloud point (T_{cp}) values obtained by the derivate of the Tr–T curve of CNC-g-POEGMA-g-PDMC (1:0.25) (A), and CNC-g-POEGMA-g-PDMC (1:1.25) (B) and the corresponding phase diagram (C), (D).	103
Figure 4. 14. The effect of salt concentration on the cloud points of CNC-g-POEGMA and CNC-g-POEGMA-g-PDMC.	105
Figure 4. 15. The effect of salt concentration on the zeta potential values of CNC-g-POEGMA and CNC-g-POEGMA-g-PDMC.	107
Figure 4. 16. Effect of CPD1(A), CPD2 (B) on the turbidity and the corresponding turbidity removal percentage (C), (D) of bentonite as a function of dosage at different settling temperatures.	108
Figure 4. 17. Effect of CPD1 (A) and CPD2 (B) on the zeta potential of bentonite as a function of flocculant dosage at different settling temperatures.	109
Figure 4. 18. Effect of the CPD1 and CPD2 on the flocs size of bentonite as a function of dosage at different settling temperature.	111
Figure 4. 19. Flocs formed at optimum dosage of CPD1 and CPD2 using RMRS and RMHS protocols.	112
Figure 5. 1. FTIR spectra of CNC, CNC-Br and CNC-PDMC.	125
Figure 5. 2. The TEM images of CNC (A) and CNC-PDMC (B).	126
Figure 5. 3. Conductometric titrations of CNC-PDMC at different ratios of DMCs.	127
Figure 5. 4. Effect of pH on the zeta potential (A) and the size (B) of CNC-PDMC brushes. ...	129
Figure 5. 5. Effect of salt on the zeta potential (A) and the size (B) of CNC-PDMC brushes. .	131
Figure 5. 6. The TEM images of CNC (A), CNC-PDMC (B) and CNC-PDMC with 6 mM of NaCl (C).	131
Figure 5. 7. Effect of flocculant category on the turbidity removal of bentonite as a function of flocculant dosage at different settling time 5 min (A) and 24 h (B).	132
Figure 5. 8. Effect of flocculant category on the zeta potential of bentonite as a function of flocculant dosage at different settling time 5 min (A) and 24 h (B).	134
Figure 5. 9. Effect of ionic strength type on the zeta potential of bentonite as a function of dosage at different settling time 5 min (A) and 24 h (B).	137
Figure 5. 10. Effect of ionic strength type on the turbidity removal of bentonite as a function of dosage at different settling time 5 min (A) and 24 h (B).	138
Figure 6. 1. FTIR spectra of CNC, CNF, PDADMAC, PDADMAC-CNC, PDADMAC-CNC, PDADMAC-CNF, CNC-Br, and CNC-PDMC.	151
Figure 6. 2. Zeta potential and Z-average of PDADMAC-CNC, PDADMAC-CNF, CNC, CNC-Br, and CNC-PDMC.	153

Figure 6. 3. TEM images of CNC (A), CNC-PDMC (B), PDADMAC-CNC (C), and PDADMAC-CNF (D).....	153
Figure 6. 4. Effect of flocculant types on the zeta potential of bentonite as a function of flocculant dosage.....	154
Figure 6. 5. Effect of flocculant types on the turbidity removal of bentonite as a function of flocculant dosage.....	155
Figure 6. 6. A comparative investigation on the flocculation performance in the presence of three polyelectrolytes at different dosages.....	157
Figure 6. 7. Effect of the CNC-PDMC, PDADMAC-CNC, and PDADMAC-CNF on the floc size of bentonite as a function of dosage.....	158
Figure 7. 1. FTIR spectra of CNC, CNC-Br, CNC-PMEO ₂ MA, CNC-PMEO ₂ MA -PDMC, CNC-PDMC, and CNC-PDMC-PMEO ₂ MA.....	171
Figure 7. 2. ¹ H NMR spectra of CNC-Br, CNC-PMEO ₂ MA, CNC-PMEO ₂ MA-PDMC, and CNC-PDMC-PMEO ₂ MA.....	172
Figure 7. 3. The change in the dispersibility due to surface modification of the CNC.....	172
Figure 7. 4. Zeta potential and Z-average of CNC, CNC-Br, CNC-PMEO ₂ MA, CNC-PMEO ₂ MA -PDMC, CNC-PDMC, and CNC-PDMC-PMEO ₂ MA.....	174
Figure 7. 5. Conductometric titrations of (A) CNC-PMEO ₂ MA-PDMC [1:5], (B) CNC-PMEO ₂ MA-PDMC [1:8], (C) CNC-PDMC-PMEO ₂ MA [1:5], and (D) CNC-PDMC-PMEO ₂ MA [1:8] at different ratio of DMC.....	175
Figure 7. 6. The cloud point values obtained from the transmittance–temperature (Tr–T) curve of CNC-PMEO ₂ MA (A), and the corresponding phase diagram (B).....	176
Figure 7. 7. The cloud point values obtained from the transmittance–temperature (Tr–T) curve of CNC-PMEO ₂ MA-PDMC [1:5] (A) CNC-PMEO ₂ MA-PDMC [1:8] (B), and the corresponding phase diagram (C) ,(D) respectively.....	178
Figure 7. 8. The cloud point values obtained from the transmittance–temperature (Tr–T) curve of CNC-PDMC-PMEO ₂ MA [5:1] (A) CNC-PDMC-PMEO ₂ MA [8:1] (B), and the corresponding phase diagram (C) ,(D) respectively.....	180
Figure 7. 9. The effect of salt concentration on the cloud points of CNC-PMEO ₂ MA (A), and the corresponding phase diagram (B).....	182
Figure 7. 10. The effect of salt concentration on the cloud point values obtained from the transmittance–temperature (Tr–T) curve of CNC-PMEO ₂ MA-PDMC [1:5] (A) CNC-PMEO ₂ MA-PDMC [1:8] (B), and the corresponding phase diagram (C) ,(D) respectively.....	184
Figure 7. 11. The TEM images of CNC-PMEO ₂ MA-PDMC before the addition of KCl (A) and in the presence of KCl (B).....	184
Figure 7. 12. The effect of salt concentration on the cloud point values obtained from the transmittance–temperature (Tr–T) curve of CNC-PDMC-PMEO ₂ MA [5:1] (A) CNC-PDMC-PMEO ₂ MA [8:1] (B), and the corresponding phase diagram (C) ,(D) respectively.....	186

List of Tables

Table 2. 1. The chemical structures of clay minerals ³¹	18
Table 2. 2. The effect of cross-linking on the cloud point temperature of linear and cyclic PNiPAAm samples ⁹³	52
Table 5. 1. Zeta potential and Z-average of CNC, CNC-Br and CNC-PDMCs.....	126
Table 5. 2. Comparison between the flocculation efficiency of CNC-PDMCs and inorganic salts used in the study at their optimum dosages.	141

List of Schemes

Scheme 4. 1. (A) Graft polymerization of MEO ₂ MA and OEGMA ₃₀₀ with Ammonium persulfate initiator from the surface of Cellulose nanocrystals and (B) Graft polymerization of DMC with Ceric (IV) Ammonium Nitrate initiator from the surface of CNC-POEGMA, the generally accepted mechanism for the formation of a radical site on cellulose through persulfate and ceric ion initiators adapted from ¹⁵⁴	91
Scheme 4. 2. Schematic illustration of the aggregation observed of CNC-g-POEGMA during heating.....	101
Scheme 4. 3. Schematic representations of the proposed mechanisms responsible for the brush swelling and brush collapse transitions of CNC-g-POEGMA and CNC-g-POEGMA-g-PDMC, (the numbers in black circles indicate the order of the events).....	106
Scheme 4. 4. Schematic representations of the proposed mechanisms responsible for the flocculation of CPD1 and CPD2 using RMRS and RMHS protocols.....	113
Scheme 5. 1. Schematic illustration of synthesis procedure of (i) CNC-Br and (ii) CNC-PDMC.	124
Scheme 5. 2. Schematic illustration of the conformational change of CNC-PDMC brushes induced by change in the pH.....	129
Scheme 5. 3. Schematic illustration of the of the possible influence of salt concentration on the conformational change of CNC-PDMC brushes.....	131
Scheme 5. 4. The effect of cationic charge on the adsorption and bridging mechanism for bentonite (A) Low charge density, (B) High-charge density.....	136
Scheme 6. 1. Schematic illustration of the synthesis procedure of (1) PDADMAC-CNC, (2) PDADMAC-CNF and (3) CNC-PDMC.....	150
Scheme 6. 2. The effect of polyelectrolyte structures on the adsorption and bridging mechanism for bentonite (A) CNC-PDMC, (B) PDADMAC-CNC and (C) PDADMAC-CNF.....	160
Scheme 7. 1. Schematic illustration of the synthesis procedure of (A) CNC-Br, (B) CNC-PMEO ₂ MA, (C) CNC-PMEO ₂ MA-PDMC, (D) CNC-PDMC, and (E) CNC-PDMC-PMEO ₂ MA.	170
Scheme 7.2. Schematic illustration of the aggregation observed of CNC-PMEO ₂ MA-PDMC[1:5](A), and CNC-PMEO ₂ MA-PDMC[1:8](B) during heating.....	179
Scheme 7. 3. Schematic illustration of the aggregation observed of CNC-PDMC-PMEO ₂ MA during heating.....	181
Scheme 7. 4. Schematic representations of the proposed mechanisms responsible for the phase transition behavior of CNC-PMEO ₂ MA-PDMC (A) and CNC-PDMC-PMEO ₂ MA (B) in the presence of KCl, (the numbers in black circles indicate the order of the events).....	187

List of Abbreviations

Abbreviation	Meaning
APS	Ammonium persulfate
ARGET-ATRP	Activators ReGenerated by Electron Transfer polymerization
AsAc	Ascorbic acid
BIBB	α -bromoisobutyryl bromide
CAN	Cerium(IV) ammonium nitrate
CCC	Critical Coagulation Concentration
CHWE	Clark Hot Water Extraction Process
CNC	Cellulose nanocrystals
CNF	Cellulose nanofibers
CP	CNC-POEGMA
CPD	CNC-POEGMA-DMC
CT	Consolidated Tailings
DAAM	Diacetone acrylamide
D_h	Hydrodynamic diameter
DLS	Dynamic Light Scattering
DLVO	Derjaguin Landau Verwey Overbeek
DMAP	4-(Dimethylamino)pyridine
DMAPMA	N-(3-(dimethylamino) propyl) methacryl- amide
DMC	(2-methacryloyloxyethyl) trimethyl ammonium chloride
DMF	N,N-Dimethylformamide
EDL	Electrical Double Layer
EMA	<i>N,N</i> -ethylmethacrylamide
EtOH	Ethanol
FTIR	Fourier Transform Infrared
ΔG_{mix}	Gibbs free-energy of mixing
GTMAC	Glycidyltrimethylammonium chloride
ΔH	Enthalpy
HOBC	4'-(hexyloxy)-4-biphenylcarbonitrile
IPA	Isopropyl alcohol
LCST	Lower Critical Solution Transition
LDV	Laser Doppler Velocimetry
MEO ₂ MA	Di(ethylene glycol) methyl ether methacrylate
MFT	Mature fine tailings
MOTEGVBE	Methoxy-tetraethyleneglycol-4-vinylbenzylether
MFT	Mature fine tailings
NAGA	N-acryloylglycinamide
nPA	<i>N-n</i> propylacrylamide
OEGMA ₃₀₀	Oligo(ethylene glycol) methacrylate
PAC	Polyaluminium chloride
PAM	Polyacrylamide

PDADMAC	Poly(diallyldimethylammonium chloride)
PDMAEMA	Poly(N,N-dimethylaminoethyl methacrylate)
PEO	Poly (ethylene oxide)
PHEMA	Poly(2-hydroxyethyl methacrylate)
PiPOx	Poly(2-isopropenyl-2-oxazoline)
PmDEGMA	Poly(methoxydiethylene glycol methacrylate)
PNiPAAm	Poly(N-isopropylacrylamide)
Poly(EOVE-b-HOVE)	Poly(2-ethoxyethyl vinyl ether-b-2-hydroxyethyl vinyl ether)
PVAc	Poly(vinylacetate)
PVDMA	Poly(2-vinyl-4,4-dimethylazlactone) MOTEGVBE
QA	Quaternary ammonium groups
RMHS	Room temperature mixing and high temperature settling
RMRS	Room temperature mixing and room temperature settling
ΔS	Entropy
SAGD	Steam Assisted Gravity Drainage
TEA	Triethylamine
TEM	Transmission electron microscope
UCST	Upper Critical Solution Temperature

Chapter 1. Introduction

1.1 Statement of problem

Tailings are by-products in many mining operations. After bitumen extraction, the remaining water mixtures contain coarse sands, fine clays and residual bitumen, which is defined as tailings. Tailings are discharged and stored in large structures above ground, known as tailing ponds, or in former mine pits awaiting reclamation. Upon discharge of tailings, the coarse solids settle rapidly to form beaches along the pond edge, while the fines (silts and clays) settle slowly to form a fine tailings zone, which after several years of consolidation becomes mature fine tailings (MFT) that trap a substantial quantity of water. The water trapped could potentially be recovered and reused as recycled water to extract bitumen. Despite all the economic advantages associated with oil sands, the development of the oil sands industry is hindered by environmental challenges and societal perception. The greenhouse gas (GHG) emission, the use of clean water, and the tailings are the three key environmental issues that have to be addressed. Amongst these challenges, tailing operations present the most significant challenge to the oil sands extraction process. Tailings ponds have generated environmental and engineering issues as summarized below. First, the production and accumulation of large volumes of fine tailings poses a major environmental concern. Approximately 3.3 m³ of tailings are produced from one barrel of bitumen. Second, MFT contains toxic compounds, including naphthenic acids, polycyclic aromatic hydrocarbons, phenolic compounds, ammonia, and other trace metals that pose risks to the environment. Third, the large quantities of water required to extract and process bitumen from the oil sands has become an issue.

On average, three barrels of fresh water are consumed to produce one barrel of bitumen. Because of the expansion of the oil sands industry, there is also a growing demand for water. Therefore, we should develop processes that minimize the use of fresh water by ensuring that the water can be recovered from the tailings and recycled.

1.2 Objectives and Scope of Research

The current doctoral research focuses on studies aimed at managing the oil sands tailings using sustainable nanomaterials, replacing synthetic chemicals or polymers as flocculants. The main objectives of the research are to:

- 1- Functionalize CNCs with poly(oligo(ethylene glycol) methyl ether methacrylate) brushes.
- 2- Modify the prepared copolymer, CNC-g-POEGMA (CP), with a cationic monomer (2-methacryloyloxyethyl) trimethyl ammonium chloride (DMC).
- 3- Examine the physical properties of various CNC-g-POEGMA-g-PDMC systems and the impact of DMC composition and its role on the thermo-responsive characteristics of modified CNC-g-POEGMA systems.
- 4- Investigate the effect of polymer addition, CNC-PDMC and CNC-g-POEGMA-g-PDMC (CPD), on the flocculation of oil sands tailings using bentonite as a model.
- 5- Prepare three cationic biopolymer-based flocculants: PDADMAC-coated-CNCs, PDADMAC-coated-CNF via physical adsorption and CNC-PDMC via ARGET-ATRP.
- 6- Examine the effect of cationic charge distribution (flat-coated layer versus grafted-brushes) of these copolymers on the flocculation of bentonite.
- 7- Design CNC-based copolymers with different cationic and thermo-responsive brushes sequences using ARGET-ATRP technique.

- 8- Investigate the influence of cationic and thermo-responsive brushes sequence, the monomer composition and the addition of salt on their phase transition behavior.

1.3 Outline of the thesis

This thesis consists of 7 chapters. The results from all the research work carried out as part of this thesis are reported in the manuscript format in Chapter 4 through Chapter 7. The scope and contents of the chapters are listed as follows: Chapter 1 introduces the research objectives and the outline of the thesis. Chapter 2 describes the literature review of the types of flocculants and coagulants applied to waste-water treatment and the underlying principles as well as the background information on cellulose nanomaterials. Chapter 3 provides a short description of the analytical instruments used in this study, and Chapter 4 summarizes the study on functional cellulose nanocrystals containing cationic and thermo-responsive polymer brushes for bentonite removal. This is then expanded to examine the flocculation of bentonite by cationic cellulose nanocrystals as documented in Chapter 5. Chapter 6 describes the evaluation of cationic biopolymer-based flocculants on bentonite removal: effect of cationic charge distribution, and Chapter 7 examines the effects of chain architecture and grafting density on the thermo-responsive behavior of cationic and thermo-responsive copolymers. Chapter 8 documents the key findings and the recommendation for future studies.

Chapter 2. Literature Review

2.1. Oil sands extraction processes

Oil sands as a mixture of sand, clay, water, and a type of heavy oil referred to as “bitumen” have become one of the world’s leading sources of non-conventional petroleum. Compared with the conventional crude oil, bitumen features a higher viscosity and specific gravity, lower hydrogen-to-carbon ratio, and higher nitrogen, sulphur and metal content. The major accumulations of oil sands are distributed in eight countries including Canada, Venezuela, the United States, and Russia. The proven remaining reserves of the crude oil sands are estimated to be 27.5 billion cubic meters. Canada has the third largest oil reserves, behind only Saudi Arabia and Venezuela. There are two main industrial processes for bitumen extraction for oil sands: Steam-Assisted Gravity-Drainage (SAGD) and the Clark Hot Water Extraction (CHWE). CHWE incorporates the basic science developed by Dr. Karl Clark in collaboration with the Research Council of Alberta almost a century ago. This process is mostly used as the standard extraction process for open pit mining when the bitumen is buried less than 70 meters below the surface. Steam Assisted Gravity Drainage (SAGD) is most commonly used for extracting oil sands that are more deeply buried ¹⁻⁵.

2.1.1. Clark hot water extraction process (CHWE)

The recovery of bitumen from oil sands, is mainly achieved by the Clark Hot Water Extraction process, where hot water and sodium hydroxide are used to separate the bitumen from sands. CHWE results in accumulation of fluid waste defined as oil sands tailings. **Figure 2.1** shows the generalized processing scheme for oil sands extraction ⁴.

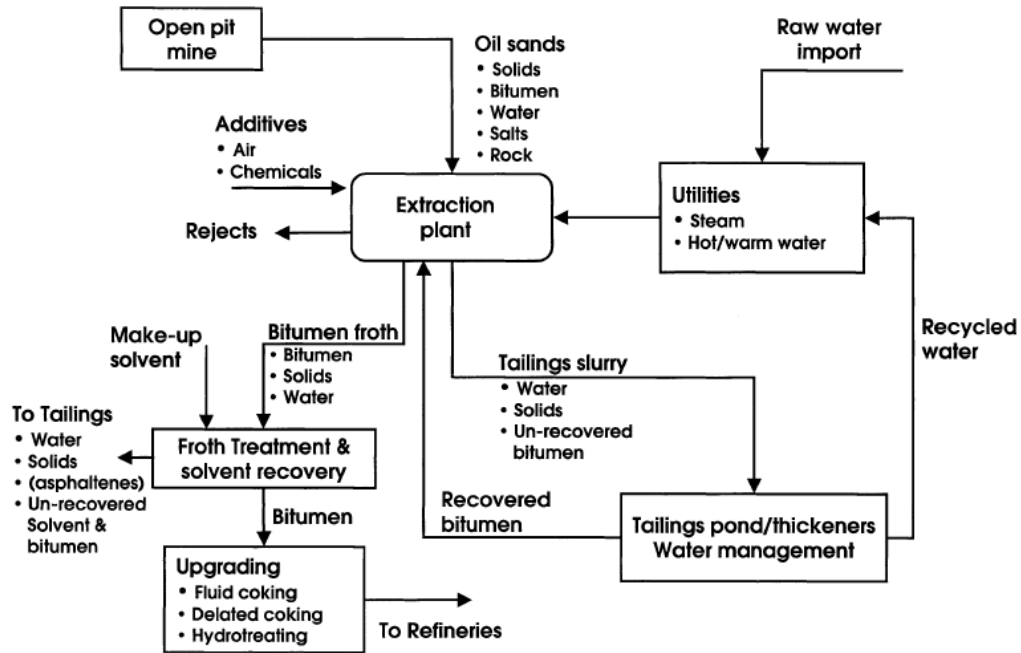


Figure 2. 1. Schematic flowsheet of Clark Hot Water Extraction process (CHWE) for oil sands ⁴.

2.2.2 Steam assisted gravity drainage process (SAGD)

In the late 1970s, Roger Butler and his colleagues at Imperial Oil developed the Steam-Assisted Gravity-Drainage (SAGD) for bitumen recovery since around 80% of the oil sands resource is located underground (around 300 m) at depths that cannot be reached by open pit mining. In SAGD, a pair of wells with horizontal sections of between 500 m and 1,000 m are drilled at an exact distance of 5 m between each other. The extracting process involves heating the oil sands layer by continuously injecting high-temperature and high-pressure steam into the horizontal well injector to liquefy the bitumen, which in turn flows down to the horizontal well producer, and the bitumen subsequently is recovered along with hot water as illustrated in **Figure 2.2** ⁵.

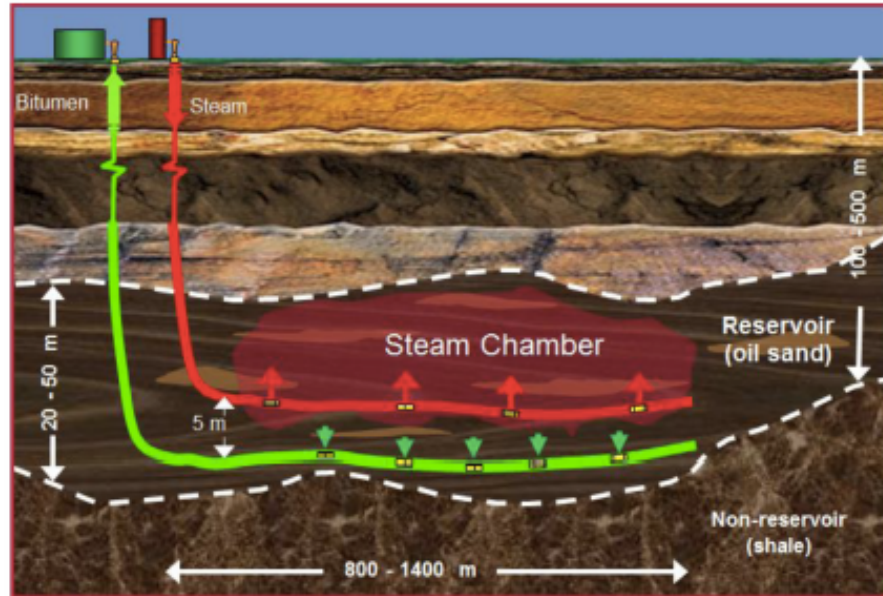


Figure 2. 2. Schematic diagram of Steam Assisted Gravity Drainage (SAGD) process ⁵.

2.2 Environmental issues posed by oil sands processing

Despite all the economic advantages associated with oil sands, the development of the oil sands industry is limited by various environmental issues. The greenhouse gas (GHG) emission, the usage of clean water, and the tailings are the three environmental concerns to be addressed. Amongst these challenges, tailings operations present the most significant of all to the oil sands extraction process ¹.

2.2.1 Issues related to tailings management

Several key issues are related to the disposal of fine tailings that pose challenges to the oil sands industry that are summarized as follows. First, the production and accumulation of large volumes of fine tailings poses a major environmental concern. Approximately 3.3 m³ of tailings are produced from one-barrel bitumen. It is estimated that Suncor will have 800 million m³ of tailings accumulated by 2033. Currently, the existing tailings ponds occupy 176 km² land in northern

Alberta, and the operation to maintain the tailings ponds costs a large amount of energy and money

⁶. Second, MFT contain toxic materials, including naphthenic acids, polycyclic aromatic hydrocarbons, phenolic compounds, ammonia, and other trace metals that pose risks to the environment. The pollutants reported to be emitted from oil sands tailings ponds which have adverse acute and chronic effects on aquatic organisms and wildlife in areas surrounding the MFT storage sites. It has been estimated that the inventory of MFT will reach two billion cubic meters in 2034 if the production proceeds as planned. Third, the large quantities of water required to extract and process bitumen from the oil sands has become an issue. On average, three barrels of fresh water is consumed to produce one barrel of bitumen. The very slow settling of the fine solids in the tailings ponds coupled with the water holding capacity of MFT and zero water discharge back into the environment, leads to the accumulation of a large water and solids waste inventory ^{4,5}.

2.2.2 Current industry practices for tailings treatment

In response to the challenge of fluid fine tailings management considering the sustainable development of the oil sands industry, various efforts have been made to improve the settling rate of fine solids and to recover the maximum volume of water in order to reduce the total MFT inventory ^{4,5,7}. The following discussion is limited to current chemical tailings treatment practices as the only technologies that have been commercially used in large-scale operations to treat oil sands tailings, which are respectively consolidated tailings technology and thickened tailings technology.

2.2.2.1 Consolidated/composite tailings technology (CT)

Consolidated Tailings (CT) technology has been practiced for MFT treatment to produce non-segregated thickened tailings. In this process, MFT is mixed with the coarse sands from extracted tailings and treated with a coagulant aid, such as gypsum as shown in **Figure 2.3**. The tailings are then discharged to the pond. With the gypsum ions destabilizing the tailings suspension, fine solids and coarse sands consolidate into a non-segregating deposit with fast release of water. However, the recycled water contains a considerable amount of calcium ions which have a detrimental effect on the recovery of bitumen extraction and generate scaling in the process units and corrosion in metallurgy ^{1,8}. Therefore, alternative tailings treatment technologies remain of great interest in order to improve the transformation of fluid fine tailings.

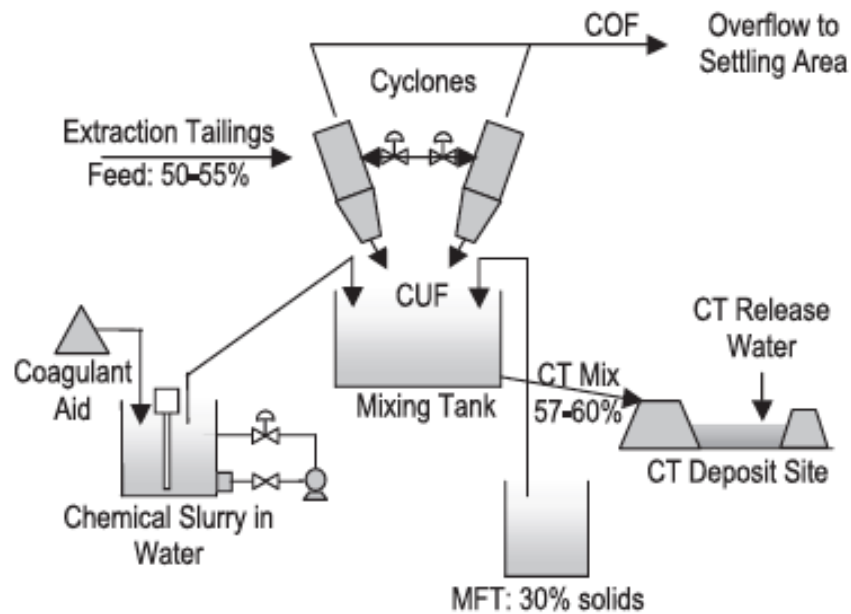


Figure 2. 3. Schematic diagram of consolidated/composite tailings (CT) technology ¹.

2.2.2.2 Thickened tailings/paste technology

Thickened tailings process has been a step-forward for MFT treatment without introducing gypsum or any divalent ions to the released water. During the operation, the high molecular weight polymeric flocculants are used to rapidly thicken fresh tailings and recover the warm water. The advantages of thickened tailings technology are that the rapidly released processed warm water can be immediately reused for the extraction process, therefore reducing energy cost and greenhouse gas emission, and this technology shortens the time of gravity settling. However, thickened tailings obtained through the polymer flocculants treatment still contain large volume of water that cannot be easily removed without the use of an external force due to the loosely packed structure of the flocs formed ^{1,4}.

2.3 Theory of coagulation and flocculation

The consolidated tailings technology is based on the coagulation concept. Coagulant aids used in CT process can change the surface charges of colloidal particles; therefore, reduce the energy barrier. The thickened tailings technology is based on flocculation, where the flocculants can bridge the gap between particles and reduce the energy barrier of agglomeration ⁷. Although the terms coagulation and flocculation have been used indiscriminately to describe the process of reducing electrical double layer forces between particles, allowing attractive van der Waals forces to dominate, there is a clear distinction between the two concepts ^{9,10}. Coagulation usually refers to the destabilization process of colloidal suspension to neutralize the surface charge leading to the formation of large particles called submicroscopic flocs by adding inorganic multivalent cations or low molecular weight cationic polyelectrolyte known as coagulants or primary coagulants. The destabilization process using inorganic coagulants (primary coagulants) is known as adsorption-charge neutralization as illustrated in **Figure 2.4** (a), while the destabilization process using

polyelectrolytes (primary coagulants) is known as electrostatic patch as shown in **Figure 2.4** (b). Flocculation is defined as the formation of macroscopic flocs of suspended particles through the adsorption of high molecular weight polymeric flocculants onto a number of colloidal particles and bridging the gap between the particles. During bridging flocculation, long-chain segments of polymeric flocculants are initially adsorbed onto one or more particles with the loops and tails extending in solution to overcome the energy barrier of agglomeration, which gives the possibility of attachment of these dangling polymer segments to other particles; thus, bridging particles together to form macroscopic flocs^{11,12}. A schematic diagram of particles bridged by flocculation is given in **Figure 2.4** (c).

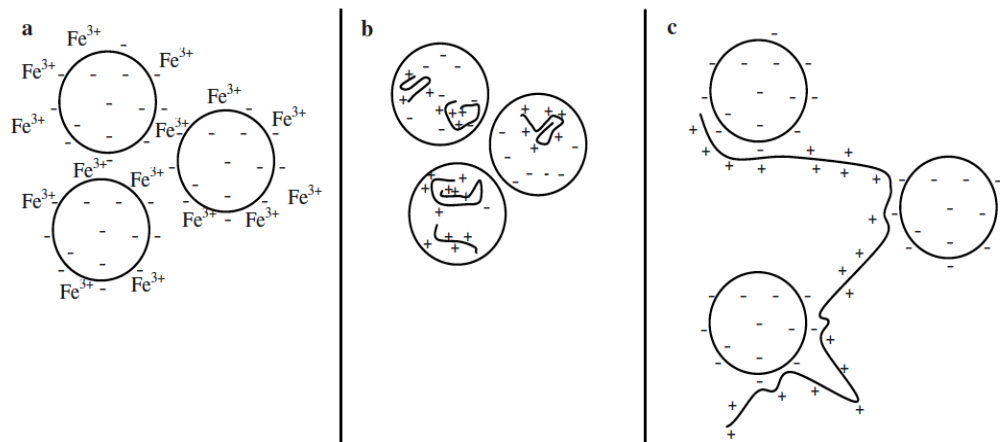


Figure 2. 4. Schematic diagram of charge neutralization mechanism using inorganic coagulants (a), electrostatic patch mechanism using cationic polyelectrolyte (b) and bridging mechanism using polymeric flocculants (c)¹¹.

2.3.1 Types of additives used

Coagulants and flocculants can be comprised of a variety of chemical compounds and their properties can be tailored based on the need of the application (shown in **Figure 2.5**). The

coagulants can be inorganic salts that precipitate in water as insoluble hydroxides, or cationic polyelectrolytes that can coagulate particles by electrostatic patching. Inorganic coagulants (salts of multivalent metals like aluminum and iron) are commonly being used because of their low cost, and availability. Nevertheless, their high dependence on pH, high sludge and high dosage requirement are drawbacks for their wide adoption and usage. Cationic polyelectrolytes induce the rapid formation of flocs that are larger and stronger than inorganic flocs. The polymer dosage requirement for cationic polyelectrolytes is less than inorganic salts ^{10,13}.

The flocculants used in waste-water treatment can be divided into three categories; (i) chemical synthetic flocculants, (ii) natural bio-flocculants and (iii) grafted flocculants. According to the polymer charge type, polymeric flocculants can be further classified into four groups: anionic, cationic amphoteric and non-ionic flocculants. Synthetic flocculants are mostly linear water-soluble polymers, in most cases, derived from oil-based and non-renewable raw materials ¹⁴. Polymers can vary in structure (linear versus branched), molecular weight, charge type, amount of charge, and composition. Although water-soluble synthetic polymers find wide applications as flocculants, their usage is debatable because their application may cause environmental consequences and health hazards that influence their widespread adoption by the industry. Toxicity of synthetic polymers used in waste-water treatment generally arises from unreacted chemicals used to produce the monomer units (such as dimethylamine, formaldehyde and epichlorohydrin) and residual unreacted monomers (such as acrylamide, ethyleneimine) ¹⁵.

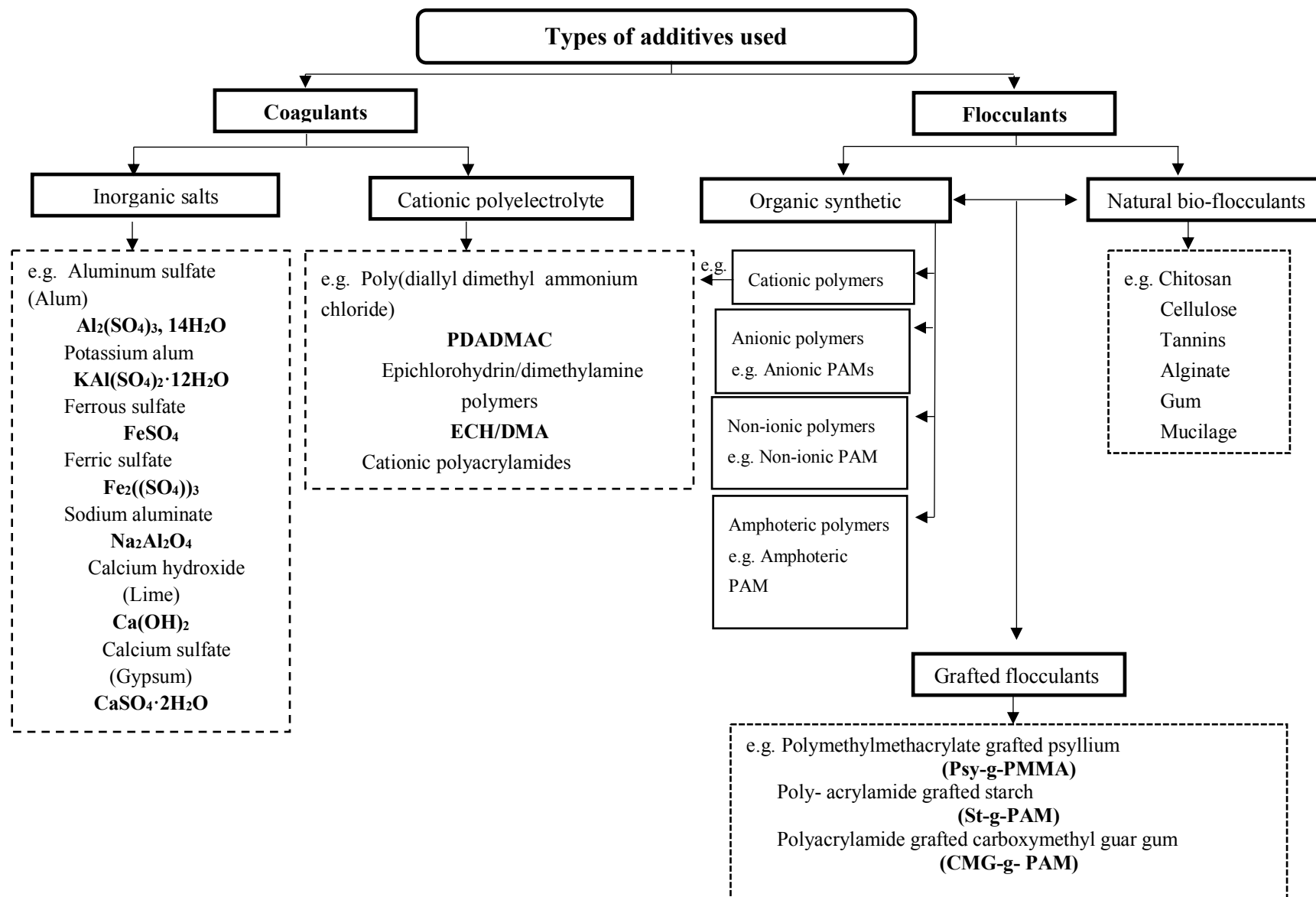


Figure 2. 5. Classification of additives used for waste-water treatment.

Furthermore, most synthetic polymer structures are resistant to biodegradation ^{13,16}, and their degraded products are considered extremely hazardous because the monomers could enter the food chain and may cause health problems ¹⁷.

As the demand for environmentally friendly materials in treating waste-water continues to increase; natural bio-flocculants have emerged as promising alternative materials to replace synthetic flocculants. Natural organic flocculants based on polysaccharides have been extensively explored because they are safe, biodegradable, fairly shear stable, easily available from reproducible agricultural resources and produce no secondary pollution compared to synthetic flocculants ¹³. In addition, since biopolymers are biodegradable, the sludge formed can be efficiently degraded by microorganisms ^{18,19}. However, natural bio-flocculants have low efficiencies and thus higher concentrations or higher dosage are needed ²⁰. Thus, grafted flocculants have emerged as new polymers that offer tremendous potential in treating waste-water due to their superior performance compared to the original components (synthetic polymeric flocculants and natural bio-flocculants) ¹³. The modification of polysaccharides has been explored as a way of combining their best properties with those of synthetic polymers to enhance the aggregating power of the flocculants formed ^{13,21,22}.

2.4 Mature fine tailings composition

Oil sands contain 7-13 wt.% bitumen, 3-7 wt.% water, and 80-85 wt.% mineral solids comprising coarser sand, silt, and fine clay particles ($> 44 \mu\text{m}$) ¹. Upon discharge of the tailings, the coarse solids settle rapidly to form beaches along the pond edge, while the fines settle slowly to form a fine tailings zone that after a few years of consolidation is defined as mature fine tailing (MFT) that traps a substantial quantity of water. MFT is a gel-like suspension containing 60 wt.%

of water and about 35 wt.% of solid materials. **Figure 2.6** presents the typical compositions of MFT compared to oil sands. The solids are mostly comprised of different clay types with over 90% of the solids with a particle diameter smaller than 44 μm . Clays in MFT are mainly kaolinite and illite, as well as mixed-layer clays. Furthermore, MFT contains small amounts of smectite which has high water holding capacity due to its swelling characteristics, although this type of clay is not present in significant quantity and may not be found in certain samples. Depending on the downstream positions of tailings and the depth of these ponds, the MFT samples will vary among the different tailings ²³.

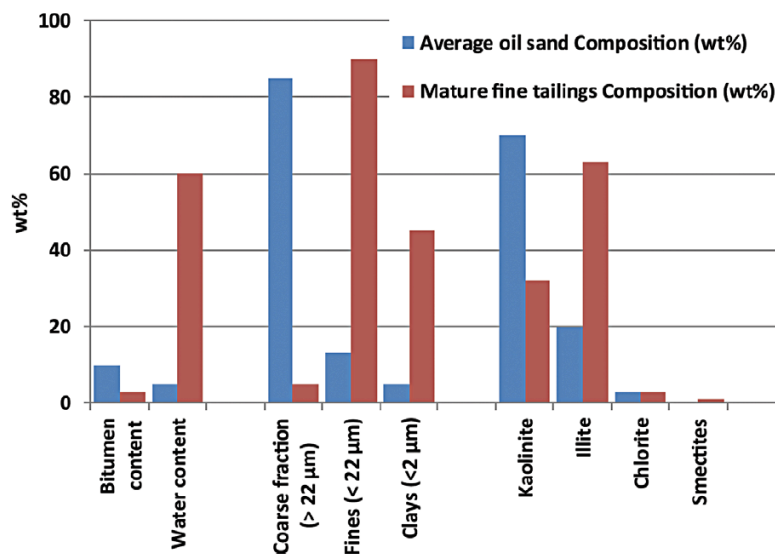


Figure 2. 6. Composition of mature fine tailings compared to that of oil sands ²³.

2.5 Mature fine tailings stability

The high stability of MFT has been attributed to the presence of clay components ^{2,23–26}. Since the majority of clays in MFT are negatively charged kaolinite clays, and the process of oil sands extraction has a pH of 8, the electrical charge on each particle produces an electrostatic repulsion force leading to the stabilization of the suspension. Beside electrical repulsion, the absorption of

water molecules on the particle surface forms hydration layers that repel each other and prevent settling. In addition, the size of ultrafine clays ($<0.3 \mu\text{m}$) afforded MFT its structure and impedes consolidation. In some studies, the stability of MFT is linked to the organic matter, consisting of chemical structures similar to humic and fulvic acids ²⁷. The proposed conceptual model on the roles of Ca^{2+} and Fe^{3+} ions in the complexation of carboxylic acid groups of the organic compounds to bitumen and clay surfaces is shown in **Figure 2.7**. Another reason for the stability of MFT might be the presence of residual bitumen during the extraction process. The unrecovered bitumen blocks the pore spaces between particles and binds the clay particles together, which decreases the hydraulic conductivity of MFT by forming restricted pathway between particles preventing water release and impeding consolidation as shown in **Figure 2.8** ²⁸.

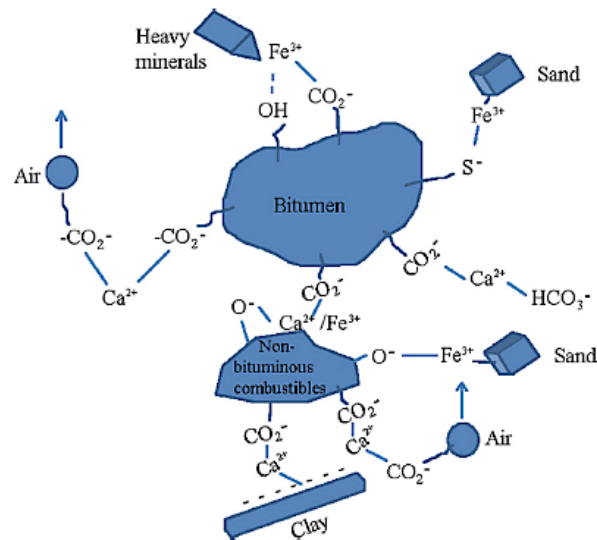


Figure 2. 7. A model for the interactions between bitumen, minerals, and non-bitumen combustibles (NBC) in tailings ²⁷.

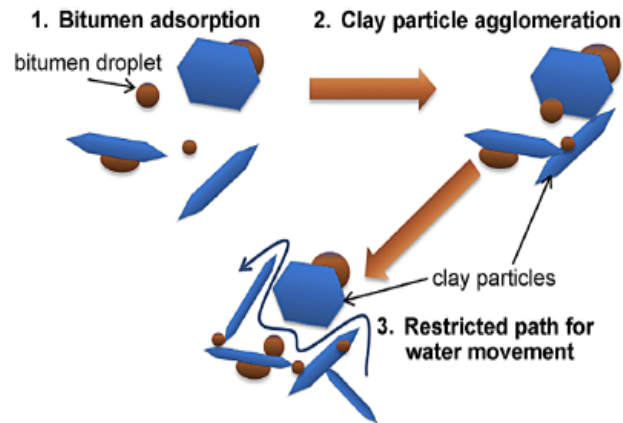


Figure 2. 8. The organic model for MFT stability and the role of bitumen²⁸.

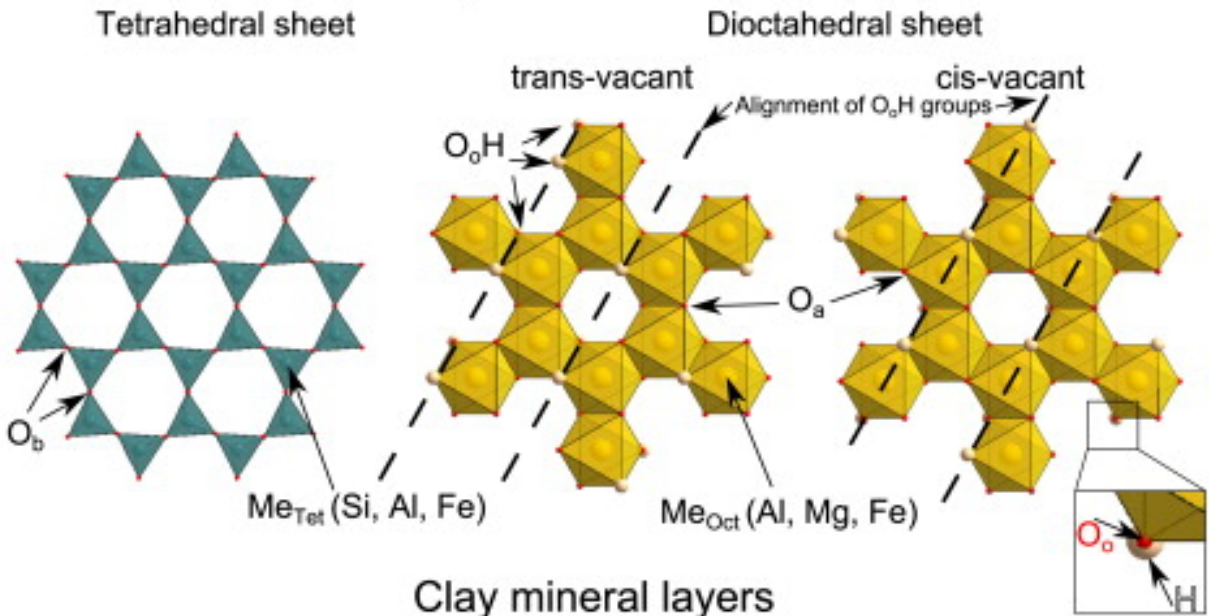
2.6 Suspensions and particle dynamics

A colloidal dispersion refers to a system containing small particles that range in size from 1 nanometer to several tens of micrometers. The particles form a homogeneously dispersed mixture in water. The complete settling of clays is hindered due to the size of the fines comprising mainly of clay minerals¹.

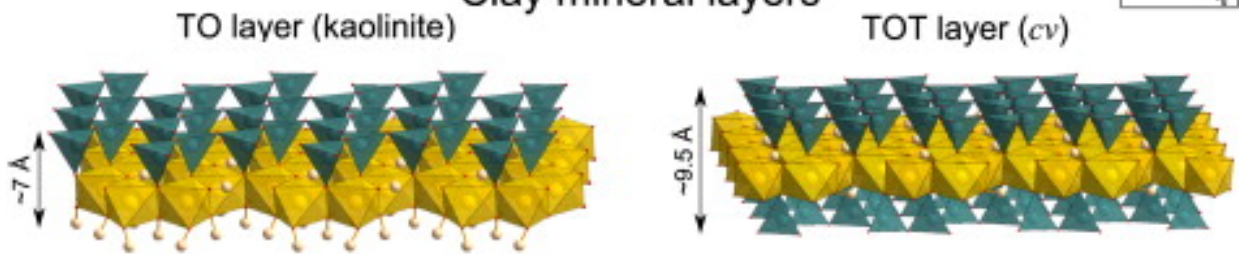
2.7 Clays and their behavior in suspension

The unit structure of clays is composed of silicon-oxygen tetrahedron (T) and aluminum or magnesium-oxygen octahedrons (O) sheets connected together in layers. **Figure 2.9** shows three different types of clay structures. There are four main unit structure arrangements. (1:1) layering, with one tetrahedral and one octahedral sheet; (2:1) layering, with two tetrahedral sheets surrounding the octahedral sheet; (2:1:1) layering, with two tetrahedral surrounding a gibbsite or brucite octahedral sheet, with another octahedral sheet between the 2:1 mica layers. The fourth type consists of amorphous clay minerals, which do not have a specific long-range arrangement in their layering. **Table 2.1** summarizes the typical structure of ideal specimens of each group²⁹⁻³¹.

Clay mineral sheets



Clay mineral layers



Clay mineral particles

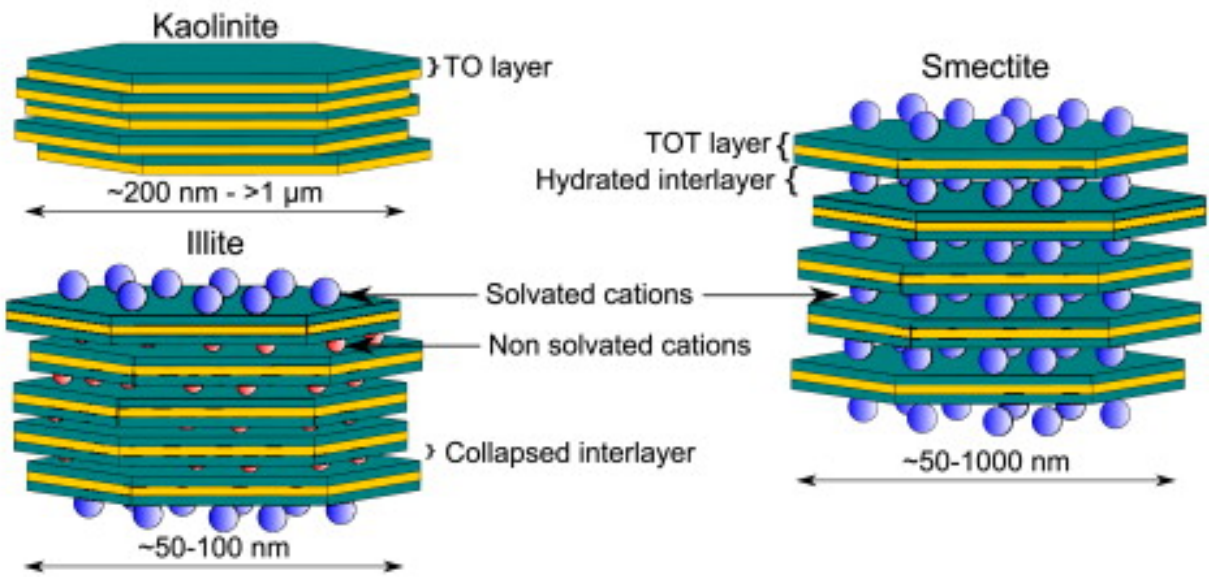


Figure 2. 9. Three-dimensional structure of the clay minerals ³⁰.

Table 2. 1. The chemical structures of clay minerals ³¹.

Mineral Name	Compound Name	Empirical Formula	Chemical Formula	Crystal System
Kaolinite	Aluminum Silicate Hydroxide	$Al_2H_4O_9Si_2$	$Al_2Si_2O_5(OH)_4$	Anorthic
Nacrite	Aluminum Silicate Hydroxide	$Al_2H_4O_9Si_2$	$Al_2Si_2O_5(OH)_4$	Monoclinic
Halloysite	Aluminum Silicate Hydroxide	$Al_2H_4O_9Si_2$	$Al_2Si_2O_5(OH)_4$	Hexagonal
Kaolinite-montmorillonite	Sodium Aluminum Silicate Hydroxide	$Al_4H_{14}Na_{0.3}O_{25}Si_6$	$Na_{0.3}Al_4Si_6O_{15}(OH)_{6.4} \cdot H_2O$	Unknown
Illite-montmorillonite	HydratePotassium Aluminum Silicate Hydroxide Hydrate	$Al_{12}H_6KO_{25}Si_8$	$K_{-}Al_4(SiAl)_8O_{20}(OH)_4 \cdot xH_2O$	Unknown
Dickite	Aluminium Silicate Hydroxide	$Al_2H_4O_9Si_2$	$Al_2Si_2O_5(OH)_4$	Monoclinic
Nontronite	Sodium Calcium Iron Aluminum Silicate Hydroxide Hydrate	$Fe_2H_4Na_{0.3}O_{13}Si_4$	$(Na, Ca)_{0.3}Fe_2(Si, Al)_4O_{10}(OH)_2 \cdot xH_2O$	Monoclinic
Rectorite	Sodium Aluminum Silicate Hydroxide Hydrate	$Al_4H_8NaO_{20}Si_8$	$NaAl_4(Si, Al)_8O_{20}(OH)_4 \cdot 2H_2O$	Hexagonal

The major clay minerals in the oil sands tailings are kaolinite and illite with minor amounts of montmorillonite, chlorite, and mixed-layer of clays ³¹. Kaolinite clay consists of (1:1) layers. In the octahedral sheet, oxygen atoms and hydroxyl groups are arranged around a central aluminum atom. In the tetrahedral sheet, the oxygen atoms surround a silicon atom ³⁰. The sheets are bonded covalently by sharing oxygen atoms, and the layers are held by van der Waals attractive forces. Kaolinite particles have a plate-like structure and consist of two basal planes that are negatively charged due to the isomorphous substitution where high valence cations are substituted by cations of lower valence (Al^{3+} for Si^{4+} , or Mg^{2+} for Al^{3+}). The charges on the T-basal plane are assumed to be permanent and independent of pH. On the edge of the plate, the primary alumina-silica bonds are broken and become positively charged in water; hence, the edge faces show pH-dependent behavior as shown in **Figure 2.10**. In alkaline conditions, the edge of the kaolinite is negatively charged and in acidic conditions, it is positively charged. At low pH, the negatively

charged basal plane may interact with the positively charged edges leading to an “edge-face” interaction (between Al-edge and Si-surface), forming a “house of cards” structure that can entrap large amounts of water within the associations and lead to the long-lasting structure of the oil sands tailings as shown in **Figure 2.11 (B)**. At high pH, the edge charge is negative, causing the edge-face electrostatic attraction to weaken resulting in the formation of a perfect crystal as shown in **Figure 2.11 (C)** ^{32,33}.

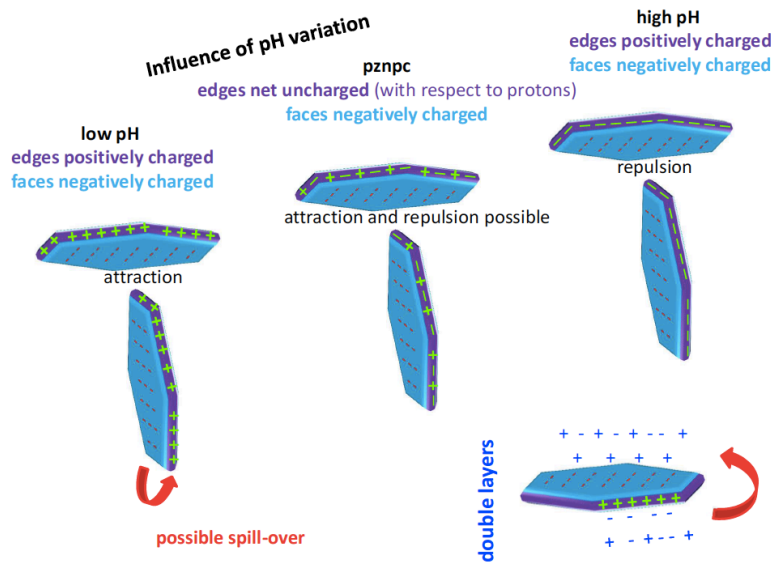


Figure 2. 10. Schematic view of clay platelets and their anisotropic charging behavior. The faces (basal planes) exhibit permanent negative charge, whereas edge faces show amphoteric, pH-dependent behavior similar to oxide minerals ³².

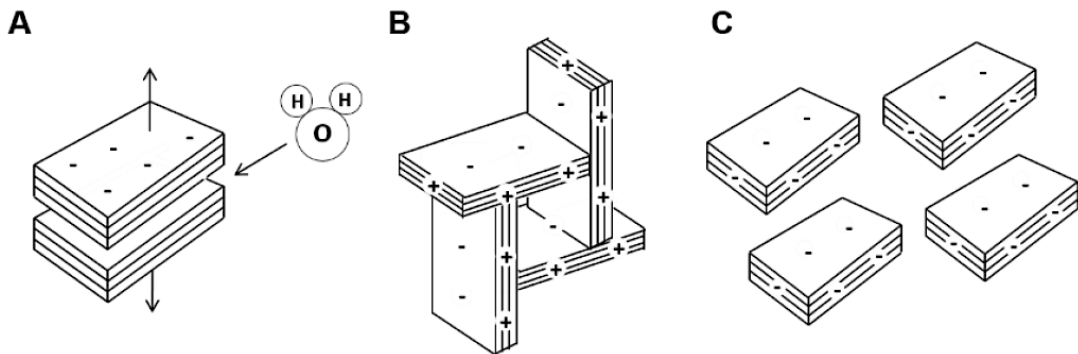


Figure 2. 11. Bentonite in solution A) swelling, B) “house of card structure” at low pH(below 7) and C) platelets dispersion at pH above 7³³.

Although smectite is not present in significant quantity, the high water holding capacity due to its swelling characteristics is of practical importance. The smectite consists of (2:1) layering, with a dioctahedral gibbsite sheet situated between two silica tetrahedral sheets³⁴. Bentonite is composed dominantly of a smectite clay minerals. In this type of clays, the charge deficiency is due to the isomorphous substitution of a small fraction of the tetrahedral Si atoms by Al and/or a fraction of the octahedral atoms (Al or Mg) by atoms of lower oxidation number³⁰. The anionic charge of the alumina-silicate layer is neutralized by hydrated cations, (e.g. Na⁺, Ca²⁺ and/or Mg²⁺). These layers are linked together by shared oxygen atoms, and the thickness of the smectite plates is less than 1 nm³⁵. The swelling capacity of bentonite depends on the sodium content where it increases 700-1000% by treating calcium bentonite with 0.25% of Na₂CO₃³⁶. A schematic diagram of the smectite structure is shown in **Figure 2.12**.

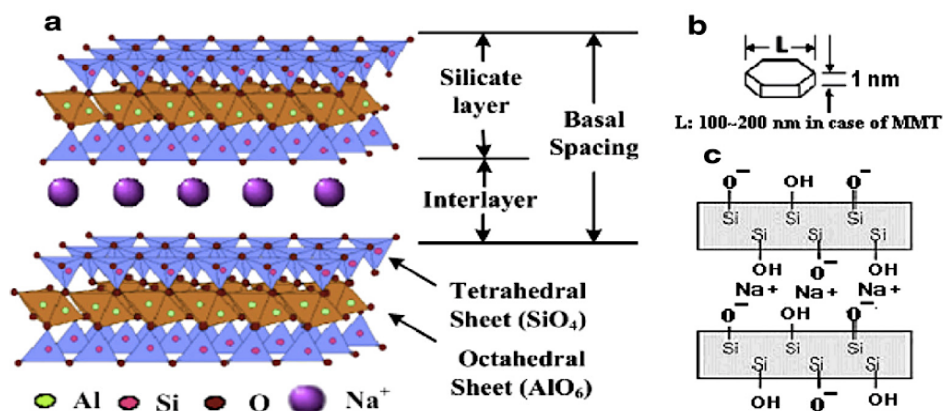


Figure 2. 12. (a) Molecular structure of MMT containing exchangeable sodium ion (MMT-Na⁺), (b) high aspect ratio clay platelet, and (c) schematic representation of side view between layers³⁵.

To understand the effectiveness of the flocculation or coagulation, it is crucial to study the surface properties of clay particles that affect the stability of the colloidal system and the interaction between clay particles, electrolytes, and additives like coagulants or flocculants.

2.8 Colloid - electrolyte interactions

The interaction between clay particles and electrolyte can be explained in terms of the formation of an electrical double layer. The clay particles exhibit negative electrical charges in water which is considered as the primary factor in controlling clay dispersion³⁷. Due to the charge variations at the interface of electrolyte and clay particles, an ionic cloud is formed around the negative clay particles called electrical double layer (EDL). As the term suggests, the EDL consists of two layers; the inner region (Stern layer) where the counter-ions (cations) and positive hydrogen ions of water molecules are firmly bonded and an outer region (Gouy–Chapman diffuse layer), where the cations are loosely held to the colloidal particles. In the Gouy–Chapman diffuse layer, the concentration of the cations gradually decreases and that of the co-ions (anions) increases until a charge equilibrium is attained. The distribution of cations and anions around the clay surface and the corresponding electric profile are shown in **Figure 2.13**. The thickness of the two layers is termed the Debye length represented by $1/\kappa$, and κ is known as Debye–Hückel parameter. The value of the Debye length can be calculated using the following **Equation (2.1)**:

$$\frac{1}{\kappa} = \left(\frac{\epsilon_o k D T}{2 e_o^2 n_o v^2} \right)^{1/2} \quad \text{Equation (2.1)}$$

where, $1/\kappa$ is the double layer thickness, ϵ_o the permittivity of vacuum ($8.854 \times 10^{-12} \text{ C}^2 \text{ J}^{-1} \text{ m}^{-1}$), k the Boltzmann constant ($1.38 \times 10^{-23} \text{ J K}^{-1}$), D the dielectric constant of the medium, T the temperature (K), e_o the electronic charge ($1.602 \times 10^{-19} \text{ C}$), n_o the ion concentration, and v the

ionic valence. According to this equation, the thickness of the double layer varies directly with the temperature and is inversely proportional to the ionic valence and the square root of the ionic concentration. By altering the concentration of electrolyte, the thickness of the electrical double layer can be attenuated to destabilize the clay particles. This means that the higher the ion concentration, the smaller is the EDL. The potential at the Stern plane is called the Stern potential. Within the Gouy–Chapman diffuse layer, Brownian motion of electrolytes produces a shear plane that strongly separates the ions associated with the fixed layer and the potential at the shear plane is known as zeta potential (ζ). The magnitude of the zeta potential varies with the double layer thickness. The thicker the EDL, the higher is the zeta potential. The zeta potential is determined to control the stability of the colloidal system and characterize the EDL. The negative charge on the clay particles is the primary factor in the stability of clay dispersion. Therefore, to overcome the electrostatic repulsion and flocculate the clay dispersion, the net negative charges must be reduced; hence, a reduction in zeta potential magnitude must be attained. At zero zeta potential, the surface charge is balanced out by the counter ions which indicates the aggregation of clay particles^{38–40}.

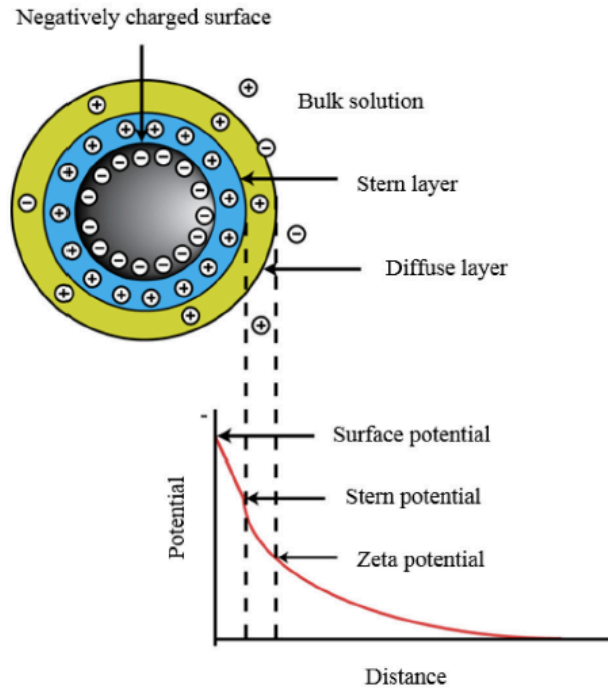


Figure 2. 13. Schematic illustration of the electrical double layer⁴⁰.

2.9 Colloid particles interactions

The stability of a colloidal system also depends on how the colloidal particles interact with each other. The DLVO theory, named for the research of Derjaguin and Landau in 1941 and Verwey and Overbeek in 1948, is used to quantify the net force between these particles and the distance separates them. Based on the DLVO theory, attractive van der Waals and the repulsive electrostatic double layer forces are considered the two balancing forces to induce dispersion or flocculation of the particles. The van der Waals forces caused by the formation of dipoles between particles and depend on the distance between particles (R) and the nature of the two colloidal particles as given in the following **Equation (2.2)**⁴¹:

$$U = CR^{-6} \qquad \text{Equation (2.2)}$$

where C is the constant depending upon the nature of the particles. The repulsive forces that are induced by the formation of the electric double layer of the colloid particles depend on the changes in cation valence, dielectric constant, electrolyte concentration and pH. Both the attraction and repulsion forces between the colloidal particles vary in magnitude with separation distance and energy barrier (**Figure 2.14**). If the attractive van der Waals forces overweigh the repulsive electrostatic double layer forces, the system is unstable and the particles are prone to aggregation. On the other hand, if the repulsive electrostatic double layer forces overweigh the attractive forces, the net force is repulsive and the particles will be dispersed and the system is stable and well dispersed; hence, an energy barrier in a suspension that prevents the aggregation of particles will occur. As a result, the colloidal particles must provide sufficient kinetic energy to overcome the potential energy barrier in order to aggregate. Based on the potential curve, that gives the sum of all the potential energy in correlation with the distance between two particles in the colloids, particles are held firmly together by van der Waals forces at the primary minimum, whereas the particles are more loosely bound in a reversible fashion at the secondary minimum. An energy barrier called the primary maximum is located between the primary and secondary potential minimum preventing the particles getting close enough to each other to experience the deep attraction at the primary minimum. The energy barrier represents the electrostatic repulsion and is related to the zeta potential: hence, the stability of the colloidal particles can be anticipated by measuring the zeta potential^{38,40,42}.

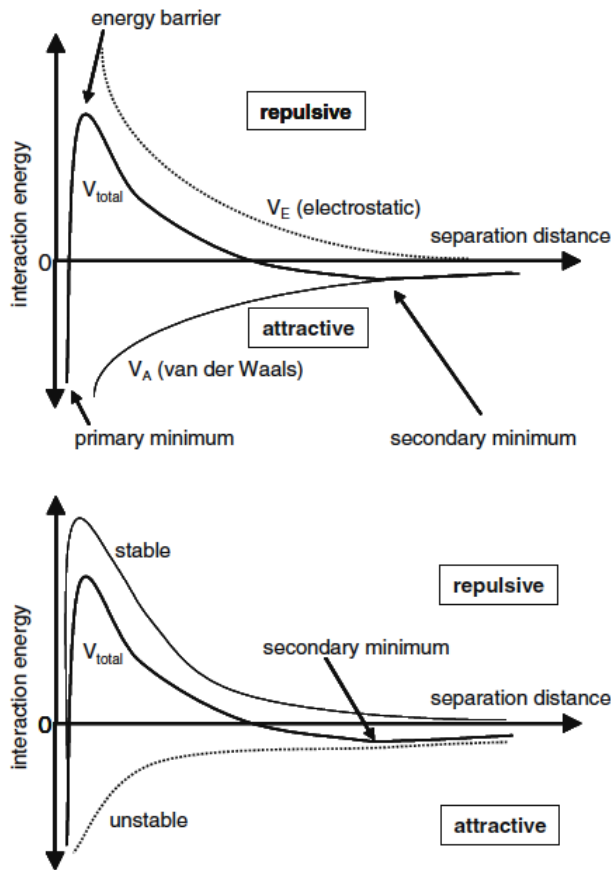


Figure 2. 14. Schematic of repulsive and attractive potential as a function of distance between particle surfaces⁴².

2.10 Colloid - Polymer Interactions

The presence of polymers in a colloidal system has a profound influence on its stability. Several processes may occur when a polymer solution is added to a colloidal system⁴³:

- 1- Transportation of polymer to the solid-liquid interface.
- 2- Adsorption of the polymer on the solid surface.
- 3- Rearrangement of adsorbed polymer chains on the solid surface.
- 4- Collision between coated colloidal particles which can cause flocculation.

Polymer chain adsorbed on the solid surface can have one or any combination of three conformations depending on the affinity of the polymer to the surface. **Figure 2.15** schematically shows the different possible conformations of polymers at solid-liquid interfaces:

- 1- Thin layers with a low adsorbed layer thickness.
- 2- Coils and loops with a moderate adsorbed layer thickness.
- 3- Trains, loops, and tails with a high adsorbed layer thickness.

A train describes the conformation where the polymer chain is directly attached to the solid surface; a loop refers to the conformation in which the polymer chains are bound by trains at either end; and a tail refers to one end of polymer chains bound to trains with the other end extended into the colloidal system as presented in **Figure 2.16 (a)**. The uncharged polymers are considered a poor flocculants of a dilute aqueous clay system because the polymer segments adopt a random coil rather than extended conformation unless the segment dimension is of the order of the mean interparticle separation. As a result, increasing the flocculant molecular weight can enhance the flocculation efficiency⁴⁴.

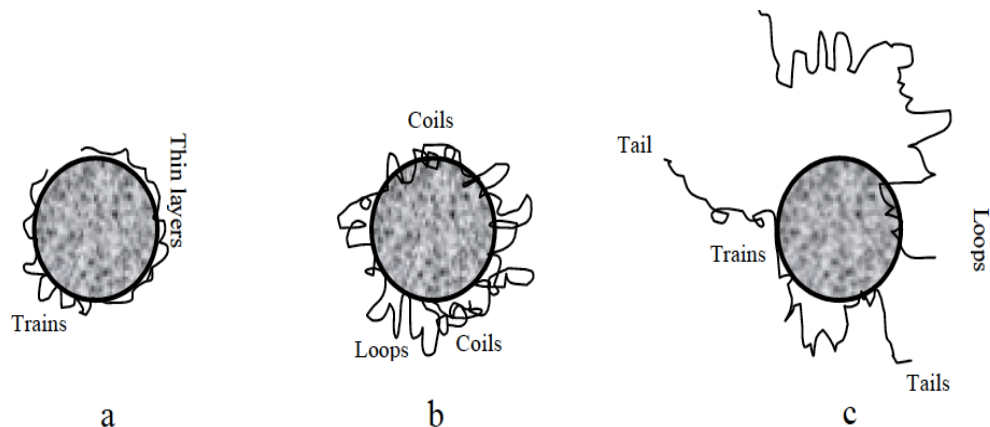


Figure 2. 15. Possible conformations of polymer chains at solid-liquid interfaces: (a) thin layers with a low adsorbed layer thickness; (b) coils and loops with a moderate adsorbed layer thickness; (c) Trains, loops, and tails with a high adsorbed layer thickness⁴⁴.

The driving force for the adsorption of uncharged polymers adsorption on the clay surface is the translation entropy (**Figure 2.17**). The positively charged polymers are effective flocculants of negatively charged colloids. The flocculation occurs due to the collision of particles; hence, the collision and the adsorption of cationic polymers neutralize the surface charge of the colloids and form bridges to hold the coated particles together. On the other hand, the anionic polymers can form bridges because the polymer segments forming hydrogen bonds are adsorbed on the particle surface and generate greater loops extending from the solid surface; accordingly, flocculation occurs. The mutual charge repulsion between polymer segments and the negatively charged colloids promotes the extension of polymer chains leading to an increase in the collision probability. The formed network through adsorption results in flocculation ⁴⁵.

DLVO theory describes the stability of colloidal particles by predicting the critical coagulation concentration (CCC). The C.C.C refers to the point where the potential energy barrier opposing coagulation disappears. For effective flocculation to occur, fractional surface coverage must be obtained whereas complete surface coverage re-stabilizes the colloids (**Figure 2.16 (b)**). Extremely low dosage does not result in flocculation because of insufficient polymer to form bridging links between the dispersed particles. When an over dosage is used, excess polymer overly coats the particle surface such that no sites are available to bridge with other particles leading to a reduction in the flocculation efficiency because of steric stabilization ¹⁰. Here the particles are said to be re-stabilized as shown in **Figure 2.16 (c)**.

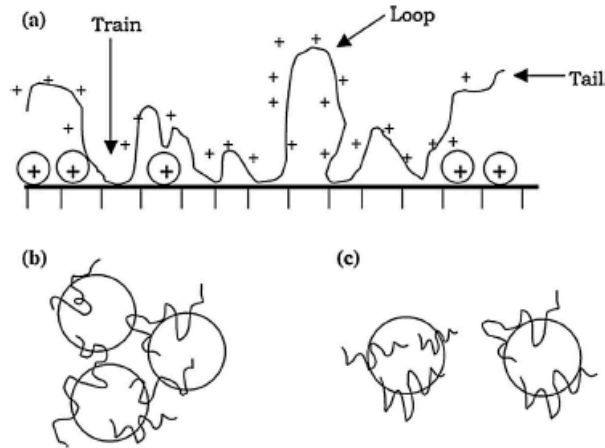


Figure 2. 16. (a) Adsorption of polymer and formation of loops available for binding. (b) Polymer bridging between particles (aggregation). (c) Re-stabilization of colloid particles (floc breakup)¹⁰.

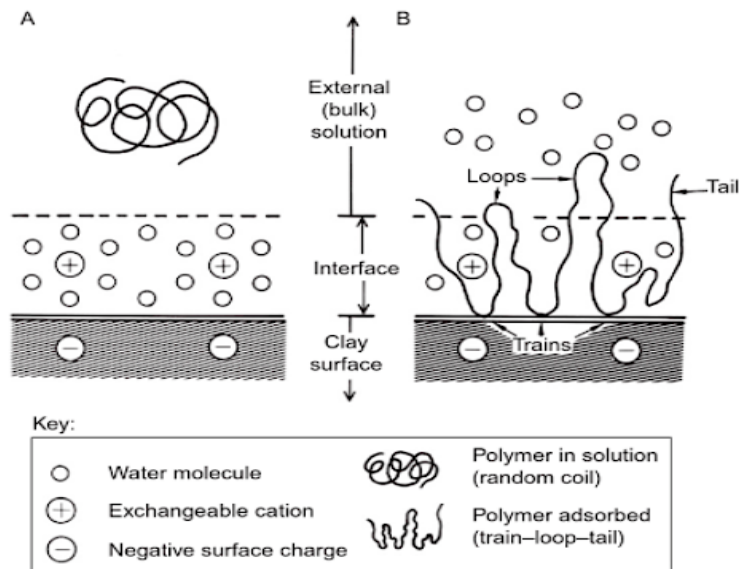


Figure 2. 17. Diagram showing the series of events when an uncharged, flexible polymer adsorbs at a clay mineral surface from a dilute aqueous solution. (A) Polymer in solution adapting a random coil conformation; (B) on adsorption, the polymer chain uncoils and adopts a train-loop-tail conformation, displacing relatively ordered water molecules from the interface into the external (bulk) solution⁴⁵.

2.10.1 Effect of polymers on zeta potential

Polymers can affect the zeta potential through charge neutralization and shear plane displacement. Zeta potential measurement is useful to predict and control the stability of colloids;

hence, it is able to characterize flocculation efficiency of polymers. The magnitude of zeta potential depends on the double layer thickness^{10,46}. Accordingly, the thickness of EDL determines the engineering performance of the polymer flocculants. Indeed, the thinner the EDL, the lower the zeta potential; therefore, the stronger the tendency of flocculation. At the optimum dosage, the observed reduction in the zeta potential of colloids by uncharged polymers is ascribed entirely to shear plane displacement. The adsorption of uncharged polymers on a negatively charged particle alters the structure of EDL around the target particles where the presence of trains modifies the Stern layer and both loops and tails modify the Gouy–Chapman diffuse layer as illustrated in **Figure 2.18**. Positively charged polymers can effectively enhance flocculation mainly by electrostatic attraction. Therefore, the reduction in the zeta potential can be attributed to the charge neutralization that causes a compression in the thickness of EDL. On the other hand, the adsorbed anionic polymers form bridging contacts between particles via hydrogen bonding, and the reduction in zeta potential can be ascribed as the shear plane displacement. The adsorbed anionic polymers change the properties of the EDL and produce a hydrodynamic effect as the ions in the diffuse double layer might be displaced from the Stern layer^{10,46}.

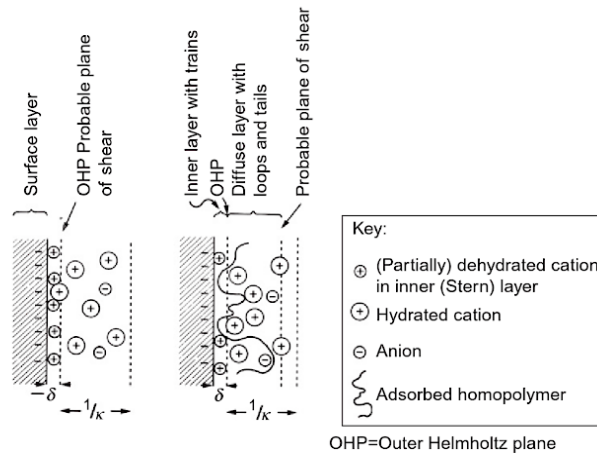


Figure 2. 18. The effect of adsorbed uncharged homopolymers on the structure of the electrical double layer at a negatively charged (clay mineral) surface¹⁰.

2.11 Cellulose

Cellulose is the most abundant, renewable, and sustainable material in the world, and it can be extracted from wood and plant fibers, tunicate and bacterial cellulose^{47,48}. The cellulose chains are homopolymers of anhydroglucose units, where the repeating segments are connected via the β -1,4-glycosidic linkages as shown in **Figure 2.19**⁴⁹⁻⁵¹. These linear homopolymers are linked together via the van der Waals forces as well as inter- and intra-molecular hydrogen bonds to form hierarchical assemblies as shown in **Figure 2.20 (a)**⁴⁹. Hence, the cellulose materials are insoluble in water as the hydroxyl groups in the chains are bonded to each other. The individual chains assemble to form microfibrils, that further assemble into macrofibers and fibers, and each microfibril consists of crystalline and amorphous regions^{48,50}.

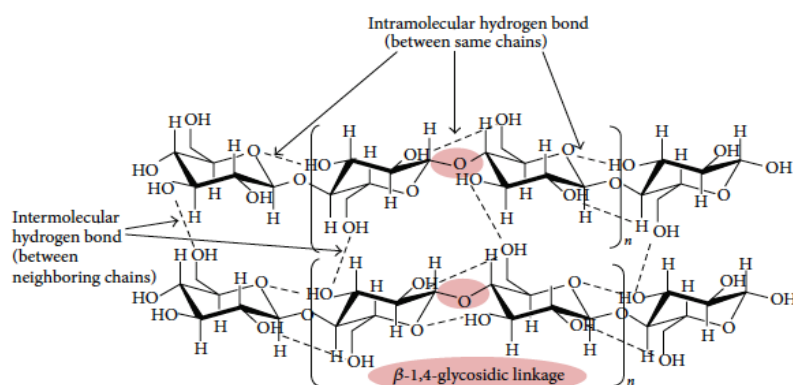


Figure 2. 19. Chemical structure of cellulose chains⁴⁹.

The acid hydrolysis of cellulose fibers disrupts its amorphous regions leaving the rigid crystalline regions intact as shown in **Figure 2.20 (b)**^{49,52}. Due to the unique properties of cellulose, and stemming from its surface chemistry, mechanical robustness, biocompatibility, and its biodegradability, cellulose has been widely applied in various industrial sectors^{51,52}.

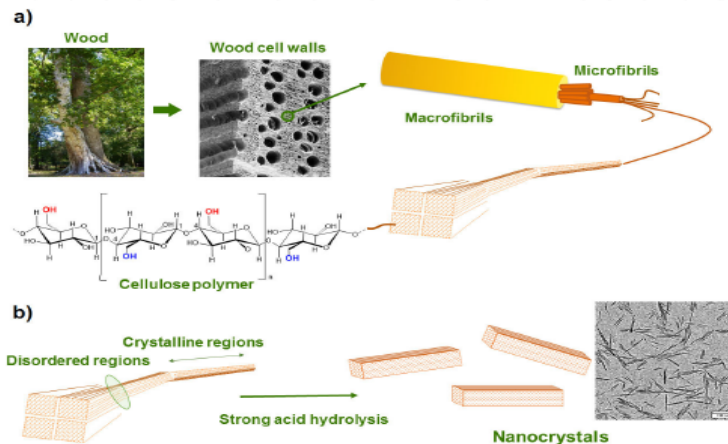


Figure 2. 20. (a) Structural hierarchy of the cellulose fiber components from the tree to the anhydroglucose, (b) preparation of nanocrystals by selective acid hydrolysis of the disorganized regions of cellulose microfibrils ⁵⁰.

2.11.1 Cellulose nanocrystals

Cellulose nanocrystals are unique nanomaterials derived from cellulose by the controlled acid hydrolysis of disordered regions, releasing individual rod-like rigid crystallites called cellulose nanocrystals (CNC) ^{49,52}. The conditions of hydrolysis during the extraction process (such as the type of acid, acid concentration, temperature, and duration) plays a critical role on the surface morphology of the CNCs. When the hydrolysis is performed with hydrochloric acid (HCl), additional carboxyl groups are produced; as a result, the suspended CNCs easily agglomerate due to hydrogen bonding between crystallites forming micron size agglomerates. When H₂SO₄ is employed, negatively charged sulfate ester groups are decorated on the surface of the crystallites preventing agglomeration and yielding a stable suspension (**Figure 2.21**) ⁵³. The resulting crystalline regions (CNCs) are rod-like in shape, having nano-scale dimensions (length from 200 – 1000 nm and diameters of 5 – 15 nm). Cellulose nanocrystals possess excellent physical properties, including high tensile modulus, similar to steel or Kevlar (100 to 160 GPa), low density (0.8 to 1.5 g/cm³) and a large surface area (~250 m²/g) ⁵⁴⁻⁵⁶. The high aspect ratio of CNCs gives

rise to percolation at low concentration which will promote floc formation. In addition, the rigidity of the CNCs minimizes gelation, preventing entanglement and improving processability^{57,58}. The surface of the rod-shaped nanocrystals are decorated with hydroxyl groups and these unique properties provide an ideal platform for surface modification to prepare nanocomposite materials with desired surface characteristics customized for a wide range of applications including wastewater treatment^{59,60}.

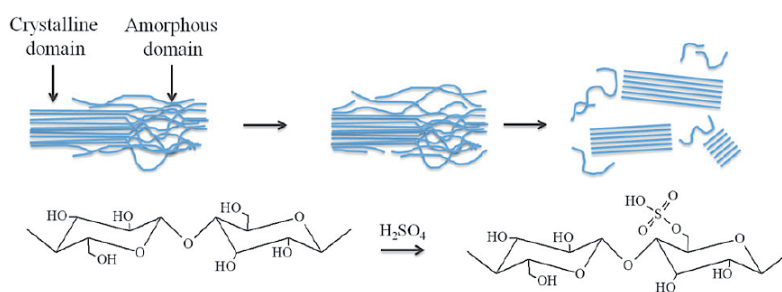


Figure 2. 21. Schematic representation of the isolation of CNC⁵³.

2.11.2 Modification of cellulose nanocrystals

CNCs have very high surface area with a large number of hydroxyl groups which make it suitable for a wide variety of functionalization, depending on their desired application^{51,52}. In most cases surface modification of CNCs can be conducted to (1) prevent self-aggregation and achieve a good dispersion of the nanoparticles in most common polar solvents or hydrophilic polymeric matrices; (2) improve the compatibility when used along with organic or hydrophobic polymer matrices by tuning the surface energy characteristics of nanocrystals; (3) introduce chemical functionality on nanocrystals for advanced functional applications⁶¹. The main challenge is to perform surface modification on the nanocrystals while preserving the original morphology and maintaining the integrity of the CNCs.

Surface modification of CNCs can be conducted by attaching small molecules or polymer brushes via covalent bonds (chemical interactions) or non-covalent bonds (physical interactions). There are various techniques that can be applied to functionalize CNCs, including physical absorption of polyelectrolytes or surfactants, chemical derivatization by coupling hydrophobic small molecules, or chemical grafting of polymeric chains and advanced functional molecules as shown in **Figure 2.22**⁶². The physical absorption is the simplest method, in comparison to chemical modification, and it is used mainly to prepare uniform dispersion of CNCs in hydrophobic solvents and polymers. This can be achieved by coating the surface of nanocrystals with surfactants, where the hydrophilic end of the surfactant molecules adheres to the surface of CNCs, while the hydrophobic end extends out providing a non-polar surface. In the field of chemical modification, polymer grafting can be performed using two approaches, namely, “grafting-to” and “grafting-from” as shown in **Figure 2.23**. The grafting to approach involves the attachment of pre-synthesized polymer to the hydroxyl groups of the CNC surface. In the grafting from approach, the polymer chains are grown from the surface of the CNCs, which first has to be functionalized with an initiator prior to performing the graft polymerization in the presence of monomers. In the first strategy, the most common approaches are: (1) the isocyanate-mediated reaction, where isocyanates are used to graft polymeric chains onto the surface of nanocrystals; (2) the carboxylation-amidation reaction in which a covalent amide bond between a primary amine-terminated polymer and carboxylated CNCs is created; (3) click chemistry where nanocrystals with advanced functions, such as fluorescent labeling, gene delivery or photo-bactericidal effect are produced. In the second strategy, different approaches have been examined including conventional free radical polymerization (CRP), ring-opening polymerization (ROP), ionic polymerization, and reversible-deactivation radical polymerization (RDRP) methods.

Another chemical modification method is derivatization, which has been proven to improve the dispersibility and compatibility of nanocrystals in polymeric matrices and solvents. Commonly used strategies for modifying CNCs are sulfonation, acetylation/esterification, silylation, TEMPO oxidation, cationization, and carbamation. In the sulfonation reaction, H_2SO_4 is used to produce a highly stable suspension because of the incorporation of sulfate groups onto the nanocrystals. Surface esterification or acetylation of CNCs imparts an ester functional group, COO^- on the surface of nanocrystals by the condensation of the carboxylic acid group ($COOH$) and alcohol group (OH). As depicted in **Figure 2.23**, CNCs can be silylated with organo-silanes having different alkyl lengths. TEMPO oxidation reaction leads to the formation of surface-carboxylated CNCs that could be further modified to introduce more moieties by several approaches. For example, the amidation of CNCs is one approach where oxidized CNCs are used as the starting material to be amidized. Cationization of CNCs is another important chemical modification, and glycidyltrimethylammonium chloride (GTMAC) or derivatives have been widely utilized to cationize the surface of CNCs. In the carbamation reaction, isocyanates can be employed for the modification of CNCs ⁶².

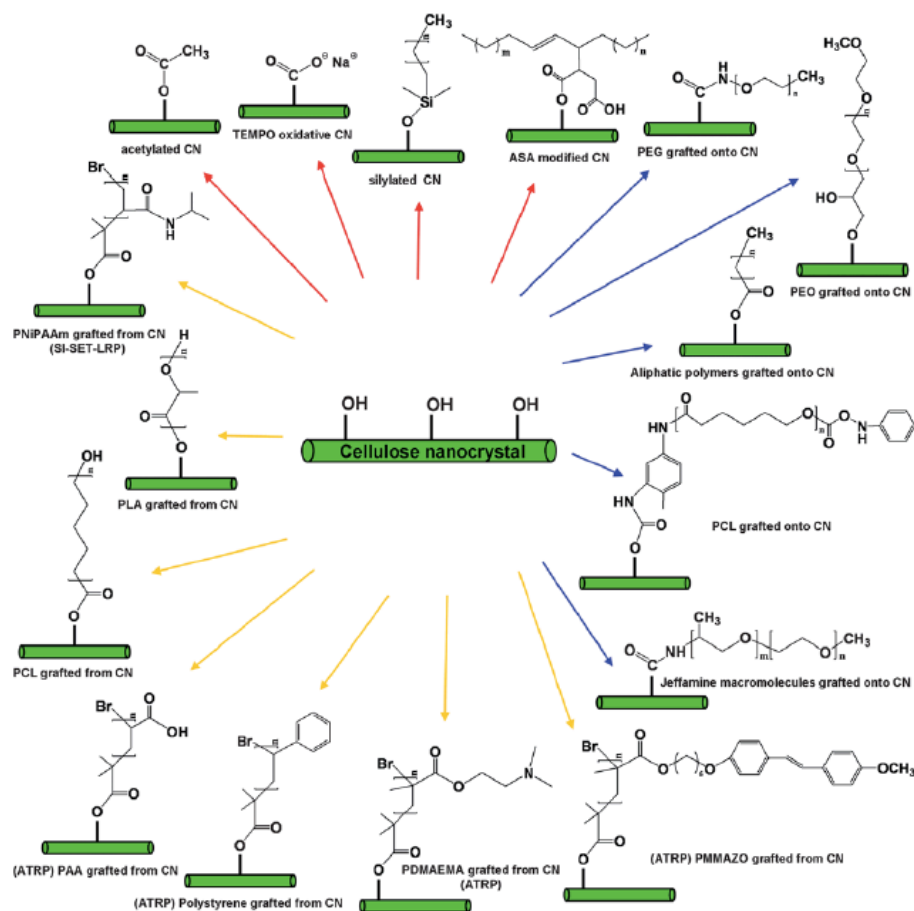


Figure 2. 22. Diverse surface modifications on cellulose nanocrystals, red arrows represent the substitution of surface hydroxyl groups with small molecules, blue arrows represent the surface modification based on the “graft onto” strategy, and yellow arrows represent the surface modification based on the “graft from” strategy⁵².

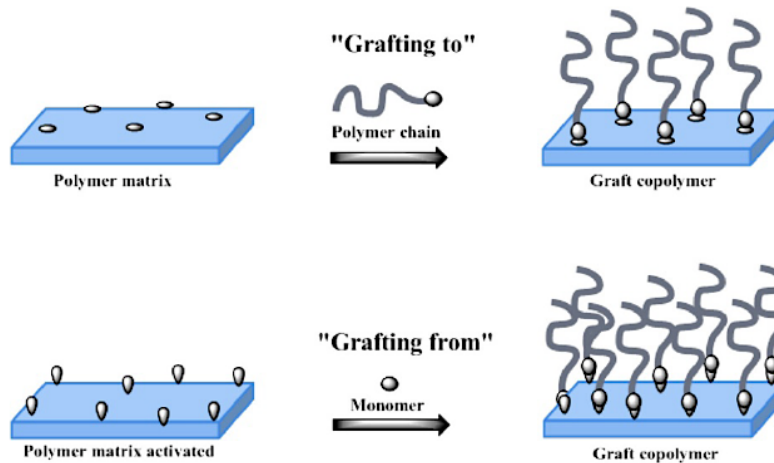


Figure 2. 23. Grafting of polymer brushes on CNCs by (a) the “grafting-to” approach whereby pre-synthesized polymer with end-functionality “B” react with CNC surface “A” groups and (b) the “grafting-from” approach whereby polymers are grown from surface-immobilized initiators (I) by adding monomers to the growing polymer chain active site⁶³.

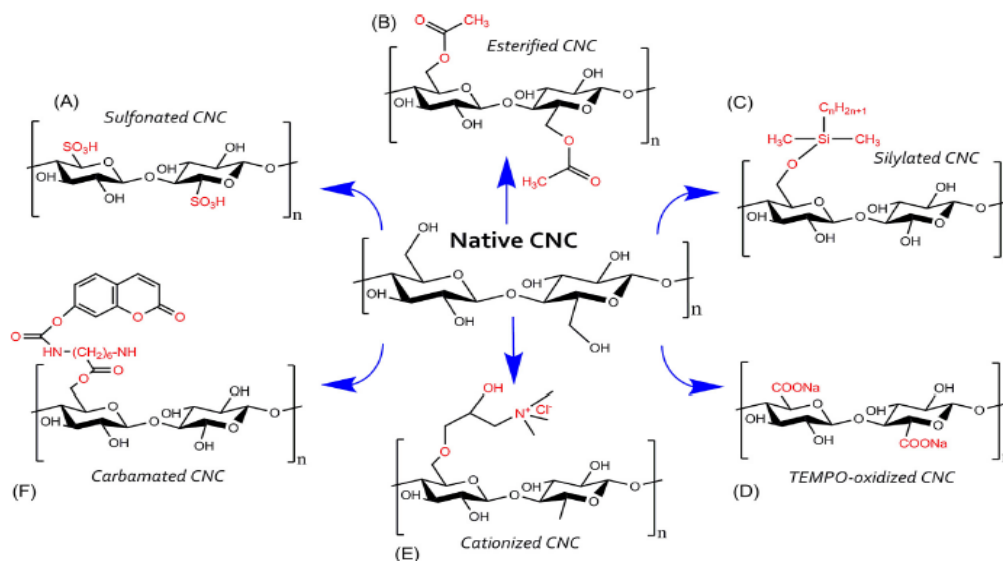


Figure 2. 24. Schematic diagram showing the common surface - OH substitution approaches classified as (A) sulfonation; (B) acetylation/esterification; (C) silylation; (D) TEMPO-oxidation; (E) cationization, and (F) carbamation. Note that the newly introduced functional groups are highlighted in red⁶².

2.12 Introduction to stimuli-responsive polymers

The chemical composition of synthetic polymers has been adjusted to generate a variety of functional forms to match the requirements of the industrial and scientific applications. Synthetic polymers can have different chemical structures and properties and on the basis of the chemical properties can be classified into different categories. Out of these, “stimuli-responsive” materials have the ability to respond to external stimuli and are also known as “smart,” or “environmental-sensitive” or “intelligent” polymers ⁶⁴⁻⁶⁶. The uniqueness of these polymers resides in their reversible responses that are manifested as changes in shape, size or solubility at the macroscopic level from hydrophilic to hydrophobic state. The driving force behind the reversible responses can be classified into three categories as presented in **Figure 2.25**: (i) chemical (pH), solvent, ionic strength; (ii) physical (temperature, magnetic field ,light, ultrasound, mechanical deformation); (iii) biological (receptors and enzymes) ^{64,67}. Stimuli-responsive polymers possess the appropriate hydrophilic–hydrophobic balance in the molecular structure to yield such characteristics ^{68,69}.

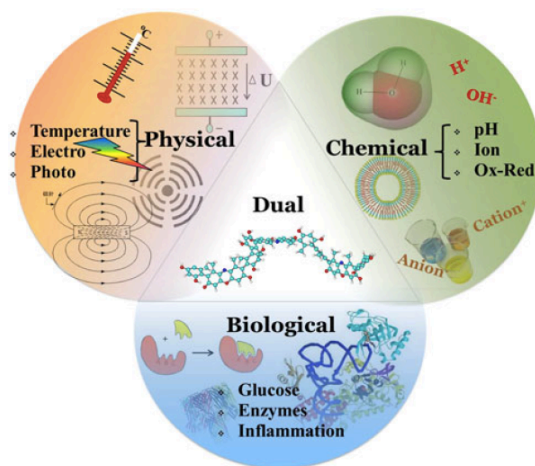


Figure 2. 25. Schematic illustration of stimuli for stimuli-responsive polymers ⁶⁷.

The stimuli-responsive polymers can be categorized into three classes according to their physical forms as shown in **Figure 2.26**. They are (i) linear free chains in solution, (ii) covalent cross-linked reversible and physical gels, and (iii) chain adsorbed or surface grafted form ‘smart’ surfaces or membranes ^{70,71}.

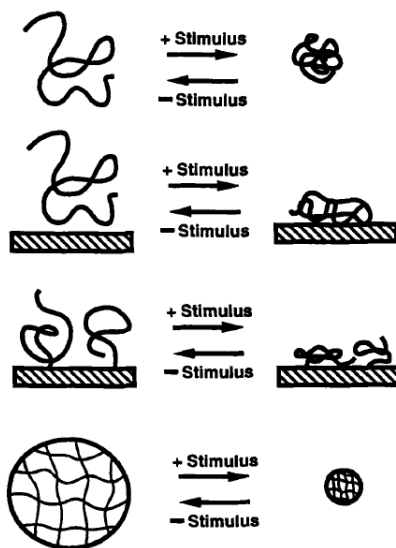


Figure 2. 26. Schematic example of the different types of responses of “stimuli” polymer systems to environmental stimuli ⁷¹.

The exploitation of polymer responses to stimuli finds wide-ranging application in the biomedical fields and non-biologically related fields that include water treatment and food packaging. There have been a number of biomedical applications in medicine and biotechnology for such smart polymers due to their unique properties, such as the ability to mimic the biopolymers adaptive behaviors, high stability, and loading capacity ⁷².

2.13. Thermo-responsive polymers

Synthetic thermo-responsive polymers have been extensively investigated, since temperature is an easy external stimuli to implement ⁷³. The thermo-responsive behavior can be divided into two

classes; those possessing a lower critical solution temperature (LCST) and upper critical solution temperature (UCST) as shown in **Figure 2.27**. Polymers with a LCST display a miscibility gap at high temperatures that induces phase separation due to the disruption of polymer-water interactions above the LCST. The responsivity of a system with UCST displays a phase separation upon cooling due to the strong polymer-polymer interactions. For example, aqueous solutions of poly(N-isopropyl acrylamide) (PNiPAAm), undergo a coil-to-globule transition upon heating beyond their respective LCST close to the physiological temperature of about 37 °C ⁷⁴. Compared to the widely studied thermo-responsive PNiPAAm, poly(ethylene oxide) (PEO) and its derivatives are a new class of uncharged, nontoxic and water-soluble bio-compatible polymers that possess LCSTs with a broader temperature range of 26 to 95 °C ⁷⁵.

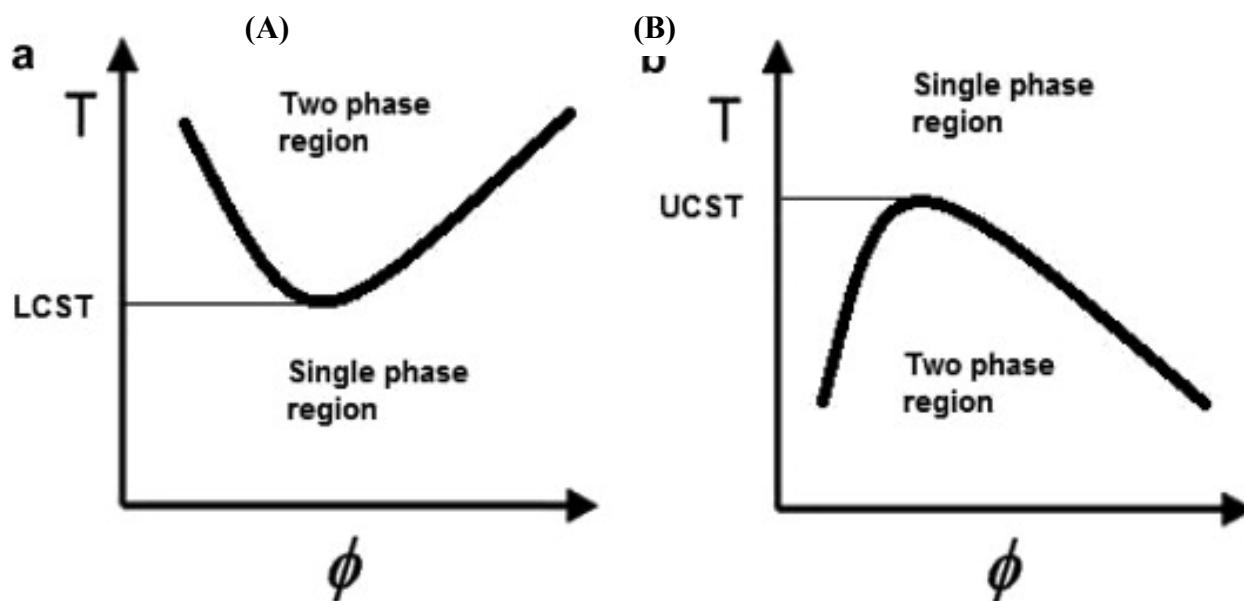


Figure 2. 27. Phase diagram for polymer solution (A) lower critical solution temperature (LCST) behavior and (B) upper critical solution temperature behavior ⁷⁶.

2.13.1. Thermodynamics of thermo-transitions

The thermodynamic reasons for phase separation can be understood on the basis of the Flory-Huggins theory that has been the foundation for the more elaborated theories. Flory-Huggins

theory can distinguish the thermodynamics of mixtures of macromolecules in comparison with their small molecule analogues, and it can also determine the interaction forces that lead to the phenomenon of phase transition. Mixing a polymer in a solvent is accompanied with changes in certain thermodynamic factors; specifically, enthalpy and entropy. In the Flory-Huggins theory, the solute-solvent system was modeled as a lattice structure, considering the solvent (water) as component 1 and the solute (small molecule) as component 2 as shown in **Figure 2.28**⁷⁷.

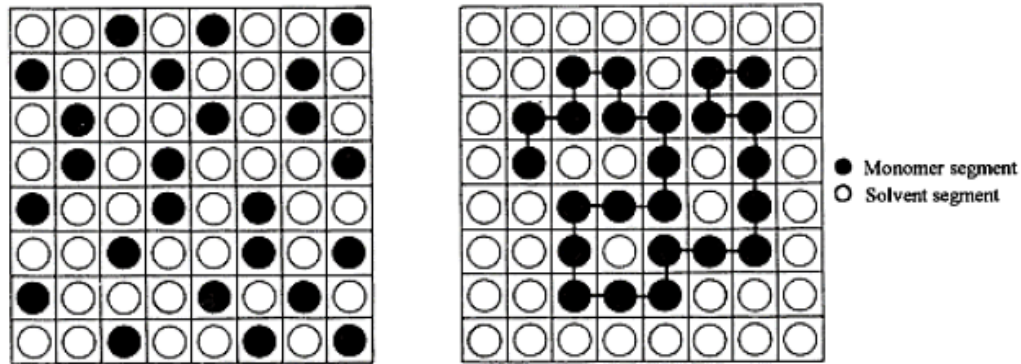


Figure 2. 28. Placement of solute molecules on a lattice. (Left) N_2 small molecules. (Right) A polymer chain occupying N_2 cells⁷⁸.

The number of possible ways to put N_2 solute molecules on a lattice leads to the well-known Flory-Huggins expression for the entropy of mixing in a polymer solution (**Equation (2.3)**):

$$\Delta S_{mix} = -k (N_1 \ln n_1 + N_2 \ln n_2) \quad \text{Equation (2.3)}$$

Where n_i , and N_i are the mole fraction and the number of molecules of component i respectively.

In the case of a polymer chain composed of x segments or repeat units, and each segment occupies a cell, the above equation is rearranged as shown in **Equation (2.4)**:

$$\Delta S_{mix} = -k (N_1 \ln v_1 + N_2 \ln v_2) \quad \text{Equation (2.4)}$$

Here v_i is the volume fractions of component i and can be defined by **Equations (2.5)** and **(2.6)**:

$$v_1 = \frac{N_1}{N_1 + xN_2} \quad \text{Equation (2.5)}$$

$$v_2 = \frac{xN_2}{N_1 + xN_2} \quad \text{Equation (2.6)}$$

This equation indicates that the number of ways that one component is arranged on the lattice sites is reduced when one of the components exists as a long chain. In this model the enthalpy of mixing ΔH_{mix} for the same polymer-solvent system can be defined using **Equation (2.7)**:

$$\frac{\Delta H_{mix}}{kTN_1v_2} = \chi = \frac{(\epsilon_{11} + \epsilon_{22} - \epsilon_{12})}{kT} \quad \text{Equation (2.7)}$$

The interaction parameter (χ) is related to the difference between the mixed interaction energy (ϵ_{12}) and sum of the pure component energies (ϵ_{11} and ϵ_{22}) according to **Equation (2.7)**. This interaction parameter is known as the Flory-Huggins interaction parameter, and it describes the miscibility, swelling equilibria of polymer solutions^{77,79,80}. The Flory Huggins interaction parameter is related to the free energy of mixing according to **Equation (2.8)**:

$$\Delta G_{mix} = -kT(N_1 \ln v_1 + N_2 \ln v_2 + \chi N_1 v_2) \quad \text{Equation (2.8)}$$

The first two terms represent the entropy gain on mixing a polymer, while the last term represents the enthalpic contribution to the free energy.

Two major features that can be derived from **Equation (2.8)** to distinguish between the thermodynamic of polymer mixtures in comparison with their small molecules: (i) polymer mixtures can undergo phase separation upon heating through a lower critical solution transition (LCST) unlike most of the small molecules analogs, (ii) the reduced entropy of mixing that originates from the random distribution of chains results in immiscibility in the absence of favorable enthalpic interactions. In addition, the Flory-Huggins interaction parameter (χ) describes the behavior of stimuli-responsive polymers at different temperatures. For values of χ greater than 0.5, the polymer-polymer interactions are more favorable than the polymer-solvent interactions and the solvent is known as a bad solvent. Accordingly, For values of χ less than 0.5, the polymer-

solvent interactions are more favorable than the polymer-polymer interactions and the solvent is known as a good solvent. The Flory-Huggins interaction parameter (χ) of 0.5 is considered to represent the Flory θ -solvent condition in which the polymer-solvent interactions are identical to the polymer-polymer interactions ⁷⁹.

2.13.2. Phase transition behaviors

The thermodynamic reasons for phase separation can be understood on the basis of the Gibbs free-energy of mixing **Equation (2.9)**, where a negative value implies that the polymer-solvent system is homogeneous.

$$\Delta G_{mix} = \Delta H - T \Delta S \qquad \text{Equation (2.9)}$$

For polymers possessing a lower critical solution temperature (LCST), both the enthalpy of mixing ΔH and the entropy of mixing ΔS are negative. At low temperature the term ΔH exceeds the ΔS ; thus, ΔG_{mix} is negative and the polymer-solvent system is miscible. When increasing the temperature, the entropy of water is increasing; thus, ΔG_{mix} is positive where the “hydrophobic effect” takes place rendering the polymer-solvent system is immiscible. On the other hand, for polymers possessing an upper critical solution temperature (UCST), both the enthalpy of mixing ΔH and the entropy of mixing ΔS are positive and the same assumption can be applied to explain phase separation upon cooling ⁷⁹.

The phase transition behaviors of polymers with LCST-type transition will be explained in this section since it is related to the current study. Polymers with LCST-type transition can exhibit two phase transition behaviors: (i) a coil-globule transition (described as intramolecular aggregation), and/or (ii) agglomeration (described as intermolecular aggregation) ⁸¹. A coil-globule transition is described as a process by which an expanded chain in a random coil conformation transitions to polymer a collapsed globule due to a change in temperature as shown in **Figure 2.29(A)**. Below

the LCST, the polymer chains are completely dispersed and adopt a random coil conformation by the formation of hydrogen bonds with the water molecules. Above the LCST, the polymer-water hydrogen bonds are disrupted and the polymer chains adopt a globular conformation. The poly(*N*-isopropylacrylamide) PNiPAAm can undergo a coil-globule transition at 32 °C and dynamic light scattering (DLS) studies were performed for its aqueous solutions below and above the lower critical solution temperature which showed a coil to globule transition behavior^{81,82} as shown in **Figure 2.29 (B)**.

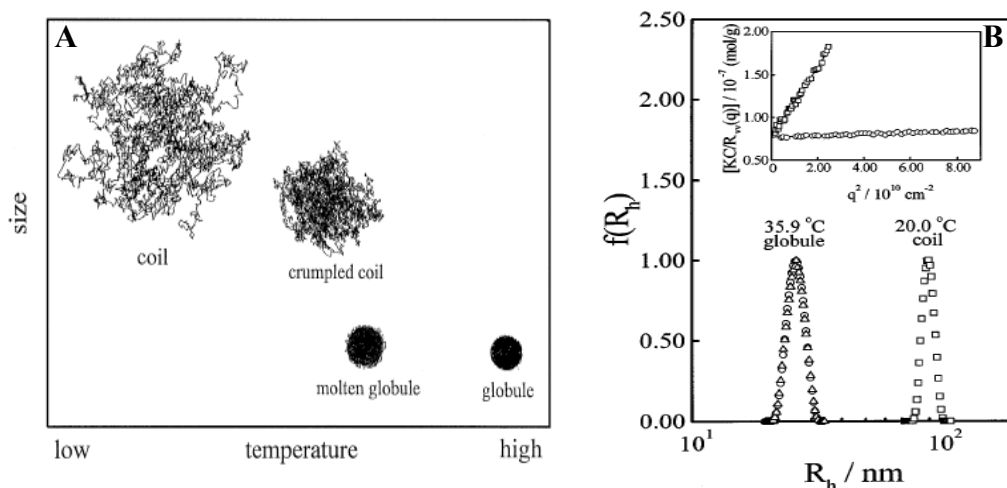


Figure 2. 29. Schematic illustration of the four thermodynamic stable states of (PNiPAAm) homopolymer, and the typical hydrodynamic radius distribution as a function of temperature for (PNiPAAm) (B)⁸².

Several studies were also conducted to examine the solution behavior of temperature-responsive molecular brushes. One example of such polymers is poly(*N,N*-dimethylacrylamide) (PDMA), which displays an LCST above 100 °C, and has shown both types of phase transition behaviors. In this study, a concentration-dependent LCST behavior was also observed as shown in **Figure 2.30**. When a 0.1 w% solution of the brush was warmed above the LCST, a decrease in hydrodynamic diameter was observed (with $D_H = 57$ nm at 20 °C leading to $D_H = 47$ nm at 55 °C) because of the side chains dehydrated on heating and favored intramolecular aggregation. On the

other hand, when the concentration of the copolymer was increased by an order of magnitude, to 1.0 w%, the hydrodynamic diameter increased as a function of temperature ($D_H = 104$ nm at 55 °C) because of the favored dehydration and subsequent intermolecular aggregation ⁸³.

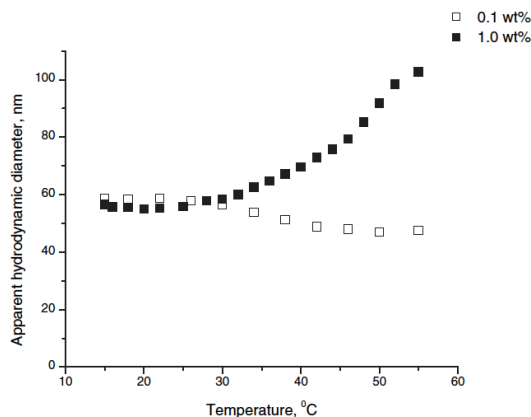


Figure 2.30. Temperature dependence of the apparent hydrodynamic average diameter for poly(BPEM-graft-DMA-stat-BA molecular brush, 0.1 wt% and 1.0 wt% solutions concentrations ⁸³.

Amphiphilic block copolymers that consist of covalently bonded hydrophobic and hydrophilic blocks can undergo a disorder-order transition (micellization) depending on the polymer concentration such as poly(2-ethoxyethyl vinyl ether-b-2-hydroxyethyl vinyl ether) (poly(EOVE-b-HOVE)) ^{81,84}. At low temperature, the copolymer chains are dispersed a random coil conformation as shown in **Figure 2.31**. However, when the copolymer chains are warmed through the critical micelle temperature, a macro-lattice formation is observed as shown in **Figure 2.31**.

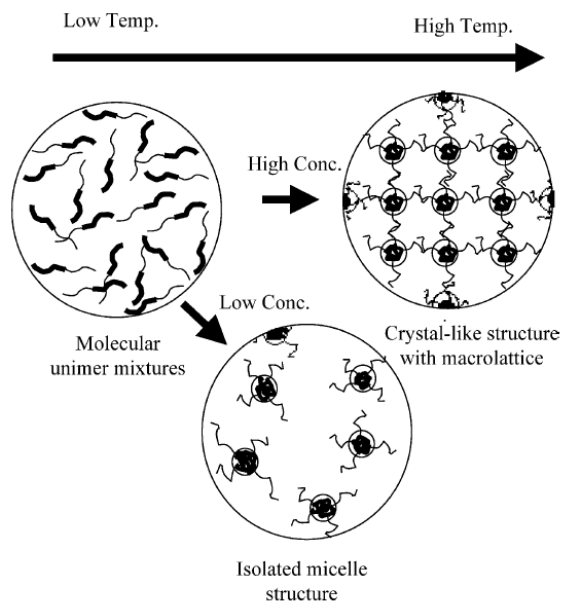


Figure 2. 31. Concentration dependence of the conformational changes of amphiphilic block copolymer ⁸⁴.

The structure of the thermo-responsive copolymers determines their thermo-transition behaviors. For example, copolymers consisting of a hydrophobic substrate and a thermo-responsive segment can switch on and off the formation of the micelles by manipulating the temperature as shown in **Figure 2.32(A)**. On the contrary, copolymers consisting of a hydrophilic substrate and a thermo-responsive segment can control the formation of micelles as shown in **Figure 2.32(B)** ⁸¹.

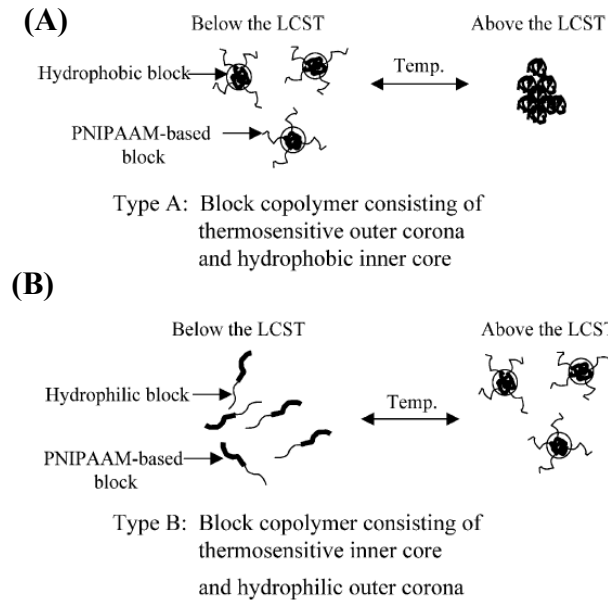


Figure 2. 32. Schematic illustration of two types of the micellar structure of a block copolymer containing PNiPAAm in aqueous dispersion ⁸¹.

2.13.3. Types of phase separation behaviors

There are three types of phase separation behaviors for thermo-responsive polymers in an aqueous dispersion that are detected with a UV-Visible spectrometer equipped with a temperature controller: (i) a fast phase separation with an overlap heating-cooling cycle curve (**Figure 2.33 A**), (ii) a fast phase separation with a **hysteresis** heating-cooling cycle curve (**Figure 2.33 B**), and (iii) a slow phase separation with a noticeable hysteresis heating-cooling cycle curve (shallow transition) (**Figure 2.33 C**). The shape of the transmittance curves depends on how fast the phase separation is and how the reversible process (the cooling cycle in case of LCST-type polymers) responds to the change in the temperature ^{81,85}.

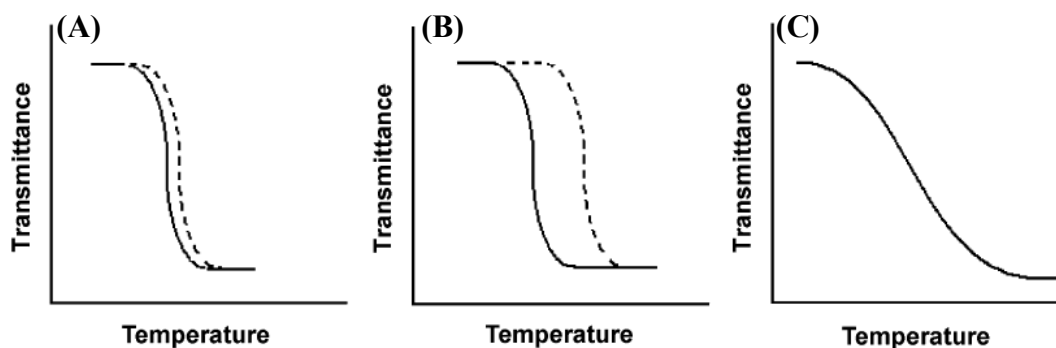


Figure 2. 33. Schematic illustration of three types of the thermo-responsive polymers in aqueous dispersion ⁸⁵.

The first type of phase separation occurs in homopolymer with appropriate hydrophobic-hydrophilic balance such as poly(phosphoester)s, acrylate- and methacrylate-based polymers, such as the copolymer poly(2-(2'-methoxyethoxy)ethyl methacrylate-*co*-oligo(ethylene glycol) methacrylate) (P(MEO₂MA-*co*-OEGMA)). The appropriate hydrophobic-hydrophilic balance of these polymers allows the solvation below the LCST; however, increasing the temperature above the LCST causes the disruption of hydrophobic-hydrophilic balance leading to a phase separation. The second type of phase separation often occurs in PNiPAAm or PNiPAAm copolymers as an example. The hysteresis in the transmittance curve is attributed to the slow diffusion of water molecules in the hydrophobic aggregates formed above the LCST due to the formation of interpolymer hydrogen bonding. The third type of phase separation often occurs in block copolymer such as poly(styrene-*b*-(*N*-isopropyl acrylamide)) di-block copolymers or P(S-*b*-NIPAAm) that are able to form micelles when the critical micelle concentration (CMC) is reached at low temperature. The micelles subsequently collapse above the LCST causing a decrease in the transmittance as shown in **Figure 2.34** ^{81,86}.

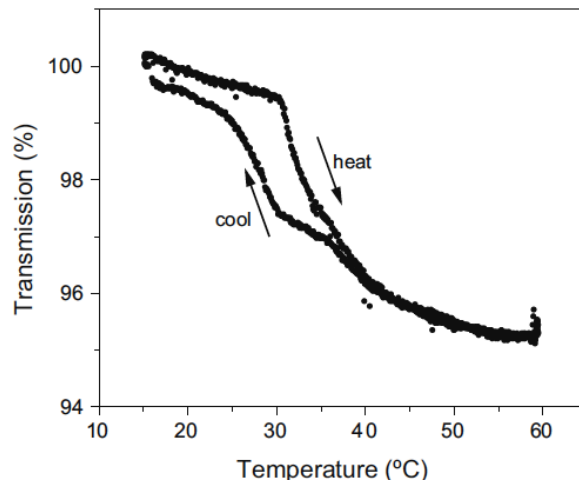


Figure 2. 34. Transmittance curve of a 0.2 mg/ml aqueous dispersion of P(S-b-NIPMA) ⁸⁶.

2.13.4. Factors affecting the LCST

Thermo-responsive polymers can be designed to meet the specific need for different applications by introducing monomer structures that contain specific functional groups and by varying the composition of these comonomers. The LCST or UCST of the thermo-responsive polymers can be further adjusted by changing the polymer chain architecture and/or the solvent conditions ^{81,87}. The effect of chain architecture, solvent conditions, and ionic interaction on the phase separation of LCST-type polymers will be illustrated in this section.

2.13.4.1. Chain architecture

2.13.4.1a. Number-averaged molecular weight

The dependence of phase transition on the number-averaged molecular weight M_n (or refer to as the degree of polymerization DP) is mainly driven by entropy ⁸⁷. For aqueous polymer solutions, the entropy of mixing (ΔS_m) is the sum of the the combinatorial entropy (ΔS_{com} which is positive) and the entropy loss caused by the hydrophobic effect (ΔS_{hpo} which is negative). When M_n

increases at a constant polymer concentration, the number of macromolecules (n_2) is lower which causes ΔS_{com} to decrease as indicated in **Equation (2.10)**:

$$\Delta S_{com} = -R (n_1 \ln v_1 + n_2 \ln v_2) \quad \text{Equation (2.10)}$$

where R is the ideal gas constant, n the molar number, v_i the volume fraction, and the subscripts 1 and 2 denote the solvent and the polymer, respectively. For LCST-type polymers, a higher M_n leads to a more negative ΔS_m which in turns decreases the LCST. For example, the LCST of PNiPAAm decreases from 40 to 36 °C as the M_n is increased from 2.8 to 26.5 kDa as shown in **Figure 2.35**⁸⁸. In the case of high hydrophobic thermo-responsive polymers, the effect of M_n on the LSCT has a narrow window compared to highly hydrophilic thermo-responsive polymers. For example, the cloud points (T_{cp}) of poly(2-hydroxyethyl methacrylate) (PHEMA) decreases from 39 to 28 °C as the DP increased from 3.9 to 5.9 kDa as shown in **Figure 2.36**⁸⁹.

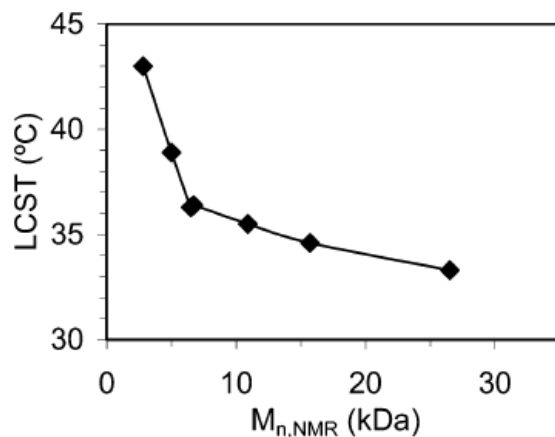


Figure 2. 35. The effect of M_n on the LCST of narrow-disperse PNiPAAm samples⁸⁸.

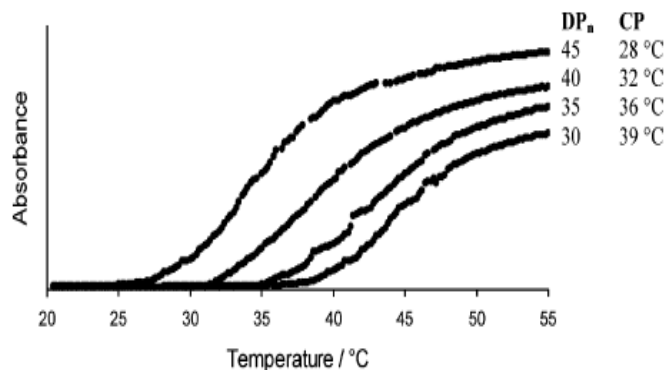


Figure 2. 36. The effect of M_n on the LCST of PHEMA samples ⁸⁹.

When two LCST-type polymers with different M_n are mixed, a cooperative aggregation behaviour is observed if these polymers show a strong weight-averaged molecular weight (M_w) dependence on their transition temperatures. The mixture produces a single turbidity curve with cloud point lying between the locations of each component. The potential to produce polymers with a cooperative aggregation of four LCST-type polymer by a simple mixing was studied. The polymers used in the study can be categorized into two types (i) M_w -dependent LCST (poly(N-vinylpiperidone) (PVPip), poly(N-vinylcaprolactam) (PVCap), PNiPAAm) and (ii) M_w -independent LCST (POEGMA). The study confirmed the hypothesis where the polymer-solvent interaction is dependent on the M_w ; as a result, mixing thermo-responsive polymers with different M_w can fine-tune the cloud points of the LCST-type polymers. **Figure 2.37** shows the turbidimetry analysis of PNiPAAm and POEGMA blends, the first polymer has a cooperative aggregation behavior while the POEGMA does not ⁹⁰.

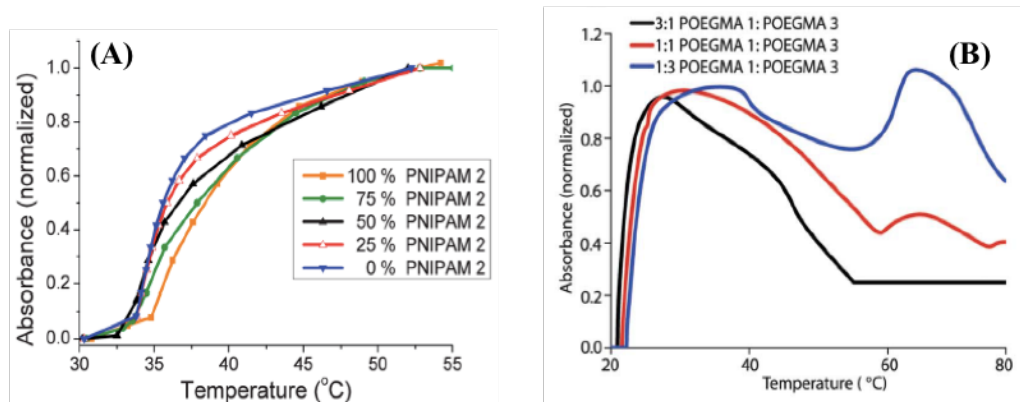


Figure 2. 37. Turbidimetry curves of (A) PNiPAAm blends and (B) POEGMA blends ⁹⁰.

2.13.4.1b. Crosslinking and branching

The dynamics of hydrophobic aggregation, ionic-interactions and hydrogen bonding are affected by the structure of amphiphilic polymers which then can determine the thermo-responsiveness of the polymers. For LCST-type polymers, addition of intramolecular crosslinking can hinder the formation of hydrophobic aggregation resulting in a less negative mixing entropy and therefore higher LCST. Several studies explored the topology effect by generated loops on the initial linear polymer chains ⁹¹ or the formation of cyclized block copolymers ^{92,93} against their linear counterpart. In the first case, PDMAEMA polymer chains were functionalized with coumarin side groups that hindered the interchain entanglement at high temperature causing an increase in the LCST ⁹¹ (**Figure 2.38**). In the second case, the formation of a cyclized poly(butyl acrylate)-block-poly(ethylene oxide) demonstrated a drastic elevation of the cloud point by 40 degrees compared to the linear counterpart. The upward shift of the cloud point temperature in these studies was attributed to the presence of the ring structures that favor the formation of intrachain H-bonds between the polymer chains restricting the intermolecular aggregation ⁹². A similar observation was made in the case of PNiPAAm solutions, where the cloud point temperature of the cyclic-PNiPAAm increased compared to the linear-PNiPAAm. Furthermore,

the cloud point temperature of the cyclic-PNiPAAm increased further as the ring size decreased due to the reduction in the transition enthalpy with decreasing ring size as shown in **Table 2.2**⁹³.

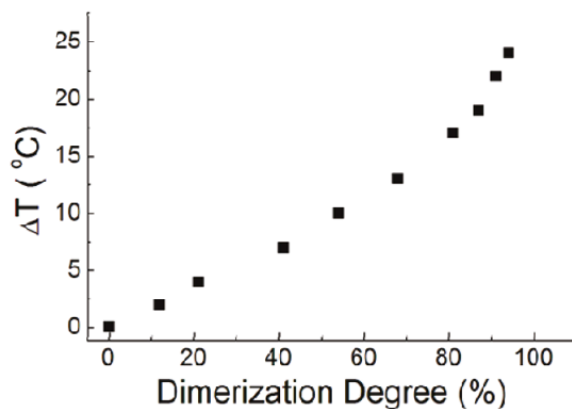


Figure 2. 38. The effect of cross-linking on the cloud point of PDMAEMA with different dimerization degrees of coumarin groups⁹¹.

Table 2. 2. The effect of cross-linking on the cloud point temperature of linear and cyclic PNiPAAm samples⁹³.

sample	M_n^a (kDa)	M_w/M_n^a	T_M^c (°C)	ΔH^c (kJ/mol)	T_{CP}^d (°C)
1-PNIPAM-6K	6.8	1.10 (55) ^b	40.3	6.06	37.0
c-PNIPAM-6K	6.9	1.11	45.8	3.86	40.4
1-PNIPAM-12K	12.7	1.08 (110) ^b	36.6	6.40	34.8
c-PNIPAM-12K	12.7	1.11	41.6	4.47	38.1
1-PNPAM-19K	19.2	1.09 (165) ^b	35.6	6.40	34.1
c-PNIPAM-19K	19.4	1.16	39.6	5.38	36.3

2.13.4.1c. Statistical copolymers

The statistical polymerization can facilitate the preparation of thermo-responsive polymers with cloud points that lie between that of their parent homopolymers as shown in **Figure 2.39 (A)**⁸⁷. The hydrophilic poly(2-isopropenyl-2-oxazoline) (PiPOx) can be converted into a thermo-responsive copolymer with a tunable LCST by partially or completely modifying its chain units

with aliphatic acids ^{94,95}. If the pendant 2-oxazoline side chains of PiPO_x are partially modified with aliphatic acids, the cloud point of the resulting PiPO_x copolymers shows a non-linear correlation with the content of the hydrophilic acids ⁹⁴. However, if the pendant 2-oxazoline side chains of PiPO_x are completely modified with multiple carboxylic acids, the cloud point of the resulting PiPO_x copolymers shows a negative-linear correlation with the content of the acid comonomers ⁹⁵. In the case of statistical copolymers of methacrylic acid (MAA) and OEGMA₁₁₀₀, the cloud point temperature is in the 22-98 °C range and can be adjusted by varying the monomer contents although the parent homopolymers do not show any LCST behavior because of the intramolecular hydrogen bonding interactions ⁹⁶. However, the LCST of some copolymers consisting of a hydrophilic comonomer and a hydrophobic comonomer does not follow a simple logic of increased or decreased overall hydrophilic–hydrophobic balance because of intra-chain or inter-chain self-assembly ⁸⁷. For example, random copolymers of methoxy-tetraethyleneglycol-4-vinylbenzylether (MOTEGVBE) and butyl maleimides yield amphiphilic copolymers with a poly-soap structure that tend to form intramolecular aggregates with distinct hydrophobic microdomains in the butyl maleimide units. The LCST of these copolymers is close to that of poly(MOTEGVBE). It is attributed to the hydrophobic groups in these microdomains, which are mostly shielded from contact with water and do not participate in the collapsing of the MOTEGVBE chain segments and therefore do not affect the phase transition temperature ⁹⁷. The presence of both hydrophobic microdomains and ionic microdomains in random copolymers made of species containing groups with opposing thermal responses shows a profound impact on their solubility and their thermo-responsiveness. For example, a ternary copolymer of poly(2-vinyl-4,4-dimethylazlactone) (PVDMA) grafted with zwitterionic sulfobetaine amine, THF amine, and benzyl amine display a dual LCST < UCST double thermo-responsiveness. The complete hydration of THF groups is

responsible for the solubility at low temperature while the complete hydration of the sulfobetaine amine is responsible for the solubility at high temperatures ⁹⁸. Some UCST copolymers can be switched into a LCST type by incorporating monomers that are able to form different types of H-bonds. For example, a series of random copolymers with tunable compositions have been synthesized by copolymerization of N-acryloylglycinamide (NAGA) and diacetone acrylamide (DAAM) that show a UCST-type transition with 90–100 mol% NAGA and a LCST-type transition with 35–55 mol % NAGA. The LCST phase transition is reported to be associated with the H-bonds and hydrophobic effect of the polymer chains ⁹⁹. A random copolymer made of comonomers from a LCST polymer and a zwitterionic UCST polymer can show both transition by the variation of the composition in the copolymer as shown in **Figure 2.39 (B)**. For example, a series of copolymers consisting of PDMAEMA and 1,3-propanesultone (PDMAPS) shows a strongly composition-dependence thermo-responsiveness. The LCST values increased with the molar fraction of sulfobetaine while the UCST values increased with the molar fraction of dimethyl amine groups in the copolymer as the sulfobetaine is more hydrophilic than the dimethyl amine group ¹⁰⁰.

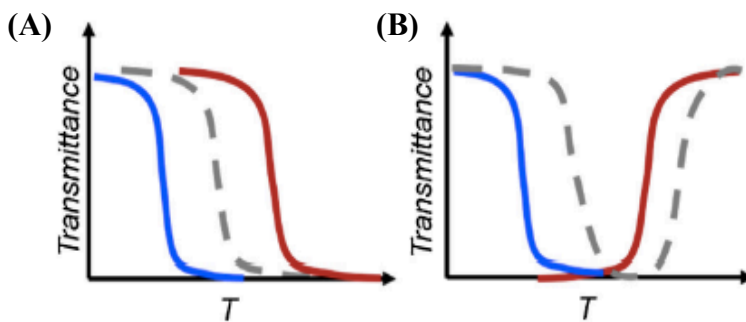


Figure 2. 39. Schematic illustrations of transmittance curves of random thermo-responsive copolymers (dashed lines) compared to their parent homopolymers (solid lines): (A) a LCST-LCST random copolymer, (B) a LCST-UCST random copolymer. In (B) the red and blue colors represent the UCST and LCST blocks ⁸⁷.

2.13.4.1d. Block copolymers

The application of temperature can alter the amphiphilicity of block copolymers, this in turn leads the copolymer chains to self-assemble into micelles as one or more of its blocks becomes insoluble. The hydrophilic (shell) blocks are oriented towards the aqueous medium while the hydrophobic (core) blocks are shielded from the solvent¹⁰¹. The solubility of each block is determined by the type of interactions between the core block and the shell block and their thermodynamic properties. Block copolymers with at least two LCST blocks can exhibit sequential changes in the temperature-dependent assembly behavior. For example, a triblock copolymer of *N*-*n* propylacrylamide (nPA), (NiPAAm), and *N,N*-ethylmethacrylamide (EMA) shows a stepwise aggregation behavior at different temperatures. PnPA is the first block starts to dehydrate at 28 °C followed by PNiPAAm at 47 °C and the PEMA is the third block to collapse at 57 °C. The phase transition of the triblock copolymer involves a multiple self-assembly behavior as shown in **Figure 2.40**¹⁰².

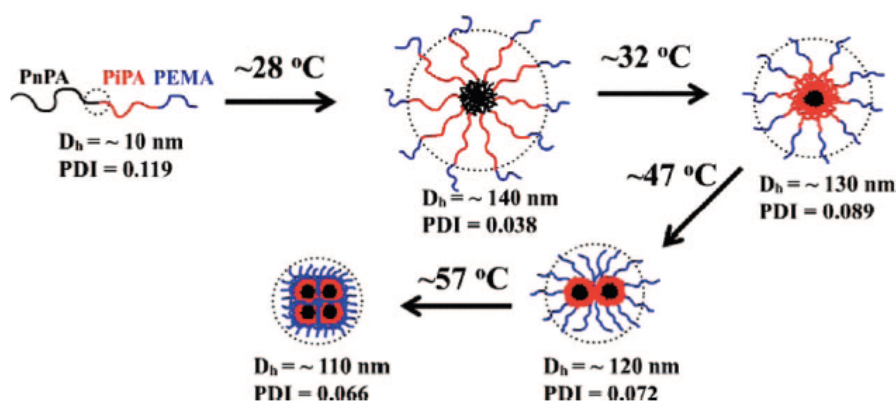


Figure 2. 40. Schematic illustration of the phase transitions of PnPA₁₂₄-b-PiPA₈₀-b-PEMA₄₄ triblock copolymer at different temperatures in aqueous solution¹⁰².

The phase transition of block copolymers exhibits a general trend where the phase transition of the lower- T_{cp} block occurs at a temperature higher than the LCST of its parent homopolymer,

while the higher- T_{cp} block occurs at a temperature lower than the LCST of its parent homopolymer as shown in **Figure 2.41**⁸⁷. This phenomenon can be explained based on the interaction between two blocks. First, the aggregation of the lower- T_{cp} block is restricted by the higher- T_{cp} block, as the later block is still hydrated creating a surface energy barrier for the aggregation. Second, the aggregation of the higher- T_{cp} block is induced by the hydrophobic interaction between the two blocks rendering the higher- T_{cp} block less soluble. However, if the hydrophilic block is long enough, the phase transition of the other block will be masked due to the increased overall hydrophilicity¹⁰³. H-bonding of the two blocks can also affect the self-assembly of the block copolymers and consequently the phase transition. For example, the block copolymers of the PnPA-b-PEMA block copolymer shows two cloud points and a complex self-assembly behavior. The first cloud point occurs because of the transition of unimers to clusters, and the H-bonding determines the formation of clusters. As the temperature continues to increase, these clusters dissociate and restructure into smaller clusters because of the disruption of H-bonding and the dehydration of PnPA block. The second cloud point occurs because of the PEMA block induces further clustering and aggregation as shown in **Figure 2.42**¹⁰⁴.

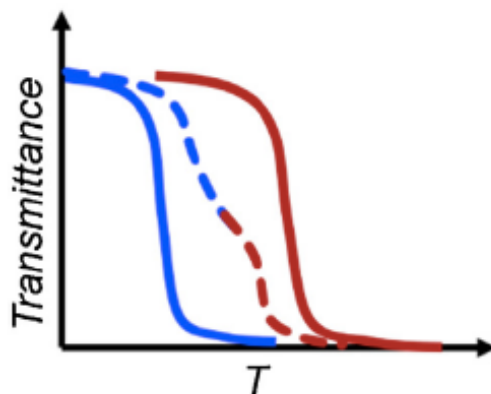


Figure 2. 41. Schematic illustrations of transmittance curves of a LCST-LCST block thermo-responsive copolymers (dashed lines) compared to their parent homopolymers (solid lines)⁸⁷.

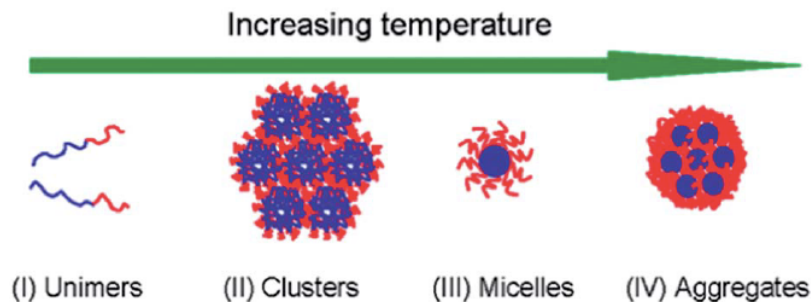


Figure 2. 42. Schematic illustration of the self-assembly structures of PnPA84-b-PEMA42 with increasing temperature ¹⁰⁴.

The block copolymers displaying both LCST and UCST behaviors can form two distinct micellar structures in aqueous solution at different temperatures and are known as “schizophrenic” or doubly thermo-responsive block copolymers. Doubly thermo-responsive copolymers can be classified into two categories based on the type of phase transition: (i) LCST-UCST, or (ii) UCST-LCST block copolymers. For the first type LCST-UCST block copolymers, when the temperature is below the LCST of the copolymer, the block copolymer form micelles where the UCST-block forms the core and LCST-block forms the corona. When the temperature is increased above the LCST but below the UCST of the copolymer, both blocks aggregate forming an insoluble phase. As the temperature continues to increase above the UCST, a reversible micelle structure forms where the LCST-block forms the core and the UCST-block forms the corona. The possible self-assembly structure for LCST-UCST block copolymers is presented in **Figure 2.43** ^{87,105}. The LCST-UCST type of behavior was found with poly(N -acryloyl-L -proline methyl ester)-b -(N -acryloyl-4-trans -hydroxy-L -proline) (P(A-Pro-OMe)-b -P(A-Hyp-OH)) diblock copolymer and is attributed to the H-bonding association and dissociation between the two block units. The block copolymer exhibits both LCST- and UCST-type transitions in acidic water that are affected by the comonomer compositions and the pH. Interestingly, this diblock copolymer can be converted into

a system exhibiting a LCST-LCST transition after methylation reaction. The proposed mechanism of the soluble-insoluble-soluble transitions are illustrated in **Figure 2.44**¹⁰⁶.

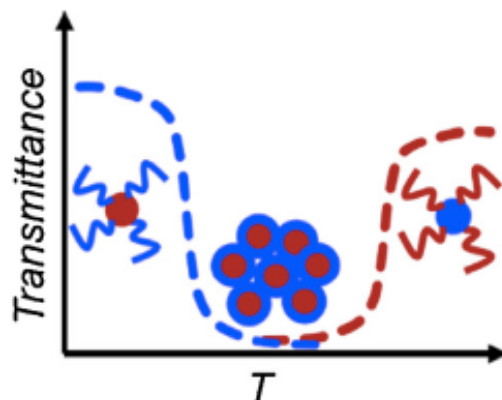


Figure 2. 43. Schematic illustrations of transmittance curves of a LCST-UCST block thermo-responsive copolymers (dashed lines) compared to their parent homopolymers (solid lines). The red and blue colors represent the UCST and LCST blocks⁸⁷.

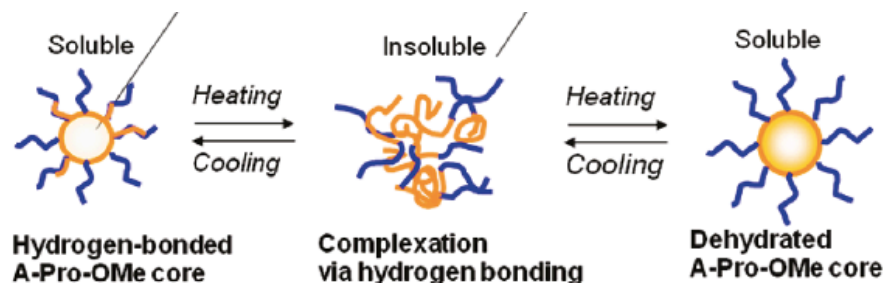


Figure 2. 44. Schematic illustrations of self-assembly behavior of P(A-Pro-OMe)-b -P(A-Hyp-OH) diblock thermo-responsive copolymer. The blue line represents the poly(A-Hyp-OH) chains and the orange line represents poly(A-Pro-OMe) chains¹⁰⁶.

For the UCST-LCST type, the copolymer forms micelles with the UCST block as the core and LCST block as the corona at low temperature. When the temperature is increased above the UCST and below the LCST, the copolymer forms unimers. As the temperature continues to increase above the LCST, a reversible micelle structure forms where the LCST-block forms the core and the UCST-block forms the corona as shown in **Figure 2.45**^{87,105}. Example of UCST-LCST type

of behavior was found with block copolymers of 2-(2-methoxyethoxy)ethyl methacrylate (MEO₂MA), oligo(ethylene glycol) methacrylate (OEGMA), and N-(3-(dimethylamino) propyl) methacryl- amide (DMAPMA) (poly(OEGMA-co-MEO₂MA)-b-poly(DMAPMA)). The LCST of the block copolymer can be adjusted by the ration of OEGMA units while the UCST can be adjusted by the degree of quaternization ¹⁰⁷.

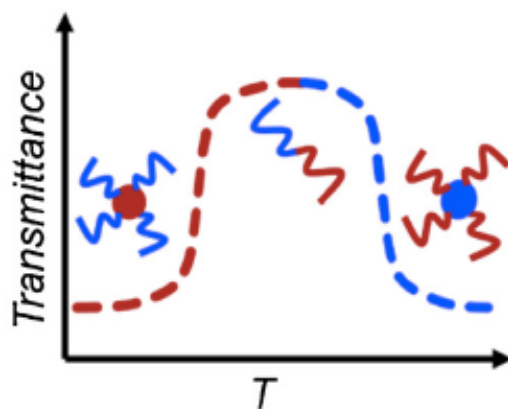


Figure 2. 45. Schematic illustrations of transmittance curves of a UCST-LCST block thermo-responsive copolymers (dashed lines) compared to their parent homopolymers (solid lines). The red and blue colors represent the UCST and LCST blocks ⁸⁷.

2.13.4.2. Solvent conditions

Thermo-responsive polymers respond differently under different solvent conditions such as dispersion concentration and salt concentration. These factors will be illustrated in this section.

2.13.4.2a. Dispersion concentration

In general, LCST-type polymers exhibit similar concentration dependence where the LCST shifts to lower temperatures as the concentration increases and shifts to higher temperatures as the concentration decreases. This phenomenon is ascribed to enhanced polymer-polymer interactions at higher dispersion concentrations and thus a drop in LCST is predicted. On the other hand, a

dilute dispersion reduces the interactions of the polymer segments resulting in phase separation and thus an increase in LCST is predicted. When the dispersion concentration is more dilute, the polymer may lose its thermo-responsive property^{69,108,109}. The concentration dependence of poly(methoxydiethylene glycol methacrylate) (PmDEGMA) illustrates the phenomenon as shown in **Figure 2.46**⁶⁹.

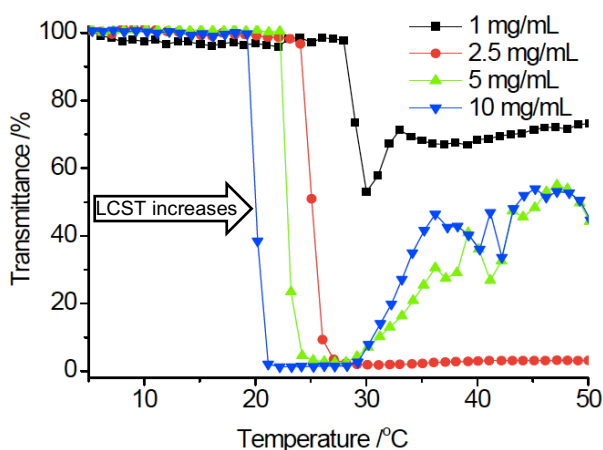


Figure 2. 46. The effect of dispersion concentration on the cloud point of PmDEGMA⁶⁹.

2.13.4.2b. Salt concentration

The phase transition of thermo-responsive polymers depends on the hydrogen bonding interactions between the solvent molecules and polymer segments. In addition, the type of additives such as salt, surfactant or co-solvent can alter the solvent quality and therefore the hydrophilic/hydrophobic balance. Hence, it is important to understand the “specific ion effects” of different ions on the structure of hydrogen bond network in water and polymer stability. Electrolytes dissociate in water to form hydrated ions that can cause the water molecules to rearrange around the ions. The Debye and Huckel model assumes that the interactions are electrostatic and considers the electric charge only which is unable to distinguish between ions of

the same surface charge density but different size or shape. On the other hand, the Hofmeister or lyotropic series explains the influence exerted by ions on the neighboring water molecules based on the type of charge and surface charge density. In the Hofmeister series, ions have been classified based on their ability to interact with water molecules into two main groups: (i) chaotropes having the ability to disrupt hydrogen-bonding networks between water molecules and (ii) kosmotropes having the ability to create water-molecule patterns. On the basis of relative intensity of interaction of ions with the surrounding water molecules, ions are ordered accordingly as shown in **Figure 2.47**. Then, this ranking of ions was later used to explain the effect of salts on the solubility of polymer segments in water. According to this series, ions to the right known as the most destabilizers because of their ability to bring order to the water molecules around themselves and therefore they can decrease the phase separation temperature. On the other hand, ions to the left known as the most stabilizers because of their ability to remove water molecules around themselves and therefore they can increase the LCST required for phase separation ^{76,87,110}.

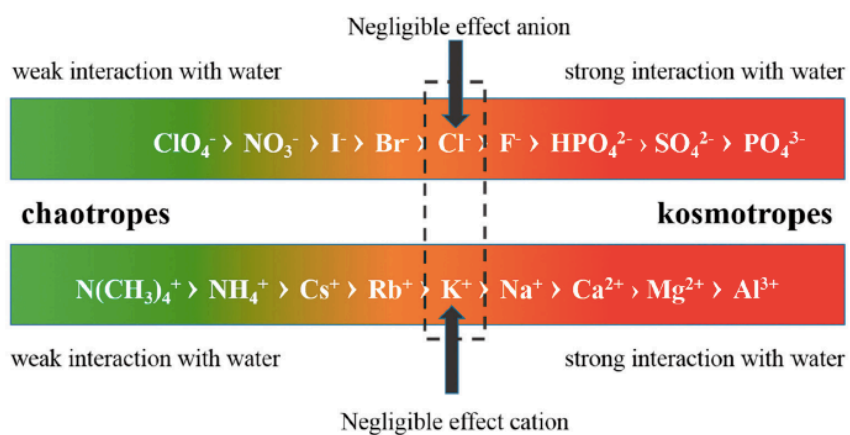


Figure 2. 47. Schematic of relative intensity of interactions of ions with the surrounding water molecules ¹¹⁰.

2.13.5. Thermo-responsive cellulose nanocrystals-based copolymers

CNCs have been the subject of extensive research for a wide range of applications because of their interesting properties including high specific area, high aspect ratio, ease of modification. Incorporating CNCs into thermo-responsive systems results in smart hybrid materials with more unique properties. The following discussion covers some recent research on CNC-containing thermo-responsive surface modifications. Particularly, the fabrication method employed to synthesize the CNC-based thermo-responsive systems and their target application. PNiPAAm is the most widely studied smart material that undergoes a coil-to-globule transition upon heating above its LCST close to the physiological temperature of about 37 °C ⁷⁴. A CNC-PNiPAAm copolymer was synthesized using the RAFT technique for controlling the growth and release of cancer spheroids in hydrogel ¹¹¹. The encapsulation of the cancer spheroids was achieved by forming the hydrogel at 37 °C from CNC-PNiPAAm aqueous suspension and the release was achieved upon hydrogel cooling. It is considered that PNiPAAm is potentially toxic which has caused a delay in its future biomedical applications. Therefore, scientists have tried to explore the possibility of using other polymers in lieu of PNiPAAm. Poly(ethylene oxide) (PEO) and its derivatives represent a new class of uncharged, nontoxic and water-soluble bio-compatible polymers that possess LCSTs with a broader temperature range from 26 to 95 °C ⁷⁵. Inspired by the biocompatibility of POEGMA, a nanocomposite material composed of CNC-POEGMA and embedded within a poly(vinylacetate) (PVAc) matrix was synthesized for biomedical applications. The prepared CNC-POEGMA/PVAc material showed a dramatic increase in stiffness (>300 MPa) upon exposure to warm water while it softened as it cooled (<1 MPa) ¹¹². Another thermo-responsive polymer used for biomedical application is Poloxamer 407 (PM) which is also referred to as Lutrol (LF 127) or Pluronic (PF 127). PM is composed of 70% of oxyethylene (OE) units

and 30% of polyoxypropylene (OP) units and is soluble at 4 °C. PM-CNC was utilized to deliver ophthalmic pharmaceutical compounds where CNCs were incorporated to enhance the gelation due to their hydrophilicity ¹¹³. Beside the biomedical applications, hybrid materials of thermo-responsive CNC-based polymers have been designed for optical devices. For example, PNiPAAm-CNC hydrogel films were prepared through UV initiated free radical polymerization that exhibited tunable optical properties. The incorporation of CNCs was to improve the mechanical properties and to control hydrogel molecular bonding. The hydrogel films were transparent below the LCST and turned opaque above the LCST due to the hydrophobic interactions inducing the PNiPAAm to change its conformation ¹¹⁴. In other study, CNCs films were used as support for the 4'-(hexyloxy)-4-biphenylcarbonitrile (HOBC) coating. The coated films displayed a chiral nematic organization, conductivity, and a thermal response. The CNCs were integrated in the films to utilize their characteristic chiral nematic structure ¹¹⁵. CNC-based thermo-responsive polymers have been also utilized in other applications including wound dressing ¹¹⁶, thermal sensors ¹¹⁷, and CNCs dispersion stabilization ^{118,119}.

Chapter 3. Analytical Instruments

The following section provides a brief overview on the major experimental techniques used to characterize the resulting polymer grafted cellulose nanocrystals.

3.1. Fourier Transform Infrared Spectrometry

FTIR stands for Fourier Transform Infrared spectroscopy, which is an analytical technique used to determine the structures of organic and inorganic molecules. In particular, FTIR enables the characterization of the chemical bonds connecting atoms. Covalent bonds in molecules experience various types of vibrations and rotations where the bonds behave like springs stretching and bending which are known as vibrational modes as shown in **Figure 3.1**. The basic theory of FTIR is that bonds within molecules tend to vibrate with frequencies that correspond to the electromagnetic radiations in the infrared region. When a material is exposed to infrared radiation, sample molecules selectively absorb energy that causes the change of dipole moment of the sample molecules. Consequently, molecules become excited and transitions occur from a ground vibrational state to an excited vibrational state. The energy difference between the ground and excited vibrational states is associated with the wavelength of the absorbed light. Eventually the molecules return to their ground state, and the energy absorbed is released as heat. In the spectrometer, infrared light with frequencies ranging from about 10^{13} to 10^{14} Hz is passed through an unknown sample. Some infrared radiation is absorbed while some of it is transmitted. A detector records the intensity of transmitted or reflected light as a function of its wavelength. The number and intensity of absorption peaks is related to the frequencies of vibrations between the bonds of the atoms making up the material which is a direct identification of different types of functional groups in the material. Most molecules that absorb infrared light are known as infrared active due to the high dipole change in the vibration and rotation of these molecules. On the other hand,

several homonuclear diatomic molecules with symmetrical bonds, such as O₂, N₂ and Cl₂ do not absorb the infrared light and they are known as infrared inactive due to the zero dipole change in the vibration and rotation of these molecules. The FTIR technique results in a spectrum presented as a plot of intensity versus wavenumber (the reciprocal of the wavelength). The FTIR spectroscopy can be employed for a range of wavenumbers between 14000 and 4 cm⁻¹. The range can be divided into far infrared (4 – 400 cm⁻¹), mid-infrared (400 – 4000 cm⁻¹) and near infrared (4000 – 14000 cm⁻¹) regions based on the selected beam splitters and detectors. The common range used is the mid-infrared (400 – 4000 cm⁻¹) because most organic and inorganic compounds absorb the radiation within this region ¹²⁰.

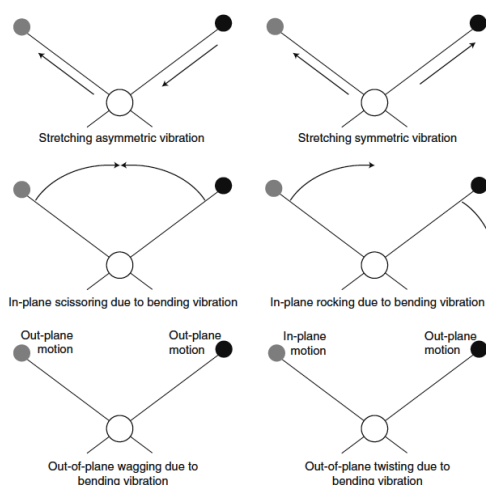


Figure 3. 1. Examples of the vibrational modes occur at characteristic frequencies that are detected using FTIR spectroscopy ¹²¹.

As shown in **Figure 3.2**, there are three basic FTIR components as follow:

- 1. Radiation source:** An infrared beam is emitted from a broadband source in a range of frequencies.

2. **Interferometer:** The commonly used interferometer is the Michelson which consists of a beam splitter, a fixed mirror and a moving mirror. The beam splitter divides the FTIR beam into two optical beams. One beam is transmitted to the fixed mirror while the second beam is reflected toward the moving mirror. After the two divided beams are reflected from the two mirrors, they recombine at the beam splitter. As a result of changes in the relative position of the moving mirror to the fixed mirror, an interference pattern is generated. This modulated beam then passes through the sample where it is absorbed at different wavelengths depending on the molecular structure of the sample.

3. **Detector:** The beam is eventually focused on the detector which is designed to measure the interferogram signal. The two most popular detectors are deuterated triglycine sulfate known as pyroelectric detector, and mercury cadmium telluride known as photon or quantum detector. The resultant interferogram is then Fourier transformed, where the intensity versus time signal is converted to the intensity versus frequency spectrum. Eventually, the ratio of the single-beam sample against a reference spectrum is taken to remove the background contributions to produce the typical infrared absorbance/transmission spectrum.

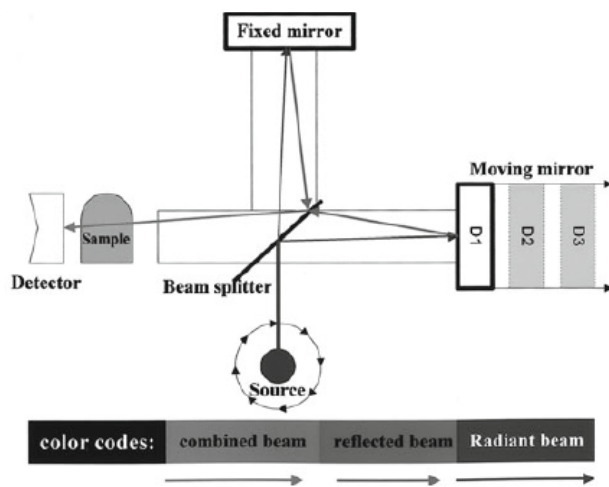


Figure 3. 2. The optical layout of an FTIR spectrometer ¹²¹.

3.2. Dynamic Light Scattering (DLS)

3.2.1. Particle size

The DLS stands for dynamic light scattering, which is also known as photon correlation spectroscopy (PCS). The DLS provides information on the hydrodynamic diameter (D_h), distribution of particles and polymers by measuring the scattered light due to Brownian motion. The relationship between the size of a particle and its motion is defined by the Stokes-Einstein Equation (3.1):

$$D_h = \frac{k_B T}{3\pi\eta D_t} \quad \text{Equation (3.1)}$$

where

- D_h is the hydrodynamic diameter
- D_t is the translational diffusion coefficient
- k_B is Boltzmann's constant
- T is the absolute temperature
- η is the dynamic viscosity

The calculations are handled by the instrument to determine the translational diffusion coefficient (D_t). The basic principle behind the DLS is that the sample is illuminated with a laser beam and the intensity fluctuations in the scattered light is analyzed at a known scattering angle θ by a fast photon detector. The rate at which these intensity fluctuations occur is inversely proportional to the size of the particles. As shown in **Figure 3.3**, the large particles cause the intensity to fluctuate less rapidly than small ones. Within the DLS instruments, a signal comparator called a digital correlator that measures the degree of similarity between two signals at varying time intervals. The particles can scatter light in all directions; therefore, the detector can be placed in any position (angle). The DLS used in this thesis can measure the mean particle size at 90° in a limited size

range (1nm to 3 μ m). The optical signal (noise) obtained by the correlator shows the random changes due to the random Brownian movements of the particles.

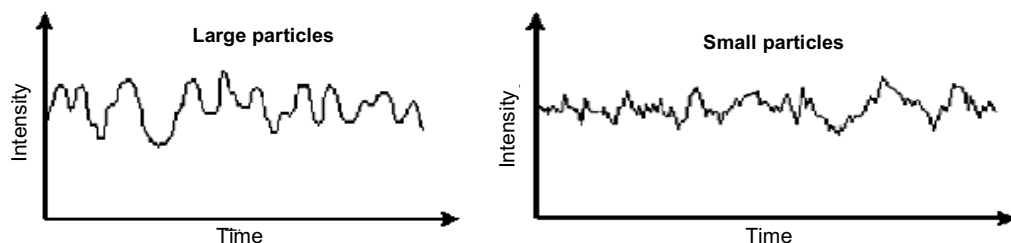


Figure 3. 3. Schematic illustration of the typical intensity fluctuations ¹²².

The software of the DLS instrument uses algorithms to extract the particle size and distribution.

Figure 3.4 (A) schematically shows the size distribution graph where the y-axis represents the relative intensity of the scattered light while the x-axis represents a distribution of sizes. The obtained graph is known as an intensity distribution that can be converted to a volume distribution using the Mie theory which can be further converted to a number distribution as shown in **Figure 3.4 (B),(C)** ^{122,123}.

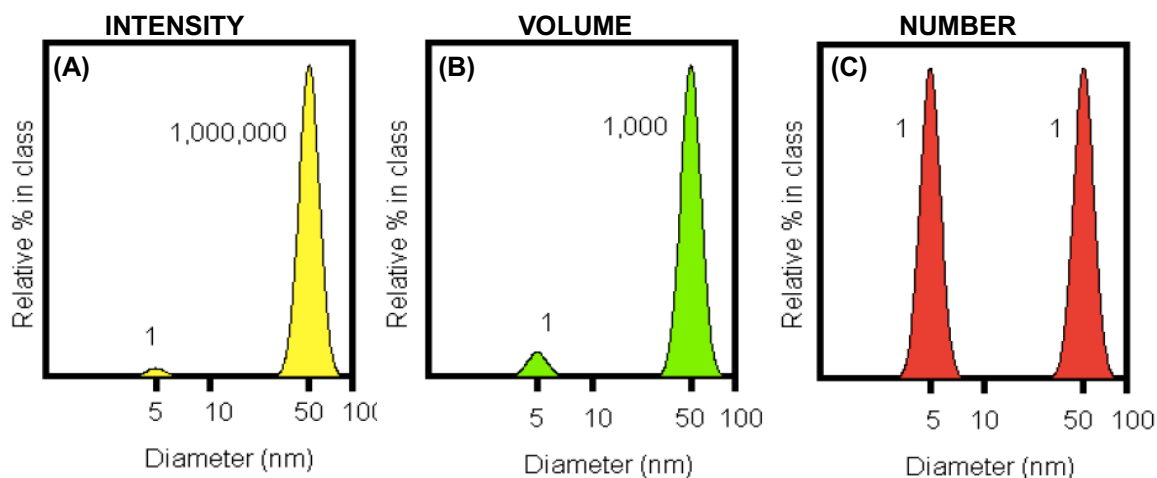


Figure 3. 4. Schematic illustration of the typical intensity (A), number (B), and volume (C) distribution ¹²².

As shown in **Figure 3.5**, the six basic DLS components are as follow:

- 1. Laser:** The laser source provides a light with low noise, the commonly used ones are helium-neon gas or diode lasers of 633 nm wavelength.
- 2. Cell:** The DLS cuvettes are made of glass or disposable plastic. They should contain 1-2 ml of sample to obtain good quality data. The translucent disposable plastic cuvettes can be provided with inbuilt electrodes which are suitable for size and zeta potential measurements.
- 3. Detector:** The DLS instruments are equipped with detectors placed at either 90° or 173° to measure the intensity of the scattered light.
- 4. Attenuator:** The attenuator is placed in front of the light source to alter the power of the laser and therefore adjust the intensity of the scattered light within a specific range.
- 5. Correlator:** The correlator is designed to measure the degree of similarity between the scattering intensity at successive time intervals and then pass the information to the computer.
- 6. Computer:** The computer is equipped with the Nano software to analyze the data and derive the size distribution ¹²³.

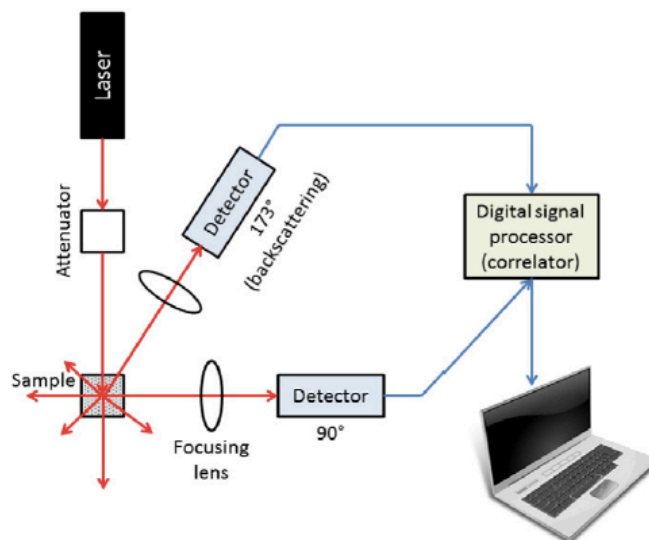


Figure 3. 5. The optical layout of the DLS instrument ¹²³.

3.2.2. Particle charge

The zeta potential is known as electro-kinetic potential used to measure the colloidal stability and to verify the presence of charged functional groups incorporated during copolymerization. The zeta potential reflects the potential difference between the electric double layers (EDL) of particles being in contact with the liquid. **Figure 3.6** illustrates the basic concept of zeta potential. The inner layer of EDL called stern layer consists of ions/molecules with opposite charge to that of the dispersed particle and remain fixed at the particle surface. The outer layer of EDL is called the Guoy-Chapman or diffuse layer and it consists of ions/molecules with both similar and opposite charges extending beyond the Stern layer ^{123,124}.

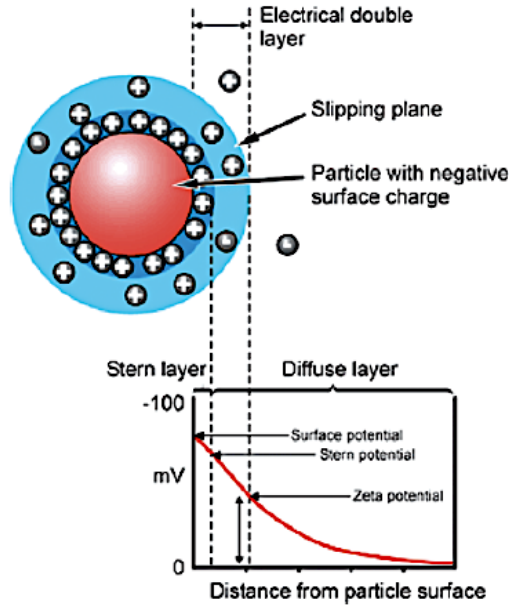


Figure 3. 6. Schematic illustration of the basic concept of zeta potential ¹²⁴.

When an electric field is applied across such dispersion, the charged particles are attracted towards the electrode of opposite charge. Within the diffuse layer there is an imaginary plane known as shear/slipping plane which acts as the interface between the moving particles, due to the applied voltage, and the dispersant phase. The potential on the particle surface is known as the Nernst potential (ψ_0) and cannot be measured. On the other hand, the potential at the stern layer and the potential at a distance x from the Stern layer are denoted as (ψ_d) and (ψ) respectively. According to the Debye law, the electrostatic field decreases with the distance (x) from the particle surface as described in **Equation (3.2)**.

$$\psi = \psi_d e^{-\kappa x} \quad \text{Equation (3.2)}$$

When the shear plane is close to the Stern layer, the surface potential at the Stern layer is equal to the zeta potential; hence, **Equation (3.2)** can be rearranged as shown in **Equation (3.3)**.

$$\psi = \zeta e^{-\kappa x} \quad \text{Equation (3.3)}$$

The exponential constant (κ) known as (Debye-Hückel parameter) varies according to **Equation (3.4)**, and it has a unit of the reciprocal length; therefore, the $(1/\kappa)$ is known as the double layer thickness.

$$\kappa^2 = \frac{N_A e^2 I}{\epsilon_r \epsilon_0 k T} \quad \text{Equation (3.4)}$$

where

- N_A is the Avogadro number
- e is the elementary charge
- I is the ionic strength
- ϵ_0 is the permittivity of free space
- ϵ_r is the relative permittivity of the medium
- k is the Boltzmann constant
- T is the absolute temperature

As illustrated in **Equation (3.4)**, the double layer thickness $(1/\kappa)$ depends inversely on the ionic strength; therefore, the double layer becomes compressed and the zeta potential decreases as the ionic strength increases. The electrophoretic mobility is obtained by the Laser Doppler Velocimetry (LDV) technique which is used together with the DLS through Malvern Zetasizer instrument as an example. The basic component of the micro-electrophoresis system is a disposable cell with inbuilt gold-plated copper electrodes at either end, where an electric field is applied as shown in **Figure 3.7**. When an electric field is applied to the sample, the particles move toward the opposite electrodes and scatter the incident laser beam. The scattered beam from the particles is combined with the reference beam to obtain the Doppler shift. The magnitude of the particle velocity is obtained by **Equation (3.5)** where V is the particle velocity and E is the electric field strength.

$$U_E = \frac{V}{E} \quad \text{Equation (3.5)}$$

Then, the zeta potential can be calculated by determining the electrophoretic mobility and then applying Henry **Equation (3.6)**.

$$U_E = \frac{2 \varepsilon \zeta f(ka)}{3 \eta} \quad \text{Equation (3.6)}$$

where

- ζ is the zeta potential
- U_E is the electrophoretic mobility
- ε is the dielectric constant
- η is the viscosity
- $f(ka)$ is the Henry's function

The Henry's function uses two values as approximations either, 1.5 or 1.0, depending on the type of media. For aqueous media, $f(ka)$ is 1.5 which is referred to as the Smoluchowski approximation. On the other hand, $f(ka)$ is 1.0 and is referred to as the Huckel approximation in non-aqueous media ^{123,124}.

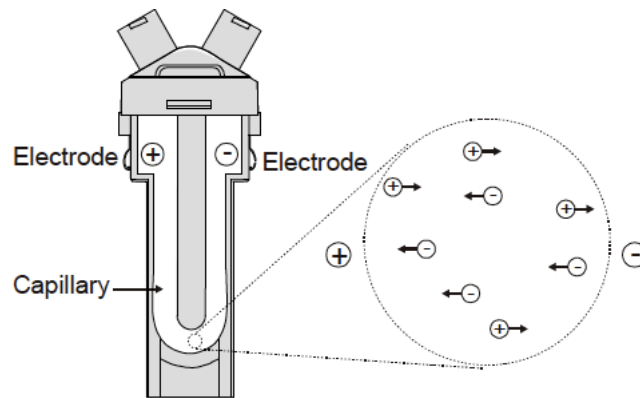


Figure 3. 7. Schematic showing the cell used for zeta potential measurement by Laser Doppler Velocimetry technique ¹²².

3.3. Transmission Electron Microscopy

A transmission electron microscopy (TEM) is a powerful imaging technique that uses a high energy beam of electrons to visualize specimens and generate a highly magnified image. Hence, TEM enables the determination of morphological features, crystallographic data, and chemical compositions. The TEM operates on the same working principle as the light microscope but uses electrons to focus and produce an image instead of light. Electrons have a shorter wavelength compared to light; therefore, the optimal resolution obtained by TEM images is about 1000x better than light microscope. TEMs employ a heated tungsten filament in the electron gun to generate electrons that are then focused by the condenser lenses on the specimen. Then, the magnetic lenses focus the electrons into a very fine beam that passes through the specimen. On reaching the specimen, the electrons either scatter and focus on the magnetic lenses to produce a clear image or hit a fluorescent screen to form a polychromatic image. An image of the specimen appears in different shades depending on the density of material being examined. The more transparent the specimen, the less electrons scatter forming a brighter image because more electron reach the screen for visualization^{125,126}. As shown in **Figure 3.8**, the basic TEM components are as follows:

1. **Electron Source:** Known as electron gun and used to generate a high coherence electron beam.
2. **Condenser lenses:** A set-up of different magnetic lenses controls the illumination area on the specimen.
3. **Objective lens:** The most important lens in the microscope that images the specimen and generate the first intermediate image. The resolution of the final image depends on the quality of the objective lens.

4. **Intermediate lens:** The intermediate lens changes the modes between imaging and diffraction.
5. **Projector lenses:** These lenses magnify the image and generate the second intermediate image.
6. **Vacuum system:** An ultra-high vacuum is essential to remove gas particles to avoid the strong scattering of the electrons in the electron gun. In addition, the vacuum system is necessary to avoid electric discharge between the cathode and anode that results in the failure of the filament.

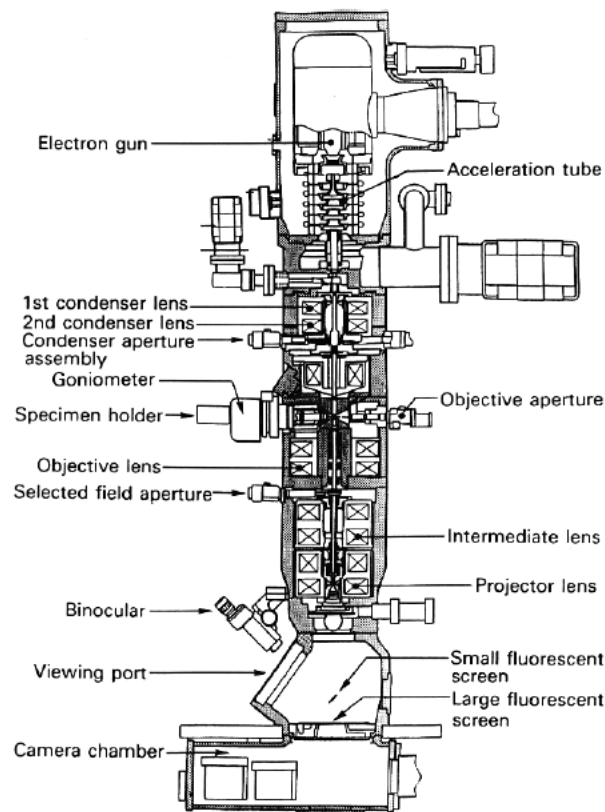


Figure 3. 8. General layout of a typical TEM ¹²⁵.

3.4. Ultraviolet-Visible (UV-Vis) Spectroscopy

Ultraviolet-visible spectroscopy is considered a quantitative and qualitative technique in analytical chemistry that can be applied to characterize organic compounds and inorganic molecules or complexes. For instance, UV-Vis spectroscopy can detect the presence of functional chromophores in a specimen, identify the extent of conjugation in polyenes, detect the configurations of isomers and determine the purity of a material. The UV-Vis region for the electromagnetic spectrum spans 6.2-1.5 eV which corresponds to a wavelength range of 200-800 nm. The technique observes the absorbance of light energy resulting from the excitation of the electrons from the ground state to a higher energy state with respect to the absorbance of a reference sample or blank. Materials containing π -electrons or n-electrons can absorb the energy in the ultraviolet-visible region and these electrons are excited to higher non-bonding levels. The possible types of transitions are (π - π^* , n- π^* , and n- σ^*). The Beer-Lambert Law can be used to determine the concentration of a chemical from its absorbance based on the linear relationship between the absorbance and the concentration of a sample as shown in **Equation (3.7)**:

$$A = \epsilon bc \qquad \text{Equation (3.7)}$$

where

- A: stands for the absorbance (unitless)
- ϵ : is the molar absorptivity of the molecule in solution ($M^{-1}cm^{-1}$)
- b : is the path length of the cuvette or sample holder (usually 1 cm)
- c : is the concentration of the solution (M)

Each wavelength of light has a particular energy that is enough to promote the outer electrons of the substance to higher energy levels. The absorbance (A) is defined as the ratio of the intensity of the incident light to the transmitted light (I_0/I). The Beer-Lambert Law can be expressed in terms of the intensity as shown in **Equation (3.8)** ^{127,128}.

$$A = \log \frac{I_0}{I}$$

Equation (3.8)

As shown in **Figure 3.9**, the four basic components of a typical spectrophotometer are:

1. **Light source:** The standard light source consists of a deuterium arc (190–330 nm) and a tungsten filament lamp (330–800 nm) which cover the whole UV-Vis region.
2. **Monochromator:** The monochromator is composed of prisms that split the light into several component wavelengths and slits that transmit only the desired wavelengths.
3. **Detector:** The detector is composed of two photocells, one photocell receives the beam from the sample cell while the second photocell receives the beam from the reference cell.
4. **Amplifier:** The main function of the amplifier is to increase the signals generated by the photocells.

There are two types of spectrophotometers based on the beam configuration: single and double beam. In the single beam spectrophotometer, the components are aligned in single beam order and the absorbance of the sample and the reference are measured separately. In a double beam spectrophotometer, the light from the source is divided into two beams after grazing on the grating in the monochromator. Hence, the measurement becomes independent for the sample and reference

127,128

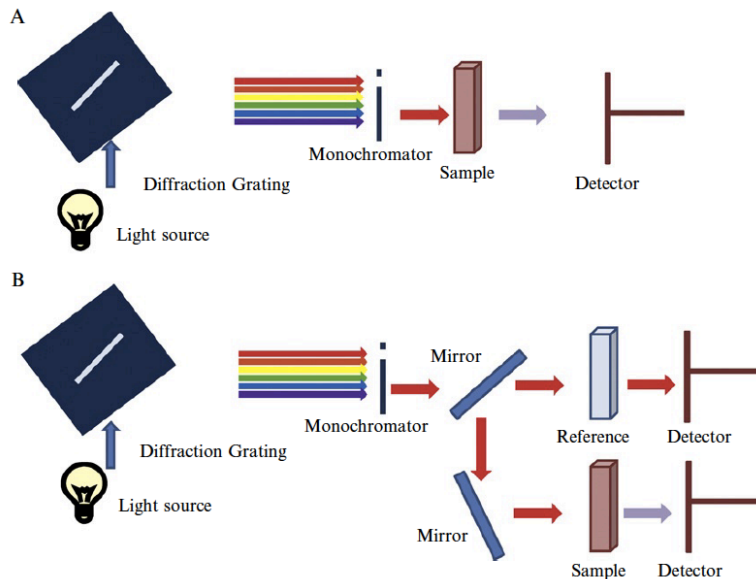


Figure 3. 9. Basic structure of single (A) and double (B) beam spectrophotometers ¹²⁸.

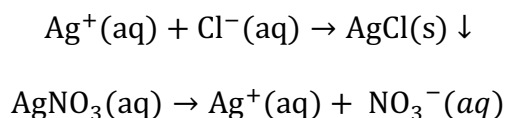
In this thesis, the UV-Vis spectrometer has a special application. It was used to study the phase transition behaviour of thermo-responsive copolymers to determine the cloud point (T_{cp}). For this application a Varian (Cary 100 Bio) UV-vis spectrometer equipped with a temperature controller was used. The spectrometer is equipped with a software to control the heating or cooling rates and cycles during which the transmission of the sample was constantly measured. To determine the cloud point, a solution of the copolymer was filled into a cuvette and placed in the spectrometer after adjusting the temperature range. The measured transmittance (%T) values were plotted versus temperature to draw the phase diagram, and then the cloud point was identified as the critical temperature at 50% transmittance ⁶⁹.

3.5. Conductometric titration

Conductometric titration is a quantitative technique in analytical chemistry used to estimate the concentration of an ionizable functional groups. The principle of conductometric titration states

that ions have different conductivity values and during the titration, one of the ions is replaced by other ions resulting in a change in the conductivity. Conductometric titration involves two processes: (1) a gradual addition of a titration agent that reacts with the ionizable functional groups in the sample and (2) simultaneous measurement of the corresponding change in the conductivity of the sample. The conductivity of the sample depends on the number of free ions in the solution and their ionic charge. During the titration experiment, a sudden change in the conductivity is observed which implies that the end point has occurred. At the end point, an equivalent concentration of the titration agent has been added to the sample which is located by graphically plotting the change in conductivity versus the volume of titrant added.

According to the nature of the chemical reaction between the sample and the titration agent, there are four types of titrations: (1) precipitation titrations, (2) acid-base titrations, (3) complex-formation titrations, (4) oxidation-reduction (redox) titrations ¹²⁹. In this thesis, the first type is used to estimate the amount of quaternary ammonium groups grafted. The principle behind the precipitation titrations is that the chemical reaction between the sample and the titration agent yields ionic compounds of limited solubility. For example, to determine the concentration of quaternary ammonium groups in a sample, silver nitrate is added. After all the chloride ions (associated with the quaternary ammonium groups) have been precipitated as white silver chloride, the first excess of silver nitrate agent results in the sudden increase in the conductivity as shown in the following reactions:



The titration data revealed two stages that were delineated by the conductivity inflection point (end point) as shown in **Figure 3.10**. The first stage displayed a slight linear decrease due to the reaction

between silver cations and chloride counterions of the quaternary ammonium groups to form silver chloride precipitates. The second stage displayed a sharp increase as a result of the dissociation of silver nitrate to form free silver cations and nitrate anions, which occurred only after the consumption of all the chloride counterions. The point of intersection corresponded to the volume of silver nitrate consumed, which was used to calculate the quaternary amine content based in **Equation (3.9)**^{130,131}.

$$[\text{NH}_3^+] \left(\frac{\text{mmol}}{\text{g}} \right) = \frac{M_{\text{AgNO}_3} (\text{mM}) \times (V_{\text{AgNO}_3}) (\text{L})}{W_s (\text{g})} \quad \text{Equation (3.9)}$$

where

- M: is the molarity (mmol/L) of the titrant
- V: is the volume (mL) of the titrant
- W_s : is the weight of the sample

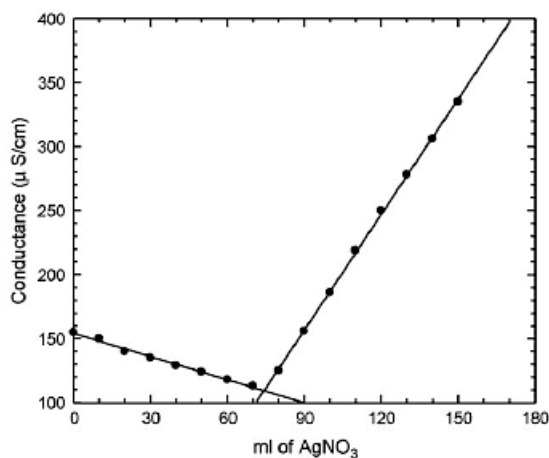


Figure 3. 10. The change in the conductance of a sample containing chloride ions during titration with added AgNO₃ solution.

Chapter 4. Functional Cellulose Nanocrystals Containing Cationic and Thermo-Responsive Polymer Brushes for Bentonite Removal

Abstract

Cationic and thermo-responsive polymer brushes were grafted from the surface of cellulose nanocrystals. Di(ethylene glycol) methyl ether methacrylate (MEO₂MA) and polyoligoethylene glycol methyl ether acrylate (OEGMA₃₀₀) and (2-methacryloyloxyethyl) trimethylammonium chloride (DMC) were grafted from cellulose nanocrystals (CNCs) via free radical polymerization. The CNC-g-POEGMA (CP) possessed a tunable lower critical solution temperature (LCST) of about 50 °C, and cloud point measurements confirmed that the LCST of the nanoparticles could be manipulated within the range of 40-47 °C by adjusting the DMC content. The salt effect was also investigated, and the results revealed a typical salting-out effect for the CNC-g-POEGMA after the introduction of KCl. On the other hand, the CNC-g-POEGMA-g-PDMC (CPD) copolymers displayed two salt-responsive characteristics; polyelectrolyte effect at lower salt concentrations, followed by the salting-out effect at higher salt concentrations. The flocculation performance of CNC-based copolymers in removing bentonite particles was examined. The effectiveness of the CNC-based copolymers was determined by measuring the zeta potential of the sediments, and the turbidity of the supernatant in two sets RMRS and RMHS to study the effect of the thermo-responsive property of the flocculants on their performance. The RMRS refers to mixing and settling at 25 °C, which was below the two copolymers LCSTs. The RMHS refers to mixing at 25 °C and settling at 50 °C, which was above the two copolymers LCSTs. The results revealed that copolymers with higher ratio of cationic brushes are more effective in the removal of bentonite, with maximum flocculation efficiency (95% at 21 mg/g). The thermo-responsive property of the copolymers offered a possibility to overcome the limitations of the RMRS

flocculation process as the efficiency of the same copolymer increased to 99% at lower dosage (18 mg/g) when the settling was conducted at 50 °C using the RMHS protocol.

*This chapter is partially adapted from “Alharthi, S., Grishkewich, N., Berry, R. M., & Tam, K. C. (2020). Functional cellulose nanocrystals containing cationic and thermo-responsive polymer brushes. *Carbohydrate polymers*, 246, 116651.

4.1. Introduction

Cellulose nanocrystals (CNCs) derived from cellulose, typically via sulfuric acid hydrolysis, possess attractive properties, including high tensile modulus, similar to steel or Kevlar (100 to 160 GPa), low density (1.5 g/cm^3) and a large specific surface area ($\sim 250 \text{ m}^2/\text{g}$)^{132–134}. The surface of the rod-shaped nanocrystals have many hydroxyl groups and these provide an ideal platform for surface modification to prepare customized nanomaterials with desired surface characteristics for a wide range of applications^{135,136}. Recent advances in cellulose nanocrystals have focused on the use of nanocellulosic substrates as nanocarriers with responsive functionalities for drug-delivery and sensing applications¹¹⁶. Related materials can respond to external stimuli, such as heat, light, and pH^{64,74,81,137}. Synthetic thermo-responsive polymers have been extensively investigated, since temperature is one of the most common external stimuli¹³⁸. Thermo-responsive polymers are a class of polymers with the appropriate hydrophilic–hydrophobic balance that impart thermo-responsive characteristic to the substrates^{68,69}. The thermo-responsive polymers can be divided into two classes; those possessing a lower critical solution temperature (LCST) and those possessing an upper critical solution temperature (UCST). Polymers with a LCST display a phase separation at high temperatures due to the disruption of polymer-water interactions above the LCST. Systems with a UCST display a phase separation upon cooling due to the strong polymer-polymer interactions. For example, aqueous solutions of poly(N-isopropyl acrylamide) PNiPAAm, undergo a coil-to-globule transition upon heating beyond their respective LCST close to the physiological temperature of about $37 \text{ }^\circ\text{C}$ ⁷⁴. Compared to the widely studied thermo-responsive PNiPAAm, polyoligoethylene glycol methyl ether acrylates are a new class of uncharged, nontoxic and water-soluble biocompatible polymers that possess LCSTs with a broader temperature range 26 to $95 \text{ }^\circ\text{C}$ ⁷⁵.

The thermo-responsive polymers have been utilized in a vast array of applications in various research areas, including waste-water treatment. The first cationic thermo-responsive polymers used to flocculate suspended clays when the solution temperature is below the LCST were prepared from N-loweralkyl substituted acrylamides¹³⁹. Similarly, the flocculation efficiency of poly(N-isopropylacrylamide) (PNiPAAm) increased the settling rate of kaolinite clay from nearly zero to 2.0 m/h upon the addition of the optimum PNiPAAm dosage of 500 ppm¹⁴⁰. Another application for thermo-responsive polymers includes oil sands extraction and tailings treatment. PNiPAAm was tested for processing oil sands, and it improved the bitumen recovery and the settling rate of tailings due to the coil-globule transition¹⁴¹. The flocculation mechanism in the presence of thermo-responsive polymers is considered to be related to bridging and hydrophobic interactions. Polymer bridging can take place at a temperature below the LCST where the polymer segments are adsorbed on the particles surface resulting in loops and tails suspended in the solution. As the temperature increases above the LCST, the polymer changes its conformation from an extended to agglomerated state where the hydrophobic attraction facilitates the formation of compact flocs¹. Several studies used AFM to examine the adhesion force between kaolinite particles below and above the LCST. The experimental results revealed that the adhesion force between kaolinite particles is very low upon the addition of PNiPAAm below the LCST resulting in minimal aggregation. However, the adhesion force between kaolinite particles increases from nearly zero to 3.5 mN/m after the addition of PNiPAAm at room temperature followed by a temperature increase to 40 °C due to an extra space available on the coil-like structure of PNiPAAm¹⁴⁰. Although the results from the solid-liquid separation studies are promising, the utilization of thermo-responsive polymers as flocculants are being re-examined due to the need to impart a thermal switch¹⁴². In addition, the application of synthetic polymers is debatable because

of their toxicity that arises from residual unreacted monomers (such as acrylamide, ethyleneimine) which are resistant to biodegradation, and their degraded products are considered to be hazardous^{16,143,144}. Nevertheless, the utilization of warm oil sands tailing can reduce the energy cost since the tailings temperature is between 30-50 °C which could be adjusted by mixing fresh tailings with room temperature tailings to the desirable temperature¹⁴². On the other hand, natural bio-flocculants have emerged as promising alternative materials for replacing synthetic flocculants. Natural organic flocculants, based on polysaccharides have been extensively explored because they are biodegradable, available from agricultural resources and produce no secondary pollution compared to synthetic flocculants¹⁴⁴. In addition, since they are biodegradable, the sludge formed can be efficiently degraded by microorganisms^{145,146}. However, natural bio-flocculants have low efficiencies and thus higher dosages are needed²⁰. Thus, grafted flocculants have emerged as a new class of polymers that offer tremendous potential in treating waste-water due to superior performance compared to original components (synthetic polymeric flocculants and natural bio-flocculants)¹⁴⁴. The modification of polysaccharides has been explored as a strategy of combining their best properties with those of synthetic polymers to enhance the aggregating capacity of the modified flocculants^{21,144,147,148}. In light of this optimisation, this study is conducted to overcome the environmental footprint of oil sands operations by developing thermo-responsive polymers that are biodegradable, capable of inducing better sediment consolidation and recovering the water for reuse in the oil sands extraction. Several studies on the thermo-responsive CNC systems with polymeric brushes, such as PNiPAAm, PEO, poly(N,N-dimethylaminoethyl methacrylate) (PDMAEMA) and poly(oligo(ethylene glycol)) methacrylate (POEGMA) have been reported^{74,149–151}.

Inspired by these nanocomposite structures, we prepared a series of cationic and thermo-responsive CNC-based copolymers by grafting of poly(OEGMA)s from the CNC surface via the conventional free radical polymerization process. Subsequently, different ratios of (2-methacryloyloxyethyl) trimethylammonium chloride (DMC) monomer were grafted from the CNC-g-POEGMA using a conventional free radical polymerization strategy. The effect of cationic brush composition, and ionic strength on the thermo-responsiveness of the prepared copolymers were examined by UV-vis spectroscopy. In addition, the current research aimed at managing the oil sands tailings using sustainable nanomaterials as flocculants, and replacing synthetic flocculants. The effectiveness of the thermo-responsive CNC-based copolymers was determined by measuring the zeta potential of the sediments, and the turbidity of the supernatant. The measurements were conducted at two settling temperatures below and above the LCST of the flocculants to study the effect of the copolymers coil-globule transition on flocculation performance.

4.2. Experimental section

4.2.1. Materials

Cellulose nanocrystals were kindly provided by CelluForce Inc. with an average charge density of 0.26 mmol/g. Di(ethylene glycol) methyl ether methacrylate (MEO₂MA, 95%), poly(ethylene glycol) methyl ether methacrylate (average Mn 300, OEGMA₃₀₀), and (2-methacryloyloxyethyl) trimethyl ammonium chloride (DMC), were purchased from Sigma-Aldrich. Cerium(IV) ammonium nitrate (CAN), ammonium persulfate (APS), and potassium chloride were used as received from Sigma-Aldrich.

4.2.2. Preparation of CNC-g-POEGMA

The desired copolymer was synthesized using the solution polymerization technique with ammonium persulfate (APS) as the initiator. CNC (1.0 g) was dispersed in 150 mL of deionized water in a 250 mL three-neck flask equipped with a magnetic stirrer and the mixture was stirred for 15 min and purged with high purity nitrogen for 1 h. Ammonium persulfate (100 mg) was charged to the flask and the temperature of the reaction mixture was slowly increased to 65 °C. MEO₂MA (4 mmol, 0.75 g) and OEGMA₃₀₀ (1 mmol, 0.3 g) (mole ratio of 4:1) were mixed with 5 mL ethanol and added dropwise to the reaction flask. After the reaction, the solution mixture was kept overnight at room temperature and the final product was dialyzed in a 0.1 micron dialysis membrane against Millipore water with regular changes of water until the conductivity of the water remained constant to remove unreacted monomers. The CNC-g-POEGMA dispersion with a measured solid content was recovered and stored in the refrigerator for future use.

4.2.3. Preparation of CNC-g-POEGMA-g-PDMC

The dual functionalized CNCs were synthesized by post-polymerization on CNC-POEGMA. CNC-POEGMA (1.0 g) in 80 mL aqueous dispersion was mixed in a three-neck flask with 0.5 mL of 70 wt% HNO₃ and gently stirred and purged with nitrogen for 1 h. The cerium(IV) ammonium nitrate (CAN) (0.1 g) was added to the reaction flask and the cerium ions produced free radicals on the CNCs backbone. After 10 minutes, the DMC monomer (0.45 mL) was introduced to initiate the polymerization (CNC-g-POEGMA:PDMC = 1:0.5), and the reaction mixture was maintained at room temperature. Acetone was then added to the mixture at a 1:1 volume ratio, and dialyzed against deionized water until the measured water conductivity remained constant.

4.2.4. Characterization

Fourier transform infrared (FTIR) spectra were recorded to confirm the new functional groups of CNC-g-POEGMA and CNC-g-POEGMA-g-PDMC. Freeze-dried samples were homogeneously mixed with KBr powder at a 1:100 weight ratio and pressed into transparent pellets. The measurements were conducted using a Tensor 27 BRUKER machine at a resolution of 4 cm^{-1} , sample scan time of 32 s, and background scan time of 32 s, with the data ranging from 4000 to 500 cm^{-1} .

Transmission electron microscopy (TEM) was conducted on a Philips CM10 at an acceleration voltage of 60 keV. The TEM samples of CNC, CNC-POEGMA, and CNC-POEGMA-PDMC were prepared from their aqueous dispersions by drop coating onto copper grids and dried at ambient temperature.

Dynamic light scattering (DLS) and zeta potential experiments were conducted using a Malvern Zetasizer Nano series at a nanoparticle concentration of 0.04 wt%. The zeta potentials were determined from the average of 3 measurements, consisting of 12 runs per measurement.

The thermal responsive properties were evaluated by performing turbidimetric measurements on a Varian (Cary 100 Bio) UV-vis spectrometer equipped with a temperature controller. All the measurements were performed at a rate of $1^\circ\text{C}/\text{min}$ and a wavelength of 500 nm.

The amounts of quaternary amine groups on the CNC-g-POEGMA-g-PDMC was determined using a Metrohm 809 Titrando auto-titrator. In brief, a 50 mL solution was prepared using 20.0 mg of the solid CNC-g-POEGMA-g-PDMC (1:1.25) sample and it was stirred at 25°C . Silver nitrate (AgNO_3 , 10 mM) was used as the standard titrant dosing into the sample at a rate of 0.05 mL/min. The conductivity as a function of the titrant volume was recorded. The degree of

quaternization was determined from **Equation (4.1)**^{130,131} where M and V are the molarity (mmol/L) and the volume (mL) of the titrant, respectively, and W is the weight of the CPD.

$$[NH_3^+] \left(\frac{mmol}{g} \right) = \frac{M_{AgNO_3} (mM) \times (V_{AgNO_3}) (L)}{W_{CPD} (g)} \quad \text{Equation (4.1)}$$

4.3. Results and Discussion

4.3.1. Preparation and characterization of the CNC-g- POEGMA-g-DMC

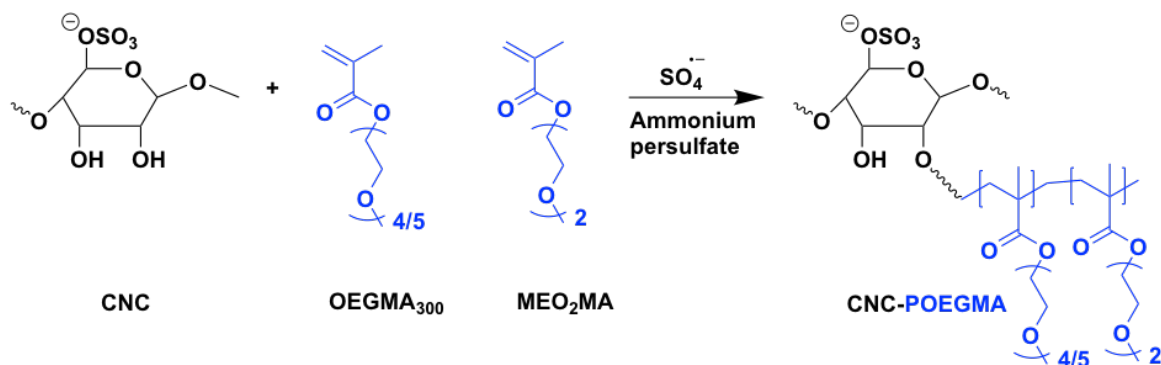
During the purification step in the first stage of the synthesis route, the resulting copolymer (CNC-POEGMA) was dialyzed in a 0.1 micron dialysis membrane against Millipore water. Thus, CNC were retained while the unreacted chemicals were removed. In the second stage of the synthesis route, cerium(IV) ammonium nitrate (CAN) was used as an initiator because it offers many advantages compared to other types of redox initiators due to its high grafting efficiency. In addition, the initiation sites for grafting are formed on the cellulose backbone as shown in **Scheme 4.1**. Therefore, no homopolymer should be produced, as the radicals are almost exclusively located on the cellulose backbone as reported in the literature^{152,153}. After these considerations, the purified CNC-g-POEGMA (CP) and CNC-g-POEGMA-g-PDMC (CPD) were characterized by FTIR, TEM, zeta potential, and TGA. The first step of the synthesis route was the grafting of thermo-responsive monomers from cellulose nanocrystals, which was followed by the second step of grafting DMC monomer from the CP. **Figure 4.1** shows the FTIR spectra obtained for the unmodified CNCs, CP, and CPD. Aside from the characteristic peaks from the stretching vibrations of hydroxyl groups on the CNCs at 3400 and 1058 cm⁻¹ and the sulfate groups at 1249 cm⁻¹, the FTIR spectra of CP and CPD exhibited a new peak appearing at 1730 cm⁻¹ that corresponded to the ester linkage between the methacrylate and oligoethylene glycol side chains of the POEGMA brushes, and the vibrating absorption of carbonyl groups in the DMC respectively. In addition, the FTIR spectra of CPD possessed two new absorption peaks at 1480

and 950 cm^{-1} which could be assigned to the methyl groups of the quaternary ammonium groups and the stretching vibration of the (C-N) bond in DMC. The appearance of new peaks in the spectra of CP, and CPD indicated that the two-step synthetic route was successful.

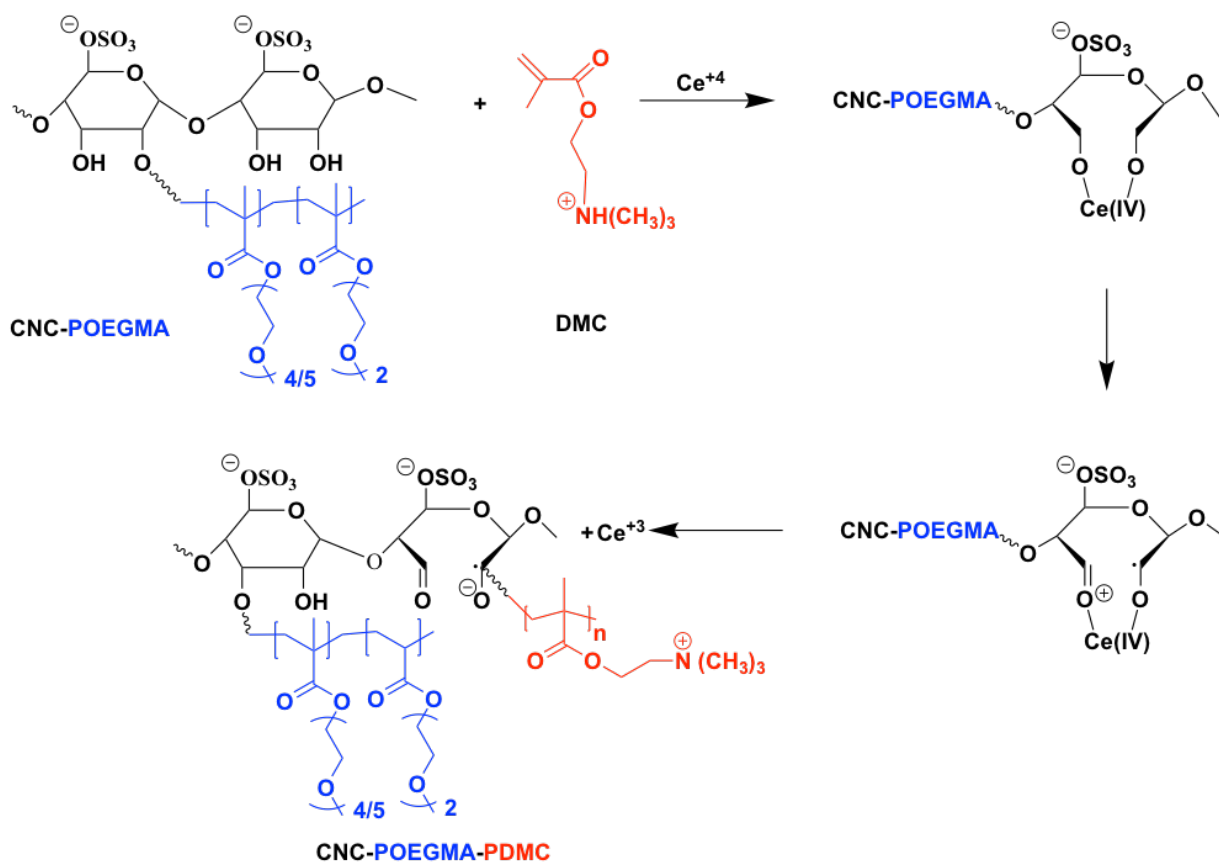
The possible changes in the morphology of CNC before and after modification was studied by TEM, as shown in **Figure 4.2**. The CNC-POEGMA and CNC-PDMC retained the rod-like morphology of pristine CNC and were well-dispersed. However, the surface grafted CNCs became slightly larger, which could be due to the presence of polymer brushes.

The successful cationization of CP was confirmed by zeta potential measurements as shown in **Figure 4.3**. The zeta potential followed the expected trend, which was initially negative for pristine CNCs with an average zeta potential of -48 mV , while the POEGMA brushes were neutral. The zeta potential of CPD was reversed to a positive value ($+28\text{ mV}$) due to the DMC (0.5) possessing quaternary ammonium groups with positive charges. The zeta potential of CPD increased continuously from approximately -26 mV using 0.25 ratio of DMC to $+35\text{ mV}$ when the ratio of DMC was increased to 1.25.

(A) Step 1: Synthesis of CNC-POEGMA



(B) Step 2: Synthesis of CNC-POEGMA-PDMC



Scheme 4. 1. (A) Graft polymerization of MEO₂MA and OEGMA₃₀₀ with Ammonium persulfate initiator from the surface of Cellulose nanocrystals and (B) Graft polymerization of DMC with Ceric (IV) Ammonium Nitrate initiator from the surface of CNC-POEGMA, the generally accepted mechanism for the formation of a radical site on cellulose through persulfate and ceric ion initiators adapted from ¹⁵⁴.

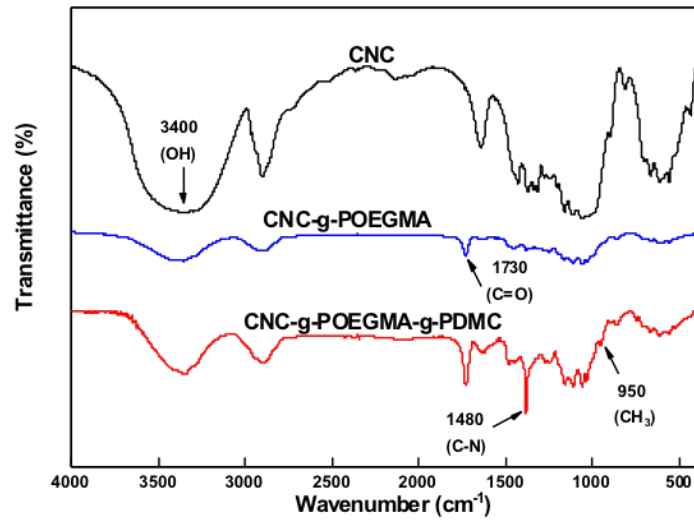


Figure 4. 1. FTIR analysis of pristine CNCs, CNC-g-POEGMA, and CNC-g-POEGMA-g-PDMC.

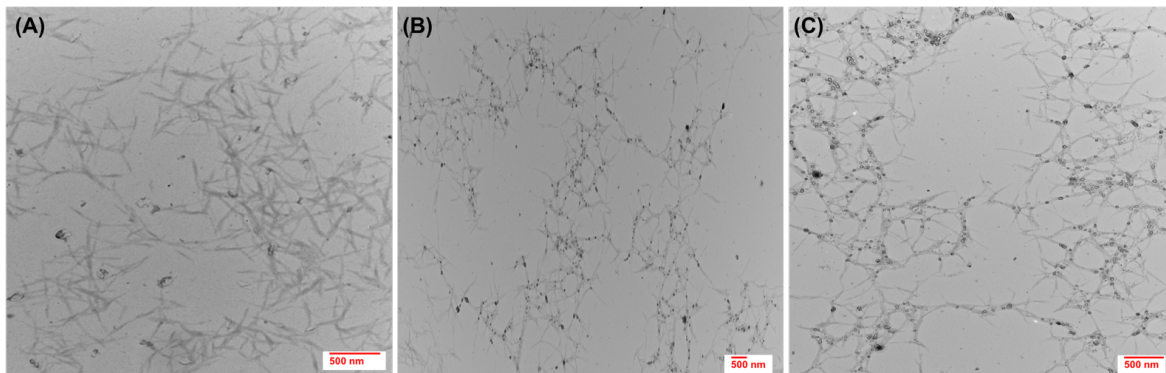


Figure 4. 2. TEM images of CNC (A), CNC-g-POEGMA (B), and CNC-g-POEGMA-g-PDMC (C).

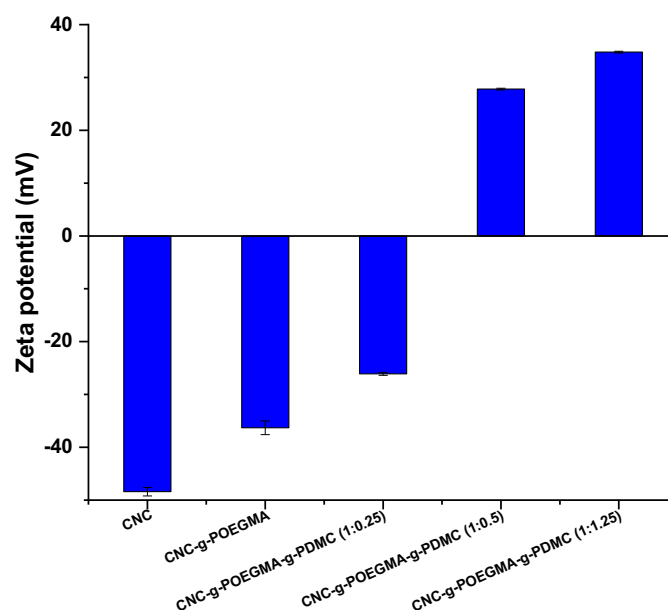


Figure 4. 3. Zeta potential of CNC-g-POEGMA, and CNC-g-POEGMA-g-PDMC.

Thermogravimetric analysis was also conducted to investigate the thermal stability and chemical changes of the CNCs following each modification step. **Figure 4.4 (A)** shows the thermal decomposition profiles of the unmodified CNC, CP, CPD. The unmodified CNCs exhibited an initial onset pyrolysis temperature of 285 °C, which is characteristic of CNCs produced via sulfuric acid hydrolysis ⁷⁴. It was observed that the polymer grafting lowered the thermal stability of the nanoparticle. The reduction of the onset decomposition temperature was previously reported for cellulosic systems that underwent modification via chemical oxidation ¹⁵⁵. The thermogram of CP displayed a two-stage decomposition, with the first stage being the initial pyrolysis of CNCs, and the second stage being the decomposition of grafted POEGMA chains. By differentiating the weight-loss thermograms in **Figure 4.4 (B)**, distinct thermal onsets could be determined. The thermal stability of the CNC was reduced by the grafting of POEGMA, where the first weight loss occurred at a lower temperature compared to the CNCs. The second weight loss occurred at a

temperature of 316 °C for the decomposition of POEGMA side chains. From the first derivative of the curves obtained from thermogravimetric analysis of **Figure 4.4 (B)**, it was possible to estimate the amounts of grafted POEGMA brushes on the CNCs by integrating the area under peak 1 (from 250 °C to 305 °C) and peak 2 (305 °C to 430 °C), which was found to be 34.7% and 44.2% respectively. Taking the first peak to be the pyrolysis of CNCs and the second as the decomposition of POEGMA side chains, a ratio of the two peaks should yield the grafting ratio of POEGMA, which was calculated to be approximately 1.3 g POEGMA/g CNCs. Compared to CP, CPD started to decompose at a temperature of approximately 188 °C which is substantially lower than that of pristine CNC samples and CNC-g-POEGMA. In addition, CPD displayed a terminal combustion temperature of 267 °C, which could be attributed to the decomposition of quaternary ammonium groups (QA) in the copolymer as the degradation of the QA groups in the side chain was reported to be between 170 to 280 °C¹⁵⁶. It could be noted that the unmodified CNCs retained 3-5% of their mass in the form of a charred carbon residue, whereas the CP, and CPD almost completely combusted. The TGA analyses provided an indirect confirmation of successful grafting of polymer brushes on CNCs.

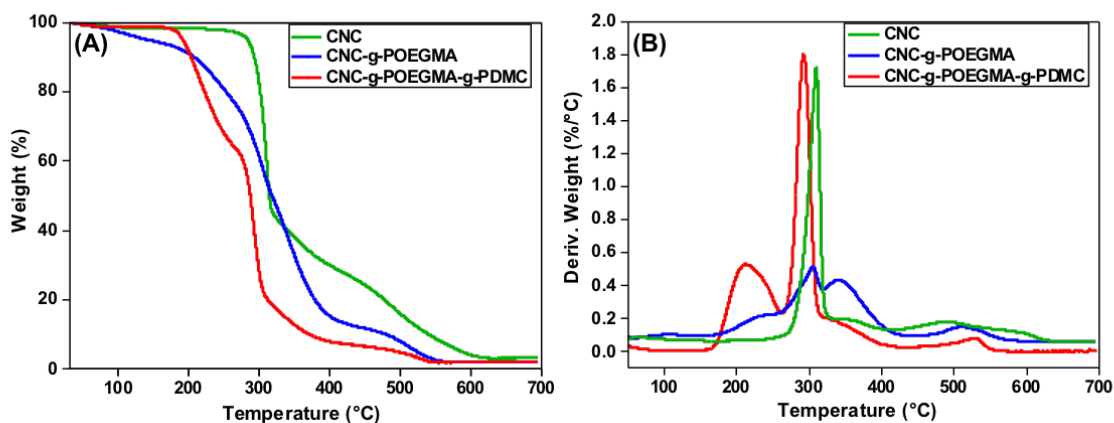


Figure 4. 4. TGA analysis of pristine CNCs, CNC-g-POEGMA, and CNC-g-POEGMA-g DMC (A) and the first derivative of thermogravimetric data (B) to assess the amount of (POEGMA) grafted from cellulose nanocrystals surface.

The amount of quaternary amine groups grafted on the CP were quantified by conductometric titration with 10 mM AgNO_3 solution. The titration data revealed two stages that were delineated by the conductivity inflection point as shown in **Figure 4.5**. The first stage displayed a slight linear decrease due to the reaction between silver cations and chloride counterions of the quaternary ammonium groups to form silver chloride precipitates. The second stage displayed a sharp increase as a result of the dissociation of silver nitrate to form free silver cations and nitrate anions, which occurred only after the consumption of all the chloride counterions. The point of intersection corresponded to the volume of silver nitrate consumed, which was used to calculate the quaternary amine content on the CPD. The concentration of quaternary ammonium groups was found to be 0.8 mmol/g for the ratio (1:0.25), 2 mmol/g for the ratio (1:0.5), and was 5 mmol/g for the ratio (1:1.25) indicating that the degree of quaternization increased with DMC ratio.

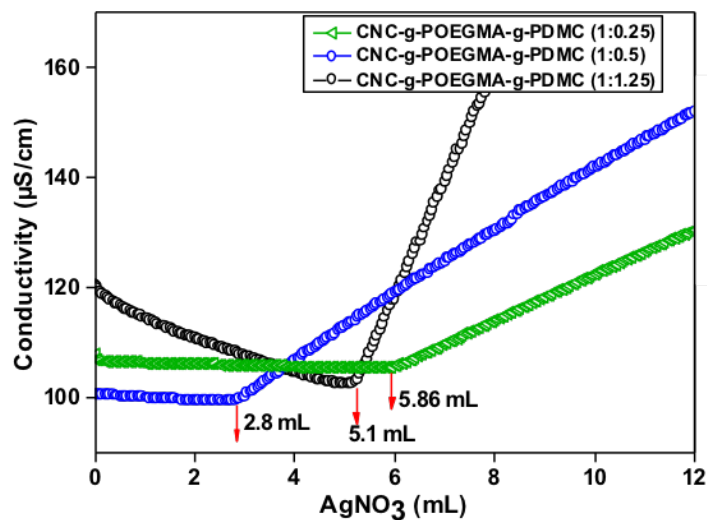


Figure 4. 5 Conductometric titrations of CNC-g-POEGMA-g-PDMC at different ratios of DMC.

4.3.2. Thermo-responsive characteristics of the copolymers

To investigate the thermo-responsive properties of the prepared copolymers and determine their LCST, different techniques were used. The transmittance-temperature profiles determined at a heating rate of 1 °C/min for the systems at different concentrations are shown in **Figure 4.6**. The general observation is that the phase transition (cloud point - T_{cp}) shifted to lower temperatures for high concentration solutions (**Figure 4.6 (A), (B)**) which were reported in the literature and attributed to greater polymer-polymer interaction at higher concentration. It is also reported that the higher observed T_{cp} for low concentration solutions (**Figure 4.6 (C),(D)**) is ascribed to the UV-Vis spectrophotometry technique that detects relatively large phase separated aggregates that were not present at the early stages of the phase separation⁶⁹. For high concentration samples, a sharp transition was observed up to 0% transmittance because of the high mass of polymer aggregates that formed which contributed to high turbidity and 0% transmittance.

To determine the LCST of the copolymers using the UV-Vis spectrophotometry technique, two proposed approaches have been used to map the phase diagram¹⁵⁷. The first method is to obtain the phase diagram from the cloud point (T_{cp}) determined from the temperature versus the transmittance plot, where T_{cp} was identified as the critical temperature at 50% transmittance. Using this method, the LCSTs for CP and CPD were determined to be 50 °C and 43 °C, respectively, as shown in **Figure 4.7 (A) & (B)**.

Since some of the samples possessed transmittance that displayed smaller changes, and the inflection point was determined from the differentiation of the turbidity-temperature curve (identified as the second method) to identify the cloud point or LCST, as shown in **Figure 4.8 (A-D)**. The LCST for CP and CPD was 48 and 43 °C, respectively, as shown in **Figure 4.9 (A), (B)**,

which is close to the results obtained from the temperature versus the transmittance plot (the first method).

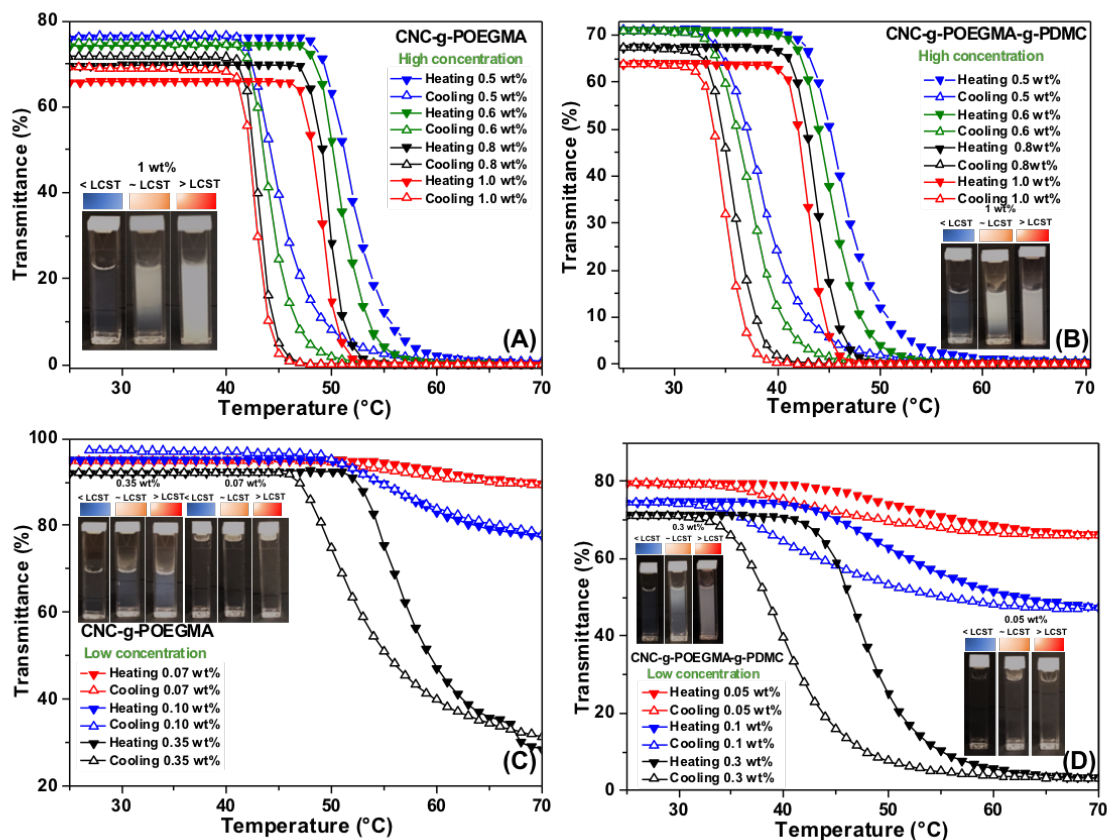


Figure 4. 6. The cloud point (T_{cp}) values obtained from the transmittance–temperature (Tr–T) curve of CNC-g-POEGMA, and CNC-g-POEGMA-g-PDMC at high concentrations (A), (B) and at low concentrations (C), (D). Insets: the corresponding photographs of the copolymers at different temperatures.

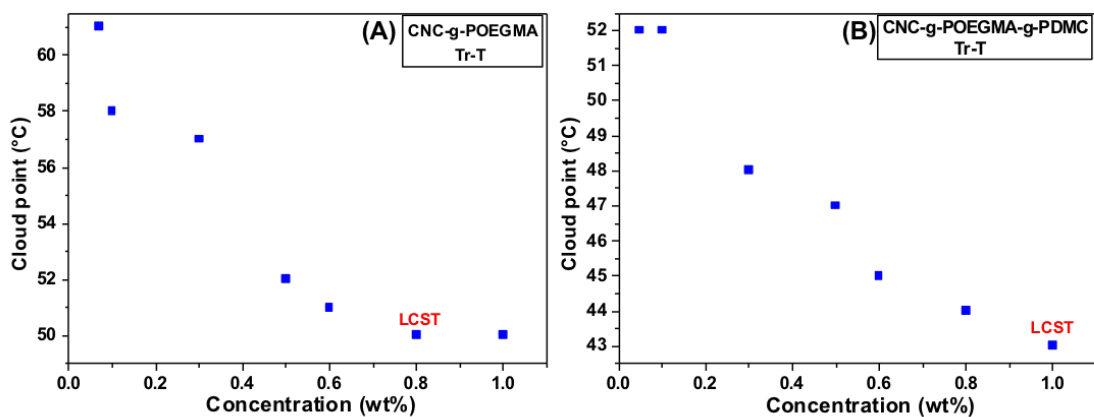


Figure 4. 7. Phase diagram of CNC-g-POEGMA (A) and CNC-g-POEGMA-g-PDMC (B) aqueous solutions using transmittance temperature (Tr-T) curve.

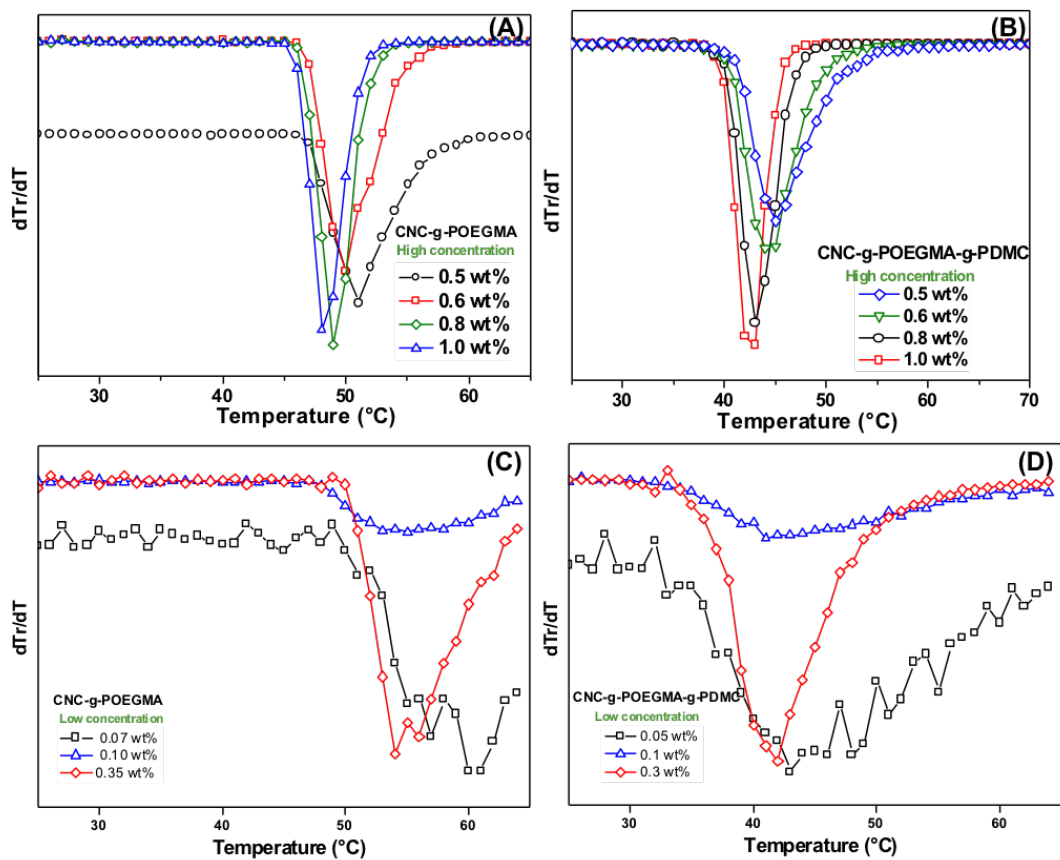


Figure 4. 8. The cloud point (T_{cp}) values obtained by the derivate of the Tr-T curve of CNC-g-POEGMA, and CNC-g-POEGMA-g-PDMC at high concentrations (A),(B) and at low concentrations (C),(D).

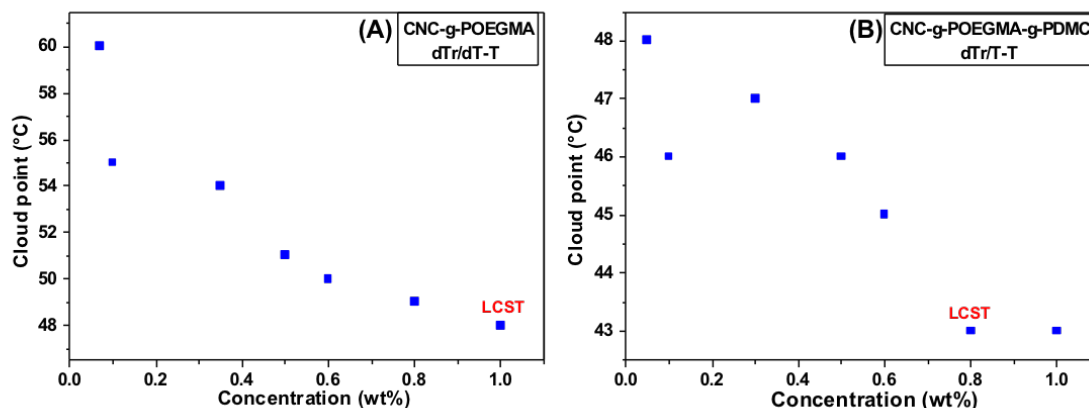


Figure 4. 9. The phase diagram of CNC-g-POEGMA (A) and CNC-g-POEGMA-g-PDMC (B) aqueous solutions obtained by the derivate of the Tr–T curve.

Another technique used to identify the LCST is dynamic light scattering (DLS). Compared to the UV–vis spectrophotometry, DLS provides information on the particle size of the nanostructure. **Figure 4.10** shows the DLS data describing the hydrodynamic radius of different concentrations of CP and CPD as a function of temperature. The size of the nanoparticles was between 40 and 80 nm at low temperatures followed by a sharp transition which became more accentuated at higher polymer concentrations. For the higher concentration solutions (0.5-1.0 wt%), interparticle-chain association was dominant, leading to the surfaces of the CNCs becoming hydrophobic, inducing the aggregation of the nanoparticles. This led to an increase in the R_h when the temperature was increased, showing a maximum in the temperature range between 50-55 °C for CP and 45-55 °C for CPD. In addition, R_h displayed a decreasing trend, which remained unstable when the temperature continued to increase. This behavior could be attributed to the inter-chain association amongst the CNCs, resulting in the decrease in R_h (contraction of the chains or shrinkage). For the lower polymer concentration (0.35 wt%), R_h increased with increasing temperature until it approached a maximum over the temperature range of 60–65 °C. At higher temperatures, R_h remained constant, reflecting the cessation of intra-chain association. In the most diluted solutions

(0.1 wt%, 0.07 wt%), there was no clear transition due to the low molar mass, where aggregation cannot occur. The LCST of CP and CPD using DLS was 44 °C and 36 °C respectively as shown in **Figure 4.11 (A),(B)** respectively. The lower LCST value obtained using DLS compared to UV-vis spectrophotometry could be ascribed to the higher sensitivity of the DLS to detect the aggregation, which did not contribute to the solution turbidity. The proposed mechanism for the effect of temperature on the aggregation and contraction behavior in solutions of CP is depicted in **Scheme 4.2**.

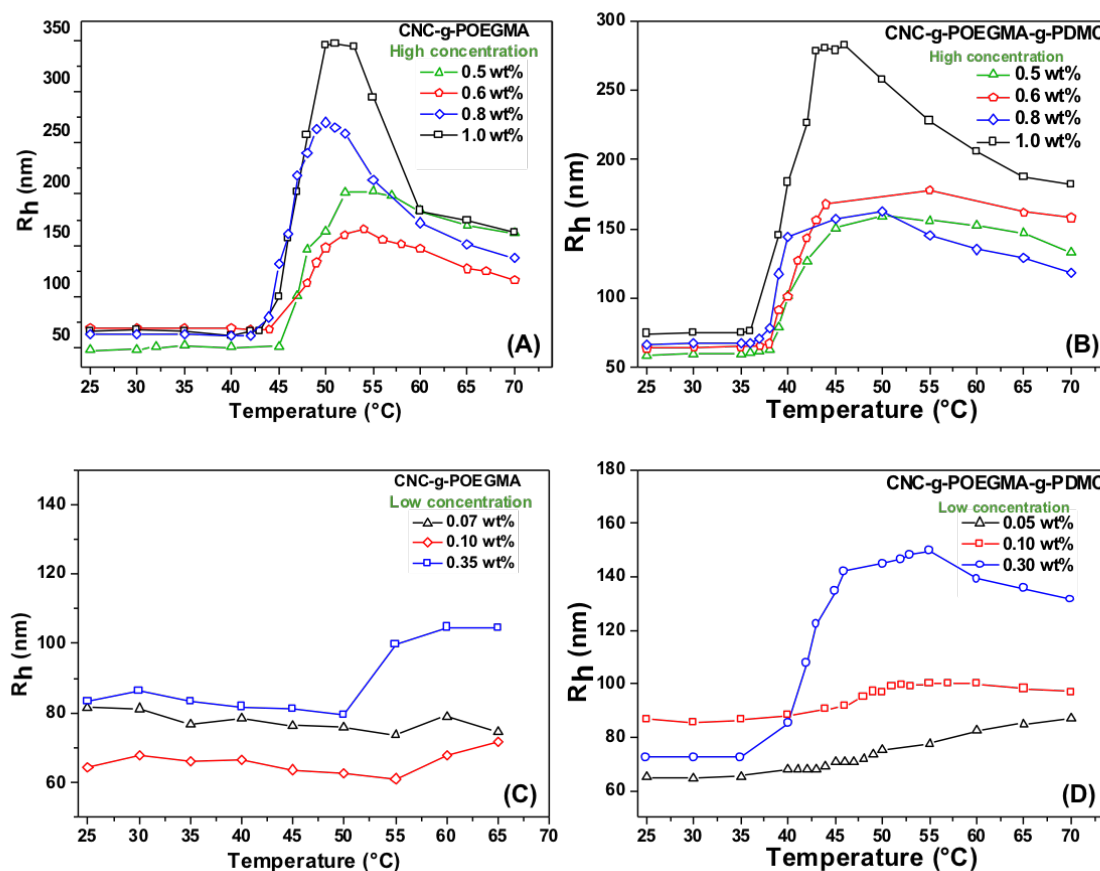


Figure 4.10. Temperature dependences of the apparent hydrodynamic radii of CNC-g-POEGMA, and CNC-g-POEGMA-g-PDMC (1:0.5) at high concentrations (A),(B) and at low concentrations (C),(D).

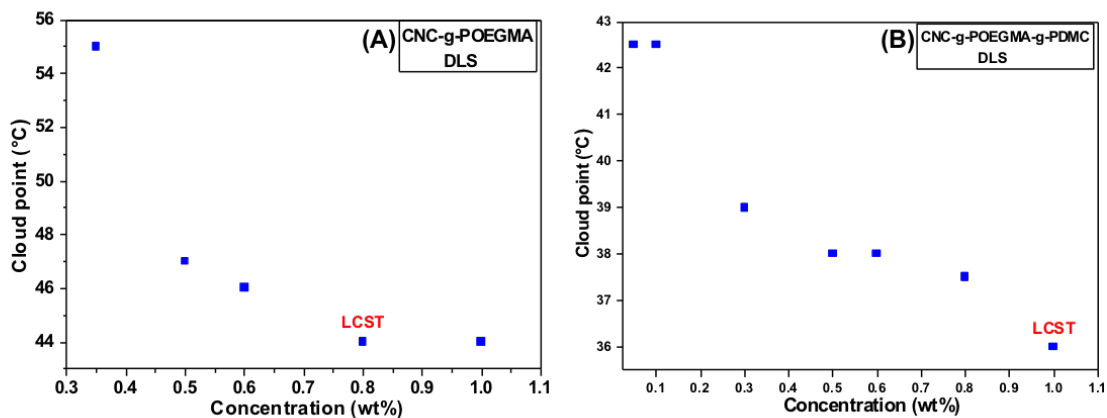
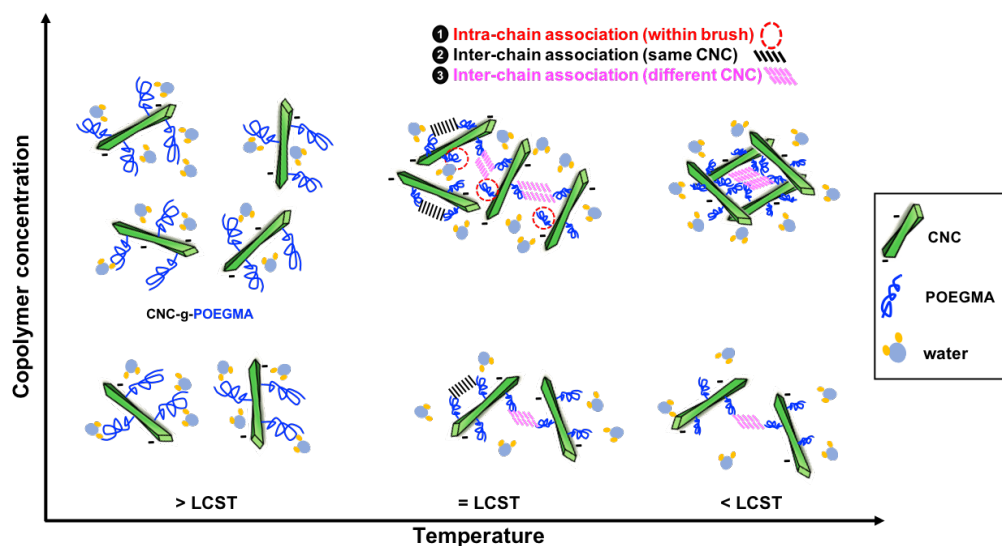


Figure 4. 11. Phase diagram of CNC-g-POEGMA (A) and CNC-g-POEGMA-PDMC (B) aqueous solutions using DLS.



Scheme 4. 2. Schematic illustration of the aggregation observed of CNC-g-POEGMA during heating.

4.3.3. The effect of DMC composition on the thermo-responsive properties of CNC-g-POEGMA-g-PDMC

To investigate the effect of the cationic monomer (DMC) on the LCST of the CP, different ratios of DMC were grafted from the surface of CNC-g-POEGMA. The transmittance-temperature of CPD at different ratios of DMC subjected to a heating rate of 1 °C/min are shown in **Figure**

4.12 (A), (B). From the phase diagrams in **Figure 4.12 (C), (D)**, we observed that the LCST for the lower ratio of DMC (CPD (1:0.25)) was 40 °C, while at higher DMC ratio (CPD (1:1.25)) the LCST was increased to 47 °C.

Using the inflection point in the derivative of T_r vs. T curves (**Figure 4.13 (A), (B)**), the LCSTs values for CPD (1:0.25) and CPD (1:1.25) was determined to be 41, and 46 °C respectively as shown in **Figure 4.13 (A), (B)**, which were close to the obtained values at 50% transmittance.

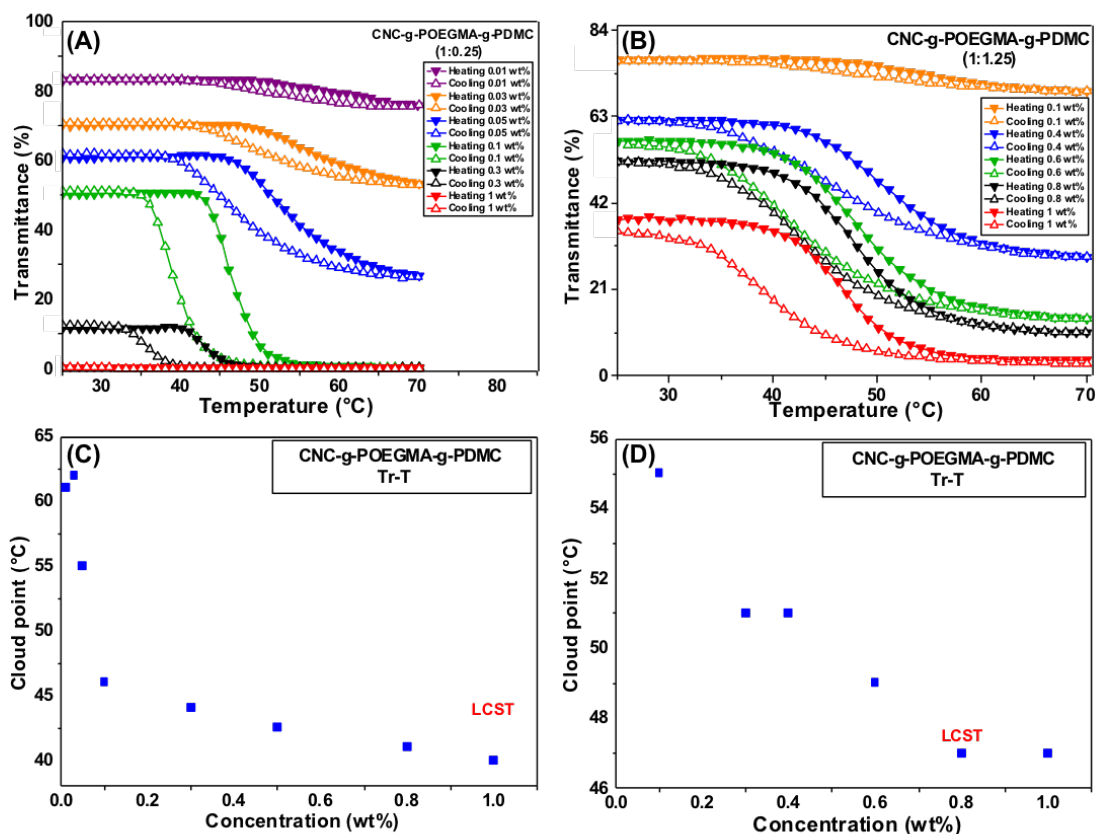


Figure 4. 12. The cloud point (T_{cp}) values obtained by the transmittance–temperature (T_r – T) of CNC-g-POEGMA-g-PDMC (1:0.25) (A), CNC-g-POEGMA-g-PDMC (1:1.25) (B), and the corresponding phase diagram (C), (D) respectively.

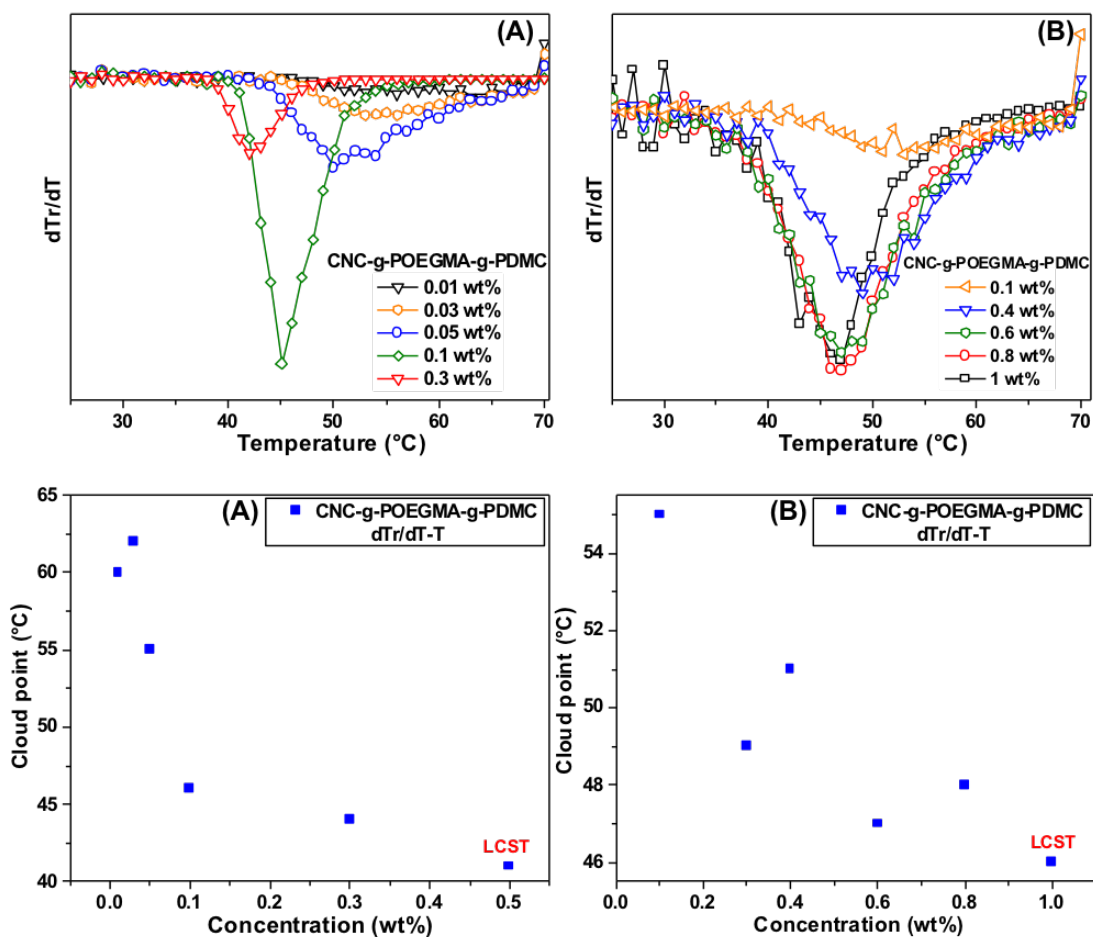


Figure 4. 13. The cloud point (T_{cp}) values obtained by the derivate of the Tr–T curve of CNC-g-POEGMA-g-PDMC (1:0.25) (A), and CNC-g-POEGMA-g-PDMC (1:1.25) (B) and the corresponding phase diagram (C), (D).

4.3.4. The effect of salt on the thermo-responsive properties of CNC-g-POEGMA-g-PDMC

The influence of KCl on the LCSTs of the CNC-copolymers were also examined. For the CNC-g-POEGMA, a typical salting-out effect was observed after the addition of KCl. As shown in **Figure 4.14**, the LCST decreased with increasing salt concentration due to chloride ions polarizing the adjacent water molecules, which in turn, weakened the interactions between the POEGMA brushes and surrounding water molecules resulting in the dehydration of the polymer chains and consequently a reduction in the LCST as illustrated in **Scheme 4.3 (A)**. The salt effect in this case

is related to the Hofmeister series as reported for PNiPAAm¹⁵⁸. For the cationic copolymers with lower ratios of DMC, different salt-responsive characteristics were observed at low and high salt concentration. For example, the LCST of CNC-g-POEGMA-g-PDMC (1:0.5) increased to 53 °C at low salt concentration (10⁻² M), however it decreased to 37 °C at high salt concentration (1 M). This phenomenon is explained by two types of interactions of salt ions with the PDMC, POEGMA brushes and their hydration shells. First, low concentrations of salt anions (Cl⁻) induced ion-pair interaction with the quaternary ammonium groups of the PDMC brushes, which facilitated the diffusion of salt cations (K⁺) to the surface of CNCs, screening the negatively charged sulfate groups. This in turn released the electrostatically bound PDMC polymer on the surface of CNCs from the surface, adopting an extended chain conformation, as seen in **Scheme 4.3 (B)(1)**. This translated to an increase in the LCST as the surface of the copolymer is further protonated from the extended PDMC brushes and forms stronger interactions with surrounding water molecules. Several studies have reported the effect of salt addition on the stability of CNCs, resulting in a gradual reduction in the zeta potential with increasing salt concentration due to electrostatic screening^{159,160}. However, higher anion concentrations led to increased ion-pair interactions with PDMC brushes that became sufficiently strong in removing the ionic hydration shells, and also increased the polarization of water molecules around the POEGMA brushes causing them to adopt a collapsed chain conformation (**Scheme 4.3 (B)(2)**). As a result, the decrease in the interaction between PDMC and water culminated in a reduction in the LCST as more salt anions removed the hydration shells around PDMC and POEGMA brushes. However, for the cationic copolymer with the highest ratio of DMC, the LCST decreased with increasing salt concentrations. This behavior is associated with the high steric hindrance (high grafting density), where the salt anions could only form ion-pair interactions, resulting in the dehydration of the polymers chains , causing them

to adopt a collapsed chain conformation since the salt cations could not diffuse to the CNC surface (Scheme 4.3 (C)). The effect of chloride ions on the hydration and conformation of PDMC homopolymer was reported to be associated with the presence of high chloride ions that led to chain dehydration because of the ion-pair interactions^{161,162}.

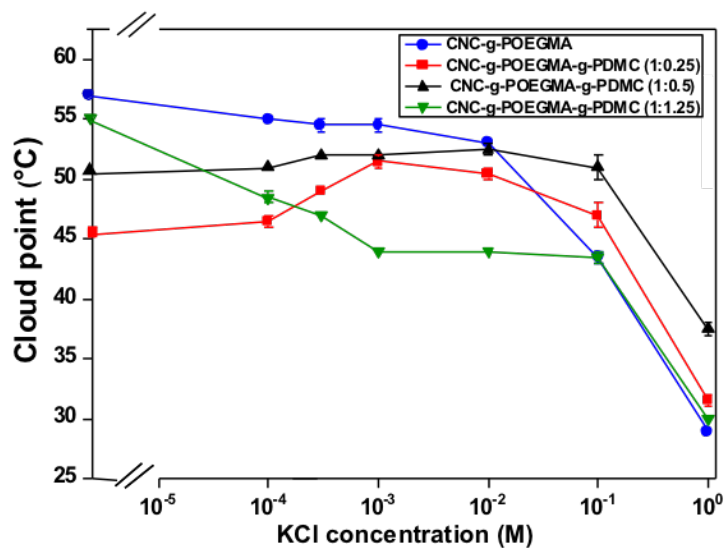
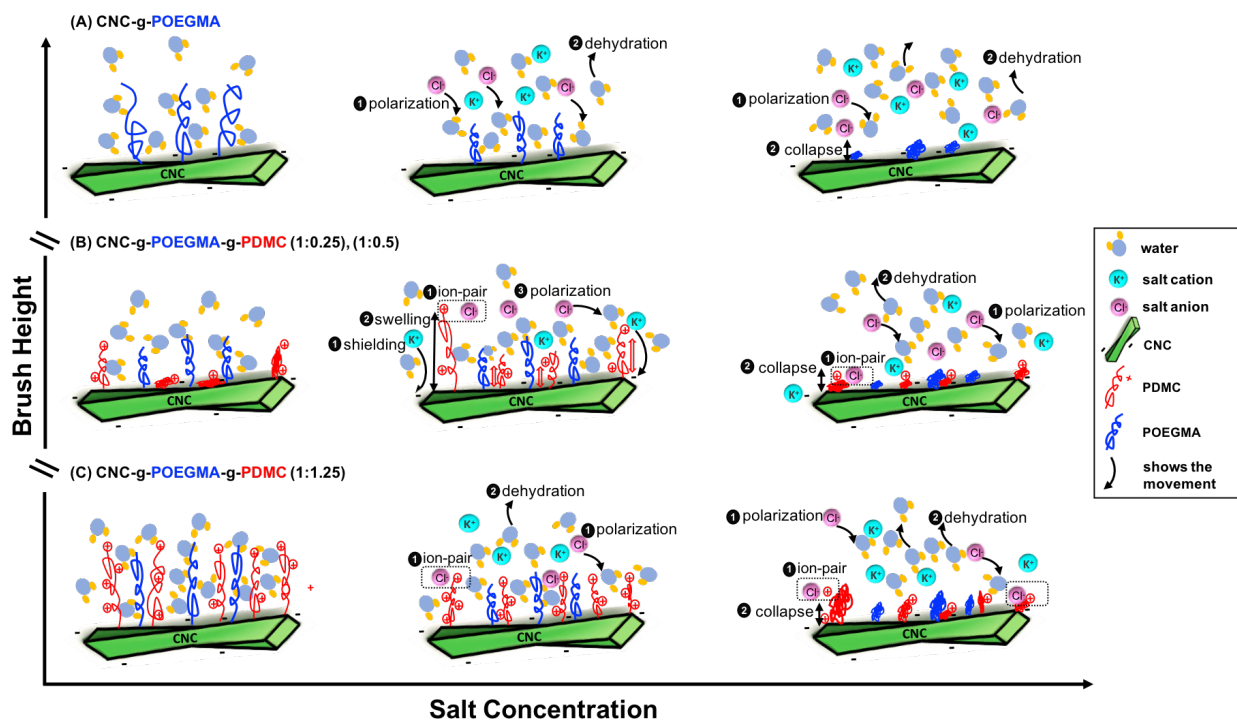


Figure 4. 14. The effect of salt concentration on the cloud points of CNC-g-POEGMA and CNC-g-POEGMA-g-PDMC.



Scheme 4. 3. Schematic representations of the proposed mechanisms responsible for the brush swelling and brush collapse transitions of CNC-g-POEGMA and CNC-g-POEGMA-g-PDMC, (the numbers in black circles indicate the order of the events).

The effect of salt on the thermal behavior of the copolymers was also evaluated using the zeta potential measurements to further confirm the observed phenomenon as shown in **Figure 4.15**. For the CNC-g-POEGMA and CNC-g-POEGMA-g-PDMC (1:1.25), the zeta potential decreased sharply from -37mV and -25mV to -8.5 mV and -2.6 mV respectively, reflecting the low stability as a result of the salting-out effect of the copolymers with the introduction of salt. In the case of the CNC-g-POEGMA-g-PDMC with ratio (1:0.5), the zeta potential increased to +32 mV at 10^{-2} M KCl due to the release of the absorbed PDMC brushes from the CNC surface as the sulfate ester groups were screened. In the presence of increasing amounts of KCl (1 M), the zeta potential of the copolymers decreased sharply, indicating the lower stability of the copolymers because of the high degree of ion-pairing interactions and the salting-out effects causing the dehydration.

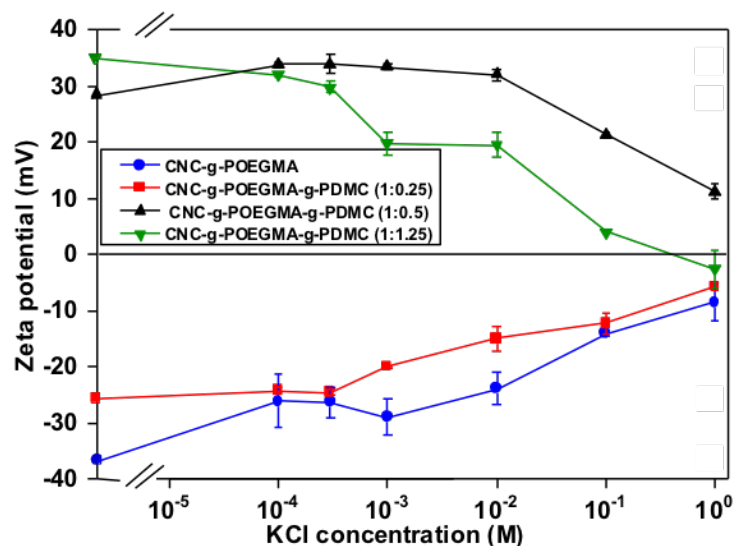


Figure 4. 15. The effect of salt concentration on the zeta potential values of CNC-g-POEGMA and CNC-g-POEGMA-g-PDMC.

4.3.5. The effect of dosage on the turbidity removal efficiency

The flocculation performance of two copolymers , i.e. CNC-g-POEGMA-g-PDMC (1:1.25) (CPD1) and CNC-g-POEGMA-g-PDMC (1:0.5) (CPD2) was examined for the removal of bentonite particles. The copolymers were added to bentonite suspensions at different temperatures to study the effect of the copolymers coil-globule transition of the copolymers on flocculation performance. Two settling conditions were considered: RMRS and RMHS. The RMRS refers to mixing and settling at 25 °C, which was below the LCST of the two copolymers. This procedure will be referred to as 25M25S. The RMHS refers to mixing at 25 °C and settling at 50 °C, which was above LCST of the two copolymers. This procedure will be referred to as 25M50S. Control experiments using bentonite only at 25 °C and 50 °C resulted in turbidities of 0.3 and 0.5 respectively as shown in **Figure 4.16**. The increase in the turbidity at 50 °C is consistent with the experimental evidences of increased stability of bentonite colloids with temperature reported in another study¹⁶³. This observation was explained based on the increase in the repulsion potential

of the particles with temperature, which is in consistent with the DLVO model predictions. Two critical observations can be noted from **Figure 4.16**. Firstly, the temperature of settling had a significant effect on bentonite stability and flocculation efficiency. Secondly, the copolymers displayed a similar trend at a different dosage, turbidity removal increased along with increasing flocculant dosage, but then the turbidity removal efficiency slightly decreased with the further dosage after the optimal treatment efficiency was obtained. The maximum in the turbidity removal efficiency for (CPD1) and (CPD2) using the RMRS protocol were 95% and 84% at optimum dosage of CPD1-21 mg/g and CPD2-30 mg/g respectively. On the other hand, the flocculation efficiency using the RMHS protocol increased about 4% and 6% for CPD1 and CPD2 at lower dosages. The optimum flocculation efficiency for the two copolymers was directly proportional to the content of quaternary ammonium groups of the copolymers.

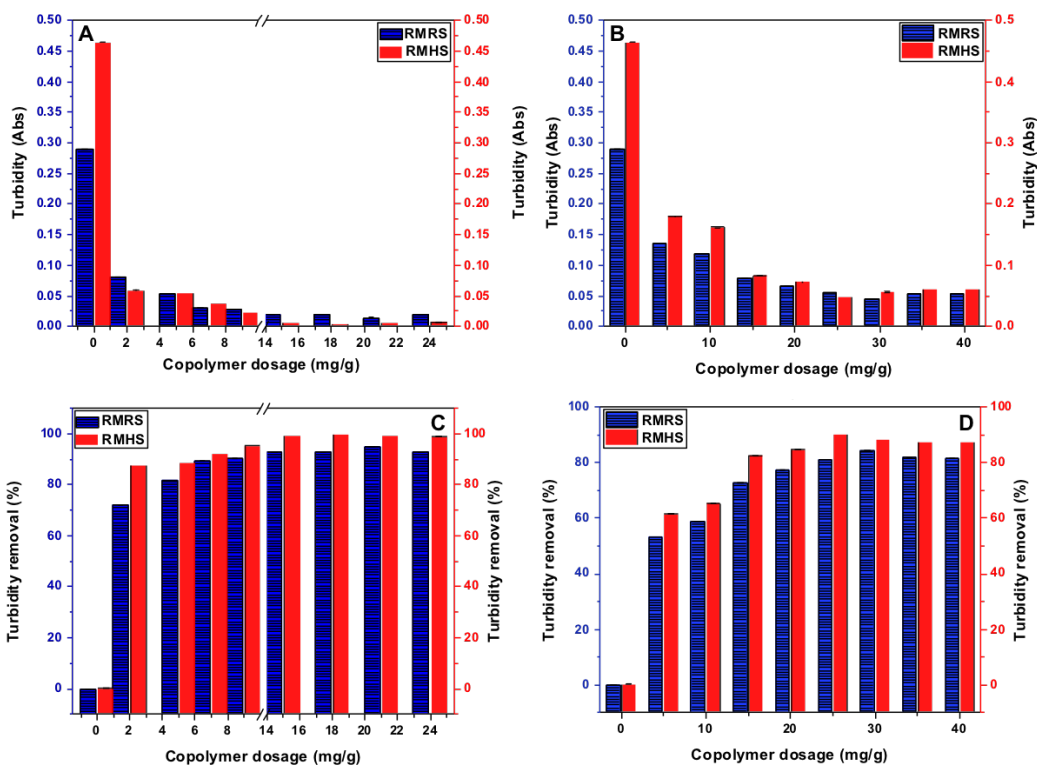


Figure 4. 16. Effect of CPD1(A), CPD2 (B) on the turbidity and the corresponding turbidity removal percentage (C), (D) of bentonite as a function of dosage at different settling temperatures.

4.3.6. The effect of dosage on the zeta potential

Adsorption bridging and charge neutralization are the main mechanism of the flocculation process. The zeta potential of the flocculation system provides direct information on the charge neutralization effect. The zeta potentials after flocculation using the RMRS protocol were increased with the increased dosage of CPD1 and CPD2 (**Figure 4.17**). However, the zeta potential values for samples treated with CPD2 were high negatively charged although the flocculation efficiencies were high (>80%). The CPD1 copolymer yielded better treatment efficiency because of synergistic effect between bridging and cationic brush structure could effectively facilitate the flocculation process. The highest zeta potential of floc treated with CPD1 indicated that the concentrated distribution of cationic units on the CPD1 copolymer chain possessed the stronger charge neutralization capability compared to the CPD2 with less cationic charges. This phenomenon confirmed that charge neutralization played an important role in the flocculation with CPD1 while bridging mechanism was dominant for CPD2. The zeta potential of samples treated with CPD1 and CPD2 using the RMHS protocol were slightly higher than those treated using the RMRS protocol indicating that adsorption bridging significantly contributed to the flocculation mechanism in RMHS.

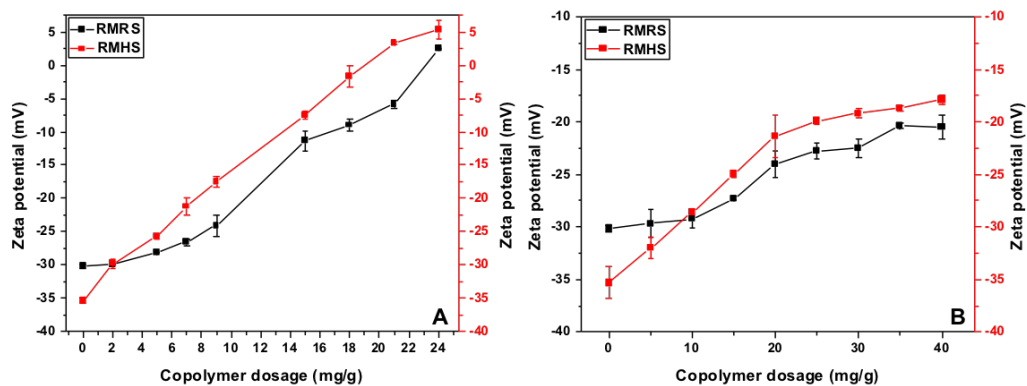


Figure 4. 17. Effect of CPD1 (A) and CPD2 (B) on the zeta potential of bentonite as a function of flocculant dosage at different settling temperatures.

Figure 4.18 shows the optical microscopic images of bentonite at 25 °C and 50 °C and the dependence of floc size on the copolymer dosage and the settling temperature. In terms of the copolymer dosage, the average size of bentonite particles at 25 °C was 650 nm, while the size decreased to 580 nm at 50 °C. By increasing the copolymer dosage, the percentage of small particles decreased while the percentage of larger aggregates increased until the maximum flocculation was achieved. The opposite case was observed beyond the optimum dosage, where the flocs became smaller and the percentage of small particles increased. In terms of the settling temperature, an increasing compactness in the flocs was observed by the darkness of the elongated structures of flocs formed. This observation implies that the floc structure changed at high temperature (cloud point T_{cp}). Presumably, the floc size reduced at the cloud point, which strengthened the bridging adsorption capability through inter-molecular hydrophobic association. The influence of the coil-globule transition on the settling rates was clearly visible for CPD1 than CPD2.

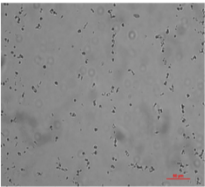
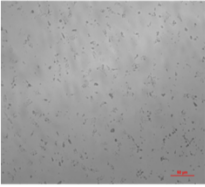
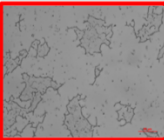
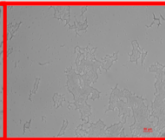
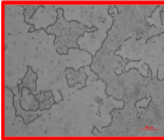
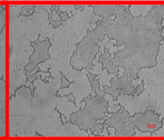
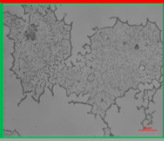
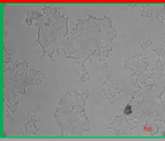
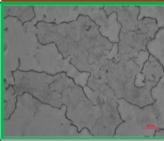
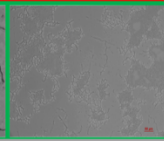
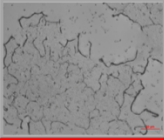
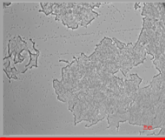
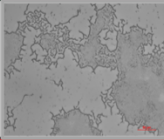
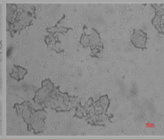
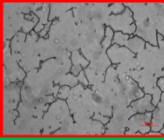
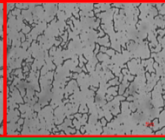
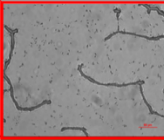
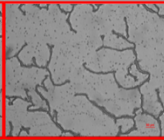
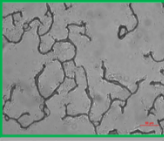
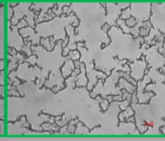
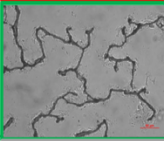
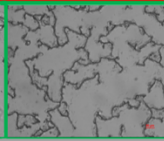
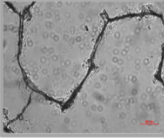
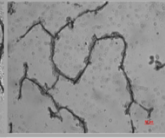
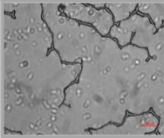
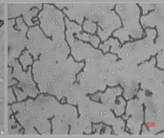
Bentonite	Protocol		Dosage			
	Sample		RMRS(25M25S)		RMHS (25M50S)	
			40x	20x	40x	20x
<p>25 °C</p>  <p>50 °C</p>  <p>Scale bar 50µ</p>	CPD1	<optimum dosage				
		=optimum dosage				
		>optimum dosage				
	CPD2	<optimum dosage				
		=optimum dosage				
		>optimum dosage				

Figure 4. 18. Effect of the CPD1 and CPD2 on the flocs size of bentonite as a function of dosage at different settling temperature.

4.3.7. Proposed mechanisms

The pictures taken at the optimum dosage of CPD1 and CPD2 using different protocols revealed the compactness of the flocs and the mechanism of flocculation as shown in **Figure 4.19**. The flocs obtained with CPD1 were large and considerably light, thus presenting a higher tendency to float. On the other hand, the flocs obtained with CPD2 were heavier and more compact which might be the result of hydrophobic interactions. In addition, the microscopic images illustrated the different mechanisms of flocculation using the CPD1 and CPD2. As can be seen in **Scheme 4.4**, the CPD1 **(A)** formed larger flocs, while CPD2 **(B)** formed flocs of smaller sizes. This observation suggested

that CPD1 brushes bound to the bentonite particles via electrostatic interactions between the negatively charged silanol groups and positively charged quaternary ammonium groups, which was accompanied by chain bridging of the bentonite particles. The large flocs formed by CPD1 cross-linked together via bridging and hydrophobic association at 50 °C due to the temperature mediated coil-globule transition, making the flocs denser as shown in **Scheme 4.4 (C)**. By contrast, charge neutralization played a dominant role in the earlier stage of flocculation because of the reduction in the positive charge density of CPD2. First, negative charges on bentonite particles were reduced by the positive charges. Second, CPD2 flocculant continued to sweep and enmesh bentonite particles with reduced charge mainly via hydrophobic interactions between POEGMA brushes as shown in **Scheme 4.4 (B)**. The structure of the flocs did not change with RMHS confirming that the bridging was the dominant mechanism for CPD2 as shown **Scheme 4.4 (D)**. The proposed mechanism is in agreement with the zeta potential measurements, as there was no significant change in the zeta potential values for both protocols (RMRS and RMHS). The temperature mediated coil-globule transition in the RMHS should make the flocs denser, where the cloud point of the optimum dosage for CPD1 and CPD2 were 50 and 45 respectively. As a result, better flocculation performance was obtained using the RMHS protocol for both copolymers.

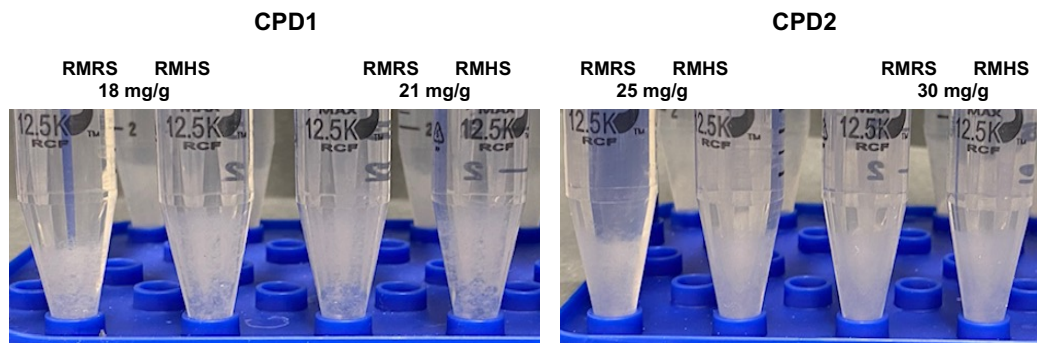
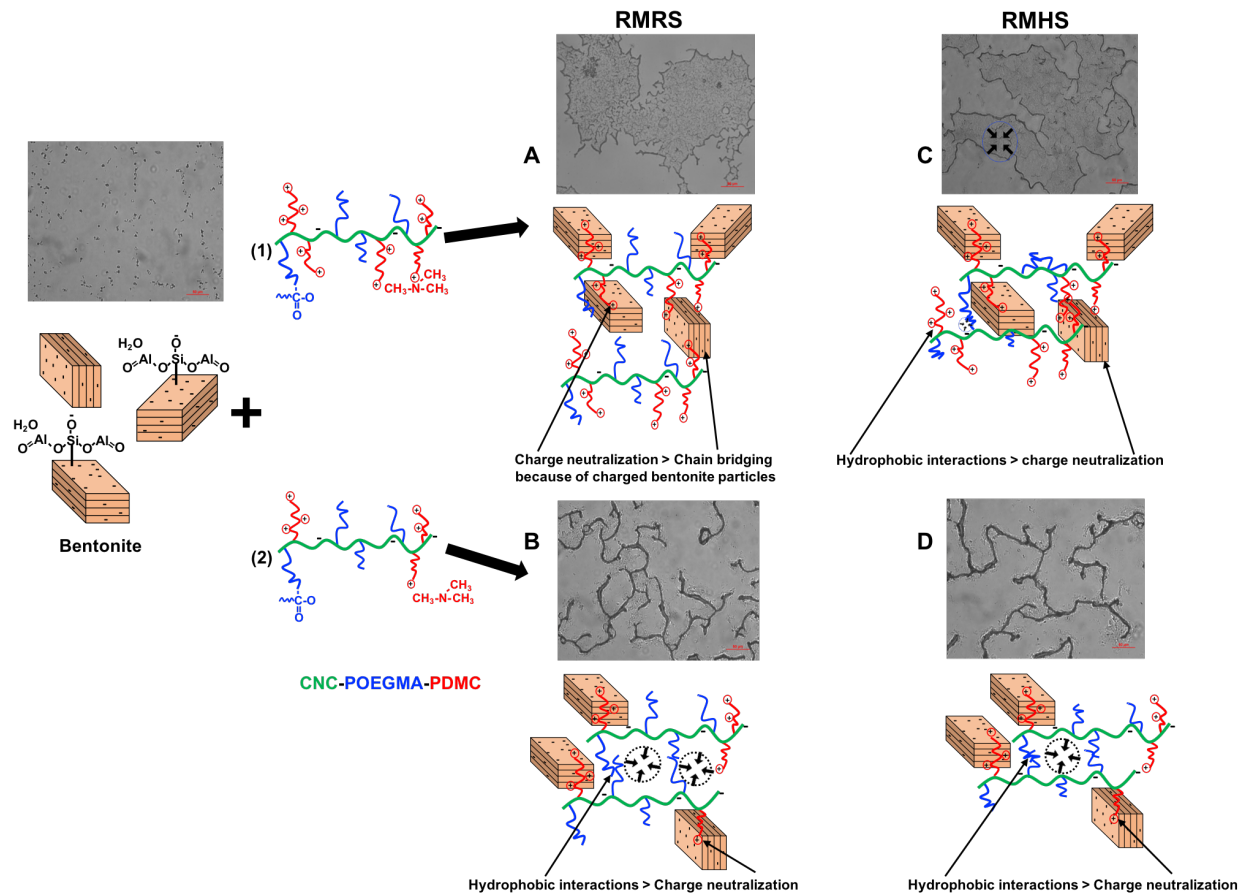


Figure 4. 19. Floccs formed at optimum dosage of CPD1 and CPD2 using RMRS and RMHS protocols.



Scheme 4. 4. Schematic representations of the proposed mechanisms responsible for the flocculation of CPD1 and CPD2 using RMRS and RMHS protocols.

4.4. Conclusions

CNC-g-POEGMA (CP) and CNC-g-POEGMA-g-PDMC (CPD) were synthesized via free radical polymerization techniques. The first step of the synthesis route was the grafting of thermo-responsive monomers (MEO₂MA and OEGMA₃₀₀) from the cellulose nanocrystals, followed by the grafting of DMC monomer from the CNC-g-POEGMA. The CNC-g-POEGMA and CNC-g-POEGMA-g-PDMC were characterized by FTIR, TEM, zeta potential and TGA, which confirmed the successful grafting of the polymer brushes on the CNC. The cloud points and LCST were determined by UV-Vis spectrophotometry and dynamic light scattering (DLS) techniques. The

lower LCST value obtained from DLS compared to UV–Vis spectrophotometry was ascribed to the higher sensitivity of the DLS in detecting aggregation, which did not contribute to the turbidity during the phase transition of the polymer brushes. The CNC-g-POEGMA (CP) possessed tunable lower critical solution temperature (LCST) of about 50 °C, and cloud point measurements confirmed that the LCST of the nanoparticles could be tuned by adjusting the DMC content. A typical salting-out effect was observed for the CNC-g-POEGMA after the addition of KCl, where the LCST decreased because of the partial dehydration caused by the chloride anions. On the other hand, the CNC-g-POEGMA-g-PDMC copolymers displayed different salt-responsive characteristics depending on the content of the cationic monomer (DMC). For the copolymer with the lower (DMC) content, the LCST increased at low salt concentration because of the ion-pair interaction that facilitated the release of the absorbed PDMC brushes from the CNC surface as the sulfate ester groups were screened. However, higher salt anion concentrations led to increased ion-pair interactions that became sufficiently strong to remove their ionic hydration shells, and also increased the polarization of water molecules around the POEGMA causing the LCST to decrease. For the copolymer with the higher (DMC) content, the LCST decreased as the salt concentration increased which could be attributed to the high steric hindrance where the salt anions could only form ion-pair interactions with PDMC brushes while the salt cations could not diffuse to the surface of the CNCs. This coupled with the polarization of water molecules around POEGMA brushes which resulted in the dehydration of the polymers chains. The flocculation efficiency of two CNC-based copolymers for bentonite removal were compared using two settling temperatures defined by the protocols RMRS and RMHS. CNC-POEGMA-PDMC [1:1.25] (CPD1) with higher ratio of cationic brushes (DMC) was more efficient than CNC-POEGMA-PDMC [1:0.5] (CPD2) in bentonite removal with maximum flocculation efficiency (95% at 21 mg/g) versus 84% at 30

mg/g respectively. The thermo-responsiveness of the copolymers resulted in higher flocculation efficiency at lower dosage and the microscopic images indicated that the copolymers yielded more compact flocs.

Chapter 5. Flocculation of Bentonite by Cationic Cellulose Nanocrystals

Abstract

Cellulose nanocrystal-based flocculants with various brush lengths were synthesized via the Activators ReGenerated by Electron Transfer polymerization (ARGET-ATRP). In this study, [2-(methacryloyloxy) ethyl]trimethylammonium chloride (DMC) was used to prepare cationic brushes on the CNC. The resulting material was characterized by zeta potential and hydrodynamic size using dynamic light scattering (DLS). The degree of substitution was determined by conductometric titration and the brush grafting by Fourier transform infrared spectroscopy (FTIR). The hydration and chain conformation of the material was responsive to pH and salt due to the specific anion effects on the hydrophobicity of ion pairs formed with the quaternary ammonium groups. The flocculation efficiency of cationic cellulose nanocrystals (CNC-PDMC) was evaluated in a jar test filled with 1 wt% of bentonite and compared to the flocculation efficiency of four inorganic electrolytes NaCl, KCl, CaCl₂·2H₂O and AlCl₃·6H₂O. The cationic cellulose nanocrystals destabilized the bentonite particles at the dosage 3 mg/g and the flocs fully settled within 5 min with up to 95% efficiency. The flocculation efficiency increased slightly after 24 h of settling. The flocculation efficiency of inorganic electrolytes varied between 17-73% at 5 min settling and increased to 77-99% after 24 h of settling at higher dosage range 3.75-90 mg/g.

5.1. Introduction

As worldwide demand for energy increases, increasing attention is paid to non-conventional fuel resources. However, non-conventional oils extraction, upgrading and export are hard to process. Several technologies have been proposed for the processing of oil sands with varying recovery levels. Open-pit mining technique is used mostly to extract oil sand ore which is a naturally occurring mixture of bitumen, water, sand and clays^{1,2,24-26}. To separate the bitumen, oil sand ore is mixed with hot water and sodium hydroxide to liberate the bitumen and this also releases natural surfactants which aid in the flotation process. After bitumen extraction, the remaining mixture of water, coarse sands, fine clays and residual bitumen (defined as tailings) are discharged and contained in large structures above ground, known as tailings ponds. Upon discharge of tailings, the coarse solids settle rapidly to form beaches along the pond edge, while the fines (silts and clays) settle slowly to form a fine tailings zone that after a few years of consolidation is defined as mature fine tailings (MFT)^{1,164-166}.

The development of the oil sands industry is limited by various environmental issues^{167,168}. The greenhouse gas emission, the usage of clean water, and the accumulation of tailings are the three environmental issues to be addressed. Amongst these challenges, tailings operations present the most significant of all in the oil sands extraction process. Tailings ponds generated environmental and engineering problems which are summarized as follows. First, the production and accumulation of large volumes of fine tailings poses a major environmental concern. Approximately 3.3 m³ of tailings are produced from one barrel of bitumen. Second, the large quantities of water required to extract and process bitumen from the oil sands has become an issue. On average three barrels of fresh water is consumed to produce a barrel of bitumen⁶. Third, the mature fine tailing MFT contains toxic materials, including naphthenic acids, polycyclic aromatic

hydrocarbons, phenolic compounds, ammonia, and other trace metals that pose risks to the environment. The MFT is considered the major reason why the tailing ponds cannot be reclaimed. The high stability of MFT has been attributed to the presence of clay components²³. Since the majority of clays in MFT are negatively charged clays, and the process of oil sands extraction has a pH of 8-9, the electrical charge on each particle produces electrostatic repulsive force that leads to the stabilization of suspension. Beside electrical repulsion, the adsorption of water molecules on the particles surface forms hydration layers that repel each other and prevent settling^{1,169}. In addition, the size of ultrafine clays (<0.3 μm) gives MFT its structure that impedes the consolidation.

The major clay minerals in the oil sands tailings are kaolinite and illite with minor amounts of montmorillonite, chlorite, and mixed-layer of clays¹⁷⁰. Smectite is not present in significant quantity, but the high water holding capacity due to its swelling characteristics is of practical importance¹⁷¹. Bentonite is composed predominantly of a smectite clay minerals. The high-negative zeta potential value of bentonite is due to two reasons: the isomorphous substitution of a small fraction of the tetrahedral Si atoms by Al and/or a fraction of the octahedral atoms (Al or Mg) by atoms of lower oxidation number, and the edge faces show pH-dependent behavior^{172,173}. Under alkaline conditions (pH 9), the octahedral Al-OH and tetrahedral Si-OH groups at the edges are deprotonated.

MFT traps water in the pores of the fine solids¹⁷⁴. Therefore, one of the main objectives of tailings treatments is to increase the settling rate of the clays so that liquid-solid separation can occur in a reasonable time. Another key objective is to recover the maximum volume of water with appropriate quality to be reused in the bitumen extraction process.

In pursuit of increasing the settling rate and the water recovery, paste technology (PT) was introduced^{175,176}. With the assistance of polymeric flocculants, paste technology is used to rapidly thicken the fresh fine oil sands tailings. Although water-soluble synthetic polymers find wide applications as flocculants, their market cost, and their debatable usage influence their development^{177,178}. In this respect, significant efforts have been devoted to prepare biopolymer-based flocculants from natural sources as substitutes for the synthetic flocculants^{175,179}.

Because flocculation performance highly depends on the choice of flocculants, ideal flocculants should be biodegradable as the biodegradability determines their long-term ecological effects. Of all the natural polysaccharides, cellulose accounts for the largest proportion of organic matter on earth^{134,180,181}. The hydrolysis of cellulose using strong acids removes the amorphous regions of cellulose and leaves behind the highly crystalline regions that are less accessible to acid degradation¹⁵⁴. Cellulose nanocrystals demonstrate excellent properties, including high tensile modulus, similar to steel or Kevlar (100 to 160 GPa), low density (0.8 to 1.5 g/cm³) and a large specific surface area (~250 m²/g)¹³²⁻¹³⁴. The high aspect ratio of CNC gives rise to percolation at low concentration which should improve floc formation. In addition, the rigidity of the CNC reduces gelation, preventing entanglement and improving processability^{57,182}. The surface of the rod-shaped nanocrystals are covered with hydroxyl groups and these unique properties provide an ideal platform for surface modification to develop nanocomposite materials with desired surface characteristics customized for a wide range of applications^{180,183}. Since the majority of clays in MFT are negatively charged clays, cationic modification of CNC is of interest²³. Therefore, in this study, we synthesized a highly efficient and environmentally friendly flocculant, where the CNC surface was modified with a cationic monomer (2-methacryloyloxyethyl) trimethyl ammonium chloride (DMC) for use as flocculating agent for the negatively charged oil sand

tailings. The effectiveness of the polymeric flocculants for tailings treatment will be determined by measuring the zeta potential of the sediments, and the turbidity of the supernatant.

5.2. Experimental section

5.2.1. Materials

Cellulose nanocrystals were kindly provided by CelluForce Inc. with an average charge density of 0.26 mmol/g. 4-(Dimethylamino)pyridine (DMAP, 99%), α -bromoisobutyryl bromide (BIBB, 98%), triethylamine (TEA), 2,2'-bipyridyl (Bipy, >99%), ascorbic acid (AsAc, >99%), copper(II) bromide (CuBr_2 , 99%) (2-methacryloyloxyethyl) trimethyl ammonium chloride (DMC), N,N-Dimethylformamide (DMF) HPLC $\geq 99.9\%$, ethanol (EtOH), and isopropyl alcohol (IPA), were purchased from Sigma-Aldrich. The DMC monomer was passed through a neutral aluminium oxide column prior to use.

5.2.2. Synthesis of the brominated CNC macroinitiators (CNC-Br)

The macroinitiators CNC-Br were synthesized by the esterification of CNC with (BIBB) as described previously¹⁸⁴. In detail, CNC (500 mg) was dispersed in DMF (50 mL) by sonication. After the addition of TEA (2.3 mL) and DMAP (1 g), BIBB (3 mL) was added dropwise to the suspension at 0 °C. After 24 h, ethanol was added to terminate the esterification. The resulting CNC-Br was centrifuged with ethanol till a clean supernatant was obtained and then it was washed twice with water. In the end, the CNC-Br was obtained by freeze-drying.

5.2.3. Synthesis of the CNC-PDMC

ARGET-ATRP of DMC was then conducted by grafting from the CNC-Br. CNC-Br was dispersed in a 1:1 isopropyl alcohol : water mixture (50 mL, v/v) in a two-neck flask under a nitrogen

atmosphere for 1 h. Then the DMC monomer (110-440 mg) was introduced. After 20 min, a solution of deoxygenated CuBr_2 (6 mg) and AsAc (90 mg) in 1:1 isopropyl alcohol : water mixture (5 mL,v/v) was then injected into the flask and the content stirred under a nitrogen atmosphere for 20 min followed by the addition of deoxygenated Biby (80 mg). After 24 h at room temperature, the flask was vented to terminate the ARGET-ATRP polymerization. The resulting CNC-PDMC was centrifuged twice with ethanol and water respectively.

5.2.4. Characterization

Fourier transform infrared spectra (FTIR) were conducted to confirm the functional groups of CNC-Br and CNC-PDMC. Freeze-dried samples were homogeneously mixed with KBr powder under a 1:100 weight ratio and pressed into transparent pellets. The measurements were conducted using a Tensor 27 BRUKER machine at a resolution of 4 cm^{-1} , sample scan time of 32 s, and background scan time of 32 s, with the data ranging from 4000 to 500 cm^{-1} .

Transmission electron microscopy (TEM) was conducted on a Philips CM10 at an acceleration voltage of 60 keV. The TEM samples of CNC and CNC-PDMC were prepared from their aqueous dispersion by drop coating onto copper grids and dried at ambient temperature.

Dynamic light scattering (DLS) and zeta potential experiments were conducted using a Malvern Zetasizer Nano series at nanoparticles concentration of 0.05 wt%. Values for zeta potential were determined from the average of 3 measurements, consisting of 12 runs per measurement.

The number of quaternary ammonium groups on the CNC-PDMC was determined using a Metrohm 809 Titrando auto-titrator. In brief, a 50 mL solution was prepared using 50 mg of the solid sample CNC-PDMCs and stirred at $25\text{ }^\circ\text{C}$, 10 mM silver nitrate (AgNO_3) was used as the standard titrant dosing into the sample vial at a rate of 0.05 mL/min. The conductivity as function of the titrant volume added was recorded. The degree of quaternization was determined from

Equation (5.1), where M and V are the molarity (mmol/L) and the volume (L) of the titrant, respectively, and W is the weight of the CNC-PDMC ^{130,131}.

$$[NH_3^+] \left(\frac{mmol}{g} \right) = \frac{M_{AgNO_3} (mM) \times (V_{AgNO_3}) (L)}{W_{CNC-PDMC} (g)} \quad \text{Equation (5.1)}$$

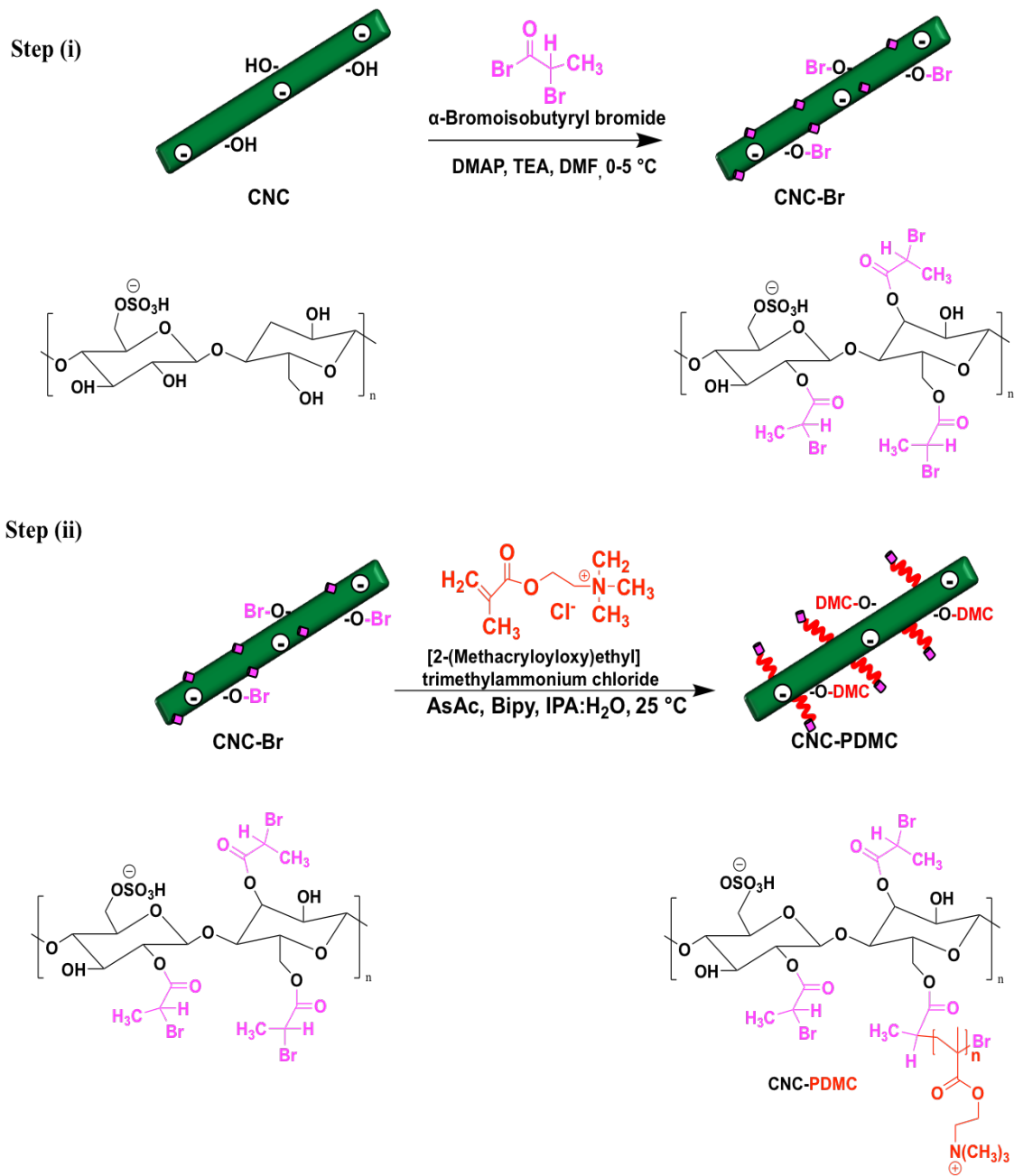
5.2.5. Flocculating characteristics

The flocculation experiment was conducted according to method previously reported in the literature ¹⁸⁵. Simulated waste-water was prepared by dispersing 1 wt% bentonite in Milli-Q water (zeta potential = -30 mV, the average particle size = 650 nm). The original pH value of the bentonite suspension was 9, and it was adjusted using either 0.1 M HCl or 0.1 M NaOH. The flocculation tests of CNC-PDMCs and inorganic salts were conducted in a 20 mL glass vial at room temperature. The waste-water (10 mL) was transferred to vials, and a predetermined dosage of flocculant was added. Rapid agitation was carried out at 380 rpm for 1 min to mix the flocculant with the bentonite suspension. Next, the flocculant solution was then transferred to a 15mL graduated cylinder which was inverted 5 times to conduct the settling tests. After that, the solutions were left for 5 min or 24 h. This period of time represented the settling time. At the end of the settling time, 3 mL of supernatant liquid was withdrawn from a depth of 1 cm and the absorbance of the supernatant liquid was measured in the Varian (Cary 100 Bio) UV-vis spectrometer. The tests were carried out at a wavelength of 500 nm. Subsequently, 3 mL of sediment liquid was removed from a depth of 1 cm and the zeta potential of the sediment was measured in a Malvern Zetasizer Nano. The absorbance of the supernatant liquid, and the zeta potential of sediment of each sample was the average value of 3 test results performed at the same test conditions.

5.3. Results and discussion

5.3.1. Preparation and characterization of CNC-PDMC

The synthesis of the cationic cellulose nanocrystals was carried out according to **Scheme 5.1**. In the first step (i), the CNC surface was modified with BIBB to produce the brominated CNC macroinitiators (CNC-Br). In the second step (ii), a series of polymerization of CNC-PDMC polymers were conducted using the ARGET-ATRP of DMC in isopropyl alcohol:water at room temperature. The quaternary ammonium content of CNC-PDMC was controlled by adjusting the feed ratio of DMC to CNC-Br macroinitiator. FTIR spectroscopy was used to confirm the successful grafting of isobutyryl bromide groups from the surface of CNC as well as the polymerization of DMC. **Figure 5.1** shows FTIR spectra obtained for the unmodified CNC, CNC-Br and CNC-PDMC of two ratios. Beside the characteristic peaks from the stretching vibrations of hydroxyl groups on the CNC at 3400 and 1058 cm^{-1} , the FTIR spectra of CNC-Br, and CNC-PDMC exhibited a new peak appearing at around 1730 cm^{-1} that corresponded to the carbonyl groups of BIBB and the vibrating absorption of ester groups in DMC respectively. In addition, the FTIR spectra of CNC-PDMC possessed two new absorption peaks, at 1480 and 950 cm^{-1} , which were assigned to the methyl groups of the quaternary ammonium groups on the DMC. The appearance of new peaks in the spectra of the CNC-Br, CNC-PDMC indicated that the two steps of the synthesis route were successful.



Scheme 5. 1. Schematic illustration of synthesis procedure of (i) CNC-Br and (ii) CNC-PDMC.

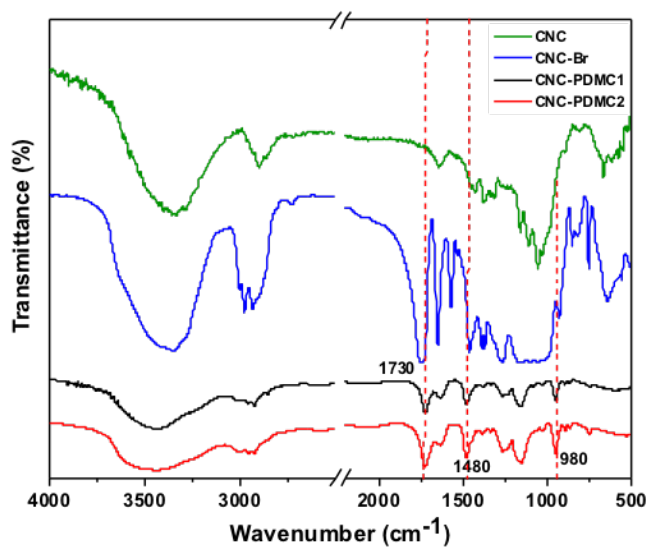


Figure 5. 1. FTIR spectra of CNC, CNC-Br and CNC-PDMC.

The morphology of the CNC-PDMC was characterized by TEM. As shown in **Figure 5.2**, the CNC-PDMC retained the rod-like morphology of the pristine CNC. The successful cationization of CNC-Br was confirmed using zeta potential measurements as shown in **Table 5.1**. The zeta potential of pristine CNC was initially negative with an average zeta potential of -48 mV, whereas CNC-Br was less negatively charged (-13 mV) because some hydrophilic hydroxyl groups (-OH) at the CNC backbone were replaced with relatively hydrophobic halogen-containing ATRP initiation groups as reported in other studies^{186,187}. The zeta potential of CNC-PDMC was reversed to a positive value due to the DMC possessing quaternary ammonium groups with positive charges.

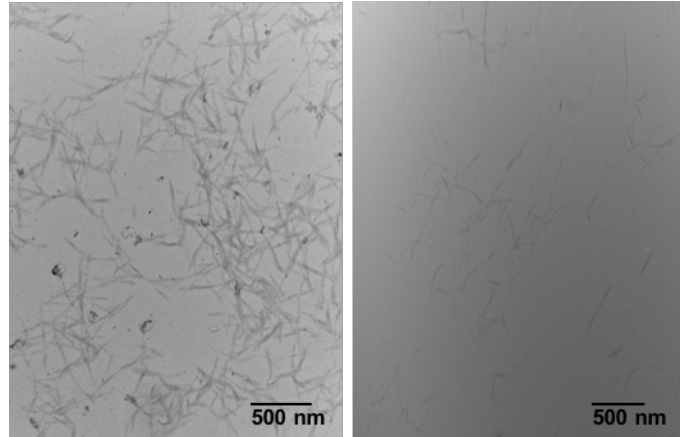


Figure 5. 2. The TEM images of CNC (A) and CNC-PDMC (B).

Table 5. 1. Zeta potential and Z-average of CNC, CNC-Br and CNC-PDMCs.

Sample	Zeta potential (mV)	Diameter (nm)
CNC	-48	200
CNC-Br	-13	1120
CNC-PDMC1 (1:0.5)	+41	643
CNC-PDMC2 (1:1)	+42	644.5
CNC-PDMC3 (1:2)	+43	696.5

The amounts of quaternary amine groups grafted from the CNC-Br were quantified by conductometric titration with AgNO_3 as the titrant. The titration data revealed two stages that were delineated by the inflection point on the conductivity curve as shown in **Figure 5.3**. The first stage shows a sharp linear decrease due to silver cations binding with chloride counterions of quaternary ammonium groups to form silver chloride precipitates. The second stage displayed a sharp increase as a result of the dissociation of silver nitrate to form free silver cations and nitrate anions, which occurred only after the consumption of all the chloride counterions. The point of intersection corresponded to the volume of silver nitrate consumed, which was used to calculate the quaternary amine content of the CNC-PDMCs. The concentration of quaternary ammonium groups was found

to be 3 mmol/g for the ratio (1:0.5), 3.5 mmol/g for the ratio (1:1), and was 4 mmol/g for the ratio (1:2) indicating that the degree of quaternization increased with DMC ratio.

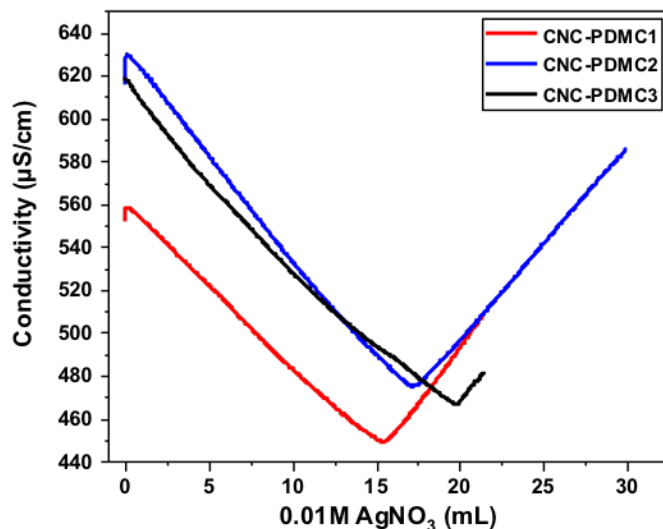


Figure 5. 3. Conductometric titrations of CNC-PDMC at different ratios of DMCs.

5.3.2. The effect of pH on the pH-responsiveness of CNC-PDMCs

The pH-responsive properties of CNC-PDMC were examined by zeta potential and size measurements using the DLS. From **Figure 5.4(A)**, it is evident that the zeta potential of CNC-PDMC brushes exhibited three distinct regimes with increasing pHs. In the first regime, the zeta potential decreased as the pH increased from 2.5 to 4.5 (CNC-PDMC1), 5.5 (CNC-PDMC2), 6.5 (CNC-PDMC3). In the second regime, the zeta potential increased when increasing the pH was increased to 5.5 (CNC-PDMC1), 6.5 (CNC-PDMC2), 8 (CNC-PDMC3). In the third regime, the zeta potential only decreased slightly with increasing pH. The three-regimes in the zeta potential corresponded to the three-stage hydration states of the CNC-PDMC brushes. That is, the hydration of the brushes decreased in the first regime, and then gradually increased in the second regime, and finally decreased in the third regime.

As the pH increased in the first regime, the concentration of (OH⁻) associating with the cationic brushes (DMC) increased. Therefore, the hydroxide anions (OH⁻) formed interchain hydrogen bonds and weakened the interactions between the PDMC brushes and surrounding water molecules resulting in the dehydration of CNC-PDMC. These findings agree with reported studies based on the Manning's counterion condensation theory¹⁸⁸⁻¹⁹⁰. The different grafting ratios of DMC led to different pH responsiveness of the CNC-PDMC. The hydrogen bond formed by hydroxide anions and the carbonyl groups on the DMC was enhanced in the following order; CNC-PDMC3 > CNC-PDMC2 > CNC-PDMC1. However, in the second regime, the zeta potential increased for the CNC-PDMC which indicated that the brushes were hydrated. The hydration of the brushes was caused by the further protonation of the CNC-PDMC as the adsorbed PDMC brushes were released from the CNC surface. Several studies have reported the effect of salt addition on the stability of CNC, where a gradual reduction in the zeta potential with increasing salt concentration was reported due to the electrostatic screening effect^{159,160}. Consequently, the observed reduction in the zeta potential in the third regime could be attributed to the dehydration of the released brushes with increasing pH resulting in more interchain hydrogen bonds between the bound hydroxide and carbonyl groups on the PDMC brushes.

The change in the size was examined at different pH as shown in **Figure 5.4(B)**. The size gradually decreased as the pH was increased suggesting the collapse of the PDMC brushes triggered by dehydration of the polymer chains. Since the dehydration of the PDMC brushes was dominant over the swelling of the adsorbed PDMC brushes from the CNC surfaces, negligible increase in the size was observed with increasing the pH. The proposed mechanism of the conformational change of CNC-PDMC brushes induced by the pH change is illustrated in **Scheme 5.2**.

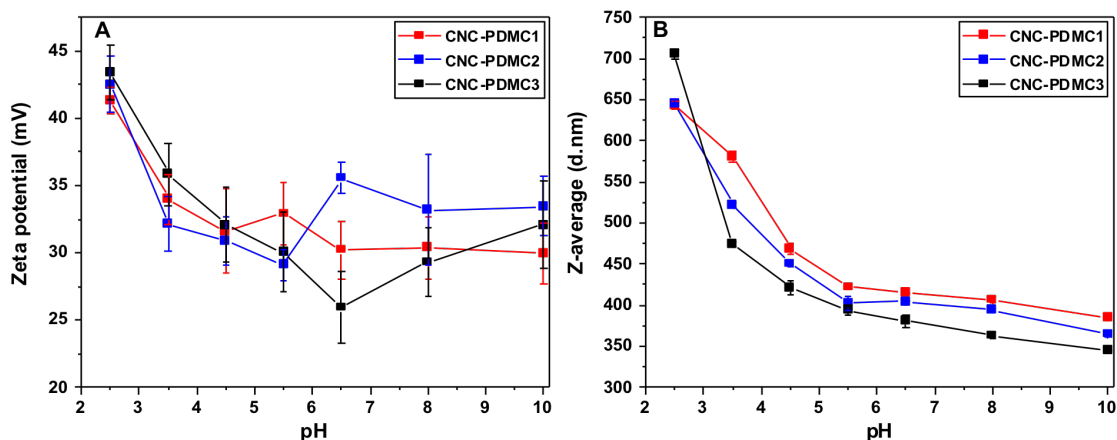
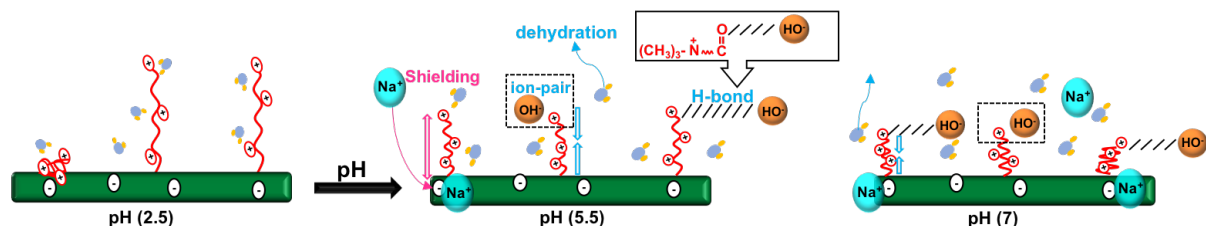


Figure 5. 4. Effect of pH on the zeta potential (A) and the size (B) of CNC-PDMC brushes.



Scheme 5. 2. Schematic illustration of the conformational change of CNC-PDMC1 brushes induced by change in the pH.

5.3.3. The effect of salt on the stability of the CNC-PDMC

The effect of salt on the stability of CNC-PDMC was examined using NaCl as shown in **Figure 5.5**. As the salt concentration was increased, the CNC-PDMC brushes also exhibited a three-regime change. However, the extent of dehydration (first regime), the hydration (second regime) and dehydration of the released PDMC brushes (third regime) after the introduction of Cl^- ions was much higher compared to the OH^- effect. To understand these findings, specific anion effects on the hydrophobicity of the ion pairs was considered. The Cl^- is a strong chaotropic anion and OH^- is a relatively strong chaotropic anion as located in the Hofmeister series¹⁶¹. As a result, the electrostatic interactions between Cl^- and the quaternary ammonium groups are sufficiently strong

to remove their ionic hydration shells to form a contact ion pair as reported in other study ¹⁶². **Figure 5.5(A)** shows the reduction in the zeta potential as a result of the dehydration of CNC-PDMC brushes in the presence of Cl⁻ in the first regime. Such a strong dehydration is associated with the collapse of the brushes, as indicated by the sharp reduction in the size (**Figure 5.5(B)**). In the second regime, the hydration of the CNC-PDMC was observed as the zeta potential increased sharply. These findings indicated that more PDMC brushes were released from the CNC surface due to the strong ion pair interactions of the Cl⁻ ions allowing more Na⁺ ions to penetrate and screened the negative charge on the CNC surface. The size measurement confirmed this phenomenon as shown in **Figure 5.5(B)**. The size increase for the CNC-PDMC1 was due to the hydration and swelling of the released PDMC. Consequently, the released DMC brushes were prone to dehydration as the salt concentration increased and more ion pairs were formed as indicated by the reduction in the zeta potential and size. The TEM also confirmed the collapse of the chain conformation in the presence of high salt concentration as shown in **Figure 5.6(C)**. In conclusion, a more chaotropic counterion Cl⁻ would induce the collapse of the chains and the dehydration of PDMC brushes caused by the stronger hydrophobic interactions between the ion pairs. These findings are in agreement with other studies conducted on the same cationic monomer in the presence of chloride ions ^{162,188}. The proposed mechanism on the influence of salt concentration on the conformational change of CNC-PDMC brushes is illustrated in **Scheme 5.3**.

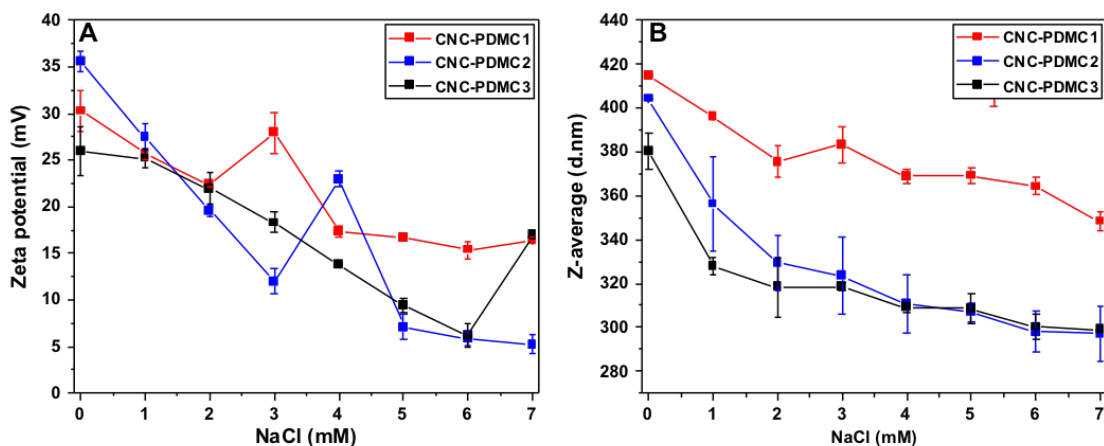


Figure 5.5. Effect of salt on the zeta potential (A) and the size (B) of CNC-PDMS brushes.

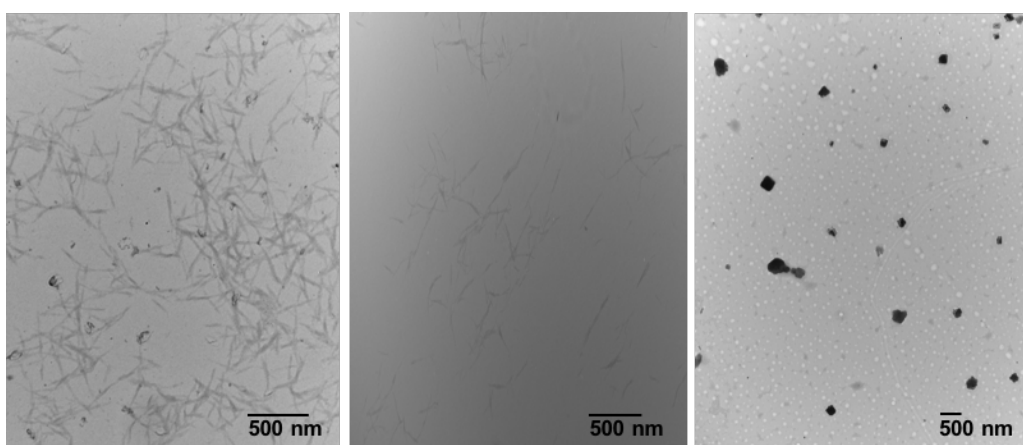
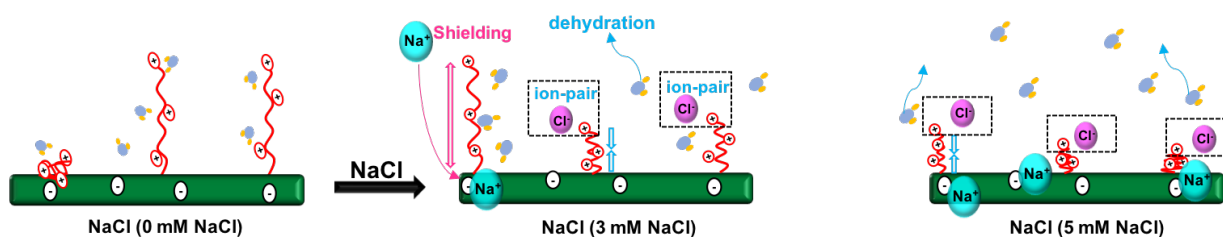


Figure 5.6. The TEM images of CNC (A), CNC-PDMS (B) and CNC-PDMS1 with 6 mM of NaCl (C).



Scheme 5.3. Schematic illustration of the possible influence of salt concentration on the conformational change of CNC-PDMS1 brushes.

5.3.4. The effect of dosage on the flocculation of bentonite clay

The maximum of the turbidity removal efficiency of bentonite clay after 5 min settling for CNC-PDMC1, CNC-PDMC2 and CNC-PDMC3 was 95%, 96% and 97% at optimum dosage of 3.75 mg/g, 3mg/g and 3 mg/g respectively (**Figure 5.7(A)**). After 24 h of settling, the turbidity removal efficiency slightly increased at the same optimum dosages. On the other hand, the flocculation efficiency increased significantly by about 50-60 % at low dosage (< 3 mg/g) after 24 h settling as shown in **Figure 5.7(B)**. The optimum flocculation performance for the three flocculants after 24 h settling was as follows: CNC-PDMC1 > CNC-PDMC2 > CNC-PDMC3. The trend was inversely proportional to the content of quaternary ammonium groups on the copolymers. Excessive CNC-PDMCs re-stabilized the suspended bentonite particles; however, the turbidity removal efficiency exhibited a very slight reduction.

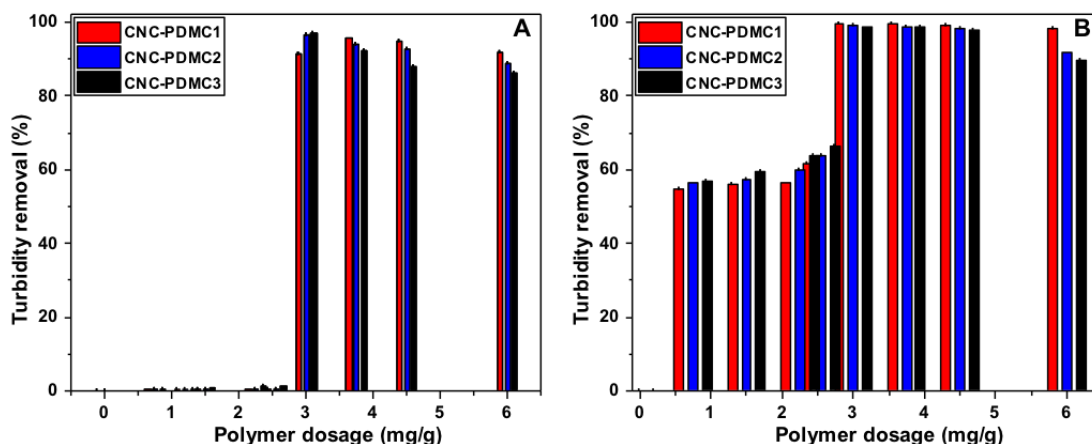


Figure 5. 7. Effect of flocculant category on the turbidity removal of bentonite as a function of flocculant dosage at different settling time 5 min (A) and 24 h (B).

5.3.5. The effect of dosage on the zeta potential

Adsorption bridging and charge neutralization are the main mechanism in the flocculation process. The zeta potential of the flocculating system provides direct information on the charge neutralization effect of the flocculant ¹⁹¹. The zeta potentials after the flocculation process using CNC-PDMC were increased as the dosage was increased (**Figure 5.8**). This phenomenon indicated that charge neutralization played an important role in the flocculation process. At the same dosage, the zeta potential of bentonite particles flocculated by CNC-PDMC3 was always higher than that of CNC-PDMC2 and CNC-PDMC1, as CNC-PDMC3 possessed a greater charge density than the other two flocculants. Isoelectric dosage (IED) is the dosage at which the charge reversal occurs ¹⁹², and the IEDs for CNC-PDMC1, CNC-PDMC2 and CNC-PDMC3 were 4.5, 3, and 3 mg/L with different turbidity removal efficiency. Thus, the charge neutralization capability has the following order: CNC-PDMC3 > CNC-PDMC2 > CNC-PDMC1.

After 5 min settling, the zeta potential for samples treated with CNC-PDMC2 and CNC-PDMC3 at optimal dosages (maximum turbidity removal) were higher than the isoelectric point (0 mV), indicating that charge neutralization significantly contributed to the flocculation mechanism (**Figure 5.8(A)**). On the other hand, the zeta potential for samples treated with CNC-PDMC1 was below the isoelectric point indicating that charge neutralization played a less important role. With the increase in settling time (after 24 h), the zeta potential of the flocculated systems at the optimum dosage did not change significantly as shown in **Figure 5.8(B)**. The increase in the removal efficiency after 24 h of settling implied that the bentonite was flocculated first by charge neutralization followed by bridging.

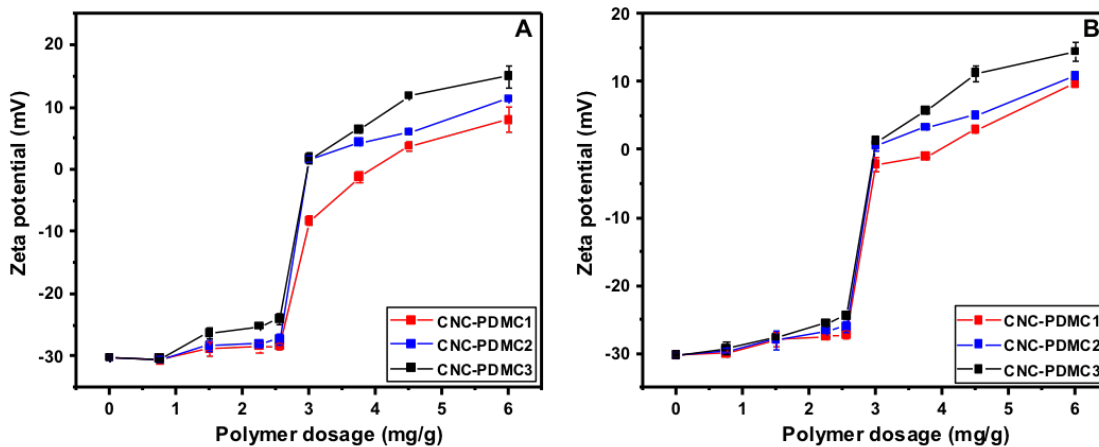


Figure 5. 8. Effect of flocculant category on the zeta potential of bentonite as a function of flocculant dosage at different settling time 5 min (A) and 24 h (B).

5.3.6. Proposed mechanisms

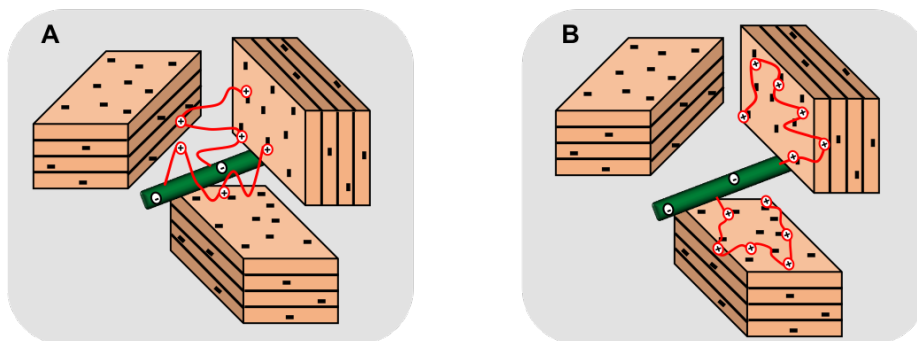
The results of the flocculation studies using the CNC-PDMCs suggest that the adsorption of a cationic copolymer is rapid at the initial stages of the treatment, thereafter it became slower as reported for the kinetics of cationic starch adsorption in kaolin suspension¹⁹³. Therefore, at the short settling time (5 min), the charge neutralization occurred first, followed by bridging. CNC-PDMC chains are absorbed on the bentonite surface via electrostatic interactions between the negatively charged silanol groups and positively charged quaternary ammonium groups. Additionally, hydrogen bonding interactions between the silanol and aluminol OH groups on the bentonite surface and ester functional groups on PDMC chains produced large floc structures. The charge repulsion generated by cellulose nanocrystals resulted in the extension of the polymer chain, which promoted the polymer bridging between the bentonite clay particles.

At low dosage (< 3 mg/g) of the CNC-PDMCs, the coverage of the bentonite particles with CNC-PDMCs was low because of the low amounts of adsorbed flocculants as reflected by the high

negative zeta potential. Under these conditions, the conformation of the adsorbed chains may evolve toward a flat conformation and the flocculation was not efficient as the turbidity removal was less than 2%. After 24 h settling, the zeta potential remained at the same level; however, the flocculation efficiency increased sharply 50-60%. This was thought to be due to the collision caused by the interactions between the particles due to the Brownian motion that facilitated the polymer bridging.

At the optimum dosage of 5 min settling, the surface coverage increased with increasing initial flocculant concentration. Under these conditions the electrostatic attraction between the positively charged CNC-PDMC chains and negatively charged bentonite surface is expected to increase; therefore, the flocculation efficiency increased beyond 95% as shown in **Figure 5.7(A)**. After 24 h of settling, the zeta potential remained at the same level; however, the flocculation efficiency increased by 3-4% indicating that the polymer bridging had occurred. In addition, the flocculation systems comprising of CNC-PDMC3 and CNC-PDMC2 with higher charge density showed lower flocculation performance after 24 h at the optimum dosage whereas the CNC-PDMC1 with the lowest charge density was more effective. These findings could be explained based on the electrostatic attraction between the positively charged CNC-PDMC chains and negatively charged bentonite surface. Because the electrostatic attraction between the positively charged CNC-PDMC chains and negatively charged bentonite surface increased with surface charge, hence the number of attachment points (quaternary ammonium groups) between the CNC-PDMC chains and bentonite surface were higher for case (B) (CNC-PDMC2,3) than case (A) (CNC-PDMC1) (**Scheme 5.4**). Therefore, bridging was diminished as the adsorption rate increased, because the surface sites available for bridging were reduced. As a result, the polymer bridging in case (A) was

more efficient than in case (B). The flocculation with the CNC-PDMC1 likely involved multiple adsorption points, and stronger polymer bridging.



Scheme 5. 4. The effect of cationic charge on the adsorption and bridging mechanism for bentonite (A) Low charge density, (B) High-charge density.

5.3.7. The effect of different electrolytes on the zeta potential of bentonite clays

The effects of various inorganic electrolytes with mono-, di-, and tri-valent cations on the zeta potential of bentonite clay were examined. Zeta potential variations according to each electrolyte concentration are shown in **Figure 5.9**, where the zeta potential curves followed a similar trend at different settling times (5 min (A), 24 h (B)). The only electrolyte that could transform the negatively charged surface bentonite into a positively charged surface was $\text{AlCl}_3 \cdot 6\text{H}_2\text{O}$ (+3.4 mV). The trend of the increasing zeta potential with increasing in the electrolyte concentration was similar as in the presence of mono-valent cations (K^+ , Na^+) (-22, -23 mV), and the zeta potential was higher with di-valent cation ($\text{Ca}^{2+} = -9.3$ mV) at the optimum dosage. This behavior is consistent with the classical theory developed by Derjaguin, Landau, Verwey and Overbeek (DLVO). According to the DLVO theory, the electrostatic repulsion can be overcome by the addition of salt to screen the electrostatic repulsion, which lowers the energy barrier against aggregation¹⁹⁴. Considering that the particle interactions are affected by the valence of the ion, one major aspect of the DLVO theory described by the Schulze–Hardy rule on the dependence of

the critical coagulation concentration (CCC) on valence of electrolytes. The destabilizing power of the electrolyte according to the Schulze-Hardy rule follows a mathematical relationship shown in **Equation (5.2)**, where z is the valence of the counter ion ^{195,196}.

$$CCC = \frac{\text{Constant}}{z^6} \quad \text{Equation (5.2)}$$

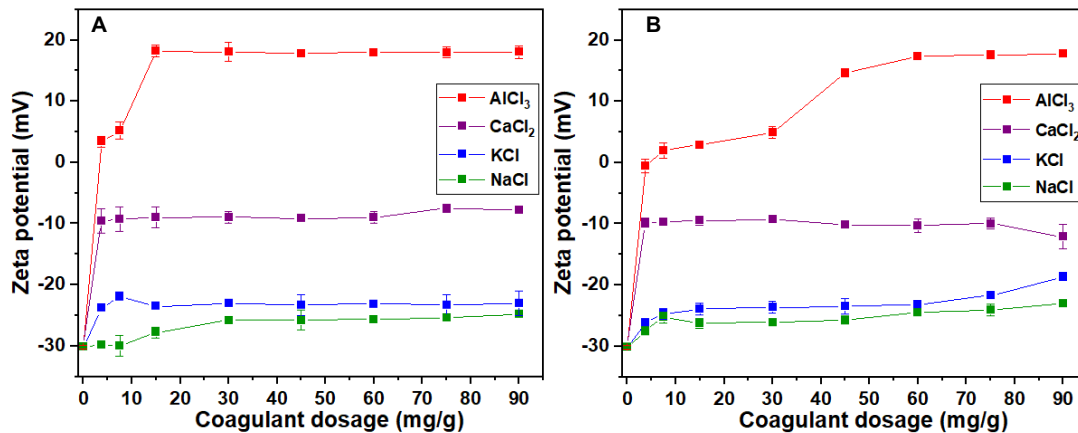


Figure 5. 9. Effect of ionic strength type on the zeta potential of bentonite as a function of dosage at different settling time 5 min (A) and 24 h (B).

5.3.8. The effect of different electrolytes on the turbidity removal efficiency

The turbidity removal efficiencies of inorganic electrolytes for treating the bentonite clays was evaluated under different doses and settling times. It can be seen from **Figure 5.10** that the flocculation efficiency increased with increasing electrolytes concentrations until the optimum dosage, which then decreased slightly as the concentrations continuously increased due to the re-stabilization. After 5 min settling, the maximum turbidity removal efficiency for Al³⁺, Ca²⁺, K⁺ and Na⁺ was 73%, 17%, 38% and 27% at optimum dosage of 3.75 mg/g, 7.5 mg/g, 7.5 mg/g and 90 mg/g respectively as shown in **Figure 5.10(A)**. The turbidity removal performance of the inorganic electrolytes varied according to the following order: AlCl₃ > KCl > NaCl > CaCl₂. After

24 h settling, the turbidity removal efficiency increased significantly and approached about 99.6%, 99.8%, 99.8% and 77% for Al^{3+} , Ca^{2+} , K^+ and Na^+ , at the dosage of 3.75 mg/g, 7.5 mg/g, 90 mg/g and 90 mg/g respectively as shown in **Figure 5.10(B)**. The turbidity removal efficiency followed the following order: $\text{AlCl}_3 > \text{CaCl}_2 > \text{KCl} > \text{NaCl}$.

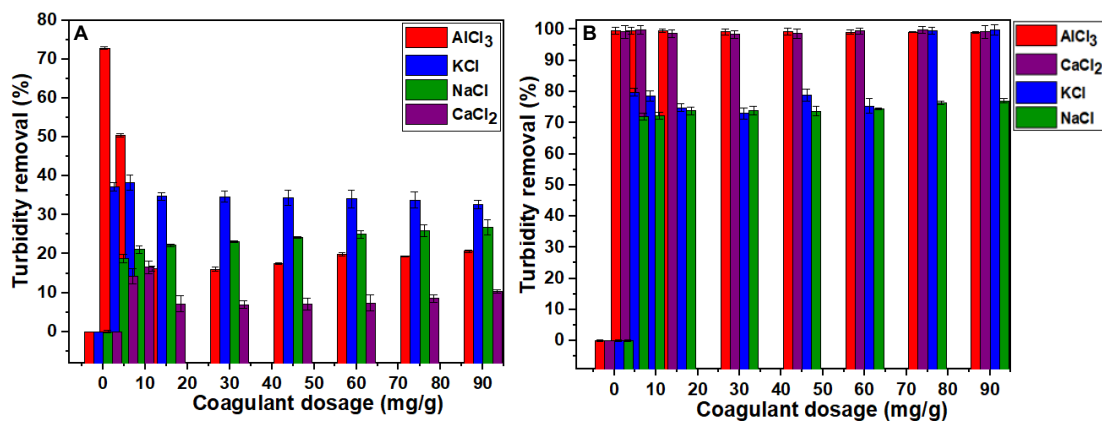


Figure 5. 10. Effect of ionic strength type on the turbidity removal of bentonite as a function of dosage at different settling time 5 min (A) and 24 h (B).

5.3.9. Proposed mechanism

After 24 h settling, a reduction in the optimum dosage with ionic valence was observed which is in accordance with the Schulze–Hardy rule¹⁹⁷. Therefore, ions of higher valences Al^{3+} and Ca^{2+} are more effective in destabilizing bentonite clays compared to ions of lower valences K^+ and Na^+ . On the other hand, the same inorganic electrolytes resulted in different flocculation efficiency after 5 min settling except Al^{3+} . Such a deviation from the DLVO theory was explained by the influence exerted by ions on the neighboring water molecules (Hofmeister effects)¹⁹⁸. Several studies have investigated the aggregation of colloidal particles influenced by electrolyte concentration, ionic valence, water-withdrawing power of ions and pH¹⁹⁶. However, the DLVO theory considers only the valence and the concentration of the counter ions in solution. Moreover, the DLVO theory predicts equal CCC for the same particles dispersed in different monovalent salt solutions^{198,199}.

However, large number of experimental literature data shows that the CCC values determined for the same-valent ions in various aggregation studies differed significantly ¹⁹⁶. In the Hofmeister series, ions have been classified based on their ability to interact with water molecules into two main groups: (i) chaotropes having the ability to disrupt hydrogen-bonding networks between water molecules and (ii) kosmotropes having the ability to create water-molecule patterns ^{200–202}. Based on the hydration effect of the cations, they obeyed to the following trend: $(\text{CH}_3)_3\text{N}^+ < \text{NH}_4^+ < \text{K}^+ < \text{Na}^+ < \text{Li}^+ < \text{Mg}^{2+} < \text{Ca}^{2+} < \text{Al}^{3+}$. Therefore, K^+ ions had the lowest CCC and the highest flocculation efficiency being the less hydrated cation compared to Na^+ and Ca^{2+} . Ions of higher valence, such as Al^{3+} follow the Schulze–Hardy rule, and the same observation was reported for the aggregation of clay ¹⁹⁶.

5.3.10. Comparison between the flocculation behavior of CNC-PDMC and inorganic electrolytes

The flocculating activities of CNC-based flocculants and inorganic electrolytes against bentonite particles (1 wt%, pH= 9) were performed under two conditions: 5 min and 24 h of settling. In both experiments, the flocculation efficiency was examined and compared in terms of changes in the turbidity and zeta potential at their optimum dosages as shown in **Table 5.2**. Overall, the different flocculation efficiency among the CNC-based flocculants and the inorganic electrolytes evaluated in this study is attributed to two factors: the structural characteristics, the size and ion specific hydration. The CNC-based flocculants possess different grafted chain lengths, depending on the DMC ratio to CNC over the grafting polymerization. The prepared CNC-PDMCs have branched pendent chains bearing a number of quaternary ammonium groups. The cationic brushes and rigid core of CNC could generate more robust flocs after the primary particles of

bentonite were flocculated within 5 min of settling; therefore, no significant increase in the flocculation efficiency was observed after 24 h of settling. In addition, the nanometric dimension of the CNC-PDMC, promotes a greater surface area of contact with the bentonite particles. The flocculation mechanism of CNC-based flocculants is mainly driven by charge neutralization between the anionic-charge bentonite and cationic PDMC chains grafted on CNC. Moreover, the cationic PDMC chains could promote the bridging where these chains would extend beyond the thickness of the electric double layer and adsorb onto bentonite particles to produce flocs.

For inorganic electrolytes, the electrostatic patch coagulation is the dominant mechanism for inducing the aggregation of bentonite particles. The metal cations could compress the double layer of bentonite particles, weaken the repulsive force and reduces the distance between the particles that lowers the energy barrier for aggregation and accelerates the precipitation process.

For the second factor affecting the flocculation mechanism, the Hofmeister series describes the effect of the hydration of cations on their interactions. As discussed earlier, the Hofmeister series rationalizes the observed dependencies of the critical coagulation concentration (CCC) on the size and hydration of ions. From the results obtained in the present study, the flocculation efficiency of the flocculants followed the following order: CNC-PDMC ($((\text{CH}_3)_3\text{N}^{+-})$) > Al^{3+} > K^+ > Na^+ > Ca^{2+} . The quaternary ammonium groups in CNC-PDMC led to the lowest CCC and the maximum reduction in the turbidity. This phenomenon could be elucidated on the basis of the hydration size of the cations. The poorly hydrated quaternary ammonium groups ($((\text{CH}_3)_3\text{N}^{+-})$) on the CNC-PDMC chains adsorb strongly to the bentonite surface, thereby reducing the surface charge, and the CCC. The Ca^{2+} (a highly hydrated cation) used in the study yielded a low flocculation efficiency compared to the mono-valent cations K^+ , Na^+ . However, after 24 h settling the flocculation

efficiency of the flocculants follows the trend: CNC-PDMC ((CH₃)₃N⁺-) > Al³⁺ > Ca²⁺ > K⁺ > Na⁺ with the CNC-PDMC being the most efficient one, which obeys the DLVO theory.

Table 5. 2. Comparison between the flocculation efficiency of CNC-PDMCs and inorganic salts used in the study at their optimum dosages.

Settling time	5 min			24 h		
Sample	Optimum dosage (mg/g)	Zeta potential (mV)	Turbidity removal (%)	Optimum dosage (mg/g)	Zeta potential (mV)	Turbidity removal (%)
CNC-PDMC1	3.75	-1.13±0.8	95.4	3.75	-1.03±0.05	99.6
CNC-PDMC2	3	1.6±0.5	96.6	3	0.67±0.9	99.2
CNC-PDMC3	3	1.8±0.9	97	3	1.34±0.17	98.7
AlCl ₃	3.75	3.38±0.9	72.8	3.75	-0.6±0.15	99.6
CaCl ₂	7.5	-9.3±2	16.6	7.5	-9.7±0.2	99.8
KCl	7.5	-21.8±0.6	38.3	90	-18.6±0.6	99.8
NaCl	90	-23±0.6	27	90	-23±0	77

5.4. Conclusions

The conclusion from this study can be summarized as follows:

1. The hydration and conformation of the CNC-PDMC are sensitive to both salt and pH.
2. The extent of the sensitivity of CNC-PDMC to the Cl⁻ is much higher than the increase in the pH due the higher hydrophobicity of the ion-pair formed between the chloride ions and the quaternary ammonium groups compared to ion-pair formed by hydroxyl groups.
3. The flocculation behavior of bentonite particles after 5 min settling agrees with the Hofmeister series based on the hydration of cations.
4. The flocculation behavior of bentonite particles after 24 h settling follows the classical DLVO theory based on the valence of cations.
5. CNC-PDMC flocculants had the advantages of low dosage amount with the highest flocculation efficiency up to 95% within 5 min of settling compared to inorganic electrolytes.

Chapter 6. Evaluation of Cationic Biopolymer-Based Flocculants on Bentonite Removal: Effect of Cationic Charge Distribution

Abstract

Three cationic polyelectrolytes grafted bio-polymers were prepared. In the first two systems, the surface of cellulose nanocrystals (CNCs) and cellulose nanofibers (CNFs) were physically modified with poly(diallyldimethylammonium chloride) (PDADMAC). The obtained PDADMAC-CNC and PDADMAC-CNF have a flat-cationic layer structure. In the third system, the CNCs surface was chemically modified by grafting [2 (methacryloyloxy)ethyl] trimethylammonium chloride (DMC) from the surface using Activators ReGenerated by Electron Transfer (ARGET-ATRP). The obtained CNC-PDMC has a branched-cationic structure. The three systems were added at varying dosages to a colloidal bentonite to quantify the effect of the cationic charge distribution on their flocculation efficiency. The CNC-PDMC was found to be the most effective with 99% of the bentonite removal at concentrations as low as 3.5 mg/g. These results indicated that the concentrated distribution of cationic units on the branches (PDMC) extended from the CNC surface facilitated the interaction with bentonite particles. On the other hand, the flat conformation of cationic PDADMAC chains on the CNCs and CNFs limited their ability to bind and flocculate the bentonite particles.

6.1. Introduction

Coagulation/ flocculation is an important separation process applied in the primary purification of industrial wastewater to remove the suspended colloidal particles and various dissolved contaminants. Coagulation refers to the destabilization process of a colloidal suspension to neutralize the surface charge to form large particles called submicroscopic flocs by adding inorganic multivalent cations or low molecular weight cationic polyelectrolytes known as coagulants or primary coagulants respectively ^{10,203}. The destabilization process using inorganic coagulants (primary coagulants) is known as adsorption-charge neutralization, while the destabilization process using polyelectrolytes is known as electrostatic patch. Flocculation is defined as the formation of macroscopic flocs of suspended particles through the adsorption of high molecular weight polymeric flocculants onto a number of colloidal particles bridging the distances between the particles. During the bridging flocculation, long-chain segments of polymeric flocculants are initially adsorbed onto one or more particles with the loops and tails extending in the solution that overcome the energy barrier of agglomeration, allowing the possibility of dangling polymer segments binding to other particles to form macroscopic flocs ^{11,12}. The conventional coagulation/ flocculation process, using inorganic polyelectrolytes, such as polyaluminium chloride (PAC), and polyacrylamide fails to align with the increasing demand for environmentally friendly reagents and technologies. The structure of these substances is resistant to biodegradation ¹³⁻¹⁶, and their degraded products are considered to be hazardous due to the release of monomers that could enter the food chain and may cause health problems ¹⁷. Many reports addressed the concerns about the potential of adverse health effects on their exposure to waste-water, which has been linked to renal failure, tremors and nervous system disorders ²⁰⁴. Therefore, the search has shifted to a better alternative with the goal of minimizing the

detrimental health, and environmental effects associated with the use of such substances. Natural bio-flocculants have emerged as promising alternative materials to replace synthetic flocculants. Natural organic flocculants, based on polysaccharides have been extensively explored because they are safe, biodegradable, readily available from agricultural resources and produce no secondary pollution ¹³. In addition, since they are biodegradable, the sludge formed can be degraded by microorganisms ^{18,19}. However, natural bio-flocculants have low efficiencies and thus higher dosages are needed ²⁰. Thus, modified flocculants have emerged as a new class of polymers that offer tremendous potential in treating waste-water due to superior performance compared to original components (synthetic polymeric flocculants and natural bio-flocculants) ¹³. The modification of polysaccharides has been explored as a strategy in combining their best properties with those of synthetic polymers to enhance the aggregating capacity of the modified flocculants ^{13,21,22,205}. In many studies, cationic polyelectrolytes have been highlighted as effective coagulants or flocculants since most natural colloid particles are negatively charged. Poly(diallyldimethylammonium chloride) (PDADMAC) is a cationic polymer that can be obtained in different MW ranges to facilitate the flocculation process ^{10,206-208}. It was observed that using low molecular weight PDADMAC can enhance the flocculation of lignosulfonate of neutral sulfite semi-chemical (NSSC) pulping process more than the PDADMAC with high molecular weight ²⁰⁹. PDADMAC was also assessed for the harvesting of microalgae and compared to chitosan and cationic polyacrylamide (Superfloc 496). It was found that PDADMAC is the most effective in harvesting 90% of the algae at lower dosage (5mg/L) within one hour ²⁰⁶. Another cationic polyelectrolyte that has been utilized as a flocculant and antimicrobial agent is poly(2-methacryloxyethyl trimethylammonium chloride) (PDMC) or known as (PMETAC) ^{210,211}. The primary factors affecting the flocculation mechanism and efficiency of biopolymers with

polyelectrolytes are structure (linear, branched), charge density, molecular weight, and dosage. The biopolymers can be modified physically or chemically. The physical modification process includes the blending of two or more types of the polymer to obtain the requisite properties. On the other hand, chemical modification includes polymer grafting where the monomer is covalently grafted to the polymeric substrate. This study aims to evaluate the flocculation efficiency of three modified natural polymers with different structures as an alternative technology to remove clays from wastewater. First, cationization of the surface of cellulose nanocrystals (CNCs) and cellulose nanofibers (CNFs) with PDADMAC using the physical modification to obtain cationic biopolymers-based flocculant. Second, cationization of the surface of cellulose nanocrystals with DMC using chemical modification (ARGET-ATRP). The first two systems PDADMAC-coated-CNCs and PDADMAC-coated-CNFs have a coated and flat-cationic layer while the third system CNC-PDMC has a branched-cationic structure. The objective of this study is to examine the effect of cationic charge distribution on the biopolymers on their flocculation efficiency. The effectiveness of the polymeric flocculants for bentonite removal will be determined by measuring the zeta potential of the sediments, and the turbidity of the supernatant and the flocs size.

6.2. Experimental section

6.2.1. Materials

Cellulose nanocrystals were kindly provided by CelluForce Inc., and cellulose nanofibrils (CNFs) were purchased from the Process Development Center (University of Maine). Poly(diallyldimethylammonium chloride) (PDADMAC) (20 wt % solution in water; MW = 100,000–20,000 g.mol⁻¹) was purchased from Sigma-Aldrich. 4-(dimethylamino)pyridine (DMAP, 99%), α -bromisobutyryl bromide (BIBB, 98%), triethylamine (TEA), 2,2'-bipyridyl (Bipy, >99%), ascorbic acid (AsAc, >99%), copper(II) bromide (CuBr₂, 99%) (2-methacryloyloxyethyl) trimethyl ammonium chloride (DMC), N,N-dimethylformamide (DMF) HPLC \geq 99.9%, ethanol (EtOH), and isopropyl alcohol (IPA), were purchased from Sigma-Aldrich. Prior to use, the DMC monomer was activated by passing it through a column of neutral aluminium oxide.

6.2.2. Preparation of the PDADMAC-coated CNCs (CNC-PDADMAC)

A method reported recently allows the synthesis of PDADMAC-Coated CNCs²¹². In brief, 2 mL of PDADMAC solution (20 wt % in water) was added to the CNC suspension (200 mL, 0.1wt %) under sonication. The sonication was continued for 1 h followed by stirring for 3h at room temperature and purification by dialysis and repeated ultrafiltration.

6.2.3. Preparation of the PDADMAC-coated CNFs (CNF-PDADMAC)

The same method used for PDADMAC-Coated CNCs except that CNCs was replaced with CNFs.

6.2.4. Synthesis of the brominated CNC macroinitiators (CNC-Br)

The macroinitiators CNC-Br were synthesized by the esterification of CNC with BIBB as described previously¹⁸⁴. In detail, CNC (500 mg) was dispersed in DMF (50 mL) by sonication. After the addition of TEA (2.3 mL) and DMAP (1 g), BIBB (3 mL) was added dropwise to the suspension at 0 °C. After 24 h, ethanol was added to terminate the esterification. The resulting CNC-Br was centrifuged with ethanol until a clean supernatant was obtained and then twice with water. In the end, the CNC-Br was obtained by freeze-drying.

6.2.5. Synthesis of the CNC-PDMC

ARGET-ATRP of DMC was conducted from the CNC-Br. CNC-Br was dispersed in a 1:1 isopropyl alcohol : water mixture (50 mL, v/v) in a two-neck flask under a nitrogen atmosphere for 1 h. Then the DMC monomer (110 mg) was then introduced. After 20 min a solution of deoxygenated CuBr₂ (6 mg) and AsAc (90 mg) in 1:1 isopropyl alcohol: water mixture (5 mL, v/v) was syringed into the flask and the content stirred under a nitrogen atmosphere for 20 min followed by adding a deoxygenated Biby (80 mg). After 24 h at room temperature, the flask was vented to the atmosphere to terminate the ARGET-ATRP process. The resulting CNC-PDMC was centrifuged twice with ethanol and twice with water.

6.2.6. Characterization

Fourier transform infrared spectra (FTIR) were recorded to confirm the functional groups of the prepared material. Freeze-dried samples were homogeneously mixed with KBr powder at a 1:100 weight ratio and pressed into transparent pellets. The measurements were conducted using a Tensor 27 BRUKER machine at a resolution of 4 cm⁻¹, sample scan time of 32 s, and background scan time of 32 s, with the data ranging from 4000 to 500 cm⁻¹.

Transmission electron microscopy (TEM) was conducted on a Philips CM10 microscope at an acceleration voltage of 60 keV. The TEM samples were prepared from their aqueous dispersion by drop coating onto copper grids and dried at ambient temperature.

Dynamic light scattering (DLS) and zeta potential experiments were conducted using a Malvern Zetasizer Nano series at nanoparticles concentration of 0.05 wt%. Values for zeta potential were determined from the average of 3 measurements, consisting of 12 runs per measurement.

6.2.7. Flocculating characteristics

The flocculation experiment was conducted according to a method previously reported in the literature.¹⁸⁵ Simulated waste-water was prepared by dispersing 1 wt% bentonite in Milli-Q water (zeta potential = -30 mV, the average particle size = 650 nm). The original pH value of the bentonite suspension was 9, and it was adjusted using 0.1 M HCl or 0.1 M NaOH, as needed. The flocculation performance tests of the three materials PDADMAC-CNC, PDADMAC-CNF, and CNC-PDMC were carried out in a 20 mL glass vials at room temperature. The wastewater (10 mL) was transferred to the vials, and a predetermined dosage of flocculant was added to the system. Rapid agitation was conducted at 380 rpm for 1 min to mix the flocculant with the wastewater. Next, the flocculant solution was then transferred to a 15 mL graduated cylinder which was inverted 5 times to perform the settling tests. After that, the solutions were left for 24 h, and the settling time was measured. At the end of the settling time, 3 mL of the supernatant liquid was withdrawn from a depth of 1 cm and the absorbance of the supernatant liquid was measured using a Varian (Cary 100 Bio) UV-vis spectrometer. The tests were carried out at a 500 nm wavelength. Subsequently, 3 mL of sediment liquid was withdrawn from a depth of 1 cm and the zeta potentials of the sediment was measured with a Malvern Zetasizer Nano. The absorbance of the supernatant

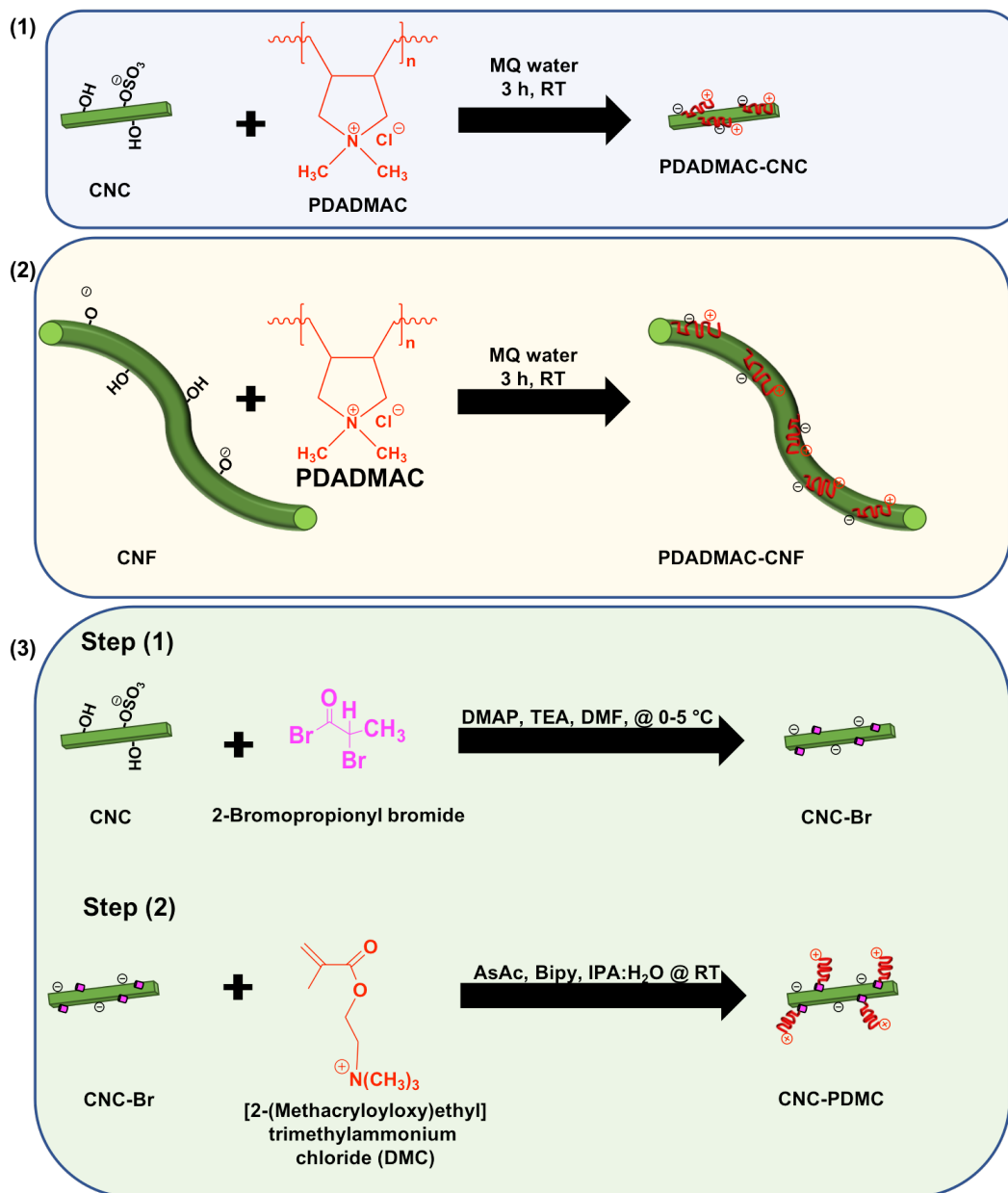
liquid, and the zeta potential of sediment of each sample was the average value of 3 test results under the same test conditions.

6.3. Results and discussion

6.3.1. Preparation and characterization of the CNC-PDMC, PDADMAC-CNC, and PDADMAC-CNF

The formation of the cationic cellulose nanocrystals and cellulose nanofibers were conducted according to **Scheme 6.1**. The molecular structure of the PDADMAC-CNC and PDADMAC-CNF was investigated using FTIR spectroscopy as shown in **Figure 6.1**. From the spectra of CNC and CNF, we observed that the (-OH) stretching was located at $3600\text{-}3200\text{ cm}^{-1}$, the (C-H) stretching at 2900 cm^{-1} , the (-OH) bending at 1635 cm^{-1} , the (-CH₂) bending and the (C-H) bending appeared at 1430 cm^{-1} and 1370 cm^{-1} respectively. The pure PDADMAC displayed the characteristic peaks at 1640 and 1450 cm^{-1} which corresponded to the stretching vibration of quaternary ammonium group (N⁺R₄) and the methyl groups respectively. The characteristic absorptions of the substrates CNC and CNF besides PDADMAC could be found in the PDADMAC-CNC and PDADMAC-CNF. As a result, we concluded that the surface of the CNCs and CNFs was successfully coated with PDADMAC via the physical adsorption. For CNC-PDMC, in the first step (i), the CNC surface was modified using BIBB to obtain the brominated CNC macroinitiators (CNC-Br). In the second step (ii), the polymerization of DMC from CNC-Br polymers was then conducted by ARGET-ATRP. FTIR spectroscopy was used to confirm the successful grafting of BIBB from the surface of CNC as well as the polymerization of DMC. Beside the characteristic peaks from the stretching vibrations the CNC hydroxyls, the FTIR spectra of CNC-Br, and CNC-PDMC exhibited a new peak appearing at around 1730 cm^{-1} that corresponded to the carbonyl group in BIBB and the vibrating absorption of the ester group in the DMC. In addition, the FTIR spectra of CNC-

PDMC possessed a new absorption peak, at 1480 cm^{-1} , which could be assigned to the methyl groups of the quaternary ammonium group in DMC. The appearance of the new peaks in the spectra of the CNC-Br, CNC-PDMC indicated that the two steps of the synthesis route were successful.



Scheme 6. 1. Schematic illustration of the synthesis procedure of (1) PDADMAC-CNC, (2) PDADMAC-CNF and (3) CNC-PDMC.

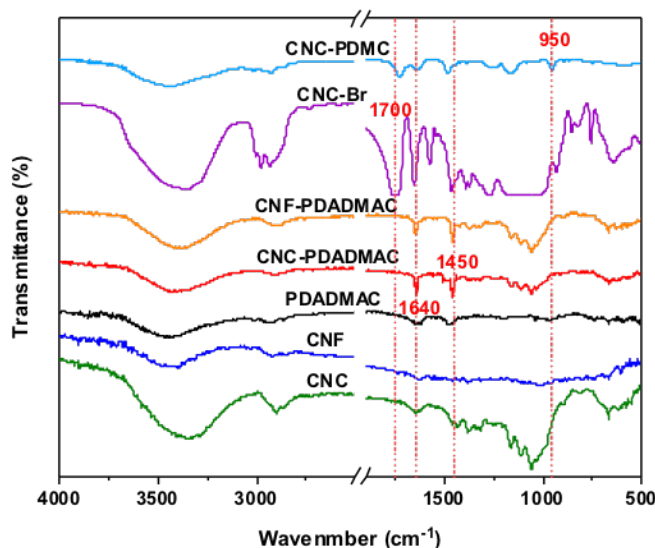


Figure 6. 1. FTIR spectra of CNC, CNF, PDADMAC, PDADMAC-CNC, PDADMAC-CNF, CNC-Br, and CNC-PDMC.

The measurement of the zeta potential is critical in monitoring the charge reversal assembly of polyelectrolytes on surfaces. The CNC was initially negatively charged (-48 mV) due to the presence of sulfate ester groups on the surface from the sulphuric acid treatment. The CNF was also negatively charged (-22.5 mV) because of chemical components, such as hemicellulose remaining after the pulping and bleaching processes²¹³. The zeta potential sign reversed when the cationic polyelectrolyte PDADMAC was adsorbed on the surface resulting in a +54 mV and +34 mV for PDADMAC-CNC and PDADMAC-CNF respectively due to the presence of quaternary ammonium groups on the surface of PDADMAC. The zeta potential of PDADMAC-CNF was less positive than PDADMAC-CNC due to the lower negative charge of the CNF surface to induce the physical adsorption compared to the high-negative CNC. Grafting of cationic DMC brushes from the CNC surface was also demonstrated by the positive zeta potential (+41 mV) from the quaternary ammonium groups on the surface of DMC. On the other hand, the Z-average of pristine

CNC and CNF was about (200 nm) and (2340 nm) respectively, while that of PDADMAC-CNC and PDADMAC-CNF was (276.5 nm) and (11400 nm) respectively. As expected, the adsorption of PDADMAC on the CNC and CNF led to an increase in the particles size. The increase in the Z-average of CNC-PDMC (643 nm) also demonstrated the grafting of DMC brushes from CNC surface. The observed zeta potential reversal with a concurrent increase in the Z-average with each subsequent adsorbed polyelectrolyte layer in the case of PDADMAC-Coated CNC and CNF or grafting DMC from CNC, indicating the successful modification as shown in **Figure 6.2**.

TEM images shown in **Figure 6.3(A)** present the rod-shaped cellulose nanocrystals having an aggregated morphology due the strong hydrogen bonding ²¹⁴. Grafting the DMC monomer from the CNCs did not alter its morphology as shown in **Figure 6.3(B)**. However, because of the electrostatic repulsion induced by the positive charge on the surface of CNC-PDMC, the modified CNCs tended to be more dispersed and displayed less aggregates. A similar behavior was also observed for PDADMAC-CNC shown in **Figure 6.3(C)**, underlining a good dispersion of these cellulose nanocrystals which agreed with the zeta potential measurements. **Figure 6.3(D)** shows the unmodified CNF with micrometric length and broad size distribution which could be due attributed to heterogeneous mechanical treatment and the aggregation of individual fibers. The TEM results of PDADMAC-CNF in **Figure 6.3(E)**, revealed that the lengths and widths of CNF increased because of the interactions between anionic CNF and cationic PDADMAC via electrostatic forces.

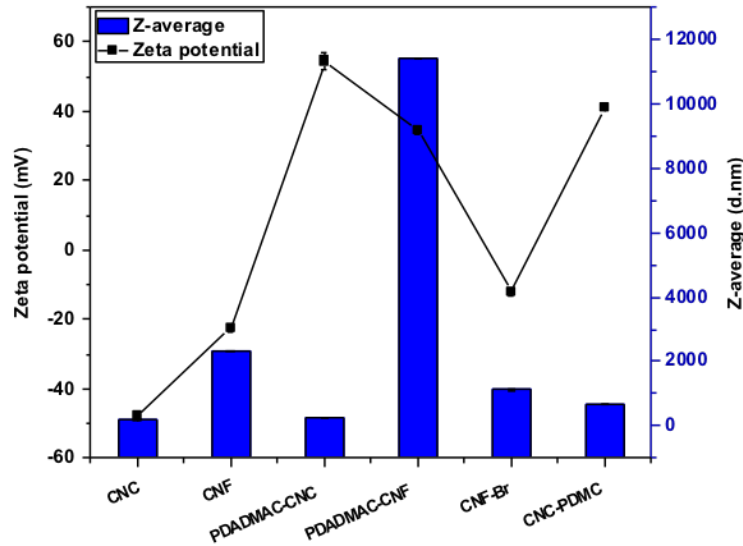


Figure 6. 2. Zeta potential and Z-average of PDADMAC-CNC, PDADMAC-CNF, CNC, CNC-Br, and CNC-PDMC.

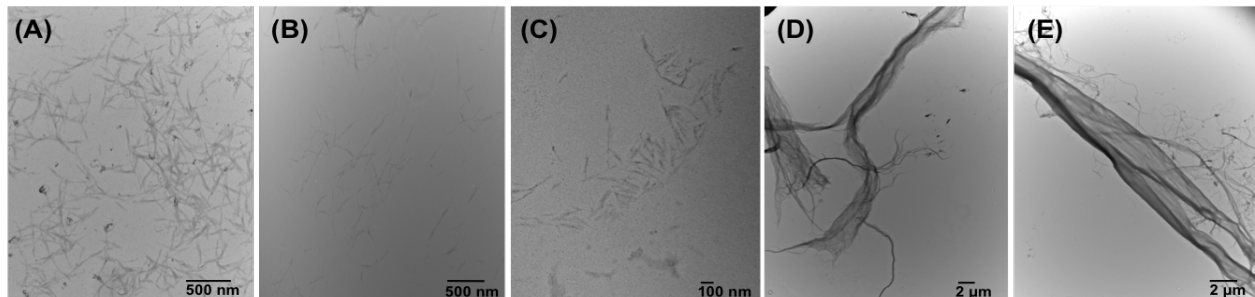


Figure 6. 3. TEM images of CNC (A), CNC-PDMC (B), PDADMAC-CNC (C), CNF (E), and PDADMAC-CNF (D).

6.3.2. The effect of dosage on the zeta potential

Adsorption bridging and charge neutralization are the main mechanism of the flocculation process. The zeta potential of flocculation system provides information on the charge neutralization effect¹⁹¹. The zeta potential after flocculation process using PDADMAC-CNC and CNC-PDMC were increased with the increased dosage as shown in **Figure 6.4**. The zeta potential of bentonite particles flocculated by the branched polyelectrolyte (CNC-PDMC) was always higher than the coated polyelectrolytes (PDADMAC-CNC, PDADMAC-CNF) although

PDADMAC-CNC had a higher charge density. The point of zero charge of the CNC-PDMC and PDADMAC-CNC occurred at 3.5 mg/g and 33 mg/g respectively, while PDADMAC-CNF did not reach the point of zero charge. At higher dosages, the zeta potential increased from -30 mV to +9 and +6 mV for CNC-PDMC and PDADMAC-CNC respectively due to the excess polymer in the solution. On the other hand, the zeta potential values for samples treated with PDADMAC-CNF were still highly negatively charged (-27 mV) although the flocculation efficiencies were high (>50%). This phenomenon indicated that charge neutralization played an important role in the flocculation process for CNC-PDMC and PDADMAC-CNC while bridging was dominant for PDADMAC-CNF.

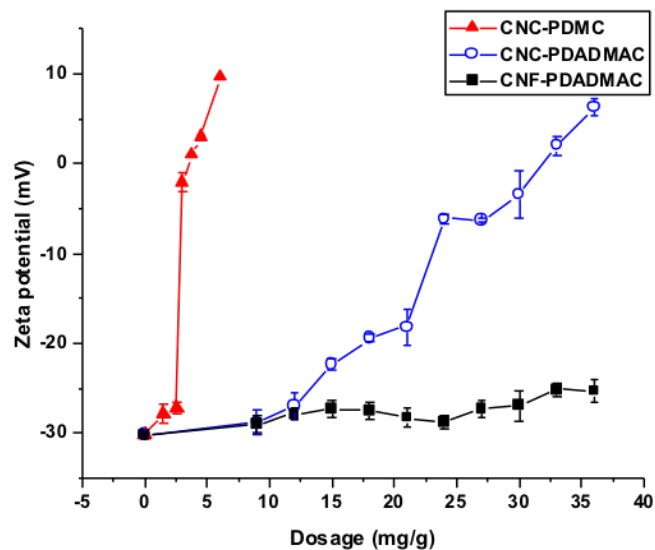


Figure 6. 4. Effect of flocculant types on the zeta potential of bentonite as a function of flocculant dosage.

6.3.3. The effect of dosage on the turbidity removal efficiency

Two critical observations are noted from **Figure 6.5**. Firstly, the highest turbidity removal was attained with the branched polyelectrolyte (CNC-PDMC) at lower dosages compared to the linear polyelectrolytes (PDADMAC-CNC, PDADMAC-CNF). Secondly, the three polymers displayed a similar trend at different dosage, turbidity removal increased along with increasing flocculant dosage, but then the turbidity removal efficiency slightly decreased with the further dosage after the optimal treatment efficiency was obtained. The maximum of the turbidity removal efficiency for CNC-PDMC, PDADMAC-CNC, and PDADMAC-CNF were 99%, 98% and 51% at optimum dosage of CNC-PDMC-3.5 mg/g, PDADMA-CNC-30 mg/g and PDADMAC-CNF-27 mg/g respectively.

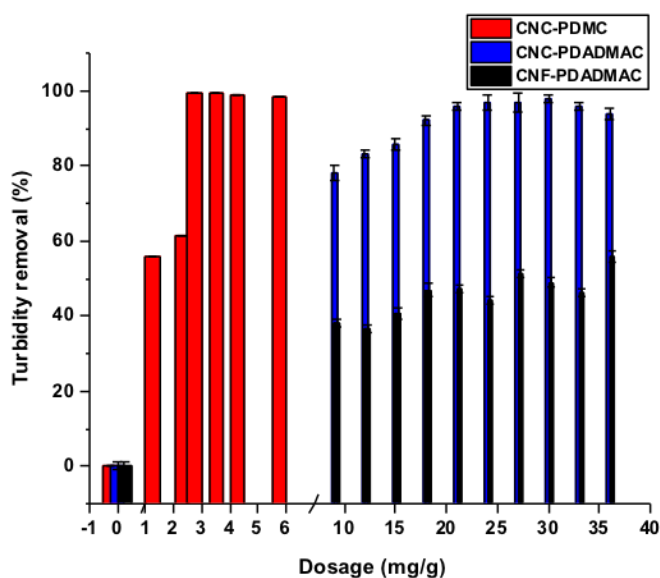


Figure 6. 5. Effect of flocculant types on the turbidity removal of bentonite as a function of flocculant dosage.

6.3.4. The effect of dosage on the floc size

A visual comparison of typical flocs formed by each of the systems is shown in **Figure 6.6**. It can be seen that the flocs formed using CNC-PDMC were more compact than PDADMAC-CNC and PDADMAC-CNF. The floc structures were examined using a digital microscope under 4x, 20x, and 40x magnifications as presented in **Figure 6.7**. The general observation is that with increasing polyelectrolyte dosage, the percentage of small particles decreased while the percentage of large aggregates increased until the maximum flocculation was obtained. The opposite case was observed above the optimum dosage, where the flocs were smaller with a larger percentage of small particles. In addition, the flocs formed using the branched CNC-PDMC were more compact with a smaller number of non-flocculated bentonite particles compared to the flocs formed using coated polyelectrolytes. The influence of the polymer structures on the flocculation efficiency and the floc size is clearly visible. The branched CNC-PDMC displayed the best flocculation performance amongst all the three flocculants examined in this study.

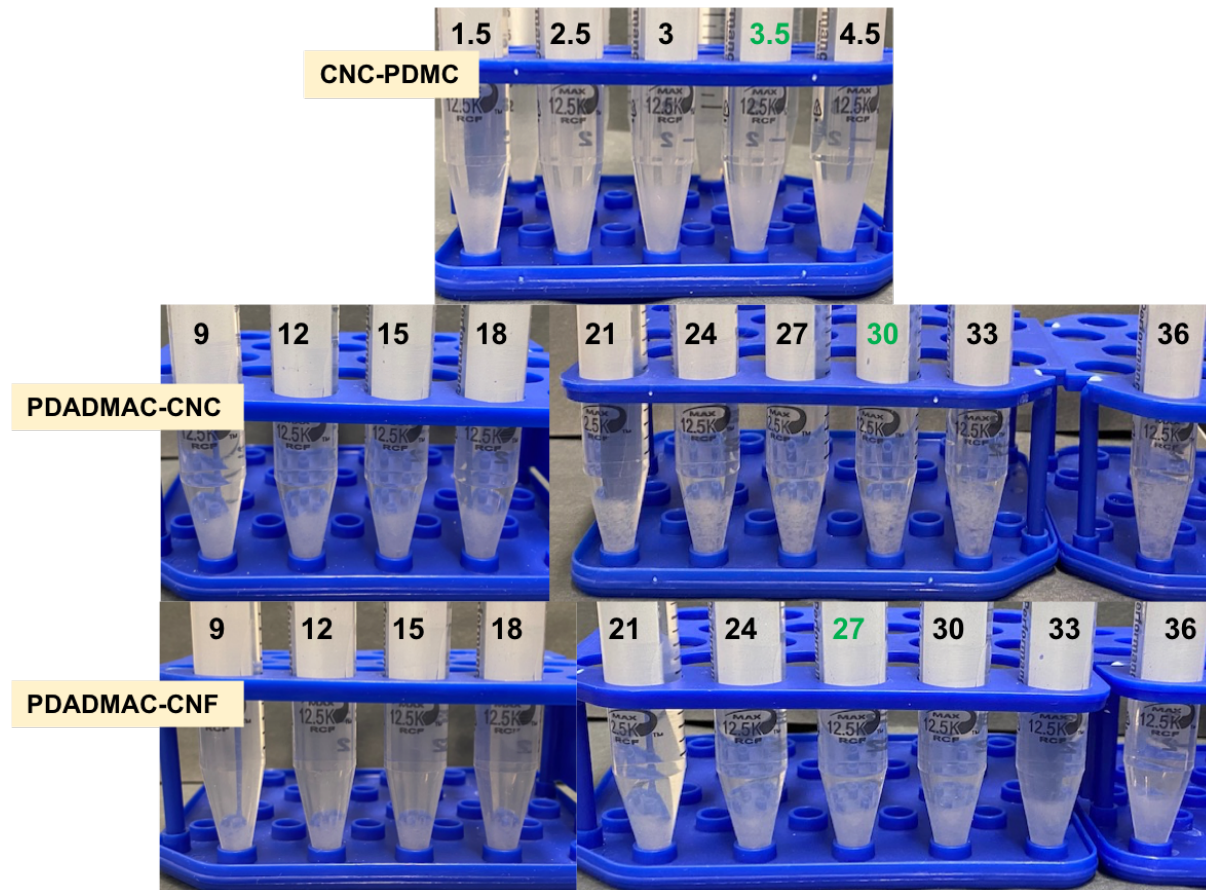


Figure 6. 6. A comparative investigation on the flocculation performance in the presence of three polyelectrolytes at different dosages.

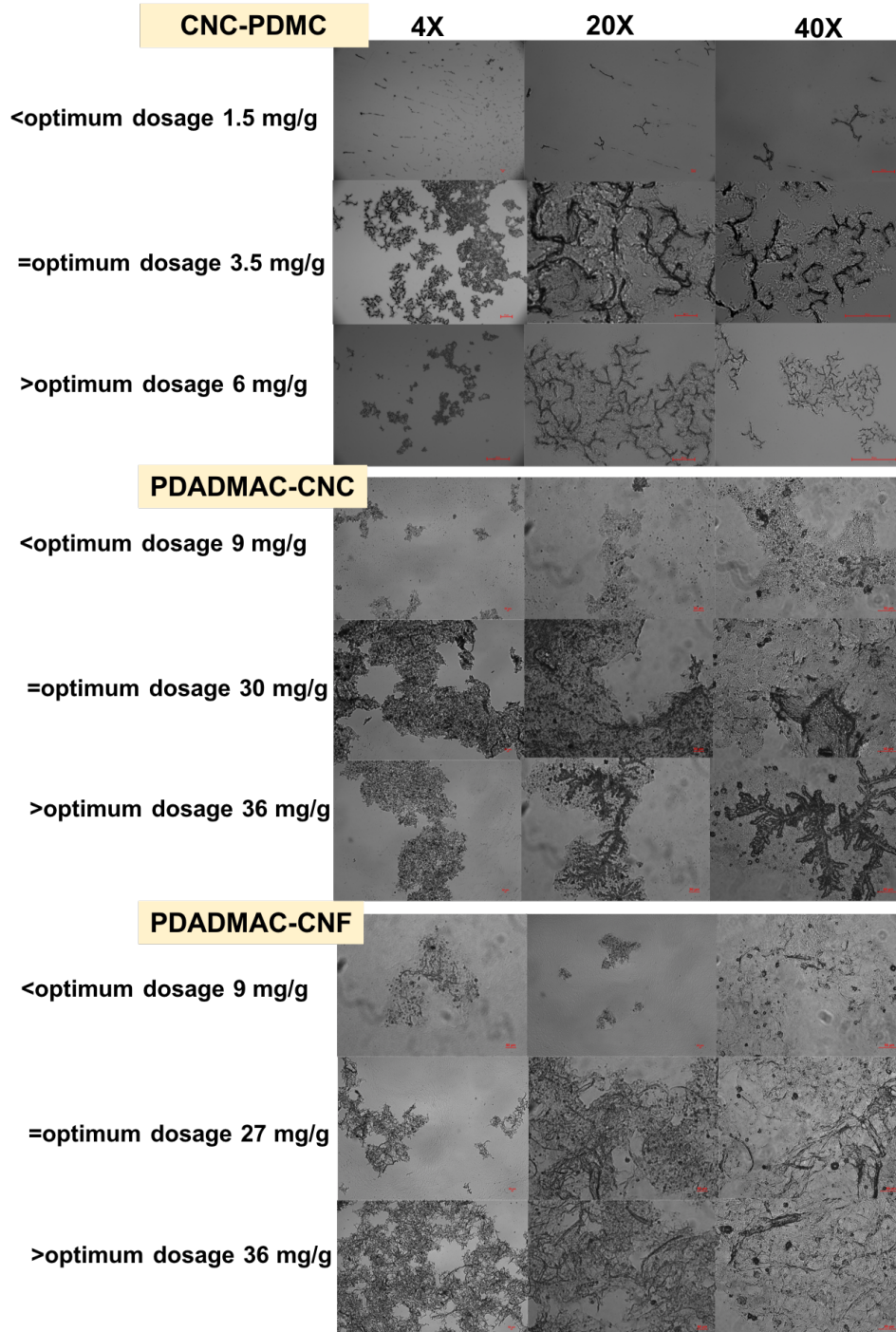
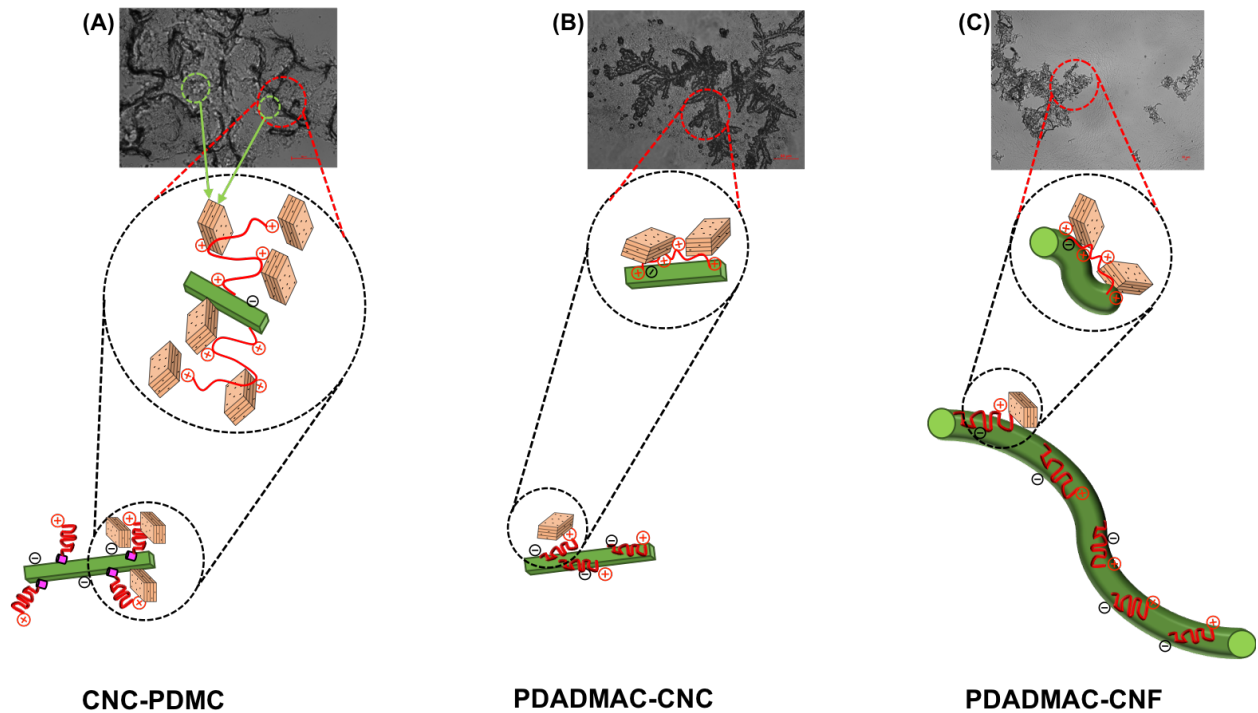


Figure 6. 7. Effect of the CNC-PDMC, PDADMAC-CNC, and PDADMAC-CNF on the floc size of bentonite as a function of dosage.

6.3.5. Proposed mechanisms

The flocculation systems using PDADMAC-CNC and PDADMAC-CNF showed lower flocculation performance whereas the CNC-PDMC was more effective. These findings can be explained based on the importance of the polyelectrolyte structures. The cationic branches of CNC-PDMC were extended from the surface of the CNCs towards bentonite particles and were capable to bind and bridge the bentonite particles according to the Singh model^{18,215}. According to the Singh model of flocculation, grafted polysaccharides are superior flocculant compared to linear polymers. Therefore, the flocculation in CNC-PDMC is more efficient as it involves multiple adsorption points, and stronger bridging capability. In addition, the charge repulsion generated by the cellulose nanocrystals resulted in the chain extension of the DMC brushes, thereby improving the polymer bridging of the bentonite particles. On the other hand, the configuration of the cationic PDADMAC coatings on the CNC and CNF for PDADMAC-CNC and PDADMAC-CNF yielded a flat conformation on the CNC and CNF surface, respectively. Therefore, the bridging is diminished since the surface sites available for bridging are reduced because of the strong adsorption of cationic PDADMAC chains on the CNC and CNF surfaces. The proposed mechanism is illustrated in **Scheme 6.2**.



Scheme 6. 2. The effect of polyelectrolyte structures on the adsorption and bridging mechanism for bentonite (A) CNC-PDMC, (B) PDADMAC-CNC and (C) PDADMAC-CNF.

6.4. Conclusions

Three types of cationic polyelectrolytes: CNC-PDMC, PDADMAC-CNC, and PDADMAC-CNF were added at varying dosages to a colloidal bentonite to quantify their flocculation behaviour. The CNC-PDMC possessed a branched-structure whereas PDADMAC-CNC, and PDADMAC-CNF have a coated and flat-cationic layer. The flocculation results of the three systems indicated that the polyelectrolyte structures had a strong influence on the flocculation efficiency. The grafted brushes of CNC-PDMC displayed better bentonite removal at lower optimum dosage compared to the other two coated-biopolymer systems (PDADMAC-CNC and PDADMAC-CNF). The higher zeta potential values of the flocs treated with CNC-PDMC suggested that the distribution of cationic charges on the DMC brushes extending from the CNC surface enhanced the binding and

bridging of the bentonite particles. On the other hand, the flat conformation of the PDADMAC chains on the CNC and CNF limited their interaction with bentonite particles. The zeta potential measurements also confirmed that charge neutralization played an important role in the flocculation process for CNC-PDMC and PDADMAC-CNC while bridging mechanism was dominant for PDADMAC-CNF. The microscope images show that the flocs produced by the CNC-PDMC are characterized by more compact structures compared to PDADMAC-CNC and PDADMAC-CNF.

Chapter 7. Effects of Chain Architecture and Grafting Composition on the Thermo-responsive behavior of Cationic and Thermo-responsive Copolymers

Abstract

Cellulose nanocrystals (CNCs) grafted with cationic- and thermo-responsive polymers based on [2-(methacryloyloxy)ethyl]trimethylammonium chloride (DMC) and diethylene glycol methyl ether methacrylate (MEO₂MA) via Activators ReGenerated by Electron Transfer (ARGET-ATRP) polymerization are examined. Two grafting schemes of copolymers brushes were considered by varying the di-block brushes sequence, for each sequence, two different grafting ratio of the DMC were prepared. The resulting copolymers were characterized by zeta potential and hydrodynamic size via dynamic light scattering (DLS); degree of substitution by conductometric titration and the main functional groups using Fourier transform infrared spectroscopy (FTIR) and proton nuclear magnetic resonance ¹H NMR. The influence of brush sequence, composition, and salt on the phase transition behavior was examined. The lower critical solution temperature (LCST) shifted to high temperatures at low PDMC grafting density on the outer layer. When the PMEO₂MA brushes occupied the outer layers of the block copolymers, the LCST was close to CNC-PMEO₂MA and not affected by the PDMC located in the inner layers. The prepared cationic and thermo-responsive copolymers exhibited a salting-out at low salt concentrations and a salting-in effect at high salt concentrations. The cationic and thermo-responsive copolymers did not show thermo-responsive behavior at very high salt concentrations.

7.1. Introduction

Stimuli-responsive polymers are defined as smart materials that respond to variation in the surrounding environmental conditions, such as pH, CO₂, light, electricity or heat. These polymers undergo physical changes by manipulating their chain conformation, structure and dynamics^{216,217}. These smart materials play an important role in a vast array of applications, for example in wastewater treatment and medicine^{64,218}. Special attention has been steadily growing in the polymer science to develop tunable thermo-responsive polymers and to understand the factors affecting their phase transition behavior. The presence of appropriate hydrophilic–hydrophobic balance imparts thermo-responsive characteristic to these polymers^{68,69}. The thermo-responsive polymers can be divided into two classes; those possessing a lower critical solution temperature (LCST) and those possessing an upper critical solution temperature (UCST). Polymers with LCST display a miscibility gap at high temperatures resulting in phase separation due to the disruption of polymer–water interactions above the LCST. Polymers with UCST display a phase separation upon cooling due to the strong polymer–polymer interactions. For example, aqueous solutions of poly(*N*-isopropyl acrylamide) PNiPAAm, undergo a coil-to-globule transition upon heating beyond their respective LCST close to the physiological temperature of about 37 °C⁷⁴. Compared to the widely studied thermo-responsive PNiPAAm, poly(oligoethylene glycol) methyl ether acrylates are a new class of uncharged, nontoxic and water-soluble biocompatible polymers that possess LCSTs with a broader temperature range of between 26 to 95 °C⁷⁵. The balance between the hydrophilic and hydrophobic components in the polymer structure has a strong effect on the phase transition behavior and the corresponding LCST. Of relevance to this study, replacing the terminal methyl group on the PEG side-chain by an ethyl group decreased the phase transition temperature to 20–25 °C due to the lower hydration level of the side-chain^{96,219,220}. Furthermore, the effect of the

chemical structure of both end groups on the LCST of POEGMA was investigated and the results indicated that the presence of hydrophobic groups at either ends of the polymer chain decreased the LCST and the influence is additive when the hydrophobic groups are located at both ends ²¹⁶. The cloud points of the thermosensitive polymer solutions are also affected by the presence of salts ²²¹. In line with this, a study initiated to examine the effect of different types of salt on POEGMA polymers revealed that the LCST depended on the nature and concentration of the salt. For example, chaotropes “water structure breaker” as NaSCN caused the salting-in effect while kosmotropes “water structure maker”, such as Na₂SO₄ caused salting-out effect of POEGMA copolymers ²²². The results are in agreement with other studies conducted on PEG-methacrylates, where the LCST decreased in the presence of NaCl or Na₂SO₄ ²²¹. Several studies have examined the effect of chain architecture on the thermos-responsive behavior of polymers. It was found that the LCST of hyperbranched POEGMA decreased to around 5-10 °C compared to the linear chains ²²³.

A key scientific issue is the design of new smart materials that possess sensing capabilities based on renewable natural resources. Of all the nanomaterials, cellulose nanocrystals (CNCs) have received much attention due to their unique properties. Cellulose nanocrystals have high tensile modulus, similar to steel or Kevlar (100 to 160 GPa), low density (0.8 to 1.5 g/cm³) and a large specific surface area (~250 m²/g) ^{54,135,181,224}. Therefore, CNCs are considered ideal substrate for the design of thermo-responsive copolymers with tunable properties. In the present study, ARGET-ATRP technique was employed to prepare cationic and thermo-responsive CNC-based copolymers in order to investigate their phase transition behavior. In particular, the influence of the cationic and thermo-responsive brushes sequence, monomers composition and the addition of salt on the LCST were examined.

7.2. Experimental section

7.2.1. Materials

Cellulose nanocrystals were kindly provided by CelluForce Inc. with an average charge density of 0.26 mmol/g. 4-(Dimethylamino)pyridine (DMAP, 99%), α -bromoisobutyryl bromide (BIBB, 98%), triethylamine (TEA), 2,2'-bipyridyl (Bipy, >99%), ascorbic acid (AsAc, >99%), copper(II) bromide (CuBr_2 , 99%) (2-methacryloyloxyethyl) trimethyl ammonium chloride (DMC), di(ethylene glycol) methylether methacrylate (MEO_2MA , 95 %), N,N-dimethylformamide (DMF) HPLC $\geq 99.9\%$, ethanol (EtOH), and isopropyl alcohol (IPA), were purchased from Sigma-Aldrich. Prior to use, the DMC monomer was prior to use activated by passing it through a column of neutral aluminium oxide.

7.2.2. Synthesis of CNC-macroinitiator (CNC-Br)

The macroinitiators CNC-Br were synthesized by the esterification of CNC with (BIBB) as described previously¹⁸⁴. In detail, CNC (500 mg) was dispersed in DMF (50 mL) by sonication. After the addition of TEA (2.3 mL) and DMAP (1 g), (BIBB) (3 mL) was added dropwise to the suspension at 0 °C. After 24 h, ethanol was added to terminate the esterification. The resulting CNC-Br was centrifuged with ethanol until a clean supernatant obtained and then twice with water. In the end, the CNC-Br was obtained by freeze-drying.

7.2.3. Synthesis of CNC-PMEO₂MA

Based on a method described elsewhere with slight modifications²²⁵, the CNC-Br sample (200 mg) was dispersed in a mixture of DMF (12 mL), H₂O (12 mL), MEO_2MA (0.01mol) inside a 50 mL round-bottom flask. After degassing with nitrogen for 30 minutes, degassed AsAc (91 mg), Bipy (87 mg), and CuBr_2 (5.5 mg) were successively added to the mixture. The reaction was

allowed to continue under constant stirring at 45 °C for 24h. The resulting dispersion was dialyzed in a 0.1 µm dialysis membrane against Millipore water with regular changes of water until the conductivity of the water remained constant. The copper catalyst was removed by passing the reaction mixture through a column of neutral alumina before characterization. After drying to constant mass, the conversion was determined by gravimetry.

7.2.4. Synthesis of CNC-PMEO₂MA-PDMC

The CNC-PMEO₂MA (500 mg) was dispersed in IPA (12 mL), H₂O (10 mL), DMC (0.05 mol) or (0.08 mol) inside a 50 mL round-bottom flask. After degassing with nitrogen for 30 minutes, degassed AsAc (100 mg), TEA (0.2 mL), and CuBr₂ (5.5 mg) were successively added into the mixture. The reaction was allowed to continue under constant stirring at room temperature for 24h. The resulting dispersion was dialyzed in a 0.1 µm dialysis membrane against Millipore water with regular changes of water until the conductivity of the water remained constant. The copper catalyst was removed by passing the reaction mixture through a column of neutral alumina before characterization. After drying to constant mass, the conversion was determined by gravimetry.

7.2.5. Synthesis of CNC-PDMC

Based on method described elsewhere with slight modifications ²²⁶, the CNC-Br sample (200 mg) was dispersed in a mixture of IPA (12 mL), H₂O (12 mL), DMC (CNC-PDMC1 0.05 mol) or (CNC-PDMC2 0.08 mol) inside a 50 mL round-bottom flask. After degassing with nitrogen for 30 minutes, degassed AsAc (100 mg), Bipy (100 mg), and CuBr₂ (6 mg) were successively added to the mixture. The reaction was allowed to continue under constant stirring at room temperature for 24h. The resulting dispersion was dialyzed in a 0.1 µm dialysis membrane against Millipore

water with regular changes of water until the conductivity of the water remained constant. The copper catalyst was removed by passing the reaction mixture through a column of neutral alumina before characterization. After drying to constant mass, conversion was determined by gravimetry.

7.2.6. Synthesis of CNC-PDMC-PMEO₂MA

The CNC-PDMC1 or CNC-PDMC2 (500 mg) was dispersed in a mixture of DMF (12 mL), H₂O (12 mL), and MEO₂MA (0.01 mol) inside a 50 mL round-bottom flask. After degassing with nitrogen for 30 minutes, degassed AsAc (91 mg), Bipy (87 mg), and CuBr₂ (5.5 mg) were added into the mixture successively. The reaction was allowed to continue under constant stirring at 45 °C for 24h. The resulting dispersion was dialyzed in a 0.1 μm dialysis membrane against Millipore water with regular changes of water until the conductivity of the water remained constant. The copper catalyst was removed by passing the reaction mixture through a column of neutral alumina before characterization. After drying to constant mass, conversion was determined by gravimetry.

7.2.7. Characterization

Fourier transform infrared spectra (FTIR) were recorded to confirm the functional groups of the prepared copolymers. Freeze-dried samples were homogeneously mixed with KBr powder at a 1:100 weight ratio and pressed into transparent pellets. The measurements were conducted using a Tensor 27 BRUKER machine at a resolution of 4 cm⁻¹, sample scan time of 32 s, and background scan time of 32 s, with the frequencies ranging from 4000 to 500 cm⁻¹.

Dynamic light scattering (DLS) and zeta potential experiments were conducted using a Malvern Zetasizer Nano series at nanoparticles concentration of 0.1 wt%. The values for the zeta potential were determined from the average of 3 measurements, consisting of 12 runs per measurement.

The number of quaternary amine groups on the CNC-PMEO₂MA-PDMC and CNC-PDMC-PMEO₂MA was determined using an 809 Titrand automatic potentiometric titrator, the Cole-Palmer Silver/Sulfide Ion Electrode a burette drive and a magnetic stirrer. In brief, a 10 mL solution was prepared using 0.5 mg of the solid sample and stirred at 25 °C, 10 mM silver nitrate (AgNO₃) was used as the standard titrant dosing into the sample vial at a rate of 0.1 mL/min. Two methods can be used to determine the endpoint. First: plotting the electric potential (mV) readings (y-axis) against the AgNO₃ volume (mL) (x-axis) to obtain the titration curve. The endpoint is determined at the steepest slope on the titration curve. Second: extracting the first derivative of the titration curve and taking the peak maximum appears during the titration procedure when the threshold value is exceeded as the equivalence point. The titration equivalence point corresponding to the volume of titrant recorded is transferred to the **Equation (7.1)** for further calculations, where V_s = sample volume (10 ml), V_t = titrant volume at equivalence point, C_t = titrant concentration (mM).

$$C_s = \left(\frac{V_t}{V_s}\right)C_t \quad \text{Equation (7.1)}$$

The thermal responsive characteristics were evaluated by performing turbidimetric measurements on a Varian (Cary 100 Bio) UV-vis spectrophotometer equipped with a temperature controller. All the measurements were performed at a rate of 1°C/min and a wavelength of 500 nm.

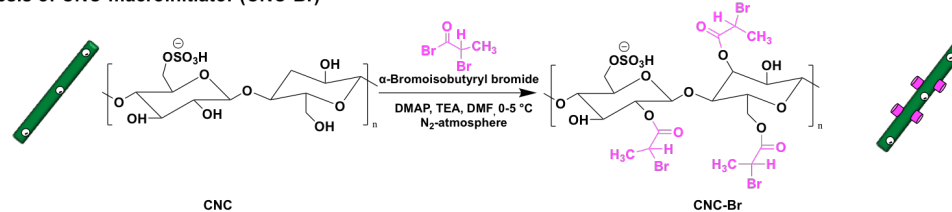
7.3. Results and discussion

7.3.1. Structural analysis

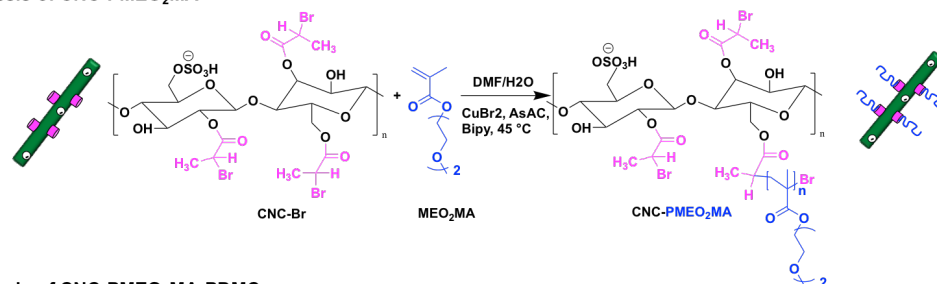
Freeze-dried CNCs were first chemically modified to introduce initiator sites for subsequent ARGET-ATRP reaction. The hydroxyl groups on the surface of CNC were esterified with α -

bromoisobutyryl bromide (BIBB) in DMF and DMAP as catalyst in the presence of base (TEA) as shown in **Scheme 7.1(A)**. The ester functionality, originating from the attachment of the isobutyryl bromide groups could be clearly seen from the appearance of the carbonyl stretching band at 1750 cm^{-1} in the FTIR spectra (**Figure 7.1**). A grafting-from approach was employed to polymerize PMEO₂MA and PDMC via ARGET-ATRP to impart thermo-responsive property and cationic charges as shown in **Scheme 7.1(B-E)**. Grafting of PMEO₂MA was confirmed by the shift of the peak corresponding to the carbonyl stretching from 1750 cm^{-1} to around 1730 cm^{-1} . In addition, the clear change of the spectrum in the region around 2900 cm^{-1} is a consequence of the dominance of methylene groups in the ethylene glycol segments of CNC-PMEO₂MA. Grafting PDMC was confirmed by the presence of two absorption peaks around 1480 cm^{-1} and 950 cm^{-1} which could be assigned to the methyl groups of the quaternary ammonium groups and the stretching vibration of the (C-N) bond in DMC. The change in the appearance of the carbonyl stretching beside the presence of new peaks at 1480 cm^{-1} and 950 cm^{-1} demonstrates the successful attachment of PMEO₂MA and PDMC to the backbone of CNC-Br.

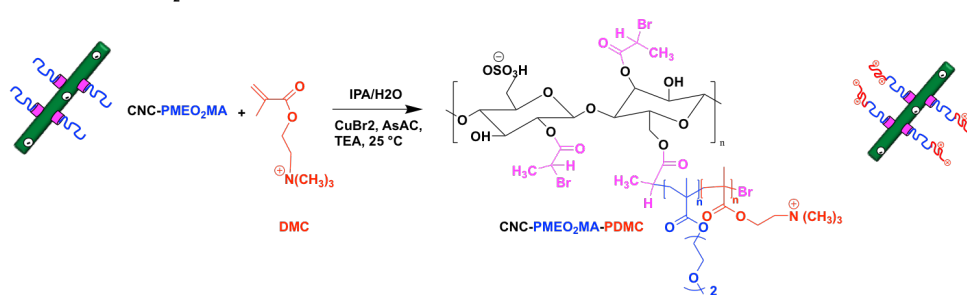
(A) Synthesis of CNC-macroinitiator (CNC-Br)



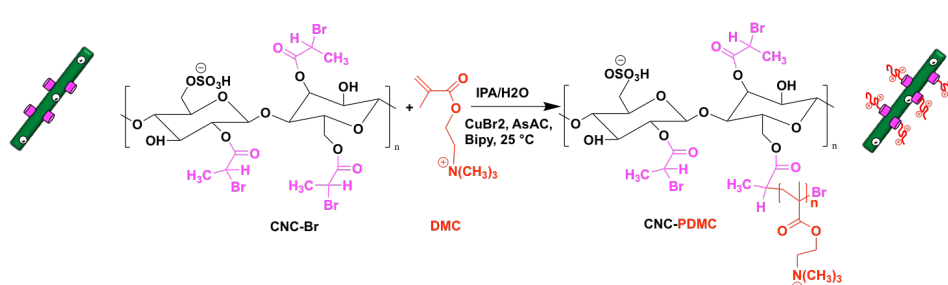
(B) Synthesis of CNC-PMEO₂MA



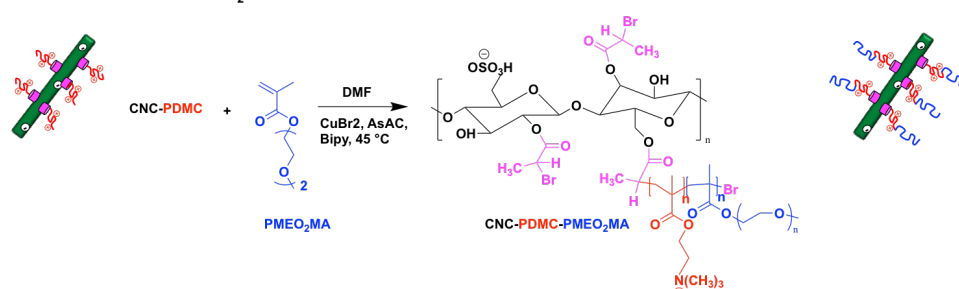
(C) Synthesis of CNC-PMEO₂MA-PDMC



(D) Synthesis of CNC-PDMC



(E) Synthesis of CNC-PDMC-PMEO₂MA



Scheme 7. 1. Schematic illustration of the synthesis procedure of (A) CNC-Br, (B) CNC-PMEO₂MA, (C) CNC-PMEO₂MA-PDMC, (D) CNC-PDMC, and (E) CNC-PDMC-PMEO₂MA.

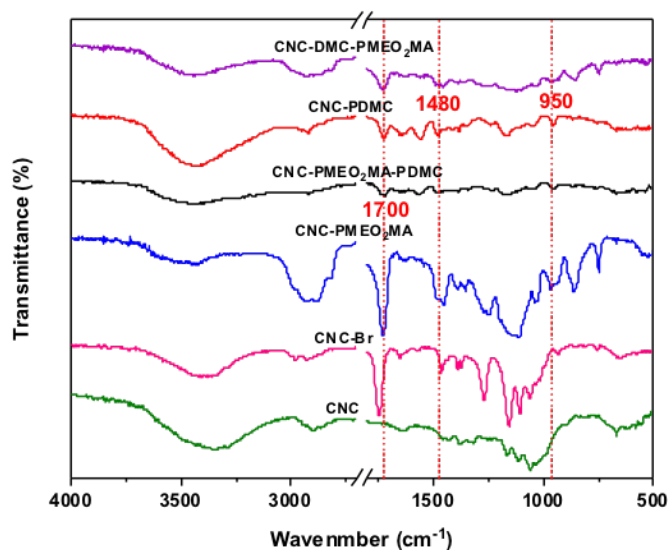


Figure 7. 1. FTIR spectra of CNC, CNC-Br, CNC-PMEO₂MA, CNC-PMEO₂MA -PDMC, CNC-PDMC, and CNC-PDMC-PMEO₂MA.

The modifications were further confirmed by ¹H NMR as shown in **Figure 7.2**. For CNC-Br, the signals at 3.9 (H6) to 4.75 (H1) ppm are due to the cellulose backbone. The chemical shifts at $\delta = 1.85$ ppm, 2 ppm (H3) are attributed to methyl groups in α -isobutyrate moieties. The chemical shift at $\delta = 3.4$ ppm (H4), $\delta = 3.5$ ppm (H5), 3.6 ppm, $\delta = 3.66$ ppm (H6), and $\delta = 4.1$ ppm (H7) in the ¹H NMR spectra of CNC-PMEO₂MA are assigned to the (OCH₃), (CH₂OCH₃), (CH₂OCH₂), and (COOCH₂) groups, respectively. In the ¹H NMR spectra of CNC-PMEO₂MA-PDMC, a significant increase in the intensity of the peaks at 1.2 ppm (H8) and 1.5 (H9) ppm corresponding to the methyl and methylene groups on the backbone was observed. These finding suggested the successful grafting of PDMC. Therefore, the spectroscopic results indicate that PME₂O₂MA and PDMC brushes have been successfully immobilized on the CNC-Br.

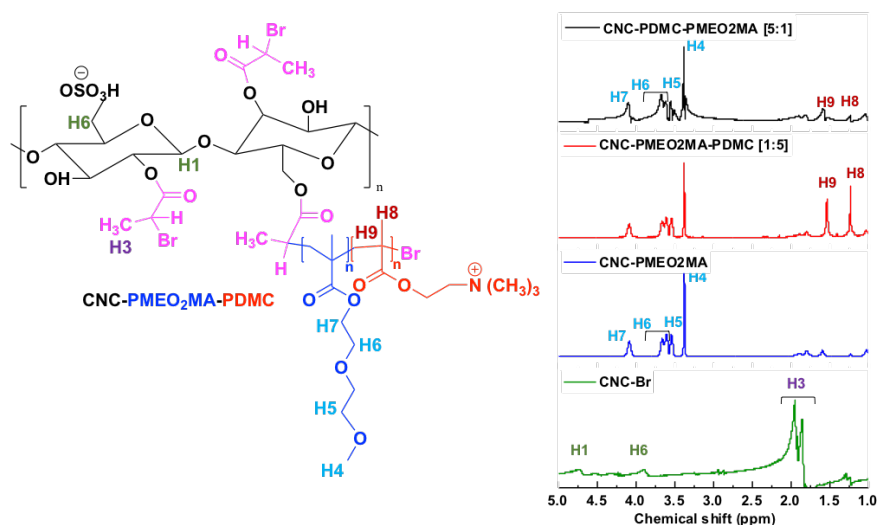


Figure 7. 2. ^1H NMR spectra of CNC-Br, CNC-PMEO₂MA, CNC-PMEO₂MA-PDMC, and CNC-PDMC-PMEO₂MA.

The modifications were accompanied with a characteristic change in the dispersibility of the CNCs. The dispersions in **Figure 7.3** demonstrated the transition from pristine hydrophilic CNC to hydrophobic CNC-Br (**B**) and then more hydrophilic for the thermo-responsive and/or cationic copolymers. The hydrophobicity of CNC-Br was reported and attributed to the substitution of some hydrophilic (-OH) groups with relatively hydrophobic isobutyrate groups. Such behavior is characteristic of BIBB immobilization on substrates possessing (-OH) groups as reported in many studies^{186,187}.

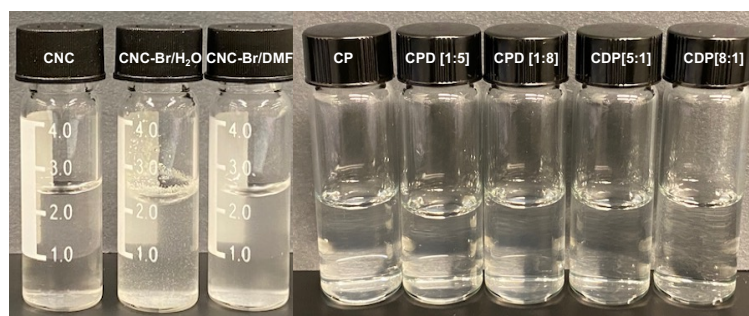


Figure 7. 3. The change in the dispersibility due to surface modification of the CNC.

The surface properties of pristine CNC, CNC-macroinitiator, the thermo-responsive and/or cationic copolymers suspensions were analyzed using DLS (**Figure 7.4**). The magnitude of the zeta potential (ZP) is an indicator of the stability and surface modification of the colloidal suspensions. For pristine CNCs, the negative surface charge ($ZP = -48 \pm 1 \text{ mV}$) is mainly due to the sulfate groups resulting from the sulfuric acid treatment. After covalent immobilization of the initiator, (α -isobutryl bromide), on CNCs, a significant reduction in the zeta potential ($ZP = +9 \pm 2 \text{ mV}$) was observed compared to pristine CNCs due to the hydrophobic BIBB groups. The zeta potential of CNC-PMEO₂MA was slightly lower ($ZP = -10 \pm 0.97 \text{ mV}$) compared to CNC-Br due to the attachment of the hydrophilic PMEO₂MA brushes. After grafting of the cationic PDMC brushes, the zeta potential became positive ($+32 \pm 2.5 \text{ mV}$), ($+29 \pm 2 \text{ mV}$) for CNC-PMEO₂MA-PDMC [1:5] and CNC-PMEO₂MA-PDMC [1:8] respectively. For the other two copolymers with different composition CNC-PDMC-PMEO₂MA [5:1] and CNC-PDMC-PMEO₂MA [8:1] the zeta potentials values were ($+25 \pm 1.3 \text{ mV}$), ($+31 \pm 1 \text{ mV}$) respectively indicating the presence of the PDMC cationic brushes. The difference in the zeta potentials of the copolymers implied that the PDMC content would result in an elevated degree of cationization on the surface of the substrate.

DLS was also used to determine the size of the prepared copolymers which were found to be in the nanometer range indicating that the size distribution of the CNCs was retained after the modifications as shown in **Figure 7.4**. With the exception of CNC-Br where the size was (2500 nm) due to the high hydrophobicity of BIBB, where the CNCs were no longer dispersible in water. However, CNC-Br formed stable colloidal dispersions in a variety of organic solvents, such as DMF and IPA, which are suitable solvents for the surface grafting polymerization of MEO₂MA and DMC monomers. These findings are in agreement with other studies conducted on CNC¹⁸⁷.

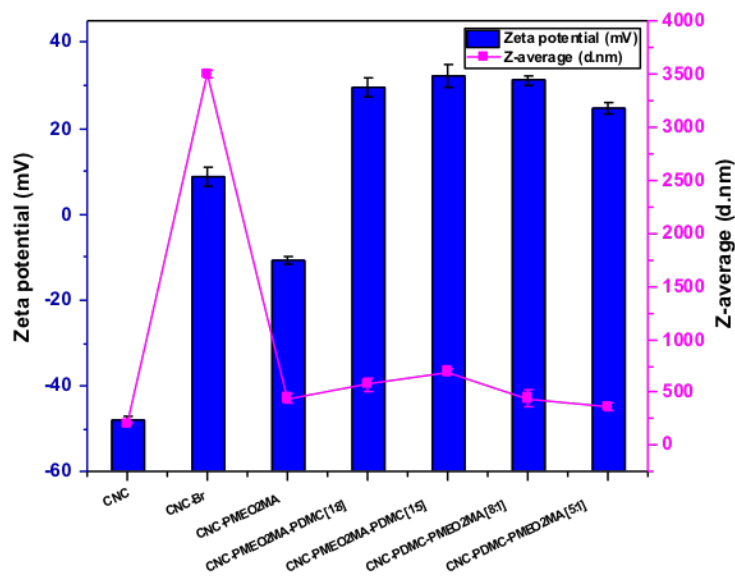


Figure 7. 4. Zeta potential and Z-average of CNC, CNC-Br, CNC-PMEO₂MA, CNC-PMEO₂MA-PDMC, CNC-PDMC, and CNC-PDMC-PMEO₂MA.

The amount of quaternary ammonium groups grafted from the CNC-Br were determined from the conductometric titration with AgNO₃. The endpoint was determined at the steepest slope on the titration curve or the maximum of the first derivative of the titration curve as shown in **Figure 7.5**. The concentration of quaternary ammonium groups was found to be 5.2 mM for CNC-PMEO₂MA-PDMC [1:5], 4 mmol/g for CNC-PMEO₂MA-PDMC [1:8], 2.6 mM for CNC-PDMC-PMEO₂MA [5:1], and 3.5 mM for CNC-PDMC-PMEO₂MA [8:1]. These titration data were in agreement with the zeta potential results for the effect of the monomer feed ratio (DMC) on the quaternary ammonium groups content of CNC-PMEO₂MA-PDMC. As the DMC content feed ratio was increased, both the zeta potential and quaternary ammonium groups content decreased. The steric hindrance of CNC-PMEO₂MA and the high viscosity associated with feed ratio of DMC impeded the propagation of chain radicals and resulted in a lower conversion. Therefore, the CNC-PMEO₂MA-PDMC [1:5] with lower feed ratio of DMC monomer showed higher zeta potential

value ($+32 \pm 2.5$ mV) and had higher quaternary ammonium groups content (5.2 mM) compared to CNC-PMEO₂MA-PDMC [1:8].

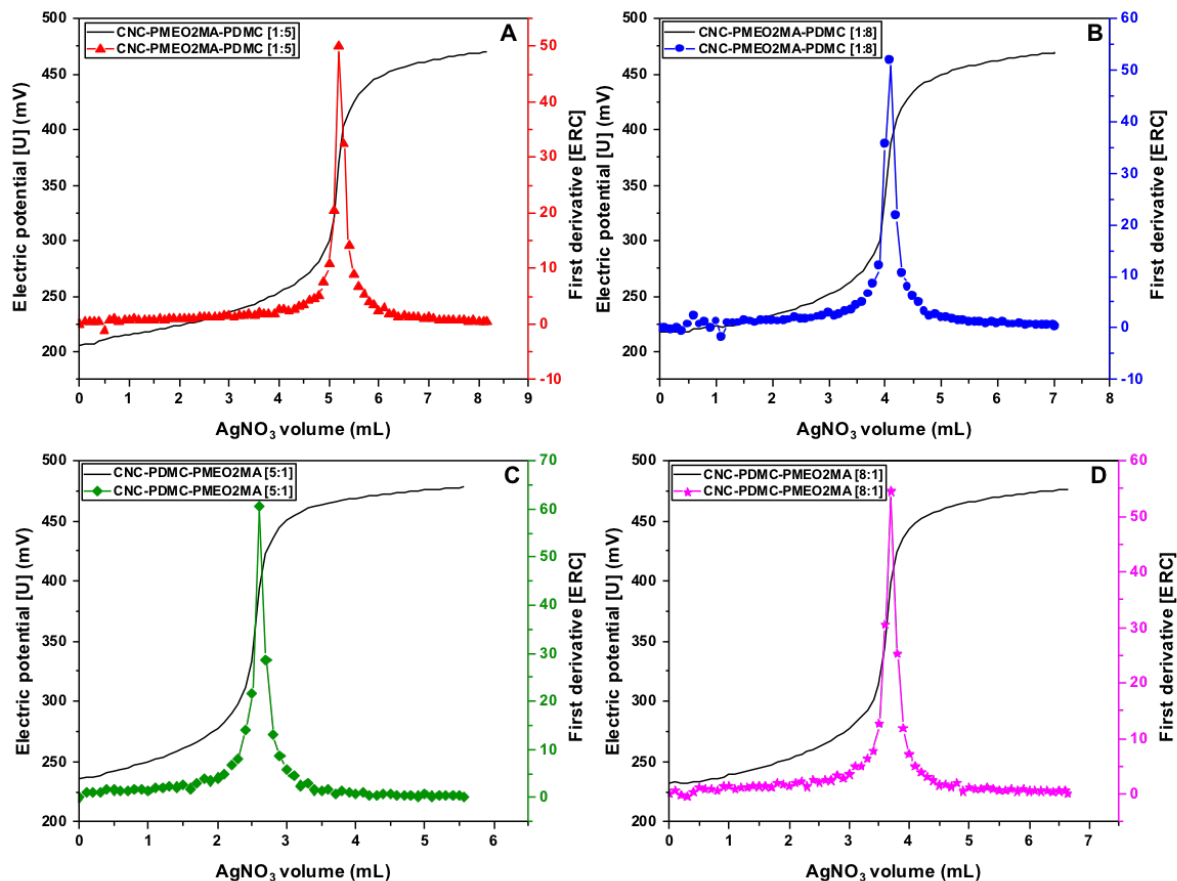


Figure 7. 5. Conductometric titrations of (A) CNC-PMEO₂MA-PDMC [1:5], (B) CNC-PMEO₂MA-PDMC [1:8], (C) CNC-PDMC-PMEO₂MA [1:5], and (D) CNC-PDMC-PMEO₂MA [1:8] at different ratio of DMC.

7.3.2. Thermo-responsive characteristics of the copolymers

The thermosensitive properties of the prepared copolymers were characterized by recording the change in transmittance of each sample in a concentration range of 0.15-1 wt%, with temperature at a wavelength of 500 nm. The cloud points (T_{cp}) at each concentration were identified as the critical temperatures at 50% transmittance, which were used to determine the phase diagrams. The LCST was associated with the lower critical solution temperature on the phase diagram. The

general observation is that the cloud points shifted to lower temperatures for high concentration solutions which was reported in the literature and attributed to greater polymer-polymer interaction at higher concentration. It is also reported that the higher observed cloud points for low concentration solutions are related to the UV-vis spectrophotometry technique that detects relatively large phase separated aggregates that were not present at the early stages of the phase separation⁶⁹. As shown in **Figure 7.6(A)** there was a sharp decrease in the transmittance for the CNC-PMEO₂MA over the whole concentration range examined. CNC-PMEO₂MA brushes underwent a structural transition from the stretched to the collapsed conformation due to thermally driven chain dehydration with temperature changing from below the LCST to above the LCST. From the phase diagram **Figure 7.6(B)**, the LCST was found to be 24.5 °C which was very close to the value reported in another study¹⁵⁰.

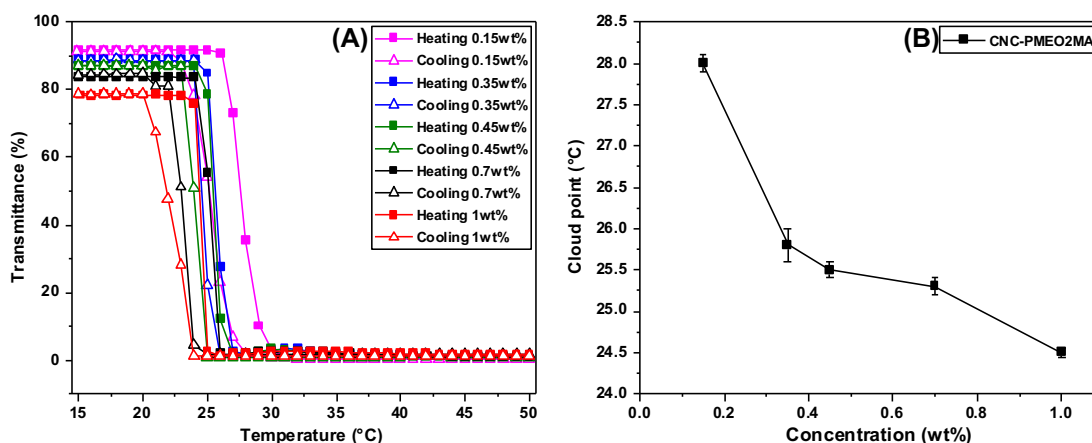


Figure 7. 6. The cloud point values obtained from the transmittance–temperature (Tr–T) curve of CNC-PMEO₂MA (A), and the corresponding phase diagram (B).

The phase transition of CNC-PMEO₂MA was examined after the grafting of two different ratios of PDMC brushes on PMEO₂MA brushes as shown in **Figure 7.7(A,B)**. Generally, the CNC-PMEO₂MA-PDMC [1:5] with higher PDMC content, resulted in a sharp transition behavior

similar to the CNC-PMEO₂MA and the LCST was 25 °C (**Figure 7.7(C)**). However, the CNC-PMEO₂MA-PDMS [1:8] with a relatively low PDMS content exhibited a broad phase transition as shown in **Figure 7.7(B)**, and the LCST was higher (28.5 °C) as shown in the phase diagram **Figure 7.7(D)**. DMC is a cation and is strongly hydrophilic; therefore, it is expected that the high degree of copolymerization of DMC from CNC-PMEO₂MA would result in the elevation of the LCST. However, this was not the case, and the LCST decreased with increasing PDMS content. The lower LCST of CNC-PMEO₂MA-PDMS [1:5], containing higher PDMS, implied that the copolymer had higher hydrophobicity. The enhanced hydrophobicity of CNC-PMEO₂MA-PDMS [1:5] was due to the higher grafting density of PDMS leading to steric hindrance of the PDMS chain on the PMEO₂MA brush segments. As a result, the hydrophobic interactions between the side chains of PDMS and PMEO₂MA brushes were enhanced while the repulsive forces between the quaternary ammonium groups became weaker reducing the water solubility of the copolymer. In addition, it was reported that the high grafting density may reduce the solvent interaction with the polymer. Thus, the degree of hydration of the densely grafted CNC-PMEO₂MA-PDMS [1:5] was lower than the sparsely grafted CNC-PMEO₂MA-PDMS [1:8]. Therefore, when the temperature was increased, the dehydration rate of CNC-PMEO₂MA-PDMS [1:5] was faster compared to CNC-POEGMA-PDMS [1:8] with lower PDMS content. Whereas in a sparsely grafted PDMS brushes of CNC-PMEO₂MA-PDMS [1:8], the repulsive forces between the quaternary ammonium groups stabilized the copolymer; therefore, lower polymer aggregates were formed above the phase transition. In addition, the brushes remained fully hydrated at all temperatures as confirmed by the gradual change in the optical density due to the non-restricted solvent penetration within the polymer brushes. As a consequence, CNC-PMEO₂MA-PDMS [1:8]

exhibited a higher LCST at 28.5 °C due to the hydrophilic nature because of the repulsive forces that retarded the dehydration. The proposed mechanism is shown in **Scheme 7.2**.

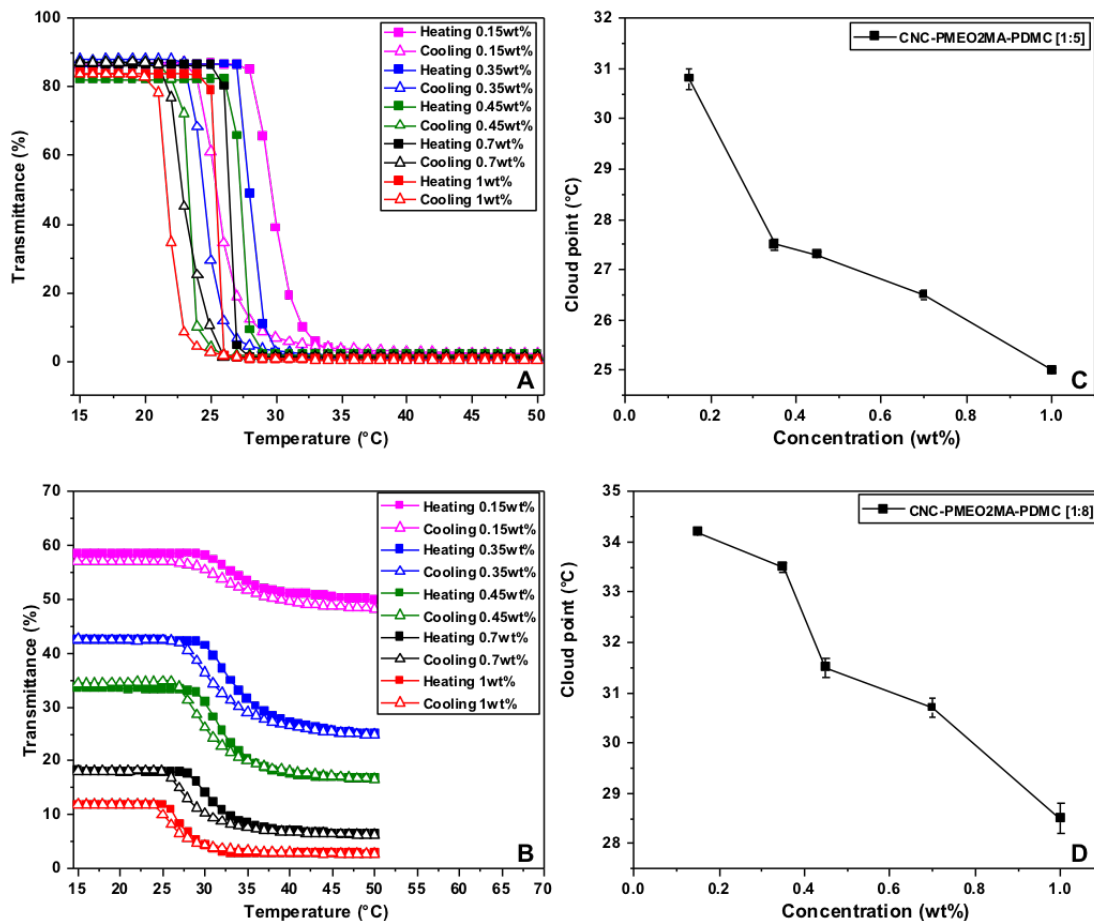
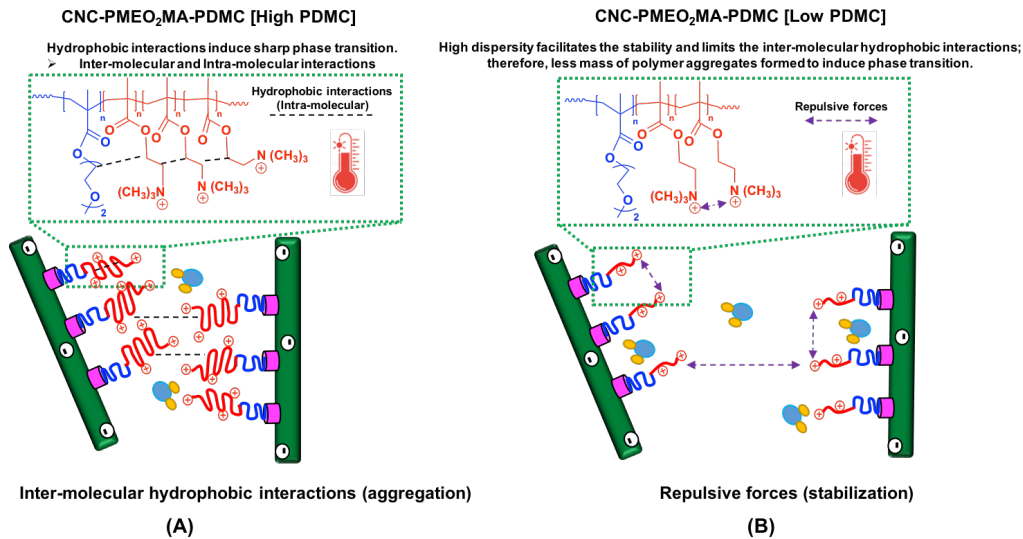


Figure 7. 7. The cloud point values obtained from the transmittance–temperature (Tr–T) curve of CNC-PMEO₂MA-PDMC [1:5] (A) CNC-PMEO₂MA-PDMC [1:8] (B), and the corresponding phase diagram (C) ,(D) respectively.



Scheme 7.2. Schematic illustration of the aggregation observed of CNC-PDME₂MA-PDMC[1:5](A), and CNC-PDME₂MA-PDMC[1:8](B) during heating.

As the thermo-responsive behavior depends on the molecular architecture, the phase transition of CNC-PDME₂MA with different ratios of PDMC was also examined as shown in **Figure 7.8(A,B)**. The phase transition behavior of the two copolymers, CNC-PDME₂MA [5:1], CNC-PDME₂MA [8:1], was relatively sharp and the LCSTs were 24.2 °C and 23.8 °C respectively. These findings indicated that the PDME₂MA brushes on the outer surfaces dehydrated at the transition temperature of CNC-PDME₂MA. Meantime, the PDMC in the inner surface interacted with PDME₂MA layers through strong hydrophobic interaction and were hindered from penetrating into the surface explaining the sharp phase transition. The mechanism behind these observations is illustrated in **Scheme 7.3**.

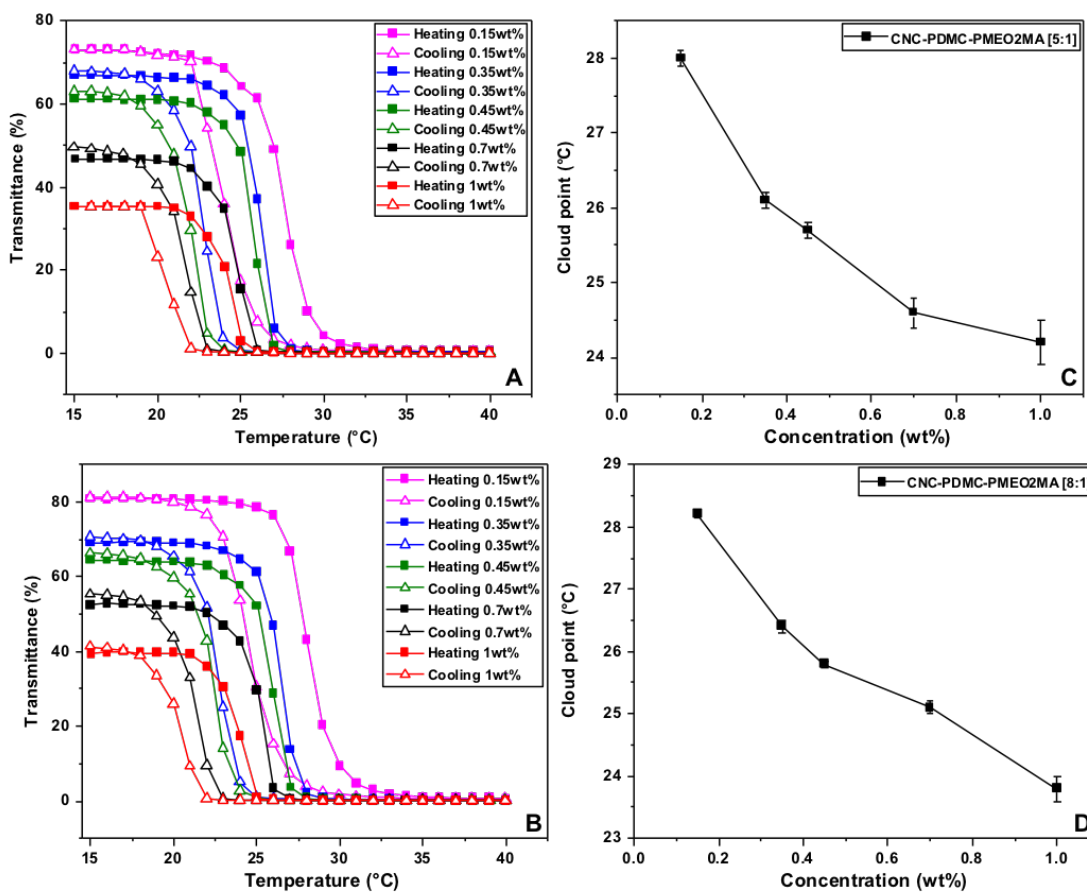
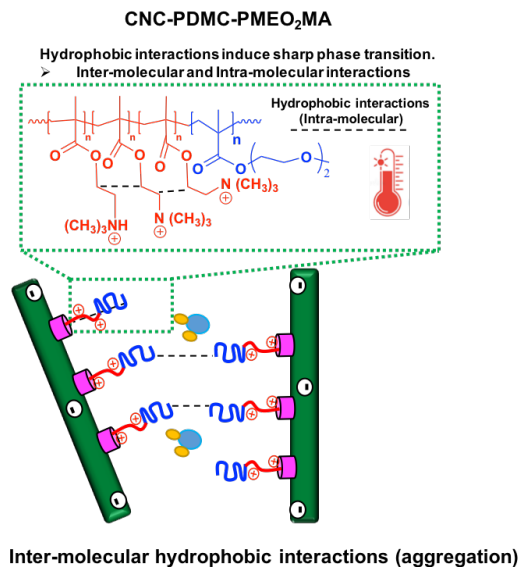


Figure 7. 8. The cloud point values obtained from the transmittance–temperature (Tr–T) curve of CNC-PDMC-PMEO₂MA [5:1] (A) CNC-PDMC-PMEO₂MA [8:1] (B), and the corresponding phase diagram (C) ,(D) respectively.



Scheme 7. 3. Schematic illustration of the aggregation observed of CNC-PDMC-PMEO₂MA during heating.

7.3.3. The effect of salt on the thermo-responsive properties of the copolymers grafted on CNCs

The phase transition behavior of the prepared copolymers was examined in the presence of KCl (displaying a moderate salting-out effect) using a UV-vis spectrometer. The results presented in **Figure 7.9 (A,B)** indicated that the addition of KCl to the aqueous solution of CNC-PMEO₂MA caused a typical salting-out effect. The cloud point decreased with increasing salt concentration due to chloride ions polarizing the adjacent water molecules, which in turn, weakened the interactions between the PMEO₂MA brushes and the surrounding water molecules resulting in the dehydration of the copolymer chains. The salt effect in this case is related to the Hofmeister series as reported previously¹⁵⁸.

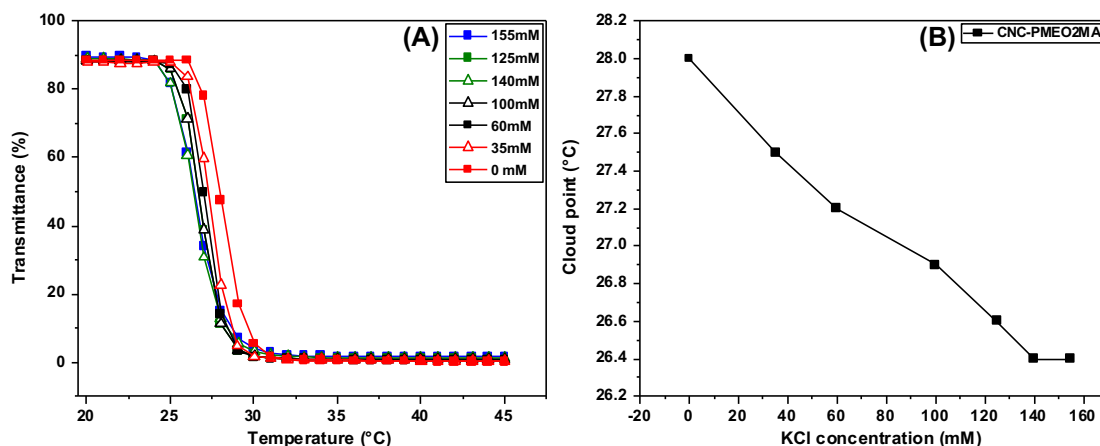


Figure 7. 9. The effect of salt concentration on the cloud points of CNC-PMEO₂MA (A), and the corresponding phase diagram (B).

The effect of salt on the phase transition behavior of CNC-PMEO₂MA-PDMC with two different grafting ratios of PDMC was also examined as shown in **Figure 7.10(A,B)**. Three main regimes of the phase transition behavior were observed after the addition of KCl presented in **Figure 7.10(C,D)**. The first regime exhibits a decrease in the cloud points at low KCl concentrations (salting-out effect). It is generally accepted that the addition of salt decreases the miscibility of the polymers by breaking the hydrogen bonding between their polar units and water (removing hydration shell) causing a coil-globule transition. It is also known that the effects are more pronounced for anions than for cations^{227,228}. The second regime results revealed that the high KCl concentrations lead to a gradual increase in the cloud points (salting-in effect). This phenomenon can be explained by the interactions between the salt ions and PMEO₂MA brushes and in turn their conformation on the CNC-Br surface. The presence of high KCl concentrations polarize the water molecules around the PMEO₂MA brushes causing them to adopt a collapsed chain conformation on the CNC-Br; as a result, the repulsive forces between PDMC brushes

stabilize the copolymers. The third regime occurred at very high KCl concentrations where the phase transition cannot be observed any more.

The presence of higher KCl concentrations induced ion-pair interaction with the quaternary ammonium groups of the PDMC brushes. Therefore, the electrostatic interaction of the quaternary ammonium groups was screened with anions (Cl^-) causing the PDMC brushes to adopt a collapsed chain conformation on the CNC-PMEO₂MA. This translated to a decrease in the brush molar mass and an increase in the stability of the copolymers as the size of the copolymer decreased as shown in the TEM image (**Figure 7.11(B)**). Subsequently, the flat brushes were not able to form inter-chain interactions and the transition of the copolymer cannot be observed any more. It can be observed that the change in the transmittance of CNC-PMEO₂MA-PDMC [1:8], containing less PDMC, was broader and did not reach 0%. In addition, CNC-PMEO₂MA-PDMC [1:8] loses its thermo-responsiveness faster than the CNC-PMEO₂MA-PDMC [1:5]. These observations can confirm that the hydrophilicity of CNC-PMEO₂MA-PDMC [1:8] was higher due to the sparse grafting that facilitates the diffusion of solvent and the salt ions. Therefore, the brushes collapsed on the surface and the size decreased in response to high salt concentration faster. The effect of chloride ions on the hydration and conformation of PDMC homopolymer was reported to be associated with the presence of high chloride ions that led to chain dehydration because of the ion-pair interactions^{161,162,229,230}. The proposed mechanism is shown in **Scheme 7.4(A)**.

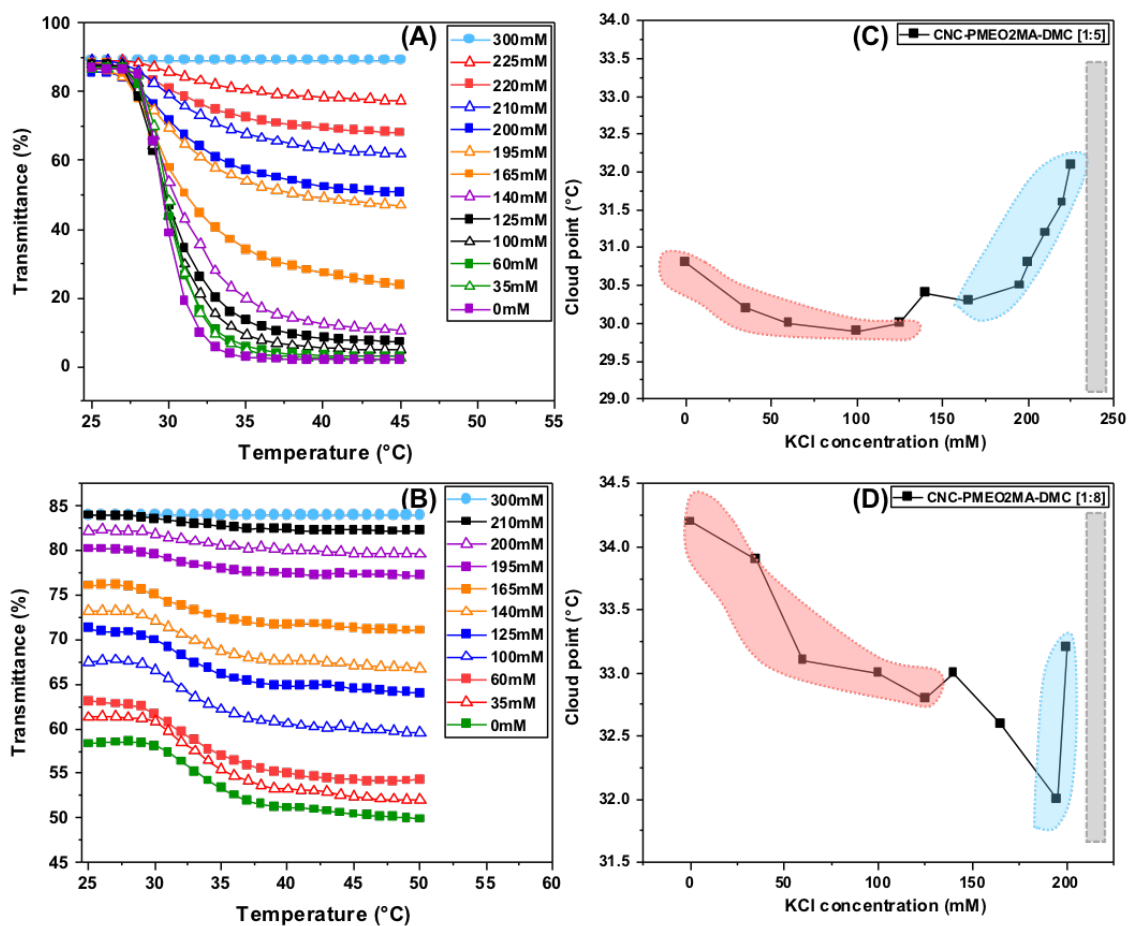


Figure 7. 10. The effect of salt concentration on the cloud point values obtained from the transmittance–temperature (Tr–T) curve of CNC-PMEO₂MA-PDMS [1:5] (A) CNC-PMEO₂MA-PDMS [1:8] (B), and the corresponding phase diagram (C) ,(D) respectively.

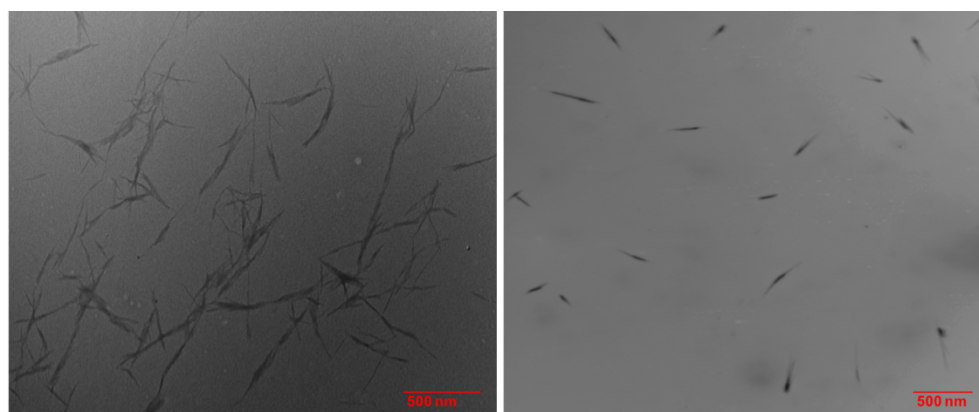


Figure 7. 11. The TEM images of CNC-PMEO₂MA-PDMS before the addition of KCl (A) and in the presence of KCl (B).

Figure 7.12(A,B) represents the effect of salt on the phase behavior of the other two copolymers CNC-PDMC-PMEO₂MA. As shown in the phase diagrams **Figure 7.12(C,D)**, two regimes were also observed which reveals that the salting-out effect took place first followed by the salting-in effect. The salting-out effect resulted also from the salt anions polarizing the hydrogen bonding between water and the polar groups of the copolymer causing the dehydration. On the other hand, the salting-in effect resulted from the change in the conformation of the PDMC brushes penetrating to the outer layer as the salt anions caused the PMEO₂MA to collapse on the CNC-Br surface. Therefore, the stability of the copolymers increased at higher salt concentrations till the copolymers lost their thermo-responsiveness due to high repulsive forces between the quaternary ammonium groups on the PDMC brushes inhibiting the dehydration. The proposed mechanism was illustrated in **Scheme 7.4(B)**.

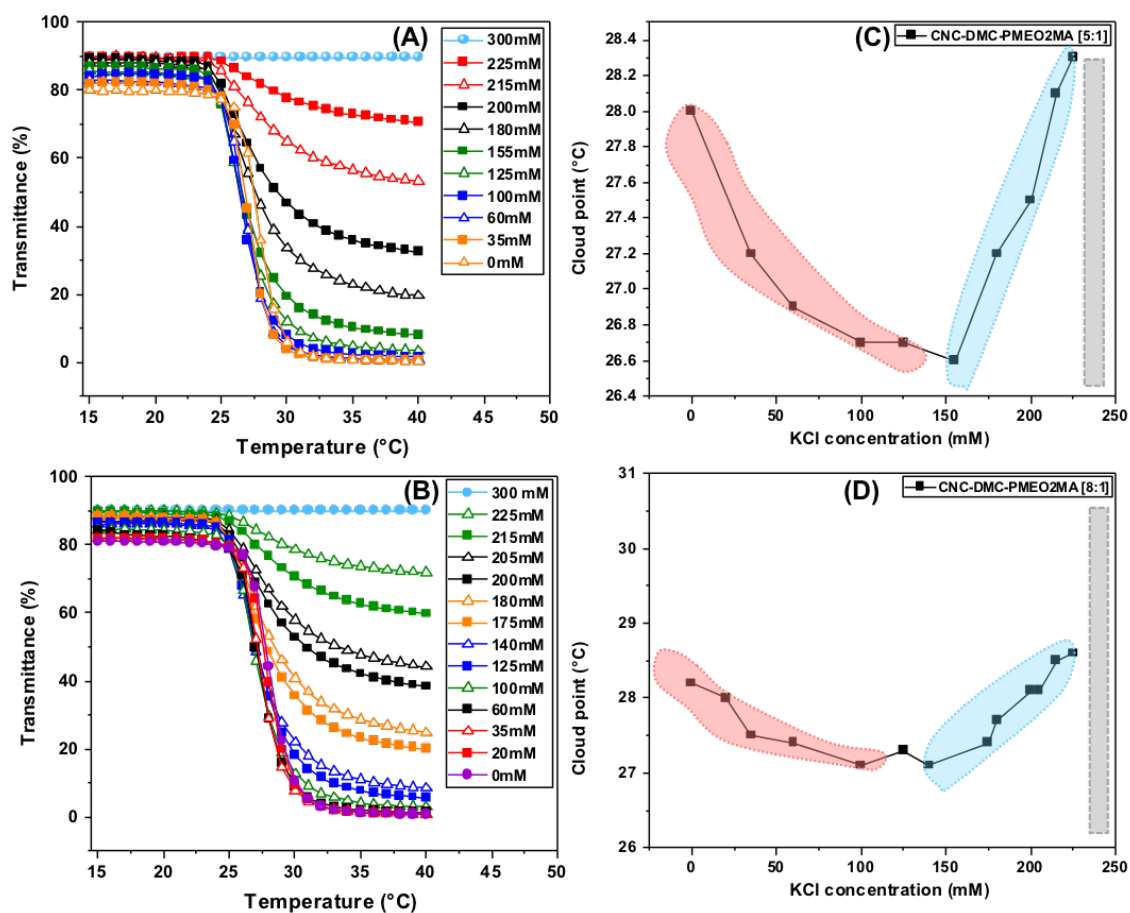
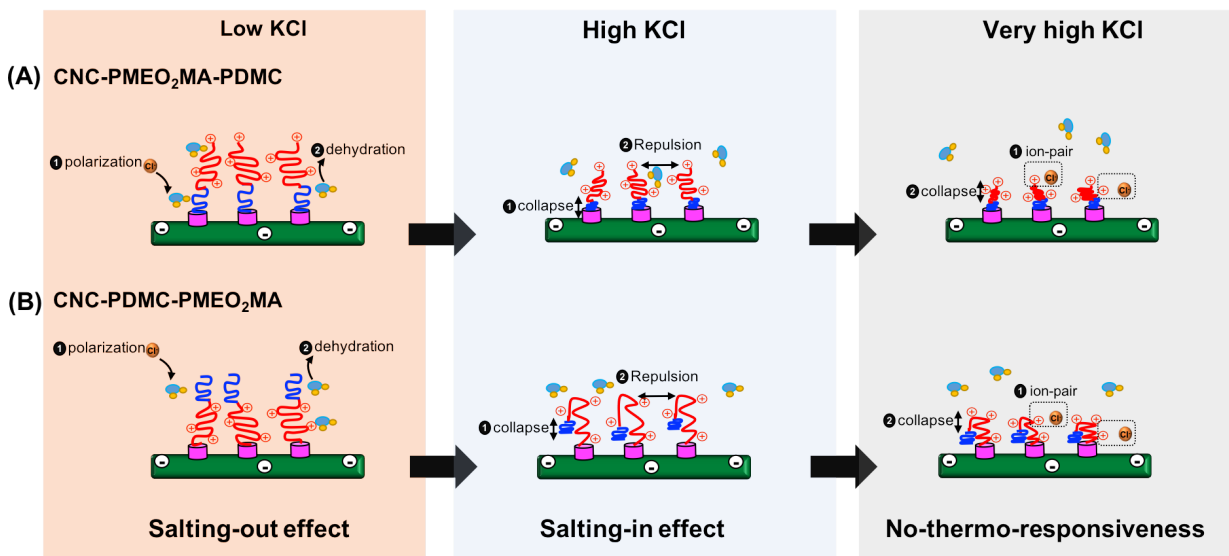


Figure 7. 12. The effect of salt concentration on the cloud point values obtained from the transmittance–temperature (Tr–T) curve of CNC-PDMC-PMEO₂MA [5:1] (A) CNC-PDMC-PMEO₂MA [8:1] (B), and the corresponding phase diagram (C) ,(D) respectively.



Scheme 7. 4. Schematic representations of the proposed mechanisms responsible for the phase transition behavior of CNC-PMEO₂MA-PDMS (A) and CNC-PDMS-PMEO₂MA (B) in the presence of KCl, (the numbers in black circles indicate the order of the events).

7.4. Conclusions

In summary, the synthesis of cellulose nanocrystals grafted with cationic- and thermo-responsive polymers based on DMC and MEO₂MA via ARGET-ATRP is reported. The CNC-PMEO₂MA-PDMS copolymer with high PDMS content exhibited a sharp transition behavior similar to the CNC-PMEO₂MA and the LCST was 25 °C. However, the CNC-PMEO₂MA-PDMS copolymer with low PDMS content showed a broad phase transition behavior and the LCST increased to 28.5 °C. These findings indicated that the higher the grafting density the less hydrated the brushes due to steric hindrance. In addition, strong hydrophobic interactions between the methacrylate backbone would take place above the LCST. For the copolymers with the opposite sequence, CNC-PDMS-PMEO₂MA, the LCST was very close to CNC-PMEO₂MA implying that the PME₂MA brushes dehydrated above the LCST and screened the PDMS repulsive forces. As confirmed using UV-vis measurements, the addition of salt plays an important role in tuning the

phase transition behavior of the prepared copolymers. The CNC-PMEO₂MA copolymer showed a typical salting-out effect. On the other hand, the CNC-PMEO₂MA-PDMC copolymers showed salting-out effect at low salt concentrations due to chloride ions polarizing the adjacent water molecules resulting in the dehydration of the copolymer chains. At high salt concentrations, the CNC-PMEO₂MA-PDMC copolymers exhibited a salting-in effect because of the chloride ions causing the PMEO₂MA to adopt a collapsed chain conformation whereas the repulsive forces between PDMC brushes stabilized the copolymers. However, the phase transition of CNC-PMEO₂MA-PDMC copolymers cannot be observed at very high salt concentrations due to the ion-pair interaction between salt anions and the quaternary ammonium groups of the PDMC brushes causing PDMC brushes to adopt a collapsed chain conformation on the CNC-PMEO₂MA. For the CNC-PDMC-PMEO₂MA copolymers, the two regimes were also observed. The salting-out effect resulted also from the salt anions destabilizing the hydrogen bonding between water and the polar groups of the copolymer causing the dehydration. On the other hand, the salting-in effect resulted from the change in the conformation of the PDMC brushes penetrating to the outer layer as the salt anions caused the PMEO₂MA to collapse on the CNC-Br surface. Therefore, tuning LCST of the block copolymer by engineering the PDMC block length, and presence of salt is achieved.

Chapter 8. Original Contributions and Recommendations for Future Studies

8.1. Original contributions to research

Oil sands tailings contain large amounts of toxic compounds and their volumes continue to increase each year. The oil sands tailings are disposed to the environment and stored in large structures known as tailings ponds. The exposure to the toxic substances present in these ponds causes nervous system disorders and skin cancer. Therefore, the treatment of oil sand tailings is urgent in order to protect biodiversity and to recover and recycle water for extracting oil sands. The flocculation process based on inorganic electrolytes and synthetic polymers is limited due to the possible link between Alzheimer's disease and residual aluminum from the use of aluminum salts or the risk of neurotoxic effects because of the presence of residual acrylamide from PAM. Therefore, modified polysaccharides have been extensively studied owing to their sustainability, biosafety and biodegradability. Cellulose nanocrystal is one of the most abundant materials and has been the subject of extensive research to enhance their potential for water treatment processes. This thesis seeks to develop CNC-based flocculants for use in oil sands tailings treatment process. The main objectives of this study include:

- (a)** development of cationic and thermo-responsive CNC-based flocculants with a tunable LCST in the range of oil extraction process and evaluate the effect of the copolymers coil-globule transition in bentonite removal as a model.
- (b)** development of cationic CNC-based flocculants with different chain length and evaluate effect of charge density in bentonite removal as a model.
- (c)** development of cationic biopolymer-based flocculants and evaluate the effect of cationic charge distribution in bentonite removal as a model.

- (d) development of cationic and thermo-responsive CNC-based copolymers and evaluate the effect of brush sequence, composition, and salt on the phase transition behavior.

The study examines both the material synthesis of CNC-based flocculants as well as their effectiveness in bentonite removal. The following sections summarize the major findings of this doctoral research.

8.1.1. Functional Cellulose Nanocrystals Containing Cationic and Thermo-Responsive Polymer Brushes for Bentonite Removal

This study focuses on the preparation of cationic and thermo-responsive CNC-based copolymer, where CNC was modified with MEO₂MA and OEGMA₃₀₀ to impart thermo-responsive property. The thermo-responsive CNC-based copolymer was further grafted with DMC to provide a cationic charge on the CNC surface. The cloud point measurements indicated that the LCST of the CNC-POEGMA could be manipulated by adjusting the DMC content. The effect of salt on the thermo-responsive characteristics of CNC-POEGMA followed a typical salting-out effect. The CNC-POEGMA-PDMC copolymers exhibited different thermo-responsiveness depending on the DMC content. For the copolymers with low DMC grafting ratio, the presence of low salt concentrations led to salting-in effect because of the released PDMC brushes as the negative charge on the CNC surface was screened while high salt concentrations caused salting-out effect due to the strong-ion pair interactions. The flocculation results indicated that the CNC-POEGMA-PDMC with higher grafting ratio of DMC is more effective with maximum flocculation efficiency of 95% at 21 mg/g. The thermo-responsiveness of the copolymers resulted in more compact flocs at lower dosage because the enhanced bridging interactions as the temperature increased above the LCST.

8.1.2. Flocculation of Bentonite by Cationic Cellulose Nanocrystals

In this study, the ARGET-ATRP technique was employed to synthesize cationic CNC-based copolymers with different chain lengths. The copolymers exhibited a pH and salt-responsiveness and the extent of sensitivity was more pronounced in the case of salt. The flocculation performance of CNC-PDMCs and inorganic electrolytes after 5 min settling followed the Hofmeister series based on the hydration of cations. Whereas the flocculation behavior of CNC-PDMCs and inorganic electrolytes after 24 h settling followed the classical DLVO theory based on the valence of cations. The CNC-PDMCs displayed better flocculation performance with up to 95% efficiency compared to inorganic electrolytes at lower dosages within 5 min.

8.1.3. Evaluation of Cationic Biopolymer-Based Flocculants on Bentonite Removal: Effect of Cationic Charge Distribution

In this study, three cationic CNC based flocculants: CNC-g-PDMC, PDADMAC-coated-CNC and PDADMAC-coated-CNF were prepared. The first was synthesized using ARGET-ATRP while the other two were prepared by physical adsorption. The CNC-g-PDMC possessed a branched-cationic structure while the other two systems have a flat-cationic layer structure. The CNC-g-PDMC was found to be the most effective in removing bentonite compared to the other two coated-polymers. These findings are based on the Singh's model that rationalized the dependence of flocculation performance on the conformation of flocculants. The extended cationic brushes from CNC-g-PDMC could approach and bind more effectively to bentonite particles while the flat conformation of the cationic-coated layer on PDADMAC-CNC and PDADMAC-CNF had limited capability due to the lower available sites for bridging.

8.1.4. Effects of Chain Architecture and Grafting Composition on the Thermo-responsive behavior of Cationic and Thermo-responsive Copolymers

In this study two cationic and thermo-responsive CNC-based copolymers with different brush sequence were synthesized using ARGET-ATRP technique. For each sequence, two grafting ratios of DMC were considered. The cloud point measurements revealed that the LCST of the CNC-PMEO₂MA shifted to high temperature when the PDMC brushes occupied the outer layer. On the other hand, when the PDMC occupied the inner layers of the copolymers (CNC-PDPMC-PMEO₂MA), the LCST was close to the one of the CNC-PMEO₂MA and not affected by PDMC brushes. The CNC-PMEO₂MA exhibited a typical salting-out effect while the CNC-PMEO₂MA-DMC and CNC-PDPMC-PMEO₂MA exhibited a salting-out effect at low salt concentrations and a salting-in effect at high salt concentrations.

8.2. Recommendations for future studies

Based on the results of the study conducted in this doctoral research, the following recommendations are suggested for future studies.

In Chapter 3, the flocculation performance of CNC-POEGMA-PDPMC was more effective when the RMHS protocol was used; however, the flocculant dosage was considered to be high. Therefore, it is recommended to use CNC-PDPMC first and then CNC-POEGMA because the high grafting density on the CNC substrate (in the case of CNC-POEGMA-DMC) could limit the capability of PDMC brushes to neutralize the bentonite particles. In addition, the compactness of the flocs could be higher after the addition of CNC-POEGMA since bentonite particles were neutralized in the first step by CNC-PDPMC. Consequently, the water recovery could be higher. This recommendation is based on the results obtained in Chapter 4 where the use of CNC-PDPMC alone resulted in 95% bentonite removal at 3 mg/g dosage within 5 min settling.

In Chapter 5, the CNC-PDMC showed better flocculation performance compared to inorganic electrolytes with flocculation efficiency of 95% within 5 min settling. The next steps will be to assess the efficiency of CNC-PDMC in the presence of inorganic electrolytes. The CNC-PDMC exhibited salt-responsiveness behavior which could alter their flocculation performance. It is recommended that we examine the validity of applying CNC-PDMC as a flocculant for wastewater containing anionic particles.

In Chapter 6, two recommended steps could be taken into consideration. First, we should compare and evaluate the flocculation performance of PDADMAC-coated-CNC and PDADMAC-coated-CNF with only the PDADMAC, where the effect of charge density can be studied in detail. Second, we should examine the flocculation efficiency of CNC-PDMC where the PDMC brushes grafted from de-sulfated CNC is compared to CNC-PDMC with sulfated CNC substrate with the same grafting ratio of PDMC. Will the presence of negative charges on CNC facilitates the repulsion between CNC-PDMCs and therefore enhancing the flocculation performance? Is the extended PDMC brushes critical to the flocculation performance of the system.

In Chapter 7, the prepared CNC-PMEO₂MA-DMC and CNC-PDMC-PMEO₂MA have a LCST not in the range of oil sands extraction, therefore, we could not examine their flocculation efficiency at the processing temperature. Hence, it is recommended that we graft OEGMA₃₀₀ and MEO₂MA from CNCs surface with the ratio 1:4 (mole ratio) as the results in Chapter 4 revealed that the LCST was 50 °C. Subsequently, we should compare the flocculation efficiency of CNC-POEGMA-PDMC with CNC-PDMC-POEGMA and evaluate the effect of chain architecture on the floc formation.

References

1. Vedoy, D. R. L. & Soares, J. B. P. Water-soluble polymers for oil sands tailing treatment: A Review. *Can. J. Chem. Eng.* **93**, 888–904 (2015).
2. Omotoso, O. E. & Mikula, R. J. High surface areas caused by smectitic interstratification of kaolinite and illite in Athabasca oil sands. *Appl. Clay Sci.* **25**, 37–47 (2004).
3. Omotoso, O., Mikula, R., Urquhart, S., Sulimma, H. & Stephens, P. Characterization of clays from poorly processing oil sands using synchrotron techniques. *Clay Sci.* (2006). doi:10.1017/CBO9781107415324.004
4. Masliyah, J., Zhou, Z. J., Xu, Z., Czarnecki, J. & Hamza, H. Understanding Water-Based Bitumen Extraction from Athabasca Oil Sands. *Can. J. Chem. Eng.* **82**, 628–654 (2008).
5. Oyeka, O., Felten, F. & Least, B. Screen-inflow-design considerations with inflow control devices in heavy oil. in *Society of Petroleum Engineers - SPE Heavy Oil Conference Canada 2014* **2**, 1070–1078 (2014).
6. Zhu, Y., Tan, X. & Liu, Q. Dual polymer flocculants for mature fine tailings dewatering. *Can. J. Chem. Eng.* **95**, 3–10 (2017).
7. Vajihinejad, V., Gumfekar, S. P., Bazoubandi, B., Rostami Najafabadi, Z. & Soares, J. B. P. Water Soluble Polymer Flocculants: Synthesis, Characterization, and Performance Assessment. *Macromolecular Materials and Engineering* (2019). doi:10.1002/mame.201800526
8. MacKinnon, M. D., Matthews, J. G., Shaw, W. H. & Cuddy, R. G. Water quality issues associated with Composite Tailings (CT) technology for managing oil sands tailings. *Int. J. Surf. Mining, Reclam. Environ.* **15**, 235–256 (2001).
9. Bratby, J. Coagulation and flocculation: with an emphasis on water and wastewater treatment. (1980). doi:10.1016/0300-9467(81)80062-7
10. Lee, C. S., Robinson, J. & Chong, M. F. A review on application of flocculants in wastewater treatment. *PROCESS SAF ENVIRON* **92**, 489–508 (2014).
11. Hjorth, M., Christensen, M. L. & Christensen, P. V. Flocculation, coagulation, and precipitation of manure affecting three separation techniques. *Bioresour. Technol.* **99**, 8598–8604 (2008).
12. Crittenden, J. C., Trussell, R. R., Hand, D. W., Howe, K. J. & Tchobanoglous, G. *MWH's Water Treatment: Principles and Design: Third Edition. MWH's Water Treatment: Principles and Design: Third Edition* (2012). doi:10.1002/9781118131473
13. Bolto, B. & Gregory, J. Organic polyelectrolytes in water treatment. *Water Research* **41**, 2301–2324 (2007).
14. Suopajärvi, T., Liimatainen, H., Hormi, O. & Niinimäki, J. Coagulation-flocculation treatment of municipal wastewater based on anionized nanocelluloses. *Chem. Eng. J.* **231**, 59–67 (2013).
15. Wu, C., Wang, Y., Gao, B., Zhao, Y. & Yue, Q. Coagulation performance and floc characteristics of aluminum sulfate using sodium alginate as coagulant aid for synthetic dyeing wastewater treatment. *Sep. Purif. Technol.* **95**, 180–187 (2012).
16. Brostow, W., Hagg Lobland, H. E., Pal, S. & Singh, R. P. Polymeric Flocculants for Wastewater and Industrial Effluent Treatment. *J. Mater. Educ. Pal Singh J. Mater. Educ.* **31**, 3–4 (2009).
17. Sharma, B. R., Dhuldhoya, N. C. & Merchant, U. C. Flocculants - An ecofriendly approach. *J. Polym. Environ.* **14**, 195–202 (2006).

18. Singh, R. P. *et al.* Biodegradable drag reducing agents and flocculants based on polysaccharides: Materials and applications. *Polym. Eng. Sci.* **40**, 46–60 (2000).
19. Renault, F., Sancey, B., Badot, P. M. & Crini, G. Chitosan for coagulation/flocculation processes - An eco-friendly approach. *Eur. Polym. J* **45**, 1337–1348 (2009).
20. Mishra, S., Usha Rani, G. & Sen, G. Microwave initiated synthesis and application of polyacrylic acid grafted carboxymethyl cellulose. *Carbohydr. Polym.* **87**, 2255–2262 (2012).
21. Lee, K. E., Morad, N., Teng, T. T. & Poh, B. T. Development, characterization and the application of hybrid materials in coagulation/flocculation of wastewater: A review. *Chemical Engineering Journal* **203**, 370–386 (2012).
22. Rabiee, A., Ershad-Langroudi, A. & Zeynali, M. E. A survey on cationic polyelectrolytes and their applications: Acrylamide derivatives. *Reviews in Chemical Engineering* **31**, 239–261 (2015).
23. Botha, L. & Soares, J. B. P. The Influence of Tailings Composition on Flocculation. *Can. J. Chem. Eng.* **93**, 1514–1523 (2015).
24. Omotoso, O., Mikula, R., Urquhart, S., Sulimma, H. & Stephens, P. Characterization of clays from poorly processing oil sands using synchrotron techniques. *Clay Sci.* **12**, 88–93 (2006).
25. Omotoso, O., Mikula, R. J. & Stephens, P. W. Surface Area of Interstratified Phyllosilicates in Athabasca Oil Sands From Synchrotron XRD. *Adv. X-ray Anal.* **45**, 391–396 (2002).
26. Kaminsky, H. A. W., Etsell, T. H., Ivey, D. G. & Omotoso, O. Distribution of clay minerals in the process streams produced by the extraction of bitumen from athabasca oil sands. *Can. J. Chem. Eng.* **87**, 85–93 (2009).
27. Sengupta, S., Tollefson, E. L. & Dalai, A. K. Recovery, Characterization and Conceptual Modelling of Non-Bituminous Organic Materials from Oil Sands. *Can. J. Chem. Eng.* **75**, 379–390 (1997).
28. Dusseault, M. B. & Scott, J. D. Tailings pond behavior and characterization of oil sand tailings sludge. *Part. Sci. Technol.* **1**, 295–309 (1983).
29. Hunter, R. J. *Foundations of Colloid Science (2nd Edition)*. Oxford University Press (2001).
30. Tournassat, C., Bourg, I. C., Steefel, C. I. & Bergaya, F. Chapter 1 - Surface Properties of Clay Minerals. in *Natural and Engineered Clay Barriers* (eds. Tournassat, C., Steefel, C. I., Bourg, I. C. & Bergaya, F. B. T.-D. in C. S.) **6**, 5–31 (Elsevier, 2015).
31. Mode, A. W., Anyiam, O. A. & Anigbogu, E. C. The effect of diagenesis on reservoir quality of Mamu Sandstone, Anambra basin, Nigeria. *J. Geol. Soc. India* **87**, 583–590 (2016).
32. Preocanin, T., Abdelmonem, A., Montavon, G. & Luetzenkirchen, J. Charging Behavior of Clays and Clay Minerals in Aqueous Electrolyte Solutions — Experimental Methods for Measuring the Charge and Interpreting the Results. in *Clays, Clay Minerals and Ceramic Materials Based on Clay Minerals* (2016). doi:10.5772/62082
33. Shamsuddin, R. M., Verbeek, C. J. R. & Lay, M. C. Settling of Bentonite Particles in Gelatin Solutions for Stickwater Treatment. in *Procedia Engineering* **148**, 194–200 (2016).
34. Grim, R. E. History of the Development of Clay Mineralogy. *Clays Clay Miner.* **36**, 97–101 (1988).

35. Motawie, A. M. *et al.* Physico-chemical characteristics of nano-organo bentonite prepared using different organo-modifiers. *Egypt. J. Pet.* **23**, 331–338 (2014).
36. Önal, M. Swelling and cation exchange capacity relationship for the samples obtained from a bentonite by acid activations and heat treatments. *Appl. Clay Sci.* (2007). doi:10.1016/j.clay.2006.12.004
37. CHOROM, M. & RENGASAMY, P. Dispersion and zeta potential of pure clays as related to net particle charge under varying pH, electrolyte concentration and cation type. *Eur. J. Soil Sci.* **46**, 657–665 (1995).
38. Speed, D. E. Environmental aspects of planarization processes. in *Advances in Chemical Mechanical Planarization (CMP)* 1–269 (2016). doi:10.1016/B978-0-08-100165-3.00010-3
39. Parsons, R. Electrical Double Layer: Recent Experimental and Theoretical Developments. *Chem. Rev.* **90**, 813–826 (1990).
40. Binazadeh, M., Xu, M., Zolfaghari, A. & Dehghanpour, H. Effect of Electrostatic Interactions on Water Uptake of Gas Shales: The Interplay of Solution Ionic Strength and Electrostatic Double Layer. *Energy and Fuels* **30**, 992–1001 (2016).
41. Derjaguin, B. & Landau, L. Theory of the stability of strongly charged lyophobic sols and of the adhesion of strongly charged particles in solutions of electrolytes. *Prog. Surf. Sci.* (1993). doi:10.1016/0079-6816(93)90013-L
42. Handy, R. D. *et al.* The ecotoxicology and chemistry of manufactured nanoparticles. *Ecotoxicology* **17**, 287–314 (2008).
43. Gregory, J. & Barany, S. Adsorption and flocculation by polymers and polymer mixtures. *Adv. Colloid Interface Sci* **169**, 1–12 (2011).
44. Somasundaran, P. & Runkana, V. Modeling flocculation of colloidal mineral suspensions using population balances. *Int. J. Miner. Process.* **72**, 33–55 (2003).
45. Theng, B. K. G. Formation and prospecties of clay- polymer complexes. (1979). doi:10.1016/0016-7037(80)90254-9
46. Mporfu, P., Addai-Mensah, J. & Ralston, J. Investigation of the effect of polymer structure type on flocculation, rheology and dewatering behaviour of kaolinite dispersions. *Int. J. Miner. Process.* **71**, 247–268 (2003).
47. Qiu, X. & Hu, S. ‘Smart’ materials based on cellulose: A review of the preparations, properties, and applications. *Materials* **6**, 738–781 (2013).
48. Rojas, J., Bedoya, M. & Ciro, Y. Current Trends in the Production of Cellulose Nanoparticles and Nanocomposites for Biomedical Applications. in *Cellulose - Fundamental Aspects and Current Trends* (2015). doi:10.5772/61334
49. Lee, H. V., Hamid, S. B. A. & Zain, S. K. Conversion of lignocellulosic biomass to nanocellulose: Structure and chemical process. *Sci. World J.* **2014**, (2014).
50. Kaushik, M., Frascini, C., Chauve, G., Putaux, J.-L. & Moores, A. Transmission Electron Microscopy for the Characterization of Cellulose Nanocrystals. in *The Transmission Electron Microscope - Theory and Applications* (2015). doi:10.5772/60985
51. Liang, H. & Hu, X. A quick review of the applications of nano crystalline cellulose in wastewater treatment. *J. Bioresour. Bioprod.* **2016**, 199–204 (2016).
52. Lin, N., Huang, J. & Dufresne, A. Preparation, properties and applications of polysaccharide nanocrystals in advanced functional nanomaterials: A review. *Nanoscale* **4**, 3274–3294 (2012).
53. Ehmann, H. M. A. *et al.* Design of anticoagulant surfaces based on cellulose nanocrystals.

- Chem. Commun.* **50**, 13070–13072 (2014).
54. Grishkewich, N., Mohammed, N., Tang, J. & Tam, K. C. Recent advances in the application of cellulose nanocrystals. *Curr. Opin. Colloid Interface Sci* **29**, 32–45 (2017).
 55. Shopsowitz, K. E., Qi, H., Hamad, W. Y. & MacLachlan, M. J. Free-standing mesoporous silica films with tunable chiral nematic structures. *Nature* **468**, 422–426 (2010).
 56. Cranston, E. D. & Gray, D. G. Birefringence in spin-coated films containing cellulose nanocrystals. *Colloids Surf, A Physicochem Eng Asp.* **325**, 44–51 (2008).
 57. Vandamme, D., Eyley, S., Van den Mooter, G., Muylaert, K. & Thielemans, W. Highly charged cellulose-based nanocrystals as flocculants for harvesting *Chlorella vulgaris*. *Bioresour. Technol.* **194**, 270–275 (2015).
 58. Eyley, S. *et al.* CO₂ controlled flocculation of microalgae using pH responsive cellulose nanocrystals. *Nanoscale* **7**, 14413–14421 (2015).
 59. Eichhorn, S. J. *et al.* Review: Current international research into cellulose nanofibres and nanocomposites. *J. Mater. Sci* **45**, 1–33 (2010).
 60. Habibi, Y., Lucia, L. A. & Rojas, O. J. Cellulose nanocrystals: Chemistry, self-assembly, and applications. *Chem. Rev.* **110**, 3479–3500 (2010).
 61. George, J. & Sabapathi, S. N. Cellulose nanocrystals: Synthesis, functional properties, and applications. *Nanotechnol. Sci. Appl.* **8**, 45–54 (2015).
 62. Lizundia, E., Meaurio, E. & Vilas, J. L. Grafting of Cellulose Nanocrystals. in *Multifunctional Polymeric Nanocomposites Based on Cellulosic Reinforcements* 61–113 (2016). doi:10.1016/B978-0-323-44248-0.00003-1
 63. Pino-Ramos, V. H. *et al.* Radiation Grafting for the Functionalization and Development of Smart Polymeric Materials. in 67–94 (2017). doi:10.1007/978-3-319-54145-7_3
 64. Kumar, A., Srivastava, A., Galaev, I. Y. & Mattiasson, B. Smart polymers: physical forms and bioengineering applications. *Prog. Polym. Sci.* **32**, 1205–1237 (2007).
 65. Galaev, I. Y. & Mattiasson, B. ‘Smart’ polymers and what they could do in biotechnology and medicine. *Trends Biotechnol.* **17**, 335–340 (1999).
 66. Hoffman, A. S. *et al.* Really smart bioconjugates of smart polymers and receptor proteins. *J. Biomed. Mater. Res.* **52**, 577–586 (2000).
 67. Cabane, E., Zhang, X., Langowska, K., Palivan, C. G. & Meier, W. Stimuli-responsive polymers and their applications in nanomedicine. *Biointerphases* **7**, 9 (2012).
 68. Seuring, J. & Agarwal, S. Non-Ionic Homo- and Copolymers with H-Donor and H-Acceptor Units with an UCST in Water. *Macromol. Chem. Phys.* **211**, 2109–2117 (2010).
 69. Zhang, Q., Weber, C., Schubert, U. S. & Hoogenboom, R. Thermoresponsive polymers with lower critical solution temperature: from fundamental aspects and measuring techniques to recommended turbidimetry conditions. *Mater. Horizons* **4**, 109–116 (2017).
 70. Bawa, P., Pillay, V., Choonara, Y. E. & Du Toit, L. C. Stimuli-responsive polymers and their applications in drug delivery. *Biomed. Mater.* **4**, 22001 (2009).
 71. Hoffman, A. S. “Intelligent” polymers in medicine and biotechnology. *Artif. Organs* **19**, 458–467 (1995).
 72. Gao, S. *et al.* Stimuli-responsive bio-based polymeric systems and their applications. *J. Mater. Chem. B* **7**, 709–729 (2019).
 73. Ward, M. A. & Georgiou, T. K. Thermoresponsive polymers for biomedical applications. *Polymers (Basel)* **3**, 1215–1242 (2011).
 74. Zoppe, J. O. *et al.* Poly (N-isopropylacrylamide) brushes grafted from cellulose nanocrystals via surface-initiated single-electron transfer living radical polymerization.

- Biomacromolecules* **11**, 2683–2691 (2010).
75. Lutz, J.-F. & Hoth, A. Preparation of ideal PEG analogues with a tunable thermosensitivity by controlled radical copolymerization of 2-(2-methoxyethoxy) ethyl methacrylate and oligo (ethylene glycol) methacrylate. *Macromolecules* **39**, 893–896 (2006).
 76. Gandhi, A., Paul, A., Sen, S. O. & Sen, K. K. Studies on thermoresponsive polymers: Phase behaviour, drug delivery and biomedical applications. *Asian J. Pharm. Sci* **10**, 99–107 (2015).
 77. Baughman, D. R. & Liu, Y. A. *Neural networks in bioprocessing and chemical engineering*. (Academic press, 2014).
 78. Aina, A. *et al.* Dissolution behavior of poly vinyl alcohol in water and its effect on the physical morphologies of PLGA scaffolds. *UK JPB* **2**, 1–6 (2014).
 79. Ruzette, A.-V. G. & Mayes, A. M. A simple free energy model for weakly interacting polymer blends. *Macromolecules* **34**, 1894–1907 (2001).
 80. Muthukumar, M. Thermodynamics of polymer solutions. *J. Chem. Phys.* **85**, 4722–4728 (1986).
 81. Gil, E. S. & Hudson, S. M. Stimuli-responsive polymers and their bioconjugates. *Prog. Polym. Sci.* **29**, 1173–1222 (2004).
 82. Wu, C. & Wang, X. Globule-to-coil transition of a single homopolymer chain in solution. *Phys. Rev. Lett.* **80**, 4092 (1998).
 83. Pietrasik, J., Sumerlin, B. S., Lee, R. Y. & Matyjaszewski, K. Solution Behavior of Temperature-Responsive Molecular Brushes Prepared by ATRP. *Macromol. Chem. Phys.* **208**, 30–36 (2007).
 84. Okabe, S., Sugihara, S., Aoshima, S. & Shibayama, M. Heat-induced self-assembling of thermosensitive block copolymer. 1. Small-angle neutron scattering study. *Macromolecules* **35**, 8139–8146 (2002).
 85. Dimitrov, I., Trzebicka, B., Müller, A. H. E., Dworak, A. & Tsvetanov, C. B. Thermosensitive water-soluble copolymers with doubly responsive reversibly interacting entities. *Prog. Polym. Sci.* **32**, 1275–1343 (2007).
 86. Troll, K. *et al.* The collapse transition of poly (styrene-*b*-(N-isopropyl acrylamide)) diblock copolymers in aqueous solution and in thin films. *Colloid Polym. Sci.* **286**, 1079–1092 (2008).
 87. Zhao, C., Ma, Z. & Zhu, X. X. Rational design of thermoresponsive polymers in aqueous solutions: A thermodynamics map. *Prog. Polym. Sci.* **90**, 269–291 (2019).
 88. Xia, Y., Yin, X., Burke, N. A. D. & Stöver, H. D. H. Thermal response of narrow-disperse poly (N-isopropylacrylamide) prepared by atom transfer radical polymerization. *Macromolecules* **38**, 5937–5943 (2005).
 89. Weaver, J. V. M. *et al.* Stimulus-responsive water-soluble polymers based on 2-hydroxyethyl methacrylate. *Macromolecules* **37**, 2395–2403 (2004).
 90. Jeong, N. S. *et al.* Polymers with molecular weight dependent LCSTs are essential for cooperative behaviour. *Polym. Chem.* **3**, 794–799 (2012).
 91. Zhao, Y., Tremblay, L. & Zhao, Y. Phototunable LCST of water-soluble polymers: exploring a topological effect. *Macromolecules* **44**, 4007–4011 (2011).
 92. Honda, S., Yamamoto, T. & Tezuka, Y. Topology-directed control on thermal stability: micelles formed from linear and cyclized amphiphilic block copolymers. *J. Am. Chem. Soc.* **132**, 10251–10253 (2010).

93. Qiu, X.-P., Tanaka, F. & Winnik, F. M. Temperature-induced phase transition of well-defined cyclic poly (N-isopropylacrylamide) s in aqueous solution. *Macromolecules* **40**, 7069–7071 (2007).
94. Jerca, F. A., Jerca, V. V., Anghelache, A. M., Vuluga, D. M. & Hoogenboom, R. Poly (2-isopropenyl-2-oxazoline) as a versatile platform towards thermoresponsive copolymers. *Polym. Chem.* **9**, 3473–3478 (2018).
95. Jerca, F. A., Jerca, V. V. & Hoogenboom, R. Well-Defined Thermoresponsive Polymethacrylamide Copolymers with Ester Pendent Groups through One-Pot Statistical Postpolymerization Modification of Poly (2-Isopropenyl-2-Oxazoline) with Multiple Carboxylic Acids. *J. Polym. Sci. Part A Polym. Chem.* **57**, 360–366 (2019).
96. Becer, C. R. *et al.* Libraries of methacrylic acid and oligo (ethylene glycol) methacrylate copolymers with LCST behavior. *J. Polym. Sci. Part A Polym. Chem.* **46**, 7138–7147 (2008).
97. Weiss, J., Li, A., Wischerhoff, E. & Laschewsky, A. Water-soluble random and alternating copolymers of styrene monomers with adjustable lower critical solution temperature. *Polym. Chem.* **3**, 352–361 (2012).
98. Zhu, Y., Batchelor, R., Lowe, A. B. & Roth, P. J. Design of thermoresponsive polymers with aqueous lcst, ucst, or both: Modification of a reactive poly (2-vinyl-4, 4-dimethylazlactone) scaffold. *Macromolecules* **49**, 672–680 (2016).
99. Sun, W., An, Z. & Wu, P. UCST or LCST? Composition-Dependent Thermoresponsive Behavior of Poly (N-acryloylglycinamide-co-diacetone acrylamide). *Macromolecules* **50**, 2175–2182 (2017).
100. Jung, S.-H. & Lee, H. Well-defined thermoresponsive copolymers with tunable LCST and UCST in water. *Bull. Korean Chem. Soc* **35**, 501 (2014).
101. Yan, Q. & Zhao, Y. Block copolymer self-assembly controlled by the “green” gas stimulus of carbon dioxide. *Chem. Commun.* **50**, 11631–11641 (2014).
102. Cao, Y., Zhao, N., Wu, K. & Zhu, X. X. Solution properties of a thermosensitive triblock copolymer of N-alkyl substituted acrylamides. *Langmuir* **25**, 1699–1704 (2009).
103. Cao, Y., Zhu, X. X., Luo, J. & Liu, H. Effects of substitution groups on the RAFT polymerization of N-alkylacrylamides in the preparation of thermosensitive block copolymers. *Macromolecules* **40**, 6481–6488 (2007).
104. Jia, Y. G. & Zhu, X. X. Complex thermoresponsive behavior of diblock polyacrylamides. *Polym. Chem.* **5**, 4358–4364 (2014).
105. Li, Q., Li, L., Tian, Q., Xu, J. & Liu, J. Doubly thermo-responsive polymers and their two-step phase transition behavior: A review. *Nanosci. Nanotechnol. Lett* **9**, 89–99 (2017).
106. Mori, H., Kato, I., Saito, S. & Endo, T. Proline-based block copolymers displaying upper and lower critical solution temperatures. *Macromolecules* **43**, 1289–1298 (2010).
107. Tian, H. Y. *et al.* Synthesis of thermo-responsive polymers with both tunable UCST and LCST. *Macromol. Rapid Commun.* **32**, 660–664 (2011).
108. Yamamoto, S. I., Pietrasik, J. & Matyjaszewski, K. The effect of structure on the thermoresponsive nature of well-defined poly(oligo(ethylene oxide) methacrylates) synthesized by ATRP. *J. Polym. Sci. Part A Polym. Chem.* **46**, 194–202 (2008).
109. Sang Beom Lee, Song, S. C., Jin, J. H. & Youn Soo Sohn. Solvent effect on the lower critical solution temperature of biodegradable thermosensitive poly(organophosphazenes). *Polym. Bull.* **45**, 389–396 (2000).
110. Zhao, L., Ma, K. & Yang, Z. Changes of water hydrogen bond network with different

- externalities. *Int. J. Mol. Sci* **16**, 8454–8489 (2015).
111. Li, Y. *et al.* Supramolecular nanofibrillar thermoreversible hydrogel for growth and release of cancer spheroids. *Angew. Chemie Int. Ed.* **56**, 6083–6087 (2017).
 112. Cudjoe, E. *et al.* Biomimetic reversible heat-stiffening polymer nanocomposites. *ACS Cent. Sci.* **3**, 886–894 (2017).
 113. Orasugh, J. T. *et al.* Effect of cellulose nanocrystals on the performance of drug loaded in situ gelling thermo-responsive ophthalmic formulations. *Int. J. Biol. Macromol.* **124**, 235–245 (2019).
 114. Sun, X. *et al.* Unique thermo-responsivity and tunable optical performance of poly (N-isopropylacrylamide)-cellulose nanocrystal hydrogel films. *Carbohydr. Polym.* **208**, 495–503 (2019).
 115. Santos, M. V *et al.* Optical sensor platform based on cellulose nanocrystals (CNC)–4'-(hexyloxy)-4-biphenylcarbonitrile (HOBC) bi-phase nematic liquid crystal composite films. *Carbohydr. Polym.* **168**, 346–355 (2017).
 116. Zubik, K., Singhsa, P., Wang, Y., Manuspiya, H. & Narain, R. Thermo-responsive poly (N-isopropylacrylamide)-cellulose nanocrystals hybrid hydrogels for wound dressing. *Polymers (Basel)*. **9**, 119 (2017).
 117. Risteen, B. *et al.* Thermally switchable liquid crystals based on cellulose nanocrystals with patchy polymer grafts. *Small* **14**, 1802060 (2018).
 118. Brinatti, C. *et al.* Controlled coagulation and redispersion of thermoresponsive poly di (ethylene oxide) methyl ether methacrylate grafted cellulose nanocrystals. *J. Colloid Interface Sci.* **538**, 51–61 (2019).
 119. Azzam, F. *et al.* Tunable aggregation and gelation of thermoresponsive suspensions of polymer-grafted cellulose nanocrystals. *Biomacromolecules* **17**, 2112–2119 (2016).
 120. Faix, O. Fourier Transform Infrared Spectroscopy. in 83–109 (1992). doi:10.1007/978-3-642-74065-7_7
 121. Khan, J. I., Kennedy, T. J. & Christian, D. R. *Basic Principles of Forensic Chemistry*. *Basic Principles of Forensic Chemistry* (2012). doi:10.1007/978-1-59745-437-7
 122. Malvern Instruments Limited. *Dynamic Light Scattering: An Introduction in 30 Minutes*. (2014).
 123. Bhattacharjee, S. DLS and zeta potential - What they are and what they are not? *J. Control. Release* **235**, 337–351 (2016).
 124. Uskoković, V. Dynamic Light Scattering Based Microelectrophoresis: Main Prospects and Limitations. *J. Dispers. Sci. Technol.* **33**, 1762–1786 (2012).
 125. Fultz, B. & Howe, J. M. *Transmission electron microscopy and diffractometry of materials*. *Transmission Electron Microscopy and Diffractometry of Materials* (2008). doi:10.1007/978-3-540-73886-2
 126. Williams, D. B. & Carter, C. B. The Transmission Electron Microscope. in *Transmission Electron Microscopy* 3–17 (Springer US, 1996). doi:10.1007/978-1-4757-2519-3_1
 127. Clark, B. J., Frost, T., & Russell, M. A. *UV Spectroscopy: Techniques, Instrumentation and Data Handling*. (London : Chapman & Hall, 1993., 1993).
 128. Nilapwar, S. M., Nardelli, M., Westerhoff, H. V. & Verma, M. Absorption spectroscopy. in *Methods in Enzymology* **500**, 59–75 (2011).
 129. Kolthoff, I. M. Conductometric Titrations. *Ind. Eng. Chem. - Anal. Ed.* **2**, 225–230 (1930).
 130. Lee, M. F. X., Chan, E. S., Tam, K. C. & Tey, B. T. Thermo-responsive adsorbent for size-selective protein adsorption. *J. Chromatogr. A* **1394**, 71–80 (2015).

131. Elwakeel, K. Z. Removal of Cr (VI) from alkaline aqueous solutions using chemically modified magnetic chitosan resins. *Desalination* **250**, 105–112 (2010).
132. Cranston, E. D. & Gray, D. G. Birefringence in spin-coated films containing cellulose nanocrystals. *Colloids Surf, A Physicochem Eng Asp.* **325**, 44–51 (2008).
133. Shopsowitz, K. E., Qi, H., Hamad, W. Y. & MacLachlan, M. J. Free-standing mesoporous silica films with tunable chiral nematic structures. *Nature* **468**, 422–425 (2010).
134. Grishkewich, N., Mohammed, N., Tang, J. & Tam, K. C. Recent advances in the application of cellulose nanocrystals. *Curr. Opin. Colloid Interface Sci.* **29**, 32–45 (2017).
135. Habibi, Y., Lucia, L. A. & Rojas, O. J. Cellulose nanocrystals: chemistry, self-assembly, and applications. *Chem. Rev.* **110**, 3479–3500 (2010).
136. Eichhorn, S. J. *et al.* Review: Current international research into cellulose nanofibres and nanocomposites. *J. Mater. Sci.* **45**, 1-33(2010).
137. Stuart, M. A. C. *et al.* Emerging applications of stimuli-responsive polymer materials. *Nat. Mater.* **9**, 101–113 (2010).
138. McKee, J. R. *et al.* Thermoresponsive nanocellulose hydrogels with tunable mechanical properties. *ACS Macro Lett.* **3**, 266–270 (2014).
139. Guillet, J. E., Heskins, M. & Murray, D. G. Polymeric flocculants. (1985).
140. Li, H., Long, J., Xu, Z. & Masliyah, J. H. Flocculation of kaolinite clay suspensions using a temperature-sensitive polymer. *AIChE J.* **53**, 479–488 (2007).
141. Long, J., Li, H., Xu, Z. & Masliyah, J. H. Improving oil sands processability using a temperature-sensitive polymer. *Energy & fuels* **25**, 701–707 (2011).
142. Ng, W. S., Connal, L. A., Forbes, E. & Franks, G. V. A review of temperature-responsive polymers as novel reagents for solid-liquid separation and froth flotation of minerals. *Miner. Eng.* **123**, 144–159 (2018).
143. Wu, C., Wang, Y., Gao, B., Zhao, Y. & Yue, Q. Coagulation performance and floc characteristics of aluminum sulfate using sodium alginate as coagulant aid for synthetic dyeing wastewater treatment. *Sep. Purif. Technol.* (2012). doi:10.1016/j.seppur.2012.05.009
144. Bolto, B. & Gregory, J. Organic polyelectrolytes in water treatment. *Water Research* (2007). doi:10.1016/j.watres.2007.03.012
145. Singh, R. P. *et al.* Biodegradable drag reducing agents and flocculants based on polysaccharides: Materials and applications. *Polym. Eng. Sci.* (2000). doi:10.1002/pen.11138
146. Renault, F., Sancey, B., Badot, P. M. & Crini, G. Chitosan for coagulation/flocculation processes - An eco-friendly approach. *Eur. Polym. J.* **45(5)**, 1337-1348 (2009). doi:10.1016/j.eurpolymj.2008.12.027
147. Wang, Y., Gao, B., Yue, Q., Wei, J. & Li, Q. The characterization and flocculation efficiency of composite flocculant iron salts-polydimethyldiallylammonium chloride. *Chem. Eng. J.* (2008). doi:10.1016/j.cej.2007.11.022
148. Rabiee, A., Ershad-Langroudi, A. & Zeynali, M. E. A survey on cationic polyelectrolytes and their applications: Acrylamide derivatives. *Reviews in Chemical Engineering* (2015). doi:10.1515/revce-2014-0056
149. Kloser, E. & Gray, D. G. Surface grafting of cellulose nanocrystals with poly(ethylene oxide) in aqueous media. *Langmuir* **26**, 13450–13456 (2010).
150. Grishkewich, N., Akhlaghi, S. P., Zhaoling, Y., Berry, R. & Tam, K. C. Cellulose nanocrystal-poly (oligo (ethylene glycol) methacrylate) brushes with tunable LCSTs.

- Carbohydr. Polym.* **144**, 215–222 (2016).
151. Alharthi, S., Grishkewich, N., Berry, R. M. & Tam, K. C. Functional cellulose nanocrystals containing cationic and thermo-responsive polymer brushes. *Carbohydr. Polym.* **246**, 116651-116659 (2020).
 152. Lizundia, E., Meaurio, E. & Vilas, J. L. Grafting of cellulose nanocrystals. in *Multifunctional Polymeric Nanocomposites Based on Cellulosic Reinforcements* 61–113 (Elsevier, 2016).
 153. Kan, K. H. M., Li, J., Wijesekera, K. & Cranston, E. D. Polymer-grafted cellulose nanocrystals as pH-responsive reversible flocculants. *Biomacromolecules* **14**, 3130–3139 (2013).
 154. Kan, K. H. M., Li, J., Wijesekera, K. & Cranston, E. D. Polymer-grafted cellulose nanocrystals as pH-responsive reversible flocculants. *Biomacromolecules* **14**, 3130–3139 (2013).
 155. Varma, A. J. & Chavan, V. B. Thermal properties of oxidized cellulose. *Cellulose* **2**, 41–49 (1995).
 156. He, M., Xiao, H., Zhou, Y. & Lu, P. Synthesis, characterization and antimicrobial activities of water-soluble amphiphilic copolymers containing ciprofloxacin and quaternary ammonium salts. *J. Mater. Chem. B* **3**, 3704–3713 (2015).
 157. Osváth, Z. & Iván, B. The Dependence of the Cloud Point, Clearing Point, and Hysteresis of Poly (N-isopropylacrylamide) on Experimental Conditions: The Need for Standardization of Thermoresponsive Transition Determinations. *Macromol. Chem. Phys.* **218**, 1600470 (2017).
 158. Zhang, Y., Furyk, S., Bergbreiter, D. E. & Cremer, P. S. Specific ion effects on the water solubility of macromolecules: PNIPAM and the Hofmeister series. *J. Am. Chem. Soc.* **127**, 14505–14510 (2005).
 159. Phan-Xuan, T. *et al.* Aggregation behavior of aqueous cellulose nanocrystals: the effect of inorganic salts. *Cellulose* **23**, 3653–3663 (2016).
 160. Prathapan, R., Thapa, R., Garnier, G. & Tabor, R. F. Modulating the zeta potential of cellulose nanocrystals using salts and surfactants. *Colloids Surf, A Physicochem Eng Asp.* **509**, 11–18 (2016).
 161. Kou, R., Zhang, J., Chen, Z. & Liu, G. Counterion Specificity of Polyelectrolyte Brushes: Role of Specific Ion-Pairing Interactions. *ChemPhysChem* **19**, 1404–1413 (2018).
 162. Zhang, J., Kou, R. & Liu, G. Effect of salt concentration on the pH responses of strong and weak polyelectrolyte brushes. *Langmuir* **33**, 6838–6845 (2017).
 163. García-García, S., Jonsson, M. & Wold, S. Temperature effect on the stability of bentonite colloids in water. *J. Colloid Interface Sci.* **298**, 694–705 (2006).
 164. Shah, A. *et al.* A review of novel techniques for heavy oil and bitumen extraction and upgrading. *Energy Environ. Sci.* **3**, 700–714 (2010).
 165. Penner, T. J. & Foght, J. M. Mature fine tailings from oil sands processing harbour diverse methanogenic communities. *Can. J. Microbiol.* **56**, 459–470 (2010).
 166. Madill, R. E. A., Orzechowski, M. T., Chen, G., Brownlee, B. G. & Bunce, N. J. Preliminary risk assessment of the wet landscape option for reclamation of oil sands mine tailings: bioassays with mature fine tailings pore water. *Environ. Toxicol. An Int. J.* **16**, 197–208 (2001).
 167. Herman, D. C., Fedorak, P. M., MacKinnon, M. D. & Costerton, J. W. Biodegradation of naphthenic acids by microbial populations indigenous to oil sands tailings. *Can. J.*

- Microbiol.* **40**, 467–477 (1994).
168. Allen, E. W. Process water treatment in Canada's oil sands industry: I. Target pollutants and treatment objectives. *J. Environ. Eng. Sci.* **7**, 123–138 (2008).
 169. Jewell, R. J. & Fourie, A. B. Paste and Thickened Tailings: A Guide-Australian Centre for Geomechanics. *Perth, West. Aust.* **6**, (2006).
 170. Hooshiar, A., Uhlik, P., Ivey, D. G., Liu, Q. & Etsell, T. H. Clay minerals in nonaqueous extraction of bitumen from Alberta oil sands: Part 2. Characterization of clay minerals. *Fuel Process. Technol.* **96**, 183–194 (2012).
 171. Grim, R. E. The history of the development of clay mineralogy. *Clays Clay Miner.* **36**, 97–101 (1988).
 172. Baik, M. H. & Lee, S. Y. Colloidal stability of bentonite clay considering surface charge properties as a function of pH and ionic strength. *J. Ind. Eng. Chem.* **16**, 837–841 (2010).
 173. Shamsuddin, R. M., Verbeek, C. J. R. & Lay, M. C. Settling of Bentonite Particles in Gelatin Solutions for Stickwater Treatment. in *4th International Conference on Process Engineering and Advanced Materials (ICPEAM)* **148**, 194–200 (Elsevier Ltd, 2016).
 174. Headley, J. V *et al.* Ultrahigh-resolution mass spectrometry of simulated runoff from treated oil sands mature fine tailings. *Rapid Commun. Mass Spectrom.* **24**, 2400–2406 (2010).
 175. Beier, N., Wilson, W., Dunmola, A. & Sego, D. Impact of flocculation-based dewatering on the shear strength of oil sands fine tailings. *Can. Geotech. J.* **50**, 1001–1007 (2013).
 176. Li, H., Long, J., Xu, Z. & Masliyah, J. H. Synergetic role of polymer flocculant in low-temperature bitumen extraction and tailings treatment. *Energy & fuels* **19**, 936–943 (2005).
 177. Criddle, J. *A review of the mammalian and aquatic toxicity of polyelectrolytes.* (National Rivers Authority, Great Britain, 1990).
 178. Wu, C., Wang, Y., Gao, B., Zhao, Y. & Yue, Q. Coagulation performance and floc characteristics of aluminum sulfate using sodium alginate as coagulant aid for synthetic dyeing wastewater treatment. *Sep. Purif. Technol.* **95**, 180–187 (2012).
 179. Bolto, B. & Gregory, J. Organic polyelectrolytes in water treatment. *Water Res.* **41**, 2301–2324 (2007).
 180. Habibi, Y., Lucia, L. A. & Rojas, O. J. Cellulose nanocrystals: Chemistry, self-assembly, and applications. *Chem. Rev.* **110**, 3479–3500 (2010).
 181. Kloser, E. & Gray, D. G. Surface grafting of cellulose nanocrystals with poly (ethylene oxide) in aqueous media. *Langmuir* **26**, 13450–13456 (2010).
 182. Eyley, S. *et al.* CO₂ controlled flocculation of microalgae using pH responsive cellulose nanocrystals. *Nanoscale* **7**, 14413–14421 (2015).
 183. Eichhorn, S. J. *et al.* Current international research into cellulose nanofibres and nanocomposites. *J. Mater. Sci.* **45**, 1–33 (2010).
 184. Zhang, Z., Sèbe, G., Wang, X. & Tam, K. C. UV-absorbing cellulose nanocrystals as functional reinforcing fillers in poly (vinyl chloride) films. *ACS Appl. Nano Mater.* **1**, 632–641 (2018).
 185. Xu, K. *et al.* A novel hyperbranched polymeric flocculant for waste-water treatment. *J. Polym. Environ.* **26**, 2782–2792 (2018).
 186. Liu, Y., Luo, M. & Lai, J. Poly (tetrafluoroethylene) Film Surface Functionalization with 2-Bromoisobutyryl Bromide as Initiator for Surface-Initiated Atom-Transfer Radical Polymerization. *Macromol. Rapid Commun.* **28**, 329–333 (2007).

187. Majoinen, J. *et al.* Polyelectrolyte brushes grafted from cellulose nanocrystals using Cu-mediated surface-initiated controlled radical polymerization. *Biomacromolecules* **12**, 2997–3006 (2011).
188. Wu, B. *et al.* Reorganization of hydrogen bond network makes strong polyelectrolyte brushes pH-responsive. *Sci. Adv.* **2**, e1600579 (2016).
189. Manning, G. S. Limiting laws and counterion condensation in polyelectrolyte solutions I. Colligative properties. *J. Chem. Phys.* **51**, 924–933 (1969).
190. Trizac, E. & Téllez, G. Onsager-Manning-Oosawa condensation phenomenon and the effect of salt. *Phys. Rev. Lett.* **96**, 38302 (2006).
191. Bean, E. L., Campbell, S. J. & Anspach, F. R. Zeta potential measurements in the control of coagulation chemical doses. *Journal-American Water Work. Assoc.* **56**, 214–227 (1964).
192. Ye, C. *et al.* Alkalinity effect of coagulation with polyaluminum chlorides: Role of electrostatic patch. *Colloids Surfaces A Physicochem. Eng. Asp.* **294**, 163–173 (2007).
193. Chen, Y., Liu, S. & Wang, G. A kinetic investigation of cationic starch adsorption and flocculation in kaolin suspension. *Chem. Eng. J.* **133**, 325–333 (2007).
194. van der Linden, M. *et al.* Microscopic origin of the Hofmeister effect in gelation kinetics of colloidal silica. *J. Phys. Chem. Lett.* **6**, 2881–2887 (2015).
195. Chu, Y. *et al.* Expanding the Schulze–Hardy Rule and the Hofmeister Series to Nanometer-Scaled Hydrophilic Macroions. *Chem. Eur. J.* **24**, 5479–5483 (2018).
196. Luo, Y., Li, H., Gao, X. & Tian, R. Description of colloidal particles aggregation in the presence of Hofmeister effects: on the relationship between ion adsorption energy and particle aggregation activation energy. *Phys. Chem. Chem. Phys.* **20**, 22831–22840 (2018).
197. Nowicki, W. & Nowicka, G. Verification of the Schulze-Hardy rule: a colloid chemistry experiment. *J. Chem. Educ.* **71**, 624 (1994).
198. Muráth, S., Sáringer, S., Somosi, Z. & Szilágyi, I. Effect of ionic compounds of different valences on the stability of titanium oxide colloids. *Colloids and Interfaces* **2**, 32 (2018).
199. Oncsik, T., Trefalt, G., Borkovec, M. & Szilagy, I. Specific ion effects on particle aggregation induced by monovalent salts within the Hofmeister series. *Langmuir* **31**, 3799–3807 (2015).
200. López-León, T., Santander-Ortega, M. J., Ortega-Vinuesa, J. L. & Bastos-González, D. Hofmeister effects in colloidal systems: influence of the surface nature. *J. Phys. Chem. C* **112**, 16060–16069 (2008).
201. Hofmeister, F. About the science of the effect of salts. *Arch. Exp. Pathol. Pharmakol* **24**, 247–260 (1888).
202. Kunz, W., Henle, J. & Ninham, B. W. ‘Zur Lehre von der Wirkung der Salze’ (about the science of the effect of salts): Franz Hofmeister’s historical papers. *Curr. Opin. Colloid Interface Sci.* **9**, 19–37 (2004).
203. Hjorth, M., Christensen, K. V., Christensen, M. L. & Sommer, S. G. Solid-liquid separation of animal slurry in theory and practice. in *Sustainable Agriculture* **2**, 953–986 (2009).
204. Dickin, S. K., Schuster-Wallace, C. J., Qadir, M. & Pizzacalla, K. A review of health risks and pathways for exposure to wastewater use in agriculture. *Environ. Health Perspect.* **124**, 900–909 (2016).
205. Wang, Y., Gao, B., Yue, Q., Wei, J. & Li, Q. The characterization and flocculation

- efficiency of composite flocculant iron salts-polydimethyldiallylammonium chloride. *Chem. Eng. J.* **142**, 175–181 (2008).
206. Gerchman, Y. *et al.* Effective harvesting of microalgae: Comparison of different polymeric flocculants. *Bioresour. Technol.* **228**, 141–146 (2017).
 207. Huang, X. *et al.* Effect of using polydimethyldiallylammonium chloride as coagulation aid on polytitanium salt coagulation performance, floc properties and sludge reuse. *Sep. Purif. Technol.* **143**, 64–71 (2015).
 208. Razali, M. A. A., Ahmad, Z., Ahmad, M. S. B. & Ariffin, A. Treatment of pulp and paper mill wastewater with various molecular weight of polyDADMAC induced flocculation. *Chem. Eng. J.* **166**, 529–535 (2011).
 209. Oveissi, F., Sitter, T. & Fatehi, P. PDADMAC as a flocculant for lignosulfonate of NSSC pulping process. *Biotechnol. Prog.* **32**, 686–691 (2016).
 210. Wang, S., Hou, Q., Kong, F. & Fatehi, P. Production of cationic xylan–METAC copolymer as a flocculant for textile industry. *Carbohydr. Polym.* **124**, 229–236 (2015).
 211. Garcia, I. M. *et al.* Quaternary ammonium compound as antimicrobial agent in resin-based sealants. *Clin. Oral Investig.* **24**, 777–784 (2020).
 212. Nasser, R., Lee, Y. & Tam, K. C. Interfacial Control of the Synthesis of Cellulose Nanocrystal Gold Nanoshells. *Langmuir* **36**, 11215–11224 (2020).
 213. Sood, Y. V., Tyagi, R., Tyagi, S., Pande, P. C. & Tondon, R. Surface charge of different paper making raw materials and its influence on paper properties. (2010).
 214. Elazzouzi-Hafraoui, S. *et al.* The shape and size distribution of crystalline nanoparticles prepared by acid hydrolysis of native cellulose. *Biomacromolecules* **9**, 57–65 (2008).
 215. Singh, R. P. Advanced turbulent drag reducing and flocculating materials based on polysaccharides. in *Polymers and other advanced materials* 227–249 (Springer, 1995).
 216. Roth, P. J., Jochum, F. D., Forst, F. R., Zentel, R. & Theato, P. Influence of End Groups on the Stimulus-Responsive Behavior of Poly [oligo (ethylene glycol) methacrylate] in Water. *Macromolecules* **43**, 4638–4645 (2010).
 217. Gibson, M. I. & O’Reilly, R. K. To aggregate, or not to aggregate? considerations in the design and application of polymeric thermally-responsive nanoparticles. *Chem. Soc. Rev.* **42**, 7204–7213 (2013).
 218. Dutta, K. & De, S. Smart responsive materials for water purification: an overview. *J. Mater. Chem. A* **5**, 22095–22112 (2017).
 219. Ishizone, T. *et al.* Anionic polymerizations of oligo (ethylene glycol) alkyl ether methacrylates: effect of side chain length and ω -alkyl group of side chain on cloud point in water. *Macromolecules* **41**, 2963–2967 (2008).
 220. Mertoglu, M., Garnier, S., Laschewsky, A., Skrabania, K. & Storsberg, J. Stimuli responsive amphiphilic block copolymers for aqueous media synthesised via reversible addition fragmentation chain transfer polymerisation (RAFT). *Polymer (Guildf)*. **46**, 7726–7740 (2005).
 221. Zhang, C., Peng, H. & Whittaker, A. K. NMR investigation of effect of dissolved salts on the thermoresponsive behavior of oligo (ethylene glycol)-methacrylate-based polymers. *J. Polym. Sci. Part A Polym. Chem.* **52**, 2375–2385 (2014).
 222. Magnusson, J. P. *et al.* Ion-sensitive “isothermal” responsive polymers prepared in water. *J. Am. Chem. Soc.* **130**, 10852–10853 (2008).
 223. Luzon, M. *et al.* Water-soluble, thermoresponsive, hyperbranched copolymers based on PEG-methacrylates: Synthesis, characterization, and LCST behavior. *J. Polym. Sci. Part A*

- Polym. Chem.* **48**, 2783–2792 (2010).
224. Nasseri, R., Deutschman, C. P., Han, L., Pope, M. A. & Tam, K. C. Cellulose nanocrystals in smart and stimuli-responsive materials: a review. *Mater. Today Adv.* **5**, 100055 (2020).
 225. Porsch, C., Hansson, S., Nordgren, N. & Malmström, E. Thermo-responsive cellulose-based architectures: tailoring LCST using poly (ethylene glycol) methacrylates. *Polym. Chem.* **2**, 1114–1123 (2011).
 226. Blok, A. J., Chhasatia, R., Dilag, J. & Ellis, A. V. Surface initiated polydopamine grafted poly ([2-(methacryloyloxy) ethyl] trimethylammonium chloride) coatings to produce reverse osmosis desalination membranes with anti-biofouling properties. *J. Memb. Sci.* **468**, 216–223 (2014).
 227. Hribar, B., Southall, N. T., Vlachy, V. & Dill, K. A. How ions affect the structure of water. *J. Am. Chem. Soc.* **124**, 12302–12311 (2002).
 228. Marcus, Y. Effect of ions on the structure of water: structure making and breaking. *Chem. Rev.* **109**, 1346–1370 (2009).
 229. Politakos, N., Azinas, S. & Moya, S. E. Responsive Copolymer Brushes of Poly [(2-(Methacryloyloxy) Ethyl) Trimethylammonium Chloride](PMETAC) and Poly (1H, 1H, 2H, 2H-Perfluorodecyl acrylate)(PPFDA) to Modulate Surface Wetting Properties. *Macromol. Rapid Commun.* **37**, 662–667 (2016).
 230. Yuan, H. & Liu, G. Ionic effects on synthetic polymers: from solutions to brushes and gels. *Soft Matter* **16**, 4087–4104 (2020).